MICROSTRUCTURAL INVESTIGATIONS ON HOT-DIP ALUMINIZED AND SUBSEQUENT DIFFUSION TREATED AISI 321 STAINLESS STEEL

Thesis

Submitted in partial fulfilment of the requirements for the degree of

DOCTOR OF PHILOSOPHY

by

PRASHANT HUILGOL

DEPARTMENT OF METALLURGICAL AND MATERIALS ENGINEERING

NATIONAL INSTITUTE OF TECHNOLOGY KARNATAKA,

SURATHKAL, MANGALORE – 575025

JUNE, 2020

DECLARATION

I hereby *declare* that the Research Thesis entitled **"MICROSTRUCTURAL INVESTIGATIONS ON HOT-DIP ALUMINIZED AND SUBSEQUENT DIFFUSION TREATED AISI 321 STAINLESS STEEL"** which is being submitted to the **National Institute of Technology Karnataka, Surathkal** in partial fulfilment of the requirements for the award of the Degree of **Doctor of Philosophy** in the **Department of Metallurgical and Materials Engineering** is a *bonafide report of the research work carried out by me*. The material contained in this Research Thesis has not been submitted to any University or Institution for the award of any degree.

PRASHANT HUILGOL

Register Number: 121201MT12F02

Department of Metallurgical and
Materials Engineering

Place: NITK Surathkal,

Date: 19/06/2020

C E R T I F I C A T E

This is to certify that the Research Thesis entitled **"MICROSTRUCTURAL INVESTIGATIONS ON HOT-DIP ALUMINIZED AND SUBSEQUENT DIFFUSION TREATED AISI 321 STAINLESS STEEL"** submitted by **Mr. Prashant Huilgol (Register Number: 121201MT12F02)** as the record of the research work carried out by him, *is accepted as the Research Thesis submission* in partial fulfilment of the requirements for the award of degree of **Doctor of Philosophy.**

Research Guides

Prof. Udaya Bhat K.   Prof. K. Rajendra Udupa

Professor   Professor

Chairman – DRPC

Dept. of Metallurgical and Materials Engineering, NITK

Dedicated

to

Lord Udupi Shri Krishna

ACKNOWLEDGEMENTS

ABSTRACT

In this study, the formation of microstructural features during hot-dip aluminizing and subsequent diffusion treatment of AISI 321 stainless steel is investigated. The mechanism of microstructural evolution is compared with the low-carbon steel/Al and AISI 430 steel/Al system. The microstructural details are characterized by scanning electron microscopy (SEM), transmission electron microscopy (TEM) and X-ray diffractometry (XRD). During solid-liquid interaction, an aluminide(intermetallic) layer is formed at the interface between steel and aluminum. The aluminide layer consisted of two phases; namely; $Al_{13}Fe_4$ and Fe_2Al_5 in case of the low-carbon steel/Al and the AISI 430 steel/Al system. The growth of the aluminide layer is parabolic following reaction-diffusion type of growth mechanism. In the case of AISI 321 steel/Al system, the constituent phases of the aluminide layer are found to depend on the dipping time. During short interaction time of 10 s, metastable microstructures were formed. These are $FeAl_m$, multiple twinned $Al_{13}Fe_4$ formed in the aluminide layer and $Al_3(NiFe)$ formed in the topcoat as one of the eutectic phases with Al. With the increase in dipping time to 10 minutes, the aluminide layer consisted of nanocrystalline Fe_2Al_5, Al_7Cr, and Al. crystalline approximant phases closely related to quasicrystals were observed. Ordered phases with ordering along [100] direction is observed. Two variants, five-layered and eight-layered ordered phases are present. O_E type of Al-Fe-Cr orthorhombic approximant phase was observed. The topcoat consisted of intermetallic phases such as Al_7Cr and $Al_{13}Fe_4$ dispersed in an Al matrix. The mechanism of microstructural evolution in case of AISI 321 steel/Al system is found to be of dissolution-nucleation type. Diffusion treatment of the aluminized AISI 321 stainless steel was carried out to investigate the phase transformation in the coating during high-temperature exposure. The coating transformed into a layered structure consisting of four layers. The outermost layer consisted of Fe_2Al_5 phase. The next layer consisted of a mixture of three phases consisting of Fe_2Al_5, disordered FeAl and a new phase with a simple cubic structure. The lattice parameter of the simple cubic structure was measured to be 7.2 Å, and that of disordered FeAl is 4.8 Å. The phase with the simple cubic structure shared a cube on cube orientation relationship with the disordered FeAl. Towards the base metal side, FeAl and ferritic layers were observed.

The ferritic layer formed by diffusion of aluminum atoms and precipitation of the NiAl phase. Finally, the hot-corrosion resistance of aluminized AISI 321 steel under the salt mixture of 60% V_2O_5 + 40% Na_2SO_4 at 700 °C and cyclic oxidation test under an open atmosphere at 900 °C was evaluated. The formation of adherent Al_2O_3 scales on the coated sample provided increased resistance to hot corrosion, while discontinuous oxide scales with cracks and spallation caused poor cyclic oxidation resistance.

CONTENTS

LIST OF FIGURES

wt.%Si

LIST OF TABLES

NOMENCLATURE

AISI   American Iron and Steel Institute

ASM   American Society for Metals

BCC   Body centered cubic

BSE   Backscatter electron

CVD   Chemical vapor deposition

EDS   Energy dispersive spectroscopy

FCC   Face centered cubic

FFT   Fast Fourier transform

HDA   Hot-Dip aluminizing

IML   Intermetallic layer

NBD   Nano beam diffraction

PVD   Physical vapor deposition

SAED   Selected area electron diffraction

SEM   Scanning electron microscopy

TEM   Transmission electron microscopy

XRD   X-ray diffraction

YSZ   Yittria stabilized zirconia

CHAPTER 1

INTRODUCTION

Steels are widely used engineering materials in the industry due to their wide range of properties (Ashby 2011; Barnes and Pashby 2000). They are used in critical industrial systems, like steam turbines, various gas turbines, nuclear power generation systems, coal gasifiers and petrochemical refiners which operate under very aggressive environments. These environments include high temperature, large temperature gradient, presence of oxidizing and corroding environments, erosion and impact conditions due to the presence of particulate materials, high pressures and large stresses (Stroosnijder et al. 1994). Steels undergo degradation under such environments. Protective coatings are employed to prevent steels from such degradation. Coatings for high-temperature application are typically alumina, chromia or silica formers. The use of Cr_2O_3 (chromia) forming coatings is limited to temperatures below 1000 °C. Above this temperature, Cr_2O_3 transforms into volatile CrO_3 according to the following reaction:

$$1/2Cr_2O_3 + 3/4O_2 \longrightarrow CrO_3. (g) \qquad (1)$$

On the other hand, SiO_2 (silica) is not suitable at low pressures as it reacts with water vapour to form volatile $Si(OH)_4$ gas (Giggins and Petit 1971). Cr_2O_3 also undergo a similar kind of water vapour enhanced volatility. For high-temperature applications, coatings that form Al_2O_3 (alumina) are preferred. Steels are coated with the aluminium (known as aluminizing) to improve high-temperature oxidation and corrosion resistance (Pérez et al. 2001; Sah et al. 2018; Dorcheh and Galetz 2016) as aluminium forms protective alumina (Al_2O_3) scales.

Aluminized low carbon steels are being increasingly used in mufflers, heaters, ovens, pipes and containers carrying corrosive liquids and baking pans. Aluminized steels used as roofing material reflects heat and helps in reducing building cooling costs. Also, these type of roofings perform better in harsh industrial and marine environments compared to the galvanized steels. During the process of hot-pressing or hot-stamping

1

oxide scales are formed due to high operating temperature. The scales formed causes additional problem for the final coating of the product. An additional step is required to remove the oxide scale which results in considerable increased cost. The aluminizing of the steel prior to processing eliminates these shortcomings and reduce processing costs. Also, the aluminide steels are reported to have better paintability and weldability (Suehiro et al. 2003). Aluminized low-carbon steels provide better resistance to water vapour enhanced high temperature oxidation and can replace high alloy steels used in automotive exhaust manifolds (Wang & Badruddin 2010). Aluminized stainless steels are being used as hydrogen permeation barriers in nuclear industries. Aluminized stainless steels of various grades have shown improved resistance to high temperature oxidation, corrosion and wear. Overall, the desired charecteristics of aluminized steels are i. The coating should protect the steel material from environmental degradation (oxidation and corrosion) ii. The coating should be adherent under high temperature and high stress conditions iii. The aluminized steel should have good weldability and iv. Coating should provide resistance to surface degradation like erosion and wear.

 Among various techniques available for coating Al on steel (Bhat 2015), hot-dip aluminizing is the preferred technique due to its low cost and ease of processing (Ryabov 1985). The coating obtained by this method is expected to have all the desired charecteristics as mentioned above. The formation of thin, compact and slow growing oxide scale provides resistance to oxidation and corrosion. Adherent coating is formed due to strong metallurgical bond formed due to reaction between steel and aluminum. The formation of hard intermetallic phases are expected to provide resistance to erosion and wear.

In the process of hot-dip aluminizing, steel is dipped in molten Al bath for a certain duration to obtain the coating. During this process, solid-liquid interaction between the steel and molten Al takes place to form an intermediate reaction layer known as the aluminide layer. The mechanism of the formation of interface microstructure is said to be of the reaction-diffusion type. The major issue during hot-dip aluminizing is the formation of undesired inherently brittle intermetallic phases at the interface due to the wide difference in metallurgical properties of steel and aluminium. A similar phenomenon occurs during the fusion welding of aluminium and steel, and

2

investigations are being carried out to control the interface microstructure (Yang et al. 2015; Qiu et al. 2009). The quality of the coating depends on the microstructure at the interface. Therefore, the main focus is on to understanding the evolution of interface microstructure, selection of proper process parameters such as time-temperature and the influence of alloying elements.

Stainless steel of grade AISI 321 is a titanium stabilized austenitic steel with chromium and nickel close to 18 wt. % and 11 wt. % respectively. It is used in jet engine parts, aerospace exhaust manifolds, components for the nuclear industry, and chemical processing equipments. It is also used as a structural material in fusion reactors. The hot-dip aluminized AISI 321 steel is being used as a hydrogen permeation barrier in nuclear industries (Cao et al. 2016; Yang et al. 2016). During exposure to high-temperature applications, the microstructure of the aluminized steel transforms due to the interdiffusion of elements between coating and substrate.

The present investigation aims to study the evolution of microstructure at the interface between the molten aluminium and stainless-steel grade AISI 321 during hot-dip aluminizing. The effect of the alloying element present in the steel on microstructural formation is studied. Further, the mechanism of microstructural formation is then established by comparing with the microstructural formation at the interface between low-carbon steel/Al and ferritic steel AISI 430/Al. The microstructural transformations of the aluminized AISI 321 steel during the diffusion treatment is studied. Detailed microstructural investigations are carried out by transmission electron microscopy, and results are discussed. The details of the study are represented in this thesis as different chapters. A brief review of the literature is presented in the second chapter. The third chapter deals with the experimental methodology and characterization techniques used in the investigation. In the fourth chapter, the growth kinetics of the aluminide layer for the three systems are investigated. Detailed analysis on the evolution of the microstructure during the interaction between AISI 321 steel and Al is presented in the fifth chapter. Phase transformations during the diffusion treatment of the aluminized 321 steel are discussed in chapter six. In the seventh chapter, the cyclic hot-corrosion and oxidation performance of the aluminized steel is discussed. Finally, inferences of

the study are presented in the eighth chapter. Scope for further studies and publications from this research work are also presented at the end.

CHAPTER 2

LITERATURE REVIEW

Aluminum alloys and steels are two widely used engineering materials in the industry due to their wide range of mechanical and physical properties. (Ashby 2011; Barnes and Pashby 2000). There is a demand for developing components with the combination of good properties like high strength and stiffness of the steel with lightweight and superior corrosion resistance of the aluminum. In particular to the automotive industry, the urge to have better efficiency and lesser CO_2 emission drives the industry to reduce the component weight by replacing part of the steel components with the aluminum alloys. This necessitates the joining of steel with aluminum. Several joining techniques are developed including both fusion and solid state processing (Sun et al. 2004; Murakami et al. 2003; Fukumoto et al. 2017; Lee and Kumai 2006).

The steels are coated with the aluminum (known as aluminizing) to improve high-temperature oxidation and corrosion resistance (Pérez et al. 2001; Sharafi and Farhang 2006; Sah et al. 2018; Dorcheh and Galetz 2016). The aluminum deposit forms alumina (Al_2O_3) during exposure to high temperatures. The alumina formed is thin, compact and slow growing oxide. It prevents base metal from further oxidation and corrosion. There are several techniques employed for the aluminizing of steels and are mentioned below.

i. Hot-dip aluminizing

ii. Chemical vapor deposition (CVD) or pack cementation

iii. Thermal spray processes

iv. Slurry aluminizing

v. Electrochemical methods

vi. Laser surface alloying

vii. Friction surfacing

viii. Foil aluminizing

ix. Other techniques like sol-gel, spray pyrolysis, reaction sintering, PVD (physical vapour deposition), and powder liquid coating

The complete process details regarding these processes are discussed in detail in the following references (Bhat 2015; ASM handbook 1994).

Among above-mentioned techniques, the most commonly used one is hot-dip aluminizing. Hot-dip aluminizing process is a liquid-based coating technique where a solid steel sample is dipped in the molten aluminum bath (Rybov 1985). The molten aluminum reacts with the steel to form intermetallic phases at the interface. This technique is taken for the study in the present investigation.

In the following sections, a brief review of the literature is summarized based on the concepts of diffusion, nucleation of intermetallic phases at the interface, the evolution of the microstructure at the solid-liquid interface (Fe-Al system), the influence of the alloying elements, the growth kinetics of intermetallic phases and phase transformations.

2.1 Development of the Microstructure at the Interface

The microstructural evolution at the interface between two dissimilar materials takes place by chemical reactions and interdiffusion. The thermodynamics gives information regarding the driving force for chemical reactions and phase stability, while the difference in the chemical potentials of the components across the interface is the driving force for the diffusion. The formation of reaction product at the interface between two components could be predicted by the equilibrium phase diagram. At the given temperature, typically all the phases present in the phase diagram should exist and the concentration of each phase could be obtained from the phase diagram.

Consider the binary phase diagram as shown in Fig. 2.1. At the temperature T, two terminal solid solutions α and β phases and an intermediate phase η are present.
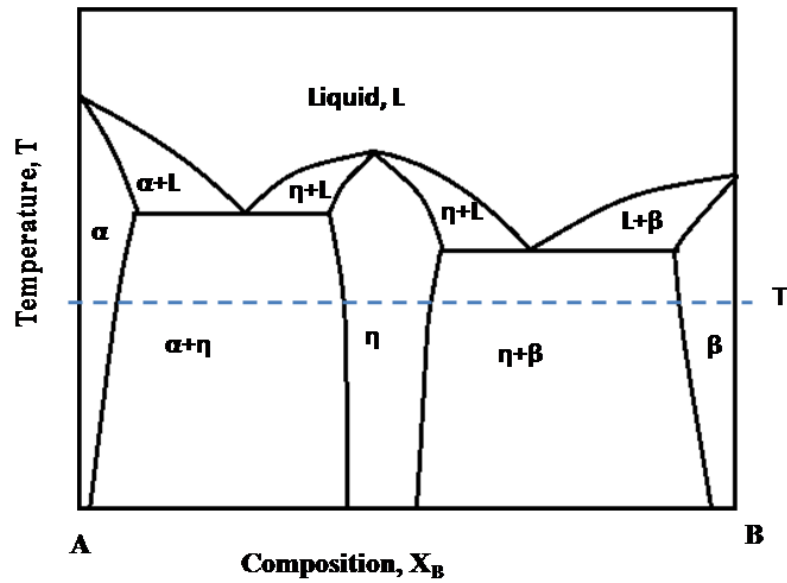
Fig. 2.1 Hypothetical binary phase diagram with two terminal solid solutions and an intermediate phase.

The corresponding free energy- composition diagram is shown in Fig. 2.2. A diffusion couple made at temperature T between two pure end members A and B is presented in Fig. 2.3.
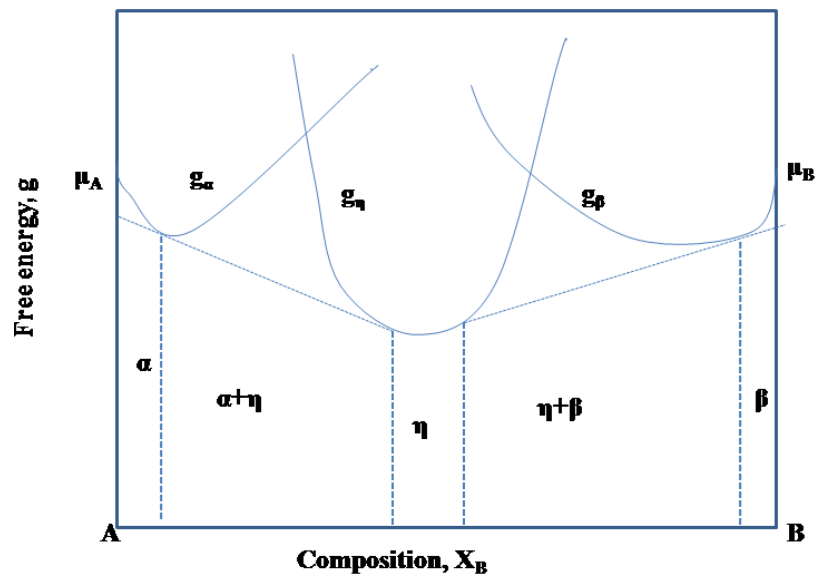
Fig. 2.2 Free energy –composition plot for the phase diagram in Fig. 2.1
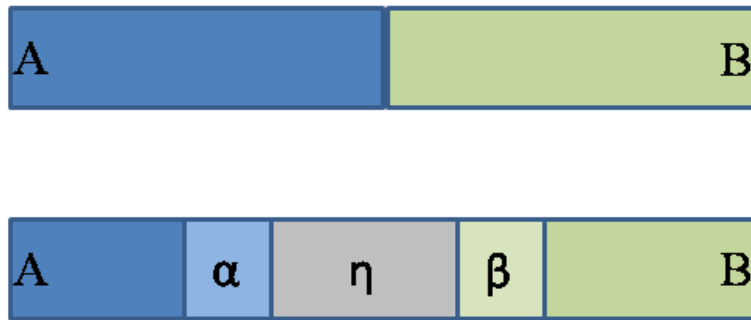
Fig. 2.3 Diffusion couple between two end members A and B.

At the temperature of interest T, five-phase regions exist between two end members (Fig. 2.1). The terminal solid solutions α and β, phase mixture of α+η, single phase η and the phase mixture of η and β. The driving force exists for diffusion due to the difference in chemical potential. From the Gibbs phase rule F=C-P+2, where F is the degree of freedom, P is the number of phases and C is the number of components. The number of components for a binary system is 2 and the experiments are carried out at constant pressure and temperature, F=2-P. Since composition is one variable, only single-phase regions are observed in a binary diffusion couple. Two-phase regions cannot grow in a binary diffusion couple as there is no chemical potential gradient in a two-phase field.

Therefore, considering the phase diagram given in Fig. 2.1, three single phases α, η and β are formed in the interdiffusion zone between the end members A and B.

2.1.1 Nucleation of the intermetallic phase

Nucleation of the new intermetallic phase at the interface is at first preceded by interdiffusion. The chemical driving force necessary for nucleation could be known from thermodynamic data or determined using CALPHAD method (Kaufman and Bernstein 1970). For example, let us consider the binary diffusion couple as shown in Fig. 2.3 (corresponding free energy curves are presented in Fig. 2.2). Let us assume that the component B diffuses much faster than A. At first, the terminal solid solution α forms by diffusion of B atoms into A. With further diffusion, α phase is supersaturated with B atoms and a driving force for nucleation of η phase exists. Therefore, η phase should nucleate when the α phase reaches equilibrium concentration X_{eq} (tangent

between α and η curves). Similarly, β is formed by diffusion of A atoms. By the nucleation of new phase η, two new interfaces are formed, i.e., α/ η and β/ η interface. The formation of interface leads to an increase in surface energy. From the classical nucleation theory (shown in Fig. 2.4) the activation energy for nucleation ΔG* is proportional to $\gamma^3/ \Delta G_v^2$.
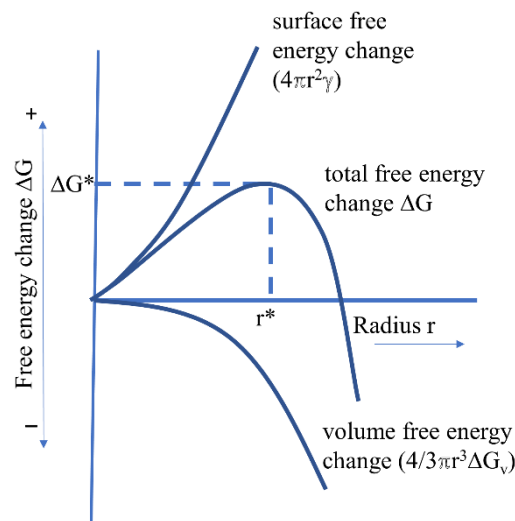
Fig. 2.4 Free energy change as a function of the size of the nucleus (Raghavan 1987).

Where γ is the surface energy per unit area and ΔG_v is the volumetric free energy change per unit volume. Formation of a nucleus causes a volume change and introduces a new energy term known as strain energy ΔG_s. The activation energy for nucleation is now proportional to $\gamma^3/ (\Delta G_v + \Delta G_s)^2$. Nucleation of critical size nucleus becomes difficult if strain energies involved is large and sometimes may lead to nucleation of the metastable phases. Therefore, nucleation of a phase is a function of surface energy γ, chemical driving force ΔG_v, strain energy ΔG_s and activation energy for growth i.e. the diffusion of elements (Laurila et al. 2012).

2.1.2 Reaction-diffusion model between solid iron and liquid aluminum.

When the solid iron comes in contact with the liquid aluminum, the reaction between the two takes place and an intermediate phase is formed at the interface. The mechanism of the intermetallic phase growth at the interface is of reaction-diffusion type. Liberski

et al. (2008) tried to explain the mechanism of growth of coating. At first, the cold iron substrate comes in contact with the molten aluminum, due to heat transfer between the cold steel and molten Al, bath temperature drops locally. Later, when the substrate temperature rises, a reaction between solid iron and the liquid aluminum takes place to form Fe-Al intermetallic phases. In the next stage, two directional diffusion known as reaction-diffusion takes place and within a relatively short span of time, the phases anticipated by binary iron–aluminum system are formed. Further, the growth of the formed phase occurs by a simultaneous process of interdiffusion (Al towards Fe & Fe towards molten Al) and dissolution of the phase that is in contact with the molten aluminum bath. A model of the reaction during hot-dipping is shown in Fig. 2.5
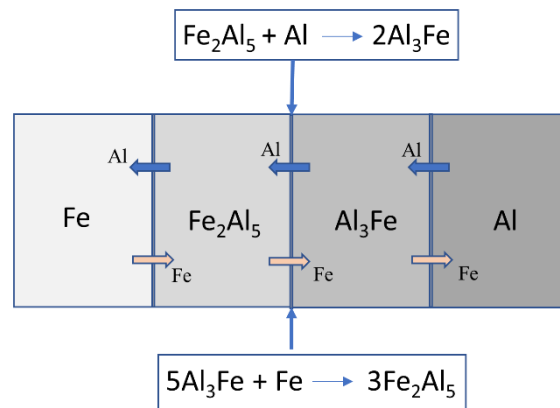
Fig. 2.5 Model of the reaction during hot dipping (Liberski et al. 2008)

Dybkov (2013) explains that the layer growth is due to continuous alteration of two consecutive steps, namely,

i. Diffusion of atoms of the reactants across its bulk in the opposite directions;

ii. Subsequent chemical transformations taking place at the layer interfaces with the participation of the diffusing atoms of one of the components and the surface atoms of another component.

This mechanism is illustrated with an example and a schematic is shown in Fig. 2.6.
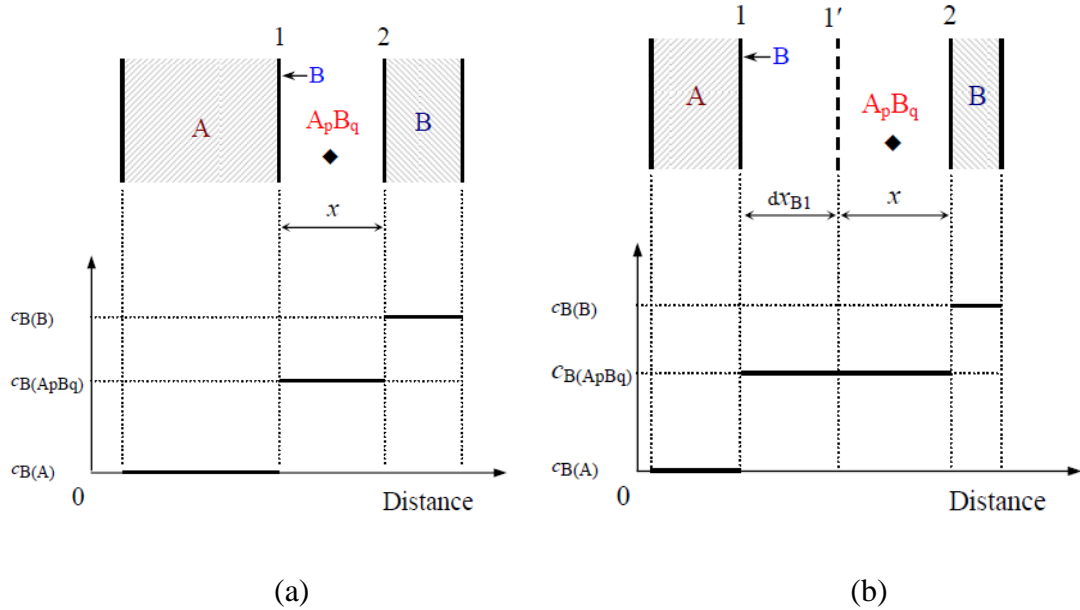
Fig 2.6 Schematic diagram to illustrate the growth process of the A_pB_q layer between elementary substances A and B at the expense of diffusion of B atoms and their subsequent chemical interaction with the surface atoms of A (a) at time t_o (b) at time t_o+dt (Dybkov 2013)

Figure 2.6 illustrates the mechanism of reaction-diffusion at the expense of the diffusion of B atoms. The graph is a plot of the composition of B vs distance. For A_pB_q compound phase to grow, B atoms have to diffuse through A_pB_q and then react with the surface of A atoms at the interface of 1 according to the equation,

$$qB_{diff} + pA_{surf} = A_pB_q \tag{1}$$

and A atoms have to diffuse through A_pB_q layer and react with the surface of B atoms at the interface 2, according to the equation

$$pA_{diff} + qB_{surf} = A_pB_q \tag{2}$$

It is to be noted that the diffusion of two components A and B across A_pB_q layer and their reactions at the interface generally are different. Hence, preferential growth of a layer on any one side is expected.

The effect of dissolution of the solid substrate in liquid metal was studied by Dybkov (2013). The rate of dissolution of any solid in the well-agitated liquid phase is described

by the form

$$\frac{dc}{dt} = \frac{kS}{v} (C_s\text{-}C) \qquad\qquad (3)$$

Where C_s is the solubility (saturation concentration) of the substrate in molten metal in kgm^{-3}, C is the concentration of the dissolved substrate in molten metal at time t, k is the dissolution rate constant, S is the surface area of the solid in contact with the molten metal and v is the volume of liquid.

The dissolution rate constant could be expressed as follows; $k = D_A /\delta$, where D_A is the coefficient of diffusion of the atoms of dissolving solid substrate across the diffusion boundary layer adjacent to the surface of the solid in contact with the liquid and δ is the thickness of diffusion boundary layer (Dybkov 2013; Nernst 1904).

Dybkov (1994) also studied the effect of dissolution of the compound layer into molten metal. If the dissolution rate is greater than the rate of chemical reaction at the interface, the layer may disappear and if the growth of the layer is diffusion controlled it does not disappear completely, instead, the layer thickness reaches some limiting value and practically remains unchanged.

2.1.3 Iron–aluminum equilibrium phase diagram

The binary Fe-Al phase diagram according to Kattner and Burton (1992) is as shown in Fig. 2.7. It exhibits two terminal solid solutions and six intermediate phases. On the iron-rich side solid solubility of Al in FCC, γ-Fe is 1.3 at. %, while that in α-Fe solubility extends up to 45 at. %.
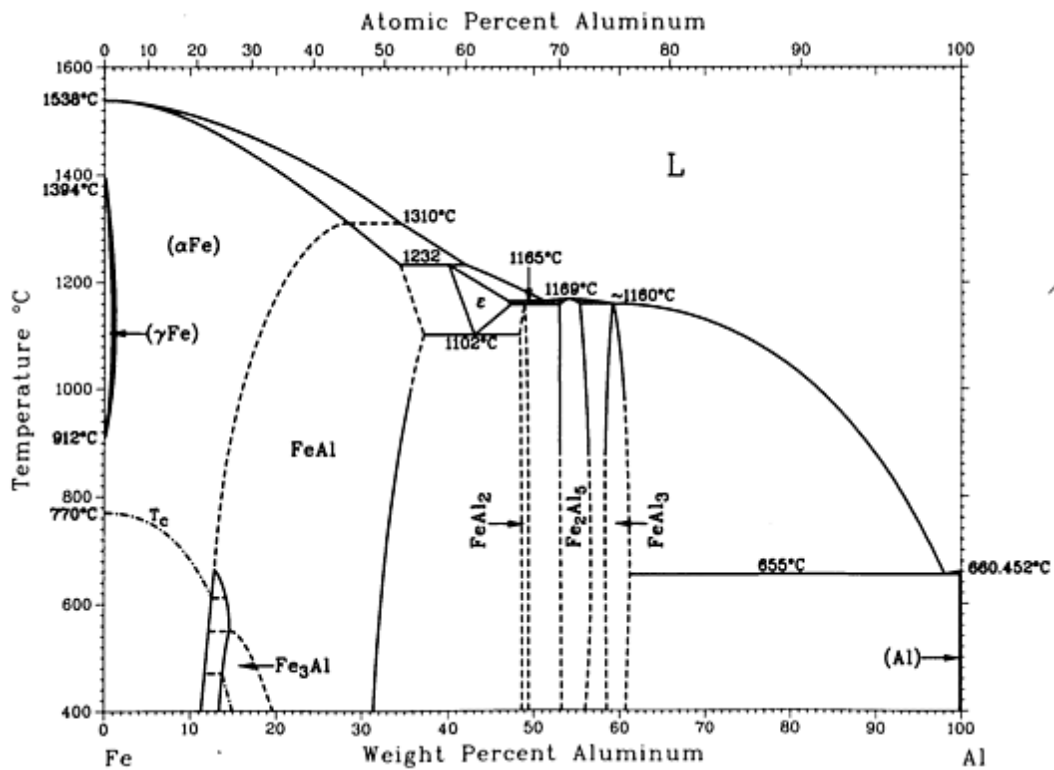
Fig. 2.7 Equilibrium phase diagram of the binary Fe-Al system (Kattner and Burton 1992)

Between 0 and 55 at. % two ordered phase exists. Ordered Fe_3Al has DO_3 structure and exists over the composition range of 23-34 at.%. It is stable below 552 °C. Another ordered phase in this system is FeAl having B2 structure. It exists over the composition range of 24 at. % to 55 at. %. Continuous small dotted lines show the transition between disordered α-Fe phase to ordered FeAl phase. Long dotted lines in the composition range of 0 to 22 at. % show a magnetic transition from ferromagnetism to paramagnetism.

ε –phase (Fe_2Al_3) is an aluminum rich phase and its crystal structure is not clearly understood. It forms by a peritectic reaction at 1232 °C. According to Kattner and Burton (1992) it has a complex cubic structure with 16 atoms per unit cell designated as Fe_2Al_3, while, Sundman et al. (2009), Stein et al. (2010) say that ε -phase is body-centred cubic structure with 52 atoms per unit cell (space group $I\bar{4}3m$, Cu_5Zn_8 type) designated as Fe_5Al_8. Vogel et al. (2010) and Stein et al. (2010) have presented the lattice parameter of ε -phase as a=8.9752 Å, at 1120 °C. The measurement is done using in-situ high-temperature neutron diffraction technique, which is 3 times that of the lattice parameter

of B2 FeAl phase. $FeAl_2$ phase (ζ) is stable in the range of 66-66.9 at. % with a triclinic crystal structure. $FeAl_2$ is formed during the peritectoid reaction at 1153 °C. It is also formed by the eutectoid decomposition of Fe_5Al_8 at 1089 °C (Sundman et al. 2009). Fe_2Al_5 (η) is a congruently melting phase which melts at 1169 °C (Pretorius et al. 1993). It crystallizes as an orthorhombic crystal structure but the number of atoms per unit cell is not yet determined. $FeAl_3$ (θ) also represented as $Al_{13}Fe_4$ in the literature (for consistency $Al_{13}Fe_4$ will be used) is an aluminum rich stable phase ranging from 74.5 at. % to 76.5 at. %. It melts at 1160 °C and crystallizes as a monoclinic crystal structure with 102 atoms per unit cell. $Al_{13}Fe_4$ is also formed during the eutectic reaction at 655 °C. The solubility of Fe in aluminum is only 0.002 at.%. A brief summary of the properties of various Fe-Al phases is presented in Table 2.1.

A few metastable phases have been reported in the literature and some are presented in Table 2.2 (Kattner and Burton 1992). Celil et al. (1998) have reported $FeAl_6$ and $FeAl_m$ (4≤ m ≤4.5) as metastable phases during direct chill casting of 1xxx series Al ingots. $FeAl_6$ formed when the cooling rate is about 10 °C/s, while $FeAl_m$ formed with cooling rates greater than 20 °C/s. Dunlap et al. (1986) have reported an icosahedral $Fe_{14}Al_{86}$ during their study on rapidly solidified Fe-Al alloys. The $FeAl_4$ phase is identified when Al 4%Fe is rapidly quenched (Dunlap et al. 1988). Bhat et al. (2013) have reported a metastable phase formed during aluminizing with Al/Fe ratio greater than 3.26. Dybkov (2013), Hanseen et al. (1958) have reported Fe_2Al_7 phase with homogeneity range indicated as 77.5 to 78.6 at. % Al. Although the composition is close to that of the $Al_{13}Fe_4$ phase, it is not clear whether it is a metastable phase or a phase similar to $Al_{13}Fe_4$.

Table 2.1 Properties of Fe-Al intermediate phases (Shahaverdi et al. 2002; Kattner and Burton 1992; and Stein et al. 2010)

Phases	Crystal Structure	Stability range (at%)	Pearson symbol	Space group	Melting/transformation temperature	Density (g/cc)
Fe solid solution	BCC	0-45	$cI2$	$Im\bar{3}m$	1310 °C-1538 °C	7.8
γ-Fe	FCC	0-1.3	$cF4$	$Fm\bar{3}m$	1394 °C	7.8
FeAl	BCC (order)	23-55	$cP8$	$Pm\bar{3}m$	1232 °C -1310 °C	5.58
Fe_3Al	DO_3	23-34	$cF16$	$Fm\bar{3}m$	552 °C	6.72
Fe_2Al_3 (ε) or Fe_5Al_8	Cubic complex	58-65	$cI16$? Or $cI52$	$I\bar{4}m$	1102-1232 °C	-
$FeAl_2$ (ζ)	Triclinic	66-66.9	$aP18$	$P1$	1165 °C	-
Fe_2Al_5 (η)	Orthorhombic	70-73	oC?	$Cmcm$	1169 °C	4.11
$Al_{13}Fe_4$ (θ)	Monoclinic	74.5-76.5	$mC102$	$C2/m$	1160 °C	3.9
Al solid solution	FCC	99.998-100	$cF4$	$Fm\bar{3}m$	660 °C	2.69

Table 2.2 Metastable phases in Fe-Al System (Kattner and Burton 1992)

Phases	Crystal structure	Stability range (at.%)	Pearson symbol	Space group
Fe_2Al_9	Monoclinic	81.8	*mP22*	*P21/c*
$FeAl_6$	Orthorhombic	85.3	*oC28*	*Cmc21*

Compounds like $FeAl_2$, Fe_2Al_5 and $Al_{13}Fe_4$ have high aluminum content and are brittle in nature. Conversely, Fe_3Al and FeAl have high iron content and less brittle in nature. They exhibit better wear resistance, oxidation and corrosion resistance, fracture toughness, specific strength and hence are candidate materials for high-temperature structural applications (Cho et al. 1999; Morris et al. 2004). Therefore, during hot-dip aluminizing preferential growth of Fe_3Al and FeAl is preferred from the application point of view. Some thermodynamic properties of Fe-Al intermediate phases are shown in Table 2.3.

Table 2.3. Thermodynamic properties of Fe-Al intermediate phases (Shahverdi et al. 2002)

Intermediate phase	ΔH_{298} (J mol^{-1})	ΔS_{298} (K^{-1} mol^{-1})	ΔG_{973} (J mol^{-1})
$Al_{13}Fe_4$ (θ)	-112560	95.6	-22869
Fe_2Al_5 (η)	-194040	166.7	-19636
$FeAl_2$ (ζ)	-81900	73.3	-16999
FeAl	-51240	51	-11090
Fe_3Al	-57372	28	-4827

2.2 Microstructure of the Hot-dip Aluminized Steel

The phases identified at the interface between steel and aluminum during hot-dip aluminizing are Fe_2Al_5 and $Al_{13}Fe_4$ (Gebhardt and Obrowski 1954; Bouche et al. 1998; Cheng and Wang 2011; Bouayad et al. 2003; Eggler et al. 1986). Gebhardt and Obrowski (1954) identified that the major intermetallic phase formed when the molten aluminum comes in contact with the solid iron or steel is Fe_2Al_5. Eggeler et al. (1986) reported that during the interaction between the solid steel with the liquid aluminum $Al_{13}Fe_4$ forms near the aluminum side and near the iron side Fe_2Al_5 intermetallic forms. Naoi and Kajihara (2007) did Al/Fe interdiffusion experiments over the temperature range 550–640 °C and found that only Fe_2Al_5 forms at the interface. Cheng & Wang (2009) identified Fe_2Al_5 as the major phase in the aluminide layer. Bhat et al. (2013) reported a metastable phase having Al/Fe ratio greater than 3.26 apart from Fe_2Al_5 & $Al_{13}Fe_4$. Bouche et al. (1998) analysed the reaction layer formed at the interface between molten aluminum and steel in the temperature range of 700 °C to 900 °C and found that the major phases are Fe_2Al_5 and $Al_{13}Fe_4$. $Al_{13}Fe_4$ formed on the aluminum side, while, Fe_2Al_5 is observed on the steel side.
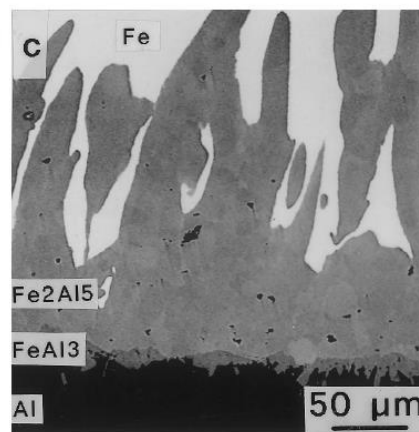
Fig. 2.8 SEM micrograph showing $Al_{13}Fe_4$ & Fe_2Al_5 phases at the interface between molten aluminum and solid iron at 800 °C, dipped for 15 min. (Bouche et al. 1998).

Typical morphology of the interface after the reaction is shown in Fig. 2.8. Also, they reported that the part of Fe_2Al_5 layer close to $Al_{13}Fe_4$ phase is polycrystalline (equiaxed) and the one close to iron is columnar in nature. The columnar grains towards the iron side are referred to as tongue like morphology. The tongue like morphology exhibited a

relationship with dipping time and it is shown in Fig. 2.9.
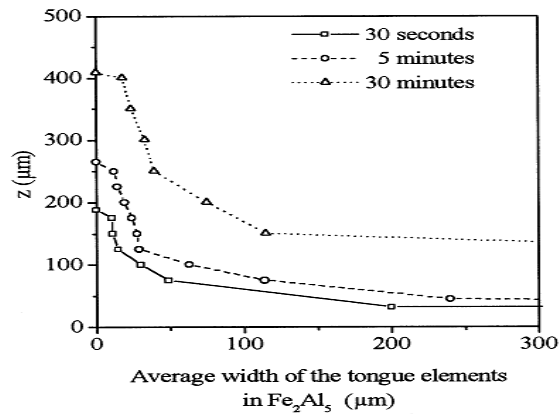
Fig. 2.9 Average width of the Fe_2Al_5 tongue like elements at 800 °C for various immersion times, Z represents the distance from $Fe_2Al_5/Al_{13}Fe_4$ interface to iron (Bouche et al. 1998).
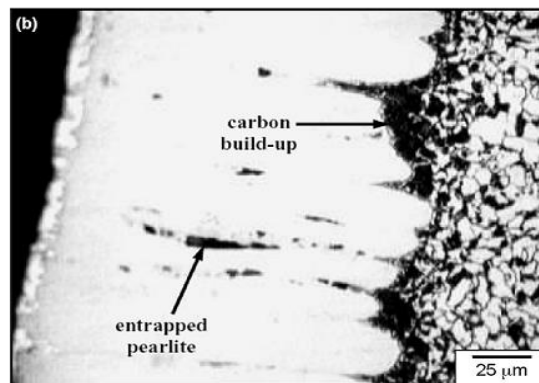
Fig. 2.10 Micrograph showing accumulation of pearlite ahead of advancing intermetallic layer (Awan et al. 2008).

Heumann and Dittrich (1959) gave an explanation for the Fe/Fe_2Al_5 interface irregularity that, this tongue-like morphology is a result of favourable conditions for aluminum atoms to diffuse along the structural vacancies in the c-axis of the Fe_2Al_5 orthorhombic. Structural vacancies assist in the movement of the aluminum atoms. Work carried out by Awan et al. (2008) showed that the growth of finger-like structure into the steel is hampered by the pearlitic areas in the microstructure of the steel. A microstructure from their investigation is shown in Fig. 2.10. They conducted

experiments with low carbon steel as well as high carbon steel and showed that finger like morphology exists for steel with very low carbon content also. This made them to conclude that finger like growth is not caused by the presence of pearlite phase but instead, it's the inherent characteristic growth of the phase during aluminizing with pure aluminum.

2.2.1 Growth mechanism of phases during hot-dip aluminizing.

Bouche et al. (1998) studied growth mechanism in the temperature range from 700 to 900 °C and found to be mainly controlled by the diffusion regime. Bouayad et al. (2003) showed that $Al_{13}Fe_4$ grew under a kinetic regime, while Fe_2Al_5 grew under diffusion regime during the aluminising of pure solid iron with pure liquid aluminum. They conducted experiments at 700, 800 and 900 °C. Glassbrenner et al. (1997) reported that the diffusion rate of aluminum towards the steel substrate is faster than that of iron in the opposite direction. Springer et al. (2011) investigated interdiffusion between low carbon steel and pure aluminum in solid-solid, solid-semisolid diffusion couples at 600 °C and solid-liquid diffusion couples at 675 °C. Both solid/solid and solid/liquid interdiffusion experiments followed a parabolic growth rate for the intermetallic layer. It was also observed that the growth rate of η-layer (Fe_2Al_5) formed during solid-solid interdiffusion with Al-Si alloy at 600 °C is significantly larger than that of reaction with pure Al at the same temperature. This contradicts earlier proposed atomistic explanations that the Si may reduce the atomic mobility in the Fe_2Al_5 phase by occupying structural vacancies. Dybkov (2013) suggests that layer growth kinetics as linear parabolic rather than simply parabolic. The formation of compound layers at the interface is due to the reaction of the diffusing species and further growth takes place by diffusion of elements. This mechanism is referred to as reaction-diffusion. During the initial stages, the thickness of the compound layer is small and the growth of the layer is governed by the reaction at the interface. After compound layer reaches a minimal thickness, diffusion of the elements through the layer is rate controlling step and thereafter growth behavior becomes parabolic.

2.2.2 Effect of ternary alloying elements

Effect of small amount of alloying additions to molten aluminum has been studied by several authors. According to the studies carried out by Yousaf et al. (2011), the addition of 11 wt. % Cu in pure Al reduces the thickness of the intermetallic layer up to 75%. This is attributed to the formation of tetragonal intermediate phases of Al_2Cu and Al_7Cu_2Fe in the outer coating of the aluminized specimen. Experiments by Glasbrenner et al. (1997) reported that during hot-dip aluminizing, the addition of small amounts of W, Mo and Nb to the molten aluminum melt reduces the thickness of the intermetallic layer. Bhat et al. (2013) showed that at high temperatures, Zinc (from the flux) dissolves in the molten aluminum bath. This dissolved zinc increases the activity of aluminum and a metastable phase with Al/Fe ratio greater than 3.26 is formed. The growth rate of the intermetallic compound layers decreases with an increase in carbon content in the steel substrate and is inhibited by the silicon atoms (Bindumadhavan et al. 2000; Kobayashi and Yakou 2002). Works done by Akdinz et al. (1994) proved that the addition of silicon to the aluminum melt has an inhibitory effect on the diffusion of the aluminum into the steel during hot-dip aluminizing, thereby preventing the thickness of the brittle intermetallic layer.

Komatsu et al. (1981) and Jones et al. (1980) have a view that the silicon accelerates the velocity of the iron enrichment in the initially iron-free aluminum melts thereby reducing the thickness of intermetallic layer. But, Eggeler et al. (1986) conducted experiments between low alloyed steel and pure aluminum as well as 2% silicon containing aluminum melt at 780 °C and 792 °C respectively. They found out that velocity of iron enrichment is same for both cases and concluded that silicon acts on the solid state side while reducing the intermetallic thickness and not by iron enrichment in the molten alloy during hot-dip aluminising. Atom probe tomography experiments by Lemmens et al. (2016) have shown that the enrichment of Si at $Al_{13}Fe_4/Fe_2Al_5$ interface could suppress the growth kinetics of Fe_2Al_5 phase

Experiments conducted by Cheng and Wang (2011) on the mild steel specimen dipped in the molten baths containing pure aluminum, Al-0.5Si, Al-2.5Si, Al-5Si and Al-10Si at 700 °C for 180 s showed that as the silicon content in the molten bath increases, the

thickness of the intermetallic layer decreases. The relative thickness values of intermetallic layer is presented in Fig. 2.11. Also the interface between intermetallic layer and the steel substrate became flat.
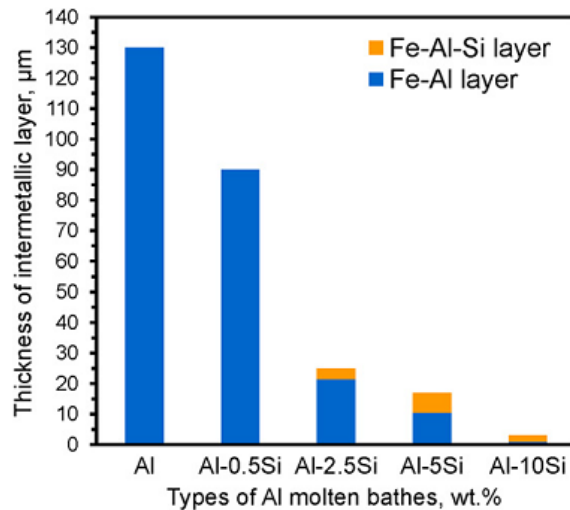
Fig. 2.11 Comparison of the thickness of intermetallic layers after mild steel is dipped in aluminum baths with various silicon additions at 700 °C for 180s (Cheng et al. 2011).

Cheng and Wang (2011) observed that when the silicon content in the bath exceeds 2.5 wt.%, the sequence of intermetallic phases observed is $Al_{13}Fe_4$ (A), Fe_2Al_5(B), $\tau_{5(c)}$-$Al_7(Fe,M)_2Si$(D) (cubic) where M is manganese, chromium or copper and τ_1-$Al_2Fe_3Si_3$(C). As the silicon content increased to more than 5 wt.%, $\tau_{5(H)}$-Al_7Fe_2Si (Hexagonal) started to appear. At around 10 wt.% Si, $\tau_{5(c)}$ disappeared, $\tau_{5(H)}$ and τ_6-Al_4FeSi phases are only observed. The evolution of microstructure with increase in the silicon percentage is shown in Fig. 2.12. Addition of 2 wt.% copper to aluminum-7 wt.% silicon reduces the growth kinetics of Fe_2Al_5 layer (Huilgol et al. 2013).

Lee et al. (2018) investigated the microstructural evolution during hot-dip aluminizing of Boron steel in Al-7 wt.% Ni-6 wt.% Si alloy at 690 °C. A ternary Al_9FeNi possessing the monoclinic crystal structure formed along with $Al_{13}Fe_4$ and Fe_2Al_5 phases by TEM investigations. Fe_3AlC formed at the interface between Fe_2Al_5 phase and the base metal. TEM investigations carried out by Shin et al. (2018) on hot-dip aluminizing of 22MnB5 steel in Al-10wt.% Si alloy observed ternary τ_1 ($Al_2Fe_3Si_3$) and τ_5 (Al_8Fe_2Si) phases and microstructural evolution were described.
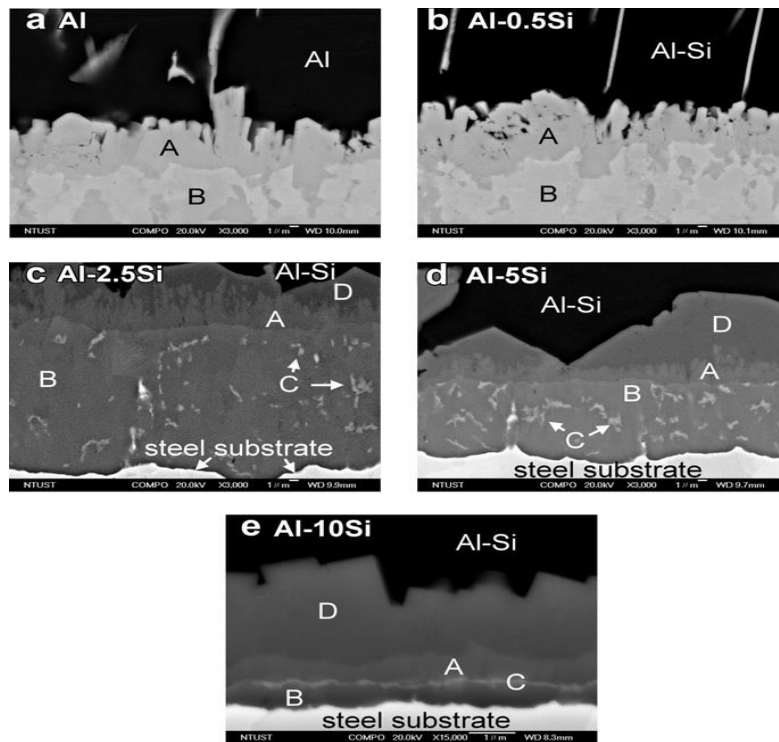
Fig. 2.12 Evolution of microstructure with increase in the percentage of silicon (a) pure Al, (b) Al-0.5 wt.%Si, (c) Al-2.5 wt.%Si, (d) Al-5wt.%Si, (e) Al-10 wt.%Si (Cheng and Wang 2011).

Dangi et al. (2018) studied the effect of a small amount of alloying additions into steel material. They considered 2 at. % addition of Mn, Ni and Si to pure iron. The study showed that the thickness of the intermetallic layer reduced with the addition of all the three elements. Silicon showed the maximum effect in reducing the intermetallic layer thickness followed by nickel and manganese. This aspect was concluded based on the diffusivities of elements in the Fe_2Al_5 phase derived from the concept of the concentration gradient and interface velocity. Hot-dip aluminizing of ferritic grade steel AISI 430 (18 wt.% Cr) formed $Al_{13}Cr_2$ (Al_7Cr) along with Fe_2Al_5 and Al_3Fe phases in the intermetallic layer (Liu et al. 2019). However, the influence of Cr on the growth kinetics was not specifically reported.

2.2.4 Microstructural changes during diffusion treatment.

The hot-dip aluminized steel consists of brittle intermetallic phases of Fe_2Al_5 and $Al_{13}Fe_4$ at the interface. Aluminum-rich brittle phases could be transformed into iron-rich ductile phases by employing diffusion treatment. Kobayashi and Yakou (2002) studied phase transformations of the aluminide layers on the 0.45 wt.% C steel aluminized in the pure aluminum bath, followed by diffusion treatment in the temperature range of 873 K to 1373 K for 1.2 ks. Their results showed that Fe_2Al_5 is the major phase at temperatures below 1273 K, while FeAl and $Al_{13}Fe_4$ phases are observed at temperatures higher than 1273 K. Deqing (2007) studied oxidation treatment in the air as well as the vacuum in the temperature range of 750 °C to 950 °C. They showed that during diffusion treatment brittle Fe_2Al_5 transforms into more ductile FeAl and Fe_3Al phases. EBSD analysis done by Cheng & Wang (2011) showed that the aluminized microstructure which initially consisted of minor volume of the $Al_{13}Fe_4$ & major volume of the Fe_2Al_5 phases transformed to $FeAl_2$ & FeAl after diffusion treatment at 750 °C for 480 h. Fig. 2.13 shows reported microstructural changes during diffusion treatment. Also, serration like morphology disappeared due to the growth of $FeAl_2$ and FeAl phases between Fe_2Al_5 and steel substrate.
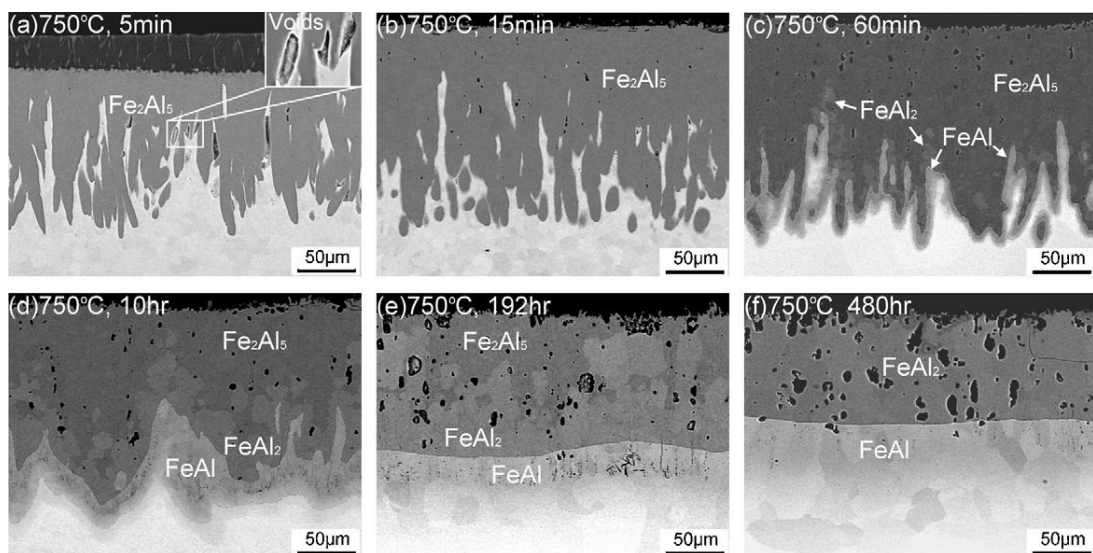
Fig. 2.13 SEM backscattered micrographs of specimens after diffusion treatment at 750°C for various times (Cheng and Wang 2011).

Cheng and Wang (2013) investigated changes in the microstructure due to silicon addition and its effect on the isothermal and cyclic oxidation behaviour of the aluminide steel. The comparative behaviour in isothermal oxidation conditions between steel samples aluminised using baths with and without 5% Si is shown in Fig. 2.14. Isothermal oxidation rates increased with increase in silicon addition. It is attributed to reduction in thickness of aluminide layers in the presence of silicon as well as due to transformation induced voids. Aluminide layer with lower silicon content showed low cyclic oxidation resistance and it is due to vertical cracking of brittle Fe_2Al_5 phase, which is thicker in case of low silicon content.
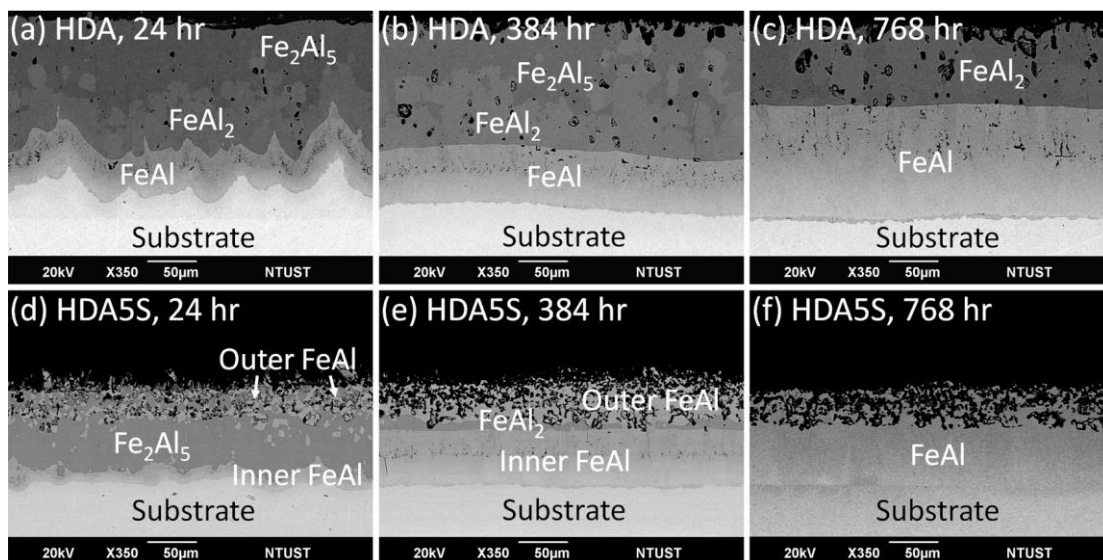
Fig. 2.14 Cross-sectional BSE micrographs of HDA and HDA5%Si after isothermal oxidation at 750 °C in air (a) and (d) 24 h oxidation, (b) and (e) 384 h oxidation, (c) and (f) 768 h (Cheng and Wang 2013).

2.3 Applications of the Aluminized Steel

2.3.1 Hydrogen permeation barrier coatings.

Materials used in nuclear industries are subjected to high hydrogen flux during the operation of a nuclear plant. Hydrogen being the smallest atom is easily transported within the materials by a diffusion process. This causes problems for materials which are sensitive to hydrogen-induced degradation. Hydrogen permeation is the process of hydrogen transportation through the materials as dissociated hydrogen atoms.

Permeation has units of (mol m^{-2} s^{-1}). According to Richardson law (Richardson 1904) permeation is expressed as

$$J = Dk/d(p^{1/2}_{high} - p^{1/2}_{low})$$ (1)

Where, J is the permeation rate, K is the Sievert's constant for the material (with units mol m^{-3} Pa$^{-1/2}$, D is the diffusion coefficient of hydrogen in the material, $(p^{1/2}_{high} - p^{1/2}_{low})$ is the hydrogen pressure difference across the thickness of the material, d is the thickness of the material.

The product of D and K is defined as the permeation coefficient or permeability of the material. Since D and K are temperature dependent, hydrogen permeability is high at higher temperatures. Apart from material degradation due to hydrogen influx other major concern in nuclear reactors is the tritium inventory in materials causing a radioactive hazard. Therefore, barriers for hydrogen permeation need to be developed to prevent material degradation as well as to reduce radioactive transport through tritium penetration.

Table 2.4 Hydrogen permeability (moles-H_2m^{-1}s^{-1}Pa$^{-0.5}$) at 500 °C (Jones 2008)

Material	Permeability
Al_2O_3	9×10^{-17}
Tungsten	4.3×10^{-15}
TiC	1 to 8×10^{-15}
Molybdenum	1.2×10^{-11}
Austenitic steels	0.7 to 1.2×10^{-11}
Ferritic steels	3×10^{-11}
Nickel	1.2×10^{-10}
Iron	1.8×10^{-10}

Titanuim	7.5×10^{-9}
Vanadium	2.9×10^{-8}

External coatings are usually preferred as the hydrogen permeation barriers. Ceramic coatings such as Al_2O_3, TiN, TiC, TiO_2, SiC, BN perform better than the metallic coatings due to their low hydrogen solubility and permeability. The successful performance of these coatings depends upon their defect structure, thermal expansion mismatch and structural integrity. Among ceramic materials, alumina possesses one of the lowest permeation rates and is the most preferred material as the permeation barrier coating. Table 2.4 lists the hydrogen permeability of some selected materials at 500 °C.

One advantage with the use of alumina coating is that apart from its low hydrogen permeability, it could also be deposited by various techniques as mentioned earlier. A uniform aluminide layer prepared by high activity pack aluminizing at 770 °C on 304 and 316 stainless steels proved to be a good tritium penetration barrier. A TPRF (tritium permeation reduction factor) upto 3-4 order of magnitude was obtained (Yang et al. 2011). Al+Cr+Si pack cemented coatings on EP 750 and EI-914 stainless steels reduce hydrogen permeation several times (Tazhibaeva et al. 2000). Oxide scales grown on the aluminide layers showed permeation reduction factors upto 4 orders of magnitude (Forcey and Ross 1991). FeCrAl alloy steels showed hydrogen permeation reduction factors of 1000 (Forcey et al. 1985). A three order of magnitude reduction in hydrogen flux was obtained on tempered martensitic steel by the deposition of 1 micrometer thick alumina scales (Levchuk et al. 2004)

2.3.2 Oxidation and corrosion resistance.

The improved corrosion resistance of the hot-dip aluminized stainless steel 310 in carbonate melt at 650 °C is reported. The corrosion rate decreased by two orders of magnitude. Formation of a 50 nm thick passive film of alumina was responsible for increased corrosion resistance (Sah et al. 2018). Surface coating of Al on 316 LN steel by DC magnetron sputtering showed improved corrosion resistance in supercritical CO_2 environment at 650 °C (Kim et al. 2018). Studies were conducted on as-deposited

sample and a pre-interdiffusion heat treated sample. Interdiffusion heat treatment transformed the coating into an outer surface layer and inner interdiffusion layer consisting of NiAl and ferrite phase. Pre-oxidation treatment resulted in the formation of an inner α-alumina layer and thereby, assisting in improved corrosion resistance. Resistance to degradation by molten salts has been reported to overcome by aluminizing (Dorcheh and Galetz 2016). Ferritic-martensitic P91steel and austenitic 304 SS were aluminized by slurry aluminizing technique. The aluminized steels showed improved corrosion resistance in the molten nitrate salts at 600 °C. Aluminizing of heat resistant HH309 steel improved oxidation resistance in air at 700 °C and 1100 °C (Sharafi and Farhang 2006). Austenitic stainless steel AISI 304 aluminized by CVD-FBR technology showed better oxidation performance than uncoated one (Pérez et al. 2001). Hot-dip aluminized SUS310 stainless steel showed better hot corrosion resistance in NaCl atmosphere at 900 °C. Kwok et al. (2006) carried out laser surface alloying of aluminum alloy on mild steel AISI 1050 steel and studied corrosion and cavitation erosion behaviour. Their study revealed significant improvement in corrosion resistance of the laser aluminized steel in 3.5 % NaCl solution at 23 °C. Laser aluminized steel exhibited 17 times higher cavitation erosion resistance than the substrate. Such an increase in erosion resistance was attributed to the presence of hard intermetallic phases of FeAl and Fe_3Al in the ferritic matrix formed during laser aluminizing. Another work carried out by Abdolahi et al. (2011) demonstrated improved corrosion resistance of the low-carbon steel following a two-step process. The two-step process is hot-dip aluminizing followed by laser surface alloying. The laser treatment transformed Al-rich intermetallic phases formed during dip aluminizing into Fe rich FeAl and Fe_3Al phases.

2.4 Objectives of the Study

Based on the literature review it can be summarized that the quality of the coating depends on the nature and thickness of the intermetallic (aluminide) layer. The weak or brittle interface may tend to crack and fail during secondary operations like bending and machining. To address this issue, the addition of alloying elements into molten Al bath were studied and showed to have a significant influence on the evolution of the microstructure at the interface (Eggeler et al. 1986; Cheng and Wang 2011; Springer et

al. 2011). Similarly, the effect of elements present in steel also reported influencing the microstructural formation at the interface (Dangi et al. 2018; Liu et al. 2019).

Austenitic stainless steel grade AISI 321 contains two major elements Cr (18 wt.%) and Ni (11wt. %). The influence of these elements on the formation and growth of the microstructure at the interface needs to be studied. This is studied by comparing the microstructure formation in the low carbon steel (Fe≈99.5 wt. %) and ferritic grade AISI 430 steel with Cr (18 wt.%) as the major alloying element.

Hence, the following objectives are framed for this investigation

- To study the evolution of microstructure at the interface between AISI 321 stainless steel and molten Al during hot-dip aluminizing.
- To establish the mechanism of microstructure formation in comparison with the microstructural formation for low-carbon steel/Al and AISI 430 steel/Al systems.
- To study the phase transformations during the diffusion treatment of the aluminized AISI 321 stainless steel.
- To evaluate hot-corrosion and cyclic oxidation performance of the aluminized AISI 321 stainless steel.

2.5 Scope of the Study

The study will help in understanding the role of alloying elements present in the steel on the evolution of microstructure at the interface between steel and Al during the process of hot-dip aluminizing. Understanding the mechanism will help in tailoring the quality of coating by controlling the process variables. Further, the study on diffusion treatment will help in understanding phase transformations within the coating during its service at high temperature, and its influence on the integrity of the coating.

CHAPTER 3

EXPERIMENTAL METHODS

This chapter deals with experimental details of hot-dip aluminizing of three grades of steel, namely, low-carbon steel, ferritic grade AISI 430 and austenitic grade AISI 321 in the molten aluminum bath. Diffusion treatment of aluminized 321 steel is carried out. Details of microstructural characterization are presented. Procedures for hot corrosion test and cyclic oxidation tests for aluminized stainless steel 321 are briefed.

3.1 Base Material

Three grades of the base material are used in the study. Low-carbon steel was procured from Jindal steels Ltd., Bellary. The material was in the form of sheets of 3 mm thickness and was processed by hot rolling. Ferritic grade steel AISI 430 with a sheet thickness of 3 mm was procured from M/s Bharath Aerospace Ltd., Mumbai. Austenitic grade steel AISI 321 with a sheet thickness of 3.5 mm was procured from Mishra Dhatu Nigam Ltd. (MIDHANI), Hyderabad. The chemical composition of the base materials is given in Table 3.1 to Table 3.3.

Table 3.1 Average chemical composition of the low-carbon steel (all in wt. %)

C	Mn	S	P	Si	Al	N	Cu	Cr	Ni	Ti	Ce	Fe
0.036	0.25	0.016	0.012	0.01	0.038	0.004	0.007	0.014	0.006	0.00	0.078	bal

Table 3.2 Average chemical composition of the ferritic grade AISI 430 stainless steel (in wt. %)

C	Mn	S	P	Si	Al	Cu	Cr	Ni	Ti	Fe
0.017	0.084	0.003	.007	0.132	0.029	0.028	17.39	0.025	0.165	bal

Table 3.3 Average chemical composition of the austenitic grade AISI 321 stainless steel (in wt. %)

C	Cr	Ni	Ti	Mn	Si	S	P	Fe
0.07	17.8	11.5	0.64	1.58	0.04	0.006	0.0012	bal

3.2 Aluminum Melt Preperation

Commercially pure aluminum (99.6 % purity) is procured from FENFE Metallurgicals, Bangalore. The melt for hot-dipping was prepared by heating these ingots in a graphite crucible placed in a temperature controlled resistance furnace. The schematic of the experimental set up is shown in Fig. 3.1.
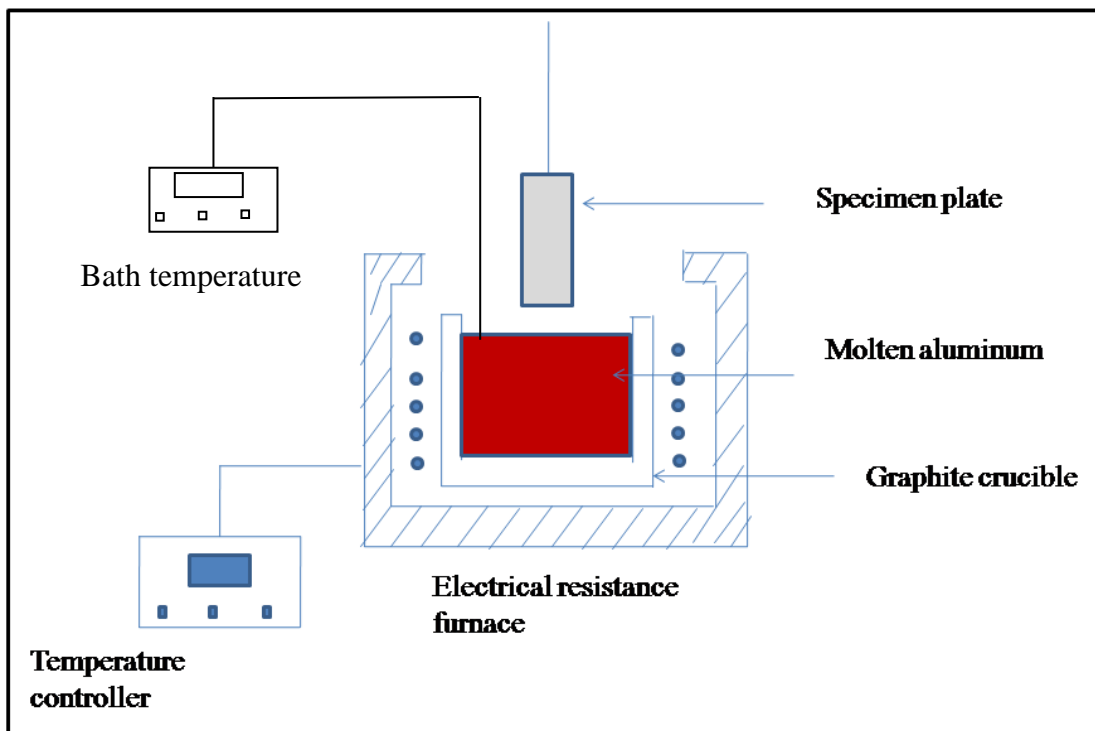
Fig. 3.1 Schematic diagram of the experimental set up for hot-dip aluminizing.

Then the melt was set to the desired temperature for hot dipping. A eutectic mixture of zinc chloride & ammonium chloride (3:1 by weight) was used as a flux for covering the melt (Commercial name: Coverall Flux) during the melting process. Base material coupons with dimensions 3 mm×10 mm×40 mm was cut, tied with a nichrome wire on

one end for dipping. Coupons were then kept immersed in molten aluminum bath for required durations and air cooled.

Coupons were then cut across the cross-section using precision saw cutting (DuCom make), and metallographically polished for microstructural analysis. Thickness measurement of various layers in the micrograph was done using Sigma-Scan Pro (Jandel Scientific) and Image J software. The other set of experiments was carried out in Al-5 wt.% Cr bath with low-carbon steel as the base material to study the effect of chromium in the bath.

3.3 Diffusion Treatment

Aluminised AISI 321 steel samples were then heated in resistance furnace in the temperature range 700 °C to 900 °C to study the microstructural changes and phase transformation during diffusion treatment. After heating in the furnace for the desired amount of time and set temperature, coupons were air cooled. The coupons were again cut across the cross-section, metallographically polished for microstructural analysis.

3.4 Characterization

3.4.1 Scanning electron microscopy

Microstructural investigations of the coating were carried out using a scanning electron microscope (SEM, JSM-6380LA, JEOL make). Cross-sectional samples were prepared and interface microstructure was analyzed in the back-scatter imaging (BSE mode) to identify various intermetallics phases. Topographical features of the hot corrosion tests and cyclic oxidation tests were carried out. EDS was carried out for the compositional analysis of the phases.

3.4.2 Transmission electron microscopy

A detailed investigation regarding microstructural formation was carried out using transmission electron microscope (TEM, JEM-2100, JEOL make) operated at 200 kV. The TEM is equipped with EDS (Oxford make). Both the bright field and dark field imaging techniques were used for image analysis. Electron diffraction studies were carried out in order to determine the crystal structures of the phases present. Different modes of diffraction analysis, like, selected area electron diffraction (SAED) and

nanobeam diffraction (NBD) techniques were used for the crystal structure analysis. For NBD appropriate spot size and convergence angle was used depending upon the size of the phase to be analysed.

Elemental compositional analysis was carried out by energy dispersive spectroscopy (EDS). Spot size in the range of 1 nm to 25 nm was used according to the size of the phase to be analysed.

Samples for TEM analysis were prepared by initially cutting a slice of 1mm from the bulk sample by a slow speed cutting machine (DuCom make). The thickness of the sample is further reduced by mechanical thinning from the base metal side until the total sample thickness of about 100 micrometers is attained. TEM samples corresponding to various regions in the coatings were prepared by polishing the known amount of thickness from the coating side to arrive at the region of interest. Total coating thickness is initially measured by following cross-sectional SEM analysis. Further, discs of 3 mm diameter were punched using a disc punching machine. The schematic of the sample preparation for TEM analysis is shown in Fig. 3.2.
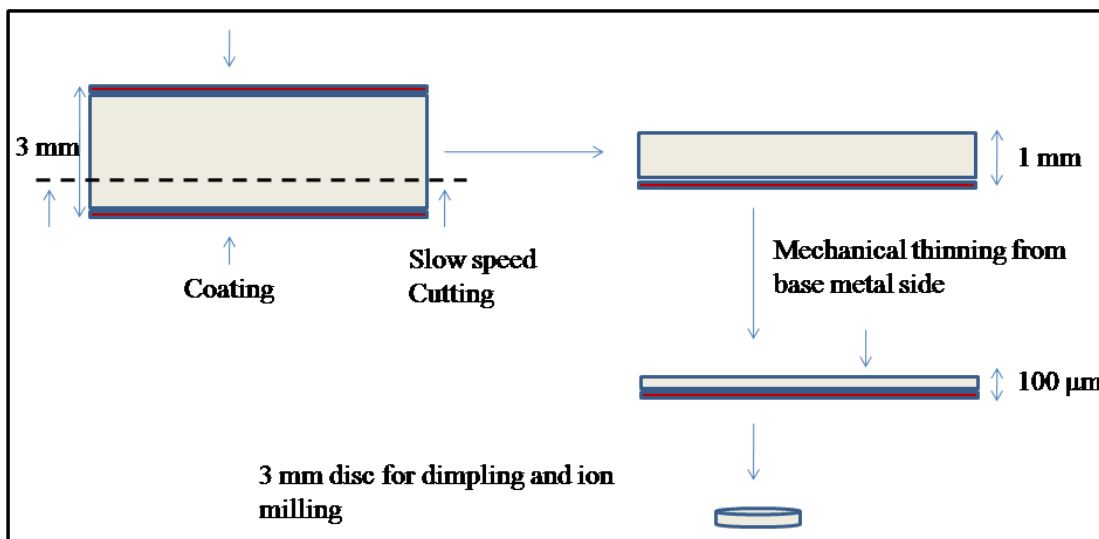
Fig. 3.2 Schematic representation of the procedure followed for TEM sample preparation

Punched discs were further subjected to dimpling. The samples were dimpled up to 5 µm at the center by using the dimpling unit. Ion milling of the dimpled sample was

carried out using precision ion polishing system (Gatan, PIPS 691). The beam energy of 4 to 5 keV and beam angle of 4 to 6 ° (both guns on topside) was used depending on the sample to be milled. Milling was carried out until the samples became electron transparent. A schematic representation for dimpling and ion milling carried out is presented in Fig. 3.3.
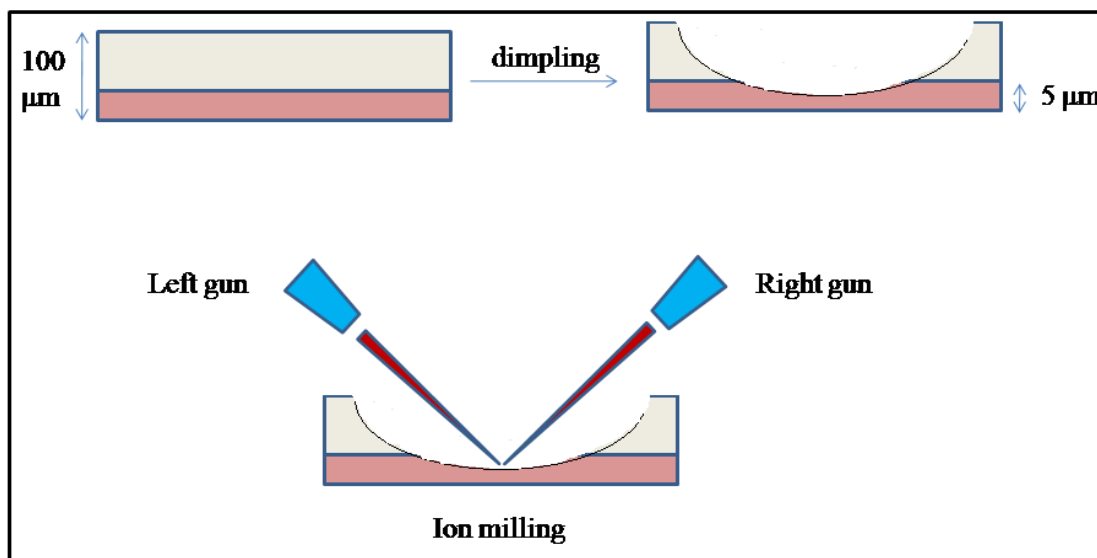
Fig. 3.3 Schematic diagram of the dimpling and ion milling procedure followed to prepare samples for TEM analysis.

3.4.3 X-Ray Diffractometry

X-ray diffraction patterns of the aluminized and diffusion treated samples were obtained by using X-Ray diffractometer (model JPX 8P, JEOL) operated at 30 kV voltage and 20 mA current. Monochromatic copper K_α (λ=1.54 Å) radiation was used for obtaining the diffraction pattern. The diffraction patterns were collected in the range of $10°$ to $100°$ at a scanning speed of $1°$/min and step size of $0.02°$. Experiments were carried out on various regions in the coating by removal of successive layers by mechanical polishing. The output data was analyzed by comparing with the standard JCPDS files to identify the phases present in the coating. In the case of metastable phases, indexing is done by comparing with the data available in the literature.

3.5 Hot Corrosion

Hot corrosion studies on the aluminized AISI 321 stainless steel was carried out in a salt mixture of 60%V_2O_5 + 40% Na_2SO_4 at 700 °C. The hot corrosion studies, under cyclic conditions, were conducted for 50 number of cycles. Each cycle consisted of 1-hour heating at 700 ℃ in a tubular furnace followed by 20 minutes cooling in air. Salt coating of uniform thickness with coverage of 3-5 mg/cm^2 of Na_2SO_4-60% V_2O_5 was applied using a Camel hairbrush on the preheated samples (200 ℃). The melting temperature of the salt mixture is close to 500 ℃. The coated samples were dried by heating in an oven at 150 ℃ for 1 hour. The boat containing the specimen was inserted into the hot zone of a tubular furnace set at a temperature of 700 °C. Holding time in the furnace was one hour (in molten salt). Later the boat along with the specimen was taken out and cooled to room temperature for 20 minutes. Further, the weight of the boat along with the specimen was measured and this constituted one cycle of the hot corrosion study. Weight change values were measured at the end of each cycle using an electronic balance with a sensitivity of 10^{-4} g. A graph of specific weight gain/loss vs no. of cycles was drawn.

3.6 Cyclic Oxidation

Cyclic oxidation behaviour of the uncoated and aluminized AISI 321 stainless steel is carried out at 900 °C. The test was conducted for 50 cycles. Each cycle consisted of heating for one hour followed by cooling to room temperature. After the end of each cycle, the weight of the sample along with the boat was measured using an electronic balance with a sensitivity of 10^{-4} g. A graph of specific weight gain vs no. of cycles is plotted and analyzed.

CHAPTER 4

MICROSTRUCTURE AT THE INTERFACE BETWEEN STEELS AND MOLTEN ALUMINUM

This chapter deals with the analysis of microstructures at the interface between the molten aluminum and steels during the process of hot-dip aluminizing. The three variants of steel material are Low-carbon steel, ferritic grade AISI 430 steel and austenitic grade AISI 321 steel. Typical microstructure at the interface of each combination was studied and the growth kinetics of intermetallic phases are discussed.

4.1 Microstructure at the Interface Between Low-carbon Steel/Al

The chemical composition of the steel materials is mentioned in the previous chapter (Table 3.1 to 3.3). For convenience the three systems are mentioned as Fe/Al for low-carbon steel-aluminum, SS 430/Al for ferritic grade AISI 430-aluminum and SS 321/Al system for austenitic grade AISI 321 steel-aluminum.

Figure 4.1 (a) shows a typical cross-sectional SEM-BSE microstructure at the interface of the Fe/Al system. The microstructure shows three distinct regions namely,

(i) aluminum topcoat

(ii) intermediate Fe-Al intermetallic layer also known as aluminide layer and

(iii) the base metal.

The aluminum topcoat is the solidified aluminum part formed during cooling to room temperature. It consists of eutectic Al_3Fe ($Al_{13}Fe_4$) phases, which are seen to be dispersed in the aluminium matrix. At the interface, an intermetallic (aluminide) layer is formed by the interaction of solid steel with liquid Al.
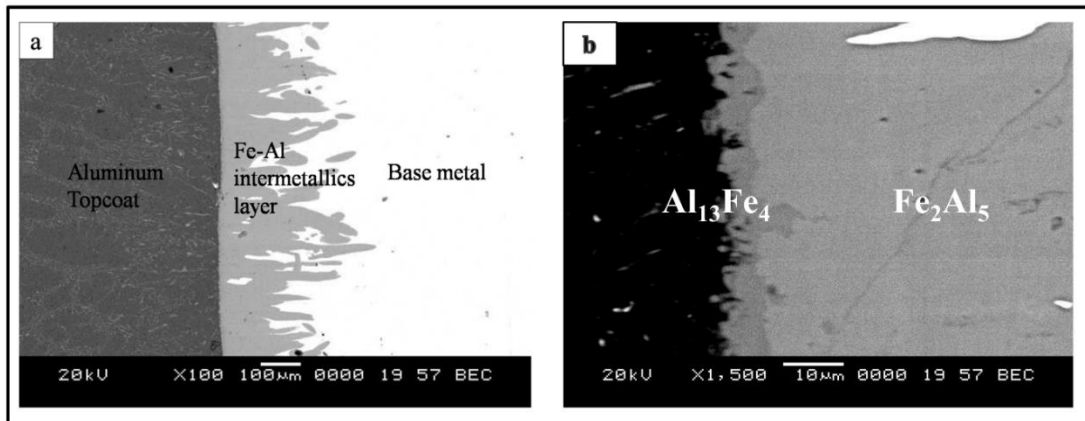
Fig. 4.1(a) Typical cross-sectional SEM-BSE micrograph at the interface of Fe/Al system showing three regions, namely, an aluminum topcoat, intermediate aluminide layer, and base metal, (b) high magnification SEM-BSE micrograph of intermetallic layer consisting of two distinct phases.

Figure 4.1 (b) shows a higher magnification micrograph of the intermetallic layer. Two distinct phases are observed based on the contrast observed in the back-scatter imaging mode. The two phases are Fe_4Al_{13} towards the Al side and an Fe_2Al_5 towards the base metal side. These phases are identified based on the literature data (Shahverdi et al. 2002, Springer et al. 2011, Lemmens et al. 2016) and also subsequently confirmed based on the SEM-EDS analysis. Phase analysis by TEM studies are reported by (Springer et al. 2011, Chen et al. 2018) and therefore, phase analysis by TEM studies are not specifically carried out in the present investigation for Fe/Al system. The thickness of $Al_{13}Fe_4$ phase is quite small compared to the Fe_2Al_5 phase which forms the major portion of the intermetallic layer. The Fe_2Al_5 phase exhibits the typical tongue-like growth morphology as seen in Fig. 4.1(a). The thickness of the intermetallic layer is expected to vary with dipping time or holding time in the molten Al bath.

4.1.1 Growth kinetics

The growth kinetics of the intermetallic layer is studied by holding the steel sample in the molten bath for different time duration.
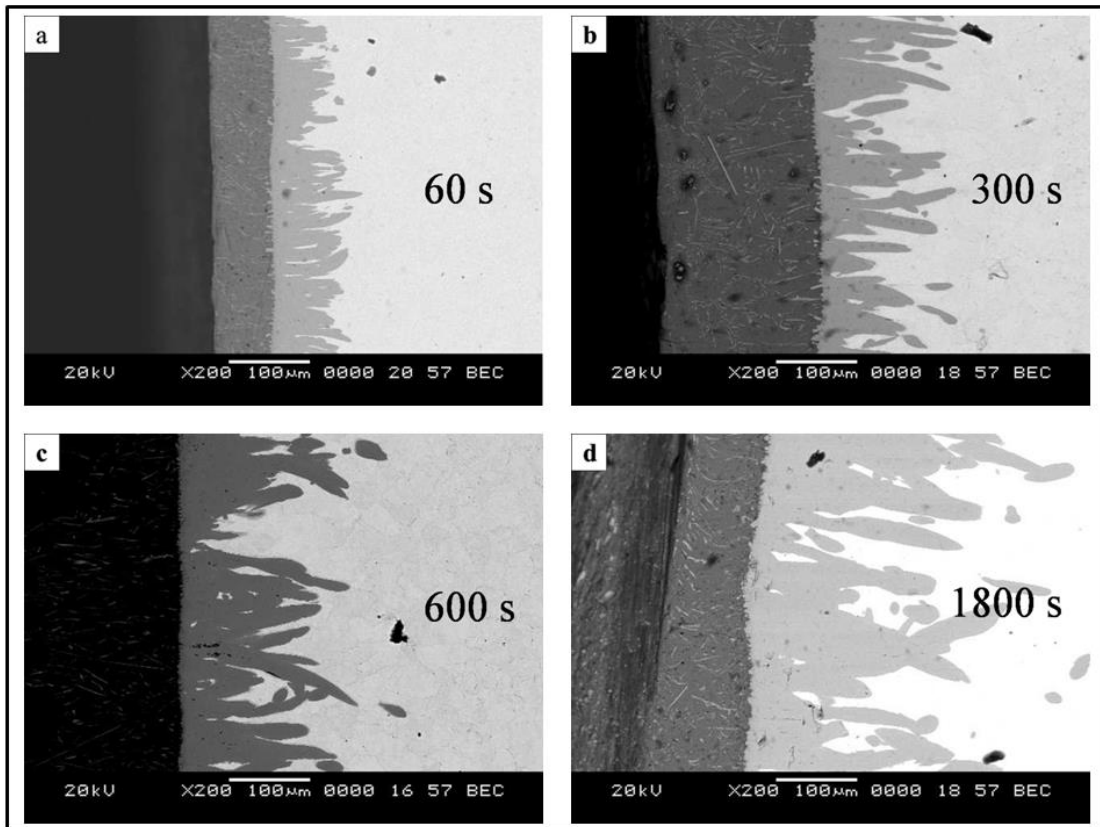
Fig. 4.2 SEM-BSE micrographs of aluminized samples with varying dipping time (a) for 60 s, (b) 300 s, (c) 600 s, and (d) 1800 s.

Figure 4.2 shows the SEM cross-sectional micrographs of the aluminized samples dipped in molten Al bath for the different time duration. The thickness of the intermetallic layer is observed to increase with the increase in dipping time. However, the thickness of $Al_{13}Fe_4$ phase is small compared to the Fe_2Al_5 phase, and the layer thickness measured is mainly for the Fe_2Al_5 phase. Further, the tongue like morphology of the Fe_2Al_5 phase is pronounced as the dipping time increases. Figure 4.3 (a) shows a plot of the variation of average intermetallic layer thickness with dipping time. The graph shows a parabolic type of growth behaviour. The intermetallic layer thickness increased from 35 μm at 10 seconds to 165 μm at 1800 seconds.
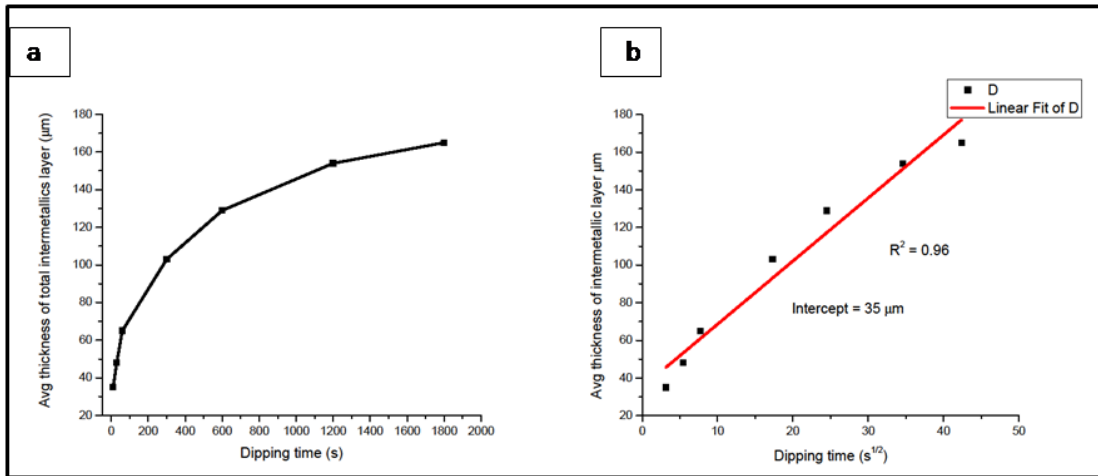
Fig. 4.3 (a) Variation of the average intermetallic layer thickness with dipping time, (b) the plot of the average thickness of the intermetallic layer with the square root of dipping time.

A plot of average intermetallic layer thickness with the square root of dipping time is plotted to study the parabolic growth rate constant as presented in Fig. 4.3 (b). It shows a good linear fit with a fitting coefficient of 0.96. The parabolic growth constant obtained from the graph (slope of the line) is around 3.35 $\mu ms^{-1/2}$. Since the thickness of $Al_{13}Fe_4$ phase is quite small compared to Fe_2Al_5 phase, the growth behaviour mainly depicts the growth of Fe_2Al_5 phase.

4.2 Microstructure at the Interface between SS 430/Al
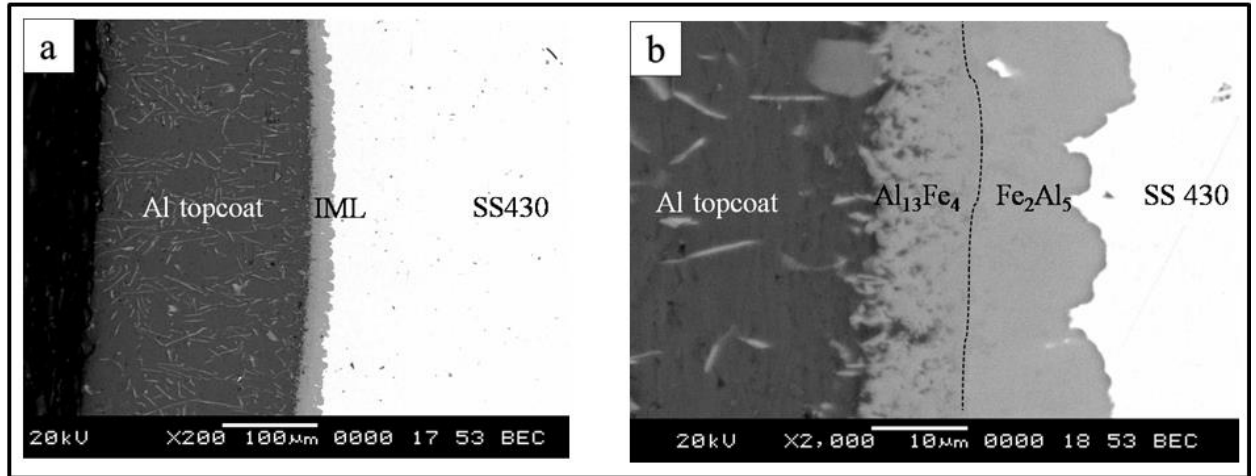
Fig. 4.4 (a) Typical cross-sectional SEM-BSE microstructure at the interface between stainless steel AISI 430 and aluminum, hot-dip aluminized at 700 °C for 180 s, (b) high magnification micrograph showing two phases present in the intermetallic layer.

The typical cross-sectional micrographs due to the interaction between stainless steel 430 with molten Al is shown in Fig 4.4. Figure 4.4 (a) shows three distinct regions, namely, the solidified Al topcoat, the intermediate intermetallic layer, and the base metal. The intermetallic layer consists of two distinct phases which are distinguished based on the contrast observed under SEM-backscatter imaging mode, as seen in the high magnification micrograph shown in Fig. 4.4 (b). The phases are identified as $Al_{13}Fe_4$ and Fe_2Al_5 phase and further confirmed by TEM studies. The morphology of the intermetallic layer in the present case is comparatively smooth compared to an uneven tongue like morphology in Fe/Al system. Figure 4.5 shows the SEM-EDS point analysis of the $Al_{13}Fe_4$ phase. The elemental composition is presented as an inset in the figure and suggests that about 4.6 at. % Cr is dissolved in the $Al_{13}Fe_4$ phase. Figure 4.6 shows the SEM-EDS point analysis of Fe_2Al_5 phase; about 5.4 at. % Cr is observed to be dissolved in this phase.

Element	Atomic %
Al	76.2
Cr	4.6
Fe	19.2

Fig. 4.5 SEM-EDS point analysis corresponding to $Al_{13}Fe_4$ phase.

Element	Atomic %
Al	72.4
Cr	5.4
Fe	22.2
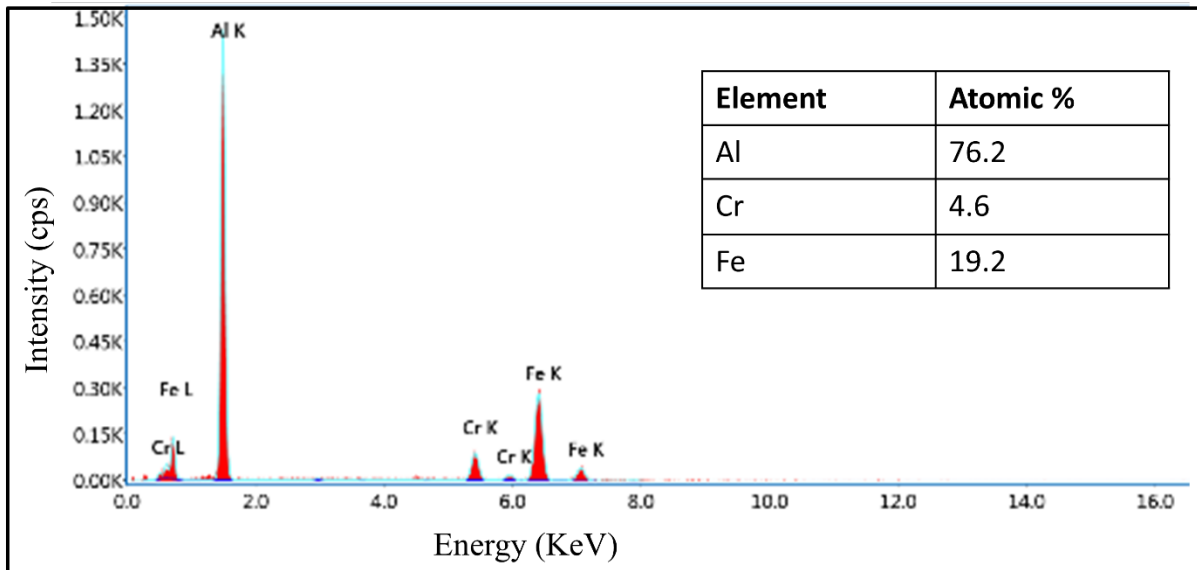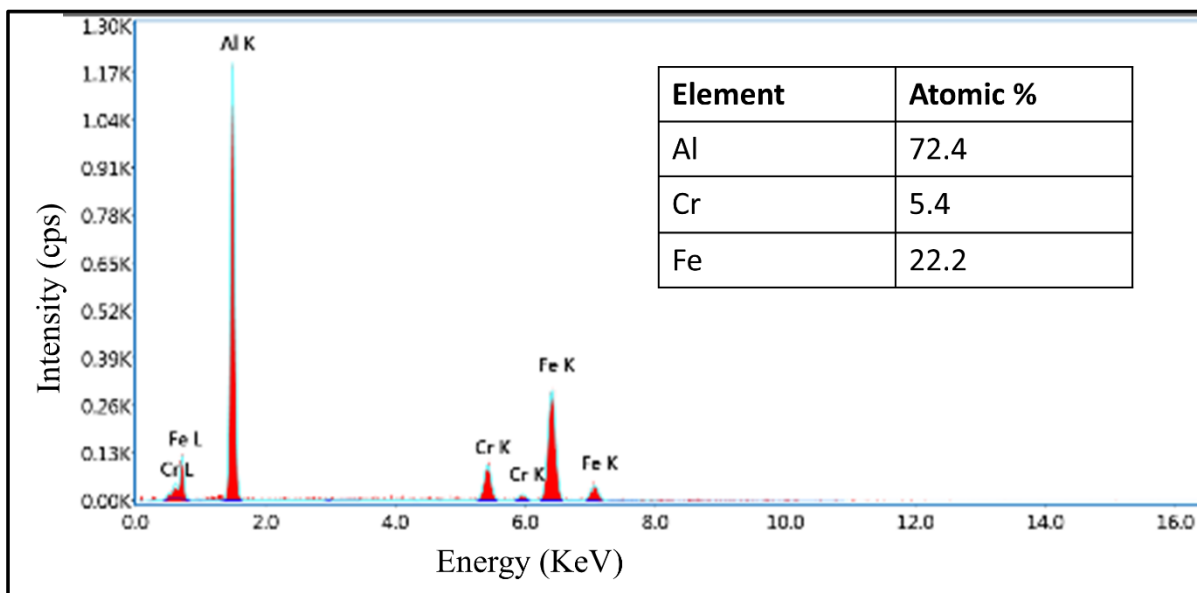
Fig. 4.6 SEM-EDS point analysis corresponding to Fe_2Al_5 phase.

4.2.1 TEM investigations

4.2.1.1 Aluminum topcoat

The aluminum topcoat is found to consist of solidified aluminum in which intermetallic phases are dispersed. Figure 4.7 (a) shows the SEM micrograph and the inset shows the region of interest for the TEM analysis.
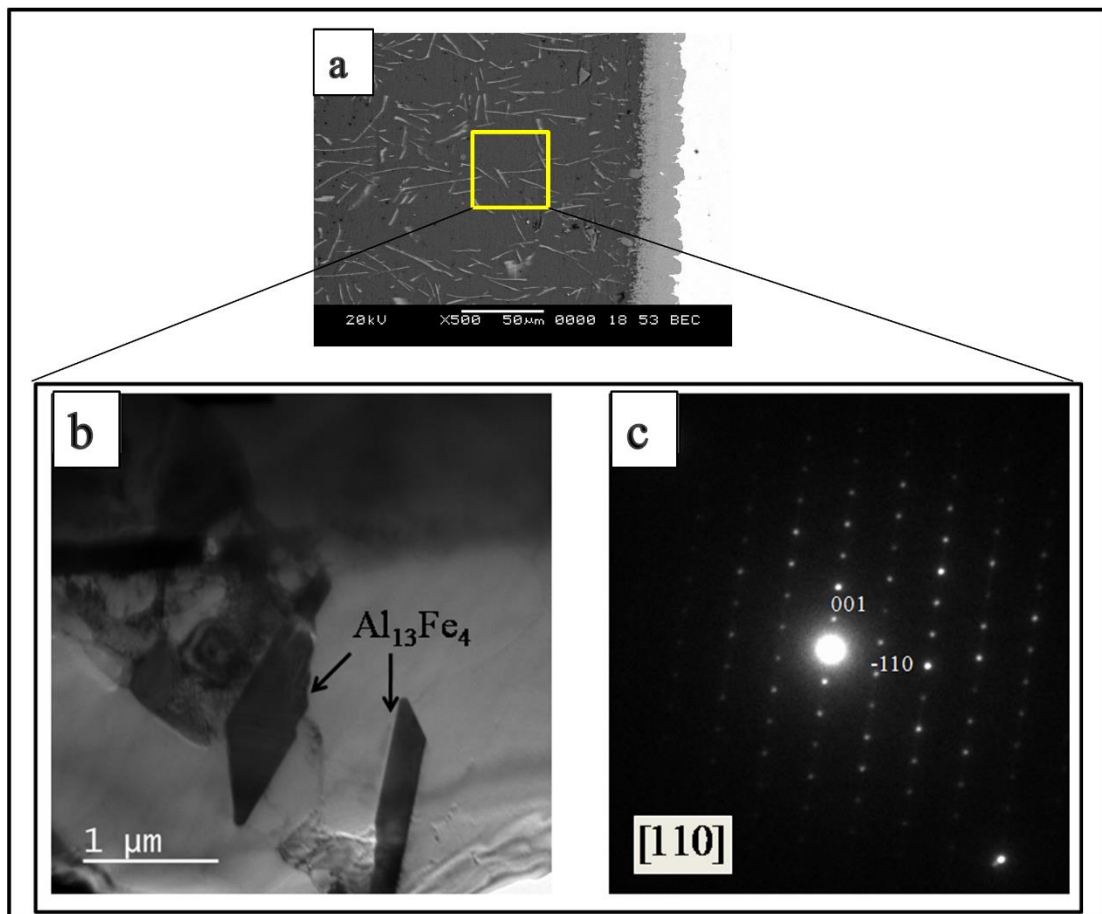
Fig. 4.7 (a) SEM-BSE micrograph; inset showing the region of interest for TEM analysis, (b) TEM bright field micrograph showing $Al_{13}Fe_4$ precipitates in the aluminum matrix, and (c) associated electron diffraction patterns along [110] orientation.

Figure. 4.7 (b) shows TEM micrograph of the topcoat revealing $Al_{13}Fe_4$ precipitates dispersed in the aluminum matrix. The size of these precipitates is in the range of 1- 2 micrometres in length and less than 0.5 micrometres in width. Figure 4.7 (c) shows

electron diffraction pattern along [110] orientation. Figure 4.8 shows TEM-EDS spectrum of $Al_{13}Fe_4$ phase. The composition corresponds to $Al_{13}Fe_4$ phase. About 1.6 at.% Cr is dissolved in this phase.

Element	Atomic %
Al	77.7
Cr	1.6
Fe	20.7
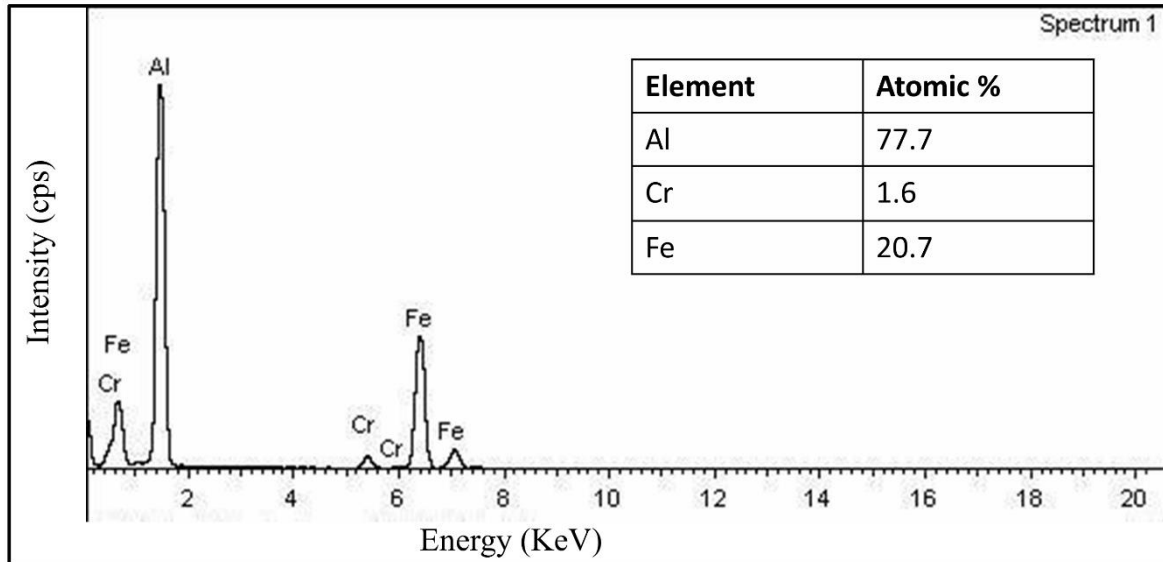
Fig. 4.8 TEM-EDS spectrum corresponding to $Al_{13}Fe_4$ phase.

4.2.1.2 Intermetallic layer

The intermetallic layer consists of two phases Fe_2Al_5 on the base metal side and $Al_{13}Fe_4$ towards the aluminum side. Close to the aluminum side, $Al_{13}Fe_4$ phase is formed in the aluminum matrix. The region of interest for the TEM studies is shown as an inset in the SEM micrograph presented in Fig. 4.9 (a). Figure 4.9 (b) & (c) shows TEM micrographs of $Al_{13}Fe_4$ phase formed in the aluminum matrix. The size of these phase ranges from sub-micrometre level to about 2-3 micrometres.
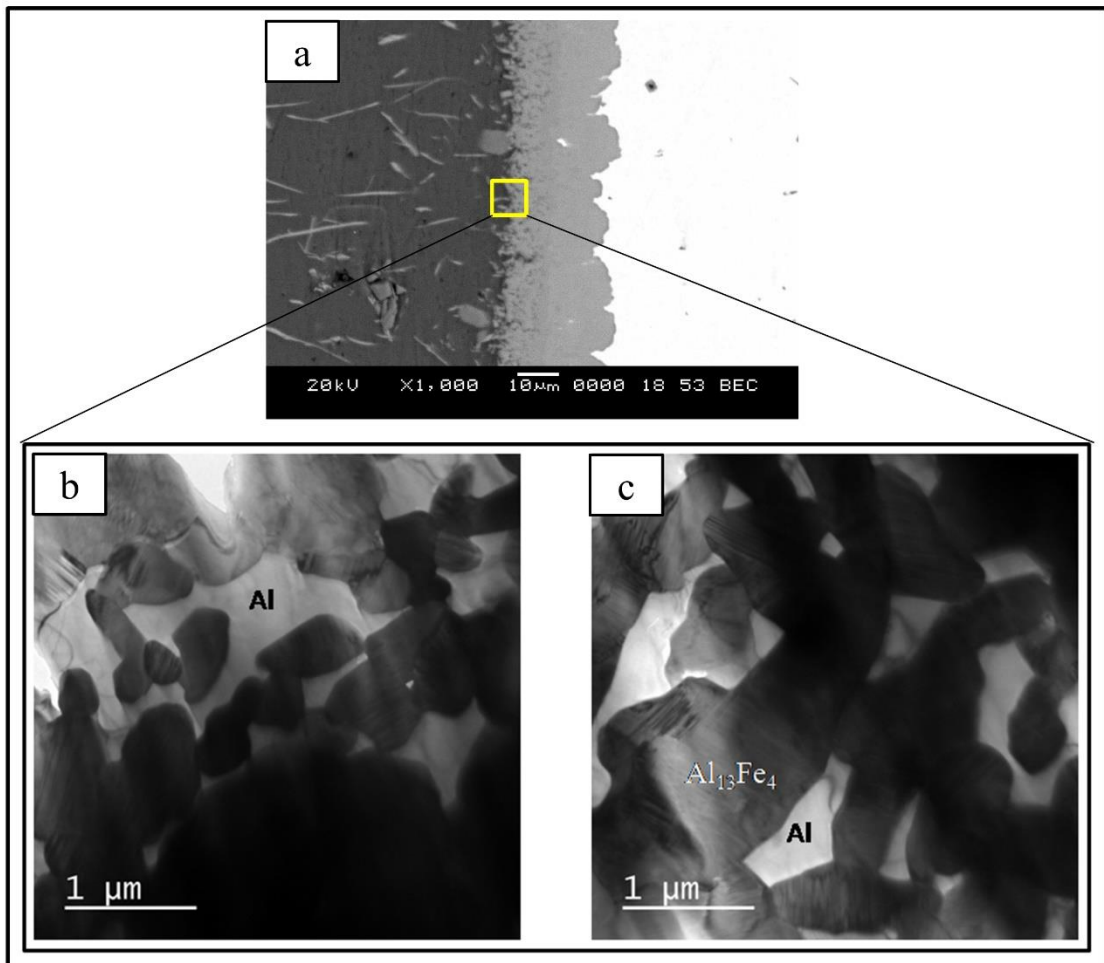
Fig. 4.9 (a) SEM-BSE micrograph; inset showing the region of interest for TEM analysis, (b) & (c) TEM micrographs of the $Al_{13}Fe_4$ phase formed in the aluminum matrix close to aluminum topcoat side.

Figure 4.10 (a) shows high magnification micrographs of the $Al_{13}Fe_4$ phase. Within this phase, fine microtwins are observed. The presence of these twins is confirmed by TEM studies. Electron diffraction pattern along [010] orientation is presented in Fig 4.10 (b). The figure reveals that twinning occurs along (100) plane. Figure 4.11 shows TEM-EDS spectrum corresponding to the $Al_{13}Fe_4$ phase which confirms the composition of the same. A small amount of chromium close to about 1.8 at. % Cr is found to be dissolved in this phase.
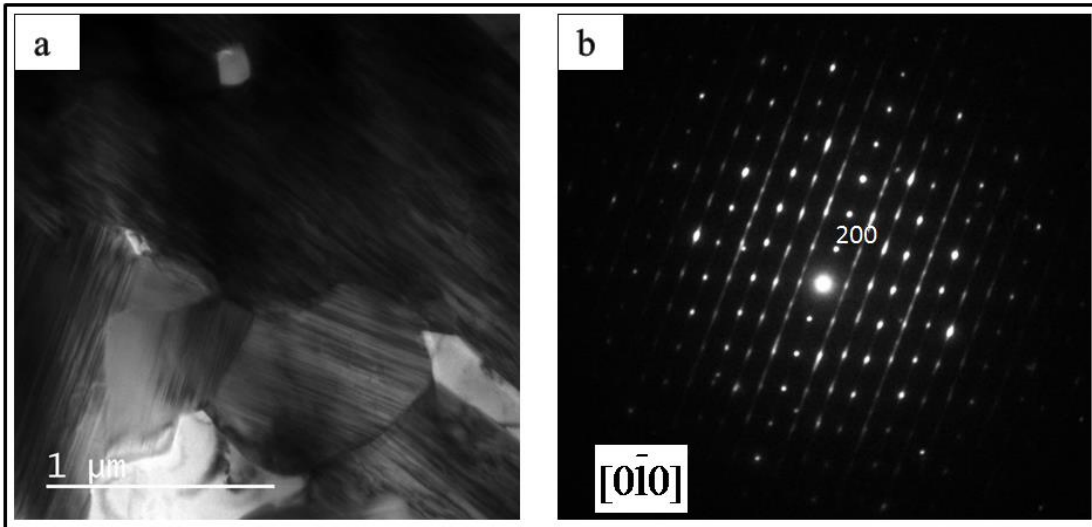
Fig. 4.10 (a) High magnification TEM micrograph showing microtwins, (b) associated electron diffraction pattern showing twinning around (100) plane.
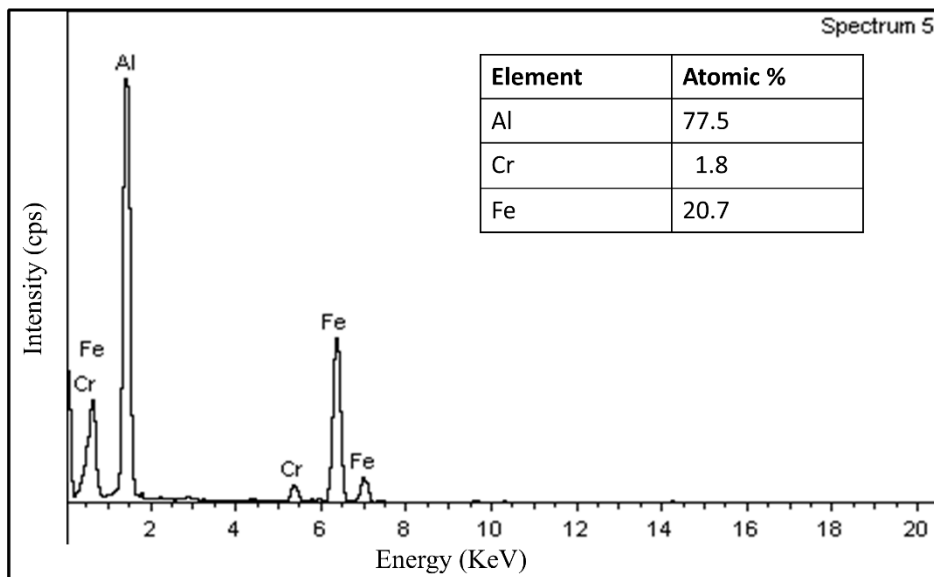
Fig. 4.11 TEM-EDS spectrum of the $Al_{13}Fe_4$ phase formed in the intermetallic layer close to aluminum topcoat.

Figure. 4.12 shows the TEM micrograph of the $Al_{13}Fe_4$ phase in the intermetallic layer. The average grain size of the phase is close to 500 nm. Even within such fine grains, microtwins and stacking faults were observed. TEM-EDS analysis shown in Fig. 4.13 reveals around 4.6 at. % Cr is dissolved.

44
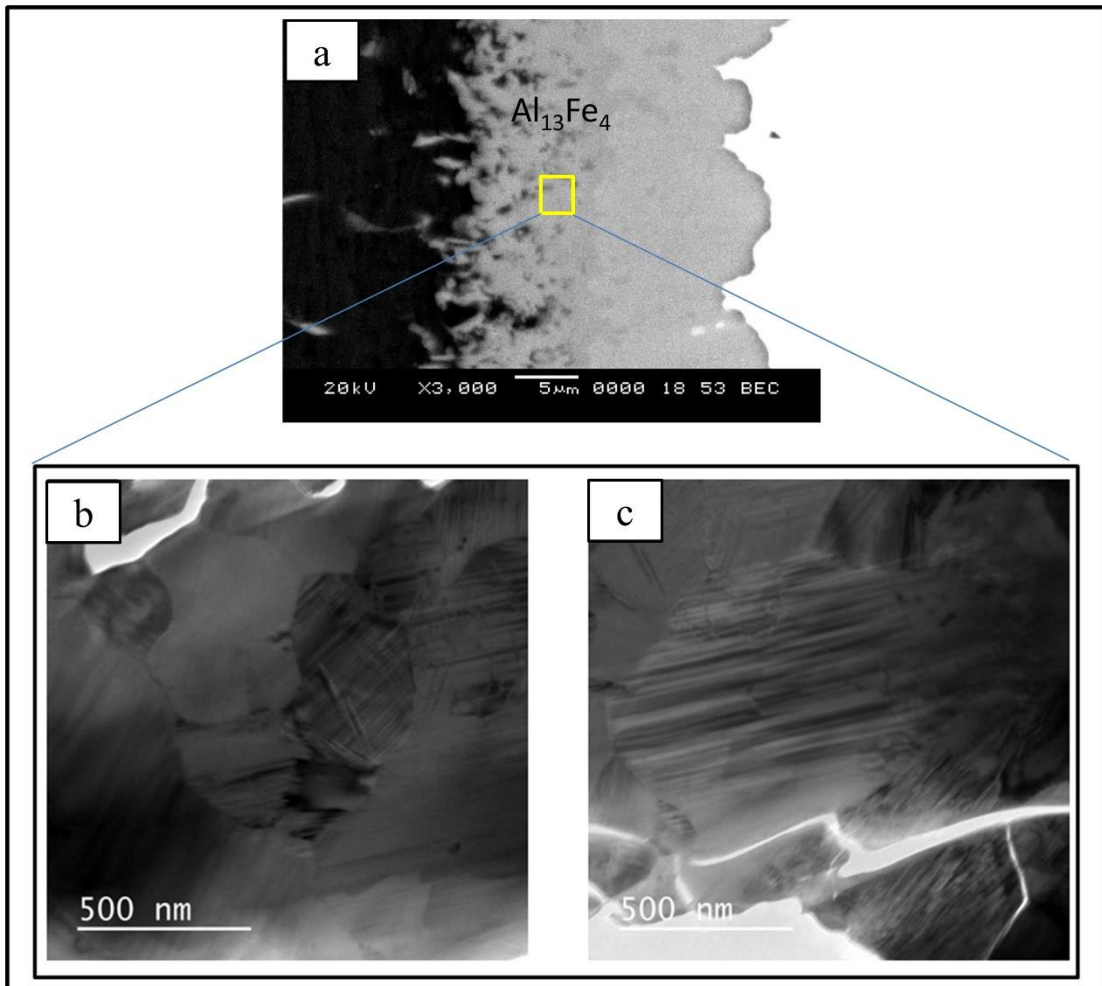
Fig. 4.12 (a) SEM-BSE micrograph; inset showing the region of interest for TEM analysis, (b) & (c) TEM micrographs of the $Al_{13}Fe_4$ phase formed in the intermetallic layer.

Element	Atomic %
Al	75.4
Cr	4.6
Fe	20
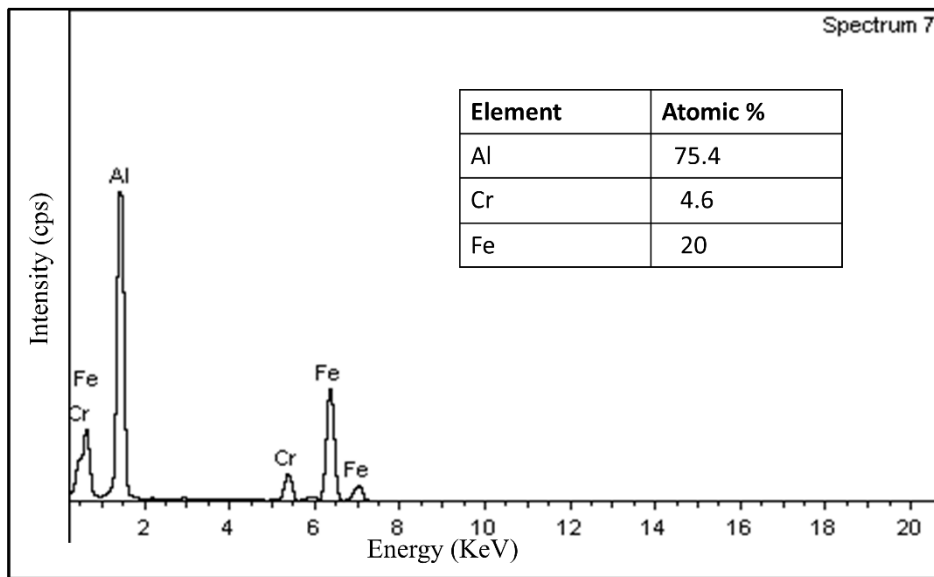
Fig. 4.13 TEM-EDS spectrum corresponding to $Al_{13}Fe_4$ phase.

The other phase in the intermetallic layer is Fe_2Al_5 phase. The TEM micrograph shown in Fig. 4.14 reveals fine-grained microstructure with the average grain size less than 500 nm. The nano-beam diffraction (NBD) analysis carried out on this phase is presented in Fig. 4.14 (c) & (d). The electron diffraction patterns are recorded along [001] and [101] zone axis orientation respectively. TEM-EDS analysis shown in Fig. 4.15 reveals close to 6 at. % Cr is dissolved in this phase.
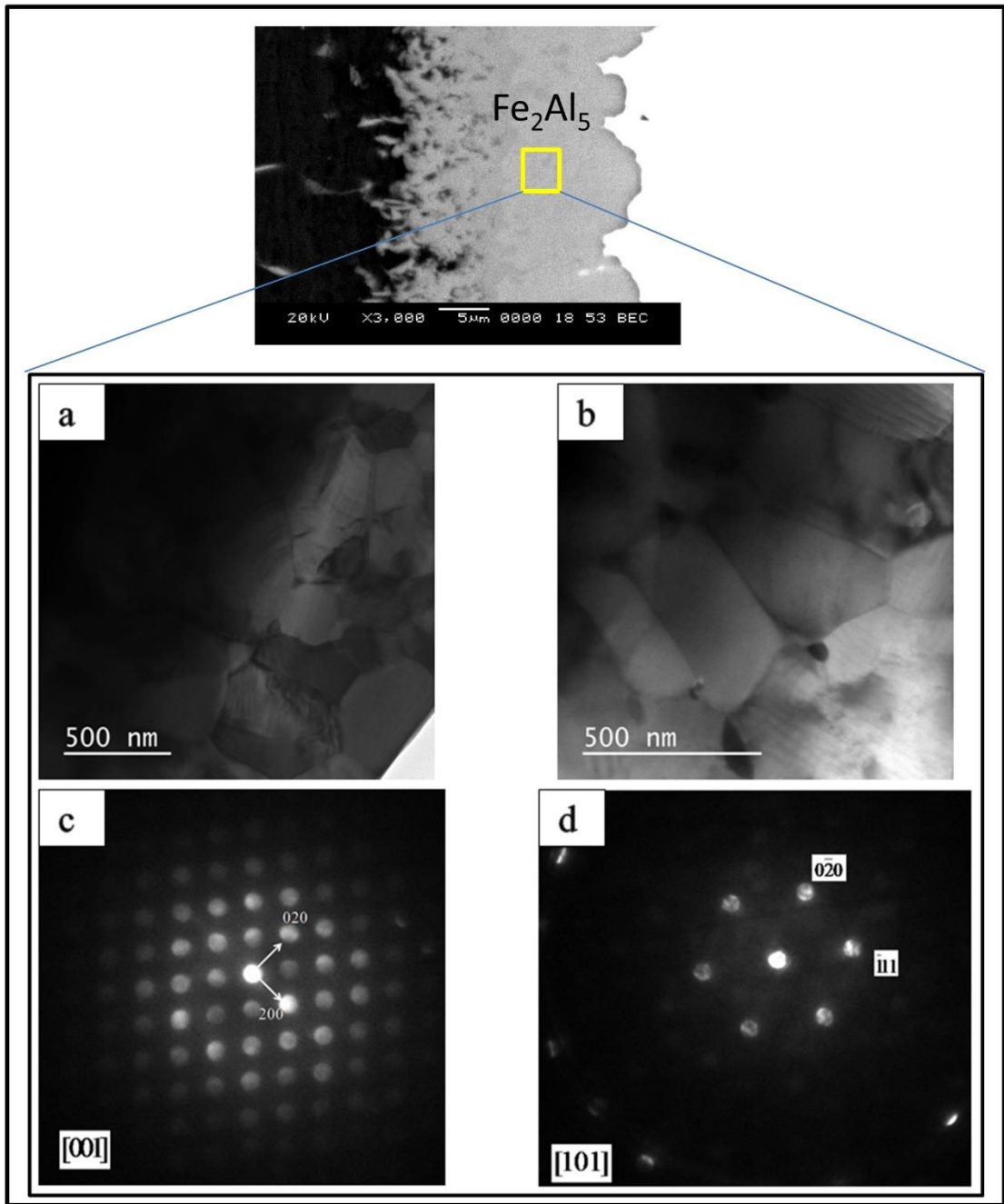
Fig. 4.14 (a) & (b) TEM micrograph of Fe_2Al_5 phase in the intermetallic layer, (c) nano-beam electron diffraction pattern along [001] direction, and (d) along [101] direction.
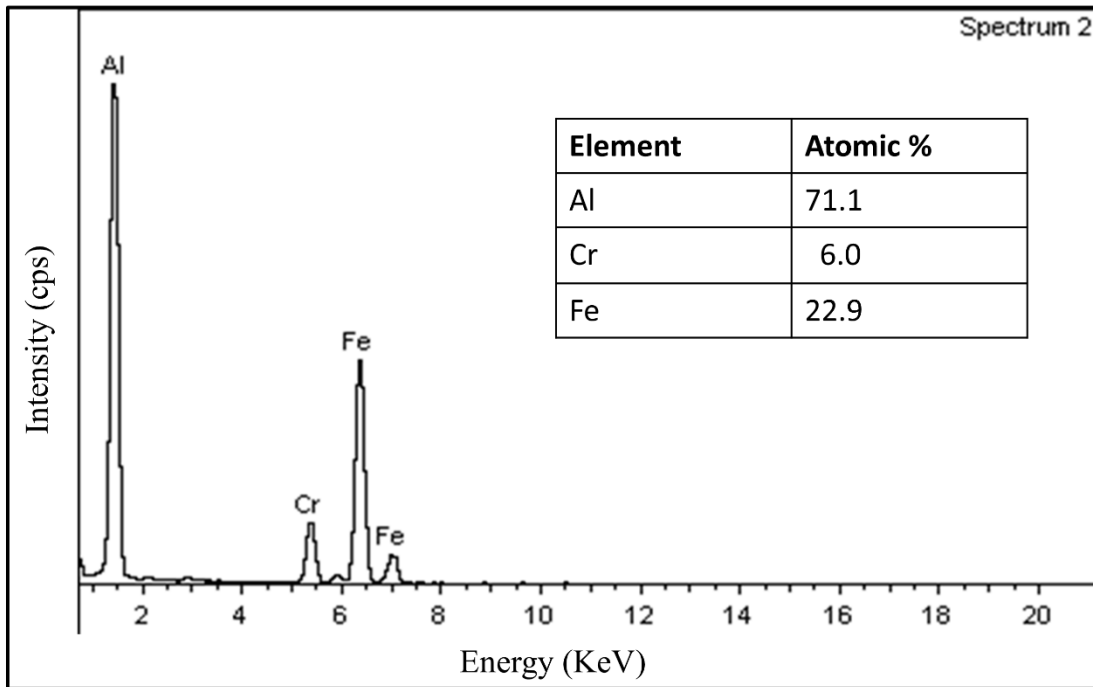
Fig. 4.15 TEM-EDS spectrum corresponding to Fe_2Al_5 phase.

The growth kinetics of the intermetallic layer is measured by holding the steel sample in the molten bath for different dipping durations.

4.2.2 Growth kinetics

It is found that the thickness of the intermetallic layer increases with an increase in dipping time. Figure 4.16 shows SEM-BSE micrograph of the aluminized samples dipped for different durations. The average thickness of the intermetallic layer increased from 9 μm at 10 seconds to 43 μm at 600 seconds. The Fe_2Al_5/ SS 430 steel interface is smoother at a short time while it becomes rough at longer dipping times. The growth is mainly observed for Fe_2Al_5 phase, while the growth of Fe_4Al_{13} phase is negligible. The growth kinetics of the intermetallic layer is studied by plotting average intermetallic layer thickness with different dipping time.
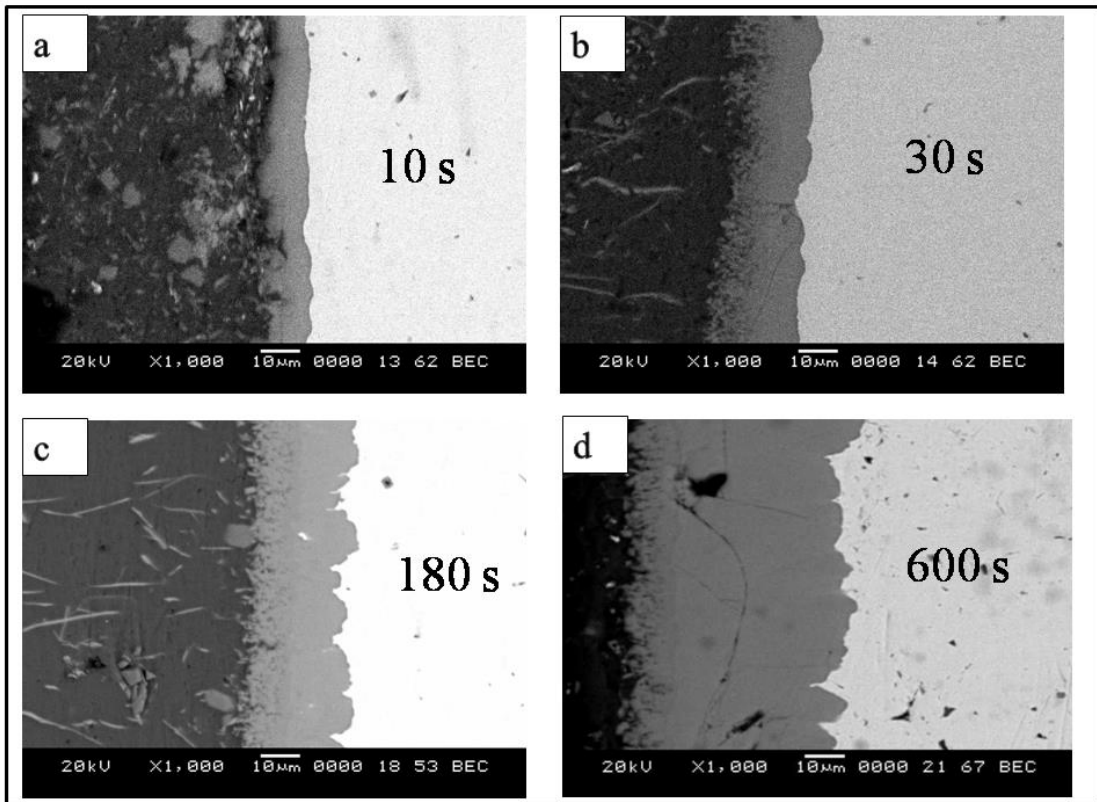
Fig. 4.16 SEM-BSE micrographs of the aluminized stainless steel 430 at various dipping durations (a) 10 s, (b) 30 s, (c) 180 s, and (d) 600 s.

Figure. 4.17 (a) shows a plot of average intermetallic layer thickness with dipping time. The growth behaviour of the intermetallic layer follows a parabolic one. The growth rate constant is calculated by plotting average intermetallic layer thickness with the square root of dipping time, as shown in Fig. 4.17 (b). The slope of the graph gives the growth constant. The growth constant K obtained from the plot is 1.34 $\mu ms^{-1/2}$. The growth rate is less in this case when compared to that of the Fe/Al system.
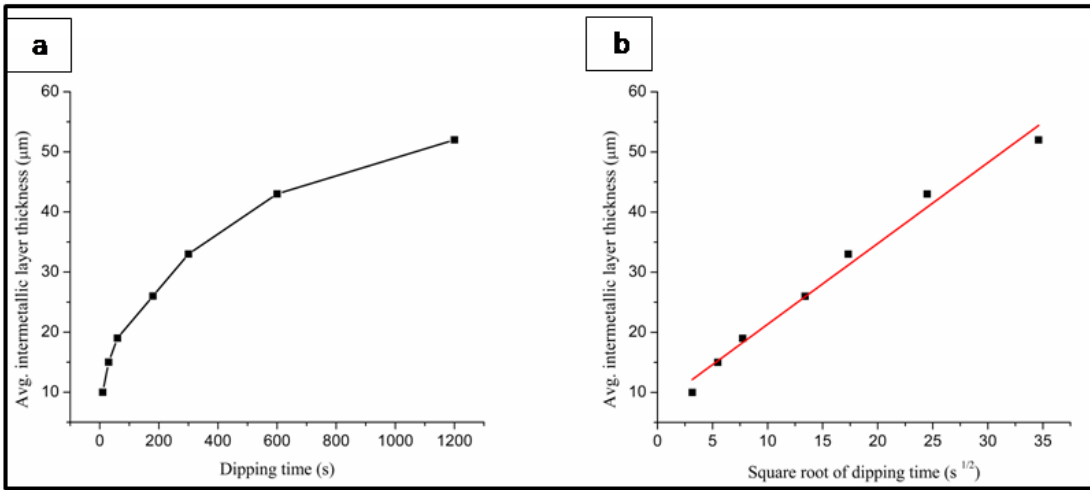
Fig. 4.17 (a) Plot of the average intermetallic layer thickness with the dipping time, (b) plot of average intermetallic layer thickness with the square root of dipping time.

4.3 Microstructure at the Interface between SS 321/Al

The typical microstructure at the interface between AISI 321 steel and molten Al after hot-dip aluminizing is shown in Fig. 4.18. The microstructure shows three distinct regions similar to the Fe/Al and SS 430/Al interfaces, the solidified aluminum topcoat, the intermediate intermetallic layer and the base metal. The aluminum topcoat consists of dispersed intermetallic phases in the aluminum matrix. High magnification micrograph of the aluminum topcoat is shown in Fig. 4.19.
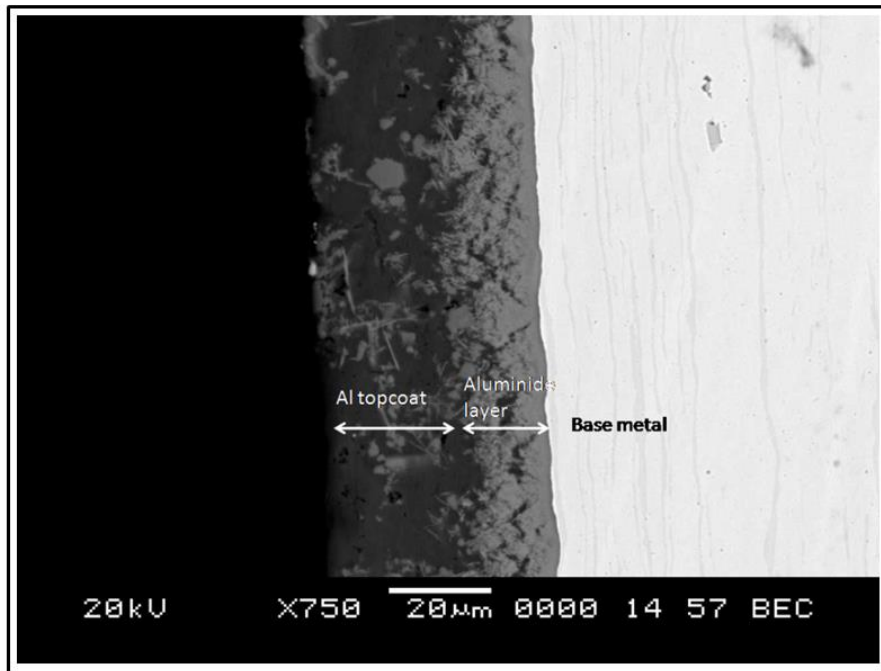
Fig. 4.18 Typical SEM-BSE micrograph at the interface between stainless steel 321 and aluminum.
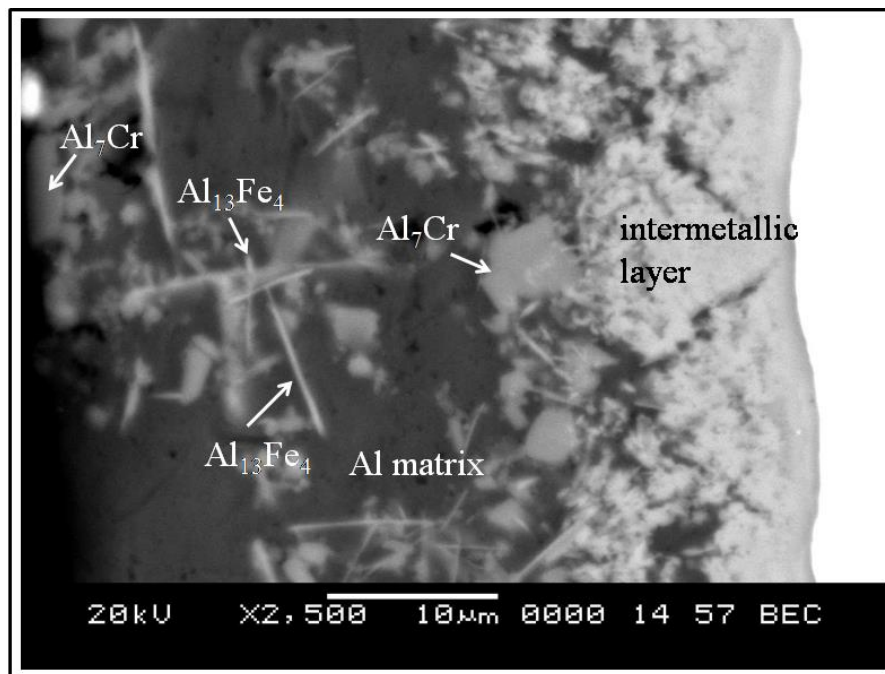
Fig. 4.19 SEM micrograph of Al topcoat, showing a polygonal-shaped Al_7Cr phase and acicular-shaped $Al_{13}Fe_4$ phase embedded in the Al matrix.

It shows two kinds of phases, one acicular or needle-like phase with the length of 2 to 3 μm and width less than 0.5 μm which are later identified as $Al_{13}Fe_4$ by TEM studies (discussed in the next chapter). The other intermetallic phase has a polygonal shape with the size ranging from submicrometer level to 5 μm which are subsequently confirmed by TEM studies as the Al_7Cr phase.

4.3.1 Growth kinetics

The growth kinetics of the intermetallic layer formed at the interface between stainless steel 321 and molten Al is studied by plotting average intermetallic layer thickness with dipping time. Figure 4.20 shows the cross-sectional micrographs of the steel samples dipped in the molten bath for different durations. The thickness of the intermetallic layer seems to be almost constant with varying dipping durations. The thickness varies in the range of 10 to 15 μm. The interface between the intermetallic layer and steel is smooth and flat, while on the topcoat side, the interface is irregular. Close observations on the aluminum topcoat show that the morphology of dispersed intermetallic phases in the aluminum matrix changes with dipping duration. At short dipping time of 10 seconds, the topcoat consists of fine eutectic dispersoids and plate-shaped intermetallic phases. With the increase in dipping duration to 600 seconds, the topcoat consists of acicular or needle-shaped phases along with polygonal-shaped ones. At the dipping duration of 1800 seconds, the topcoat consisted of long acicular shaped phases dispersed in the aluminum matrix. Figure 4.21 shows the variation in average intermetallic layer thickness with dipping time. The growth behaviour observed is independent of dipping time, with a thickness of the intermetallic layer in the range of 10 to 15 μm.
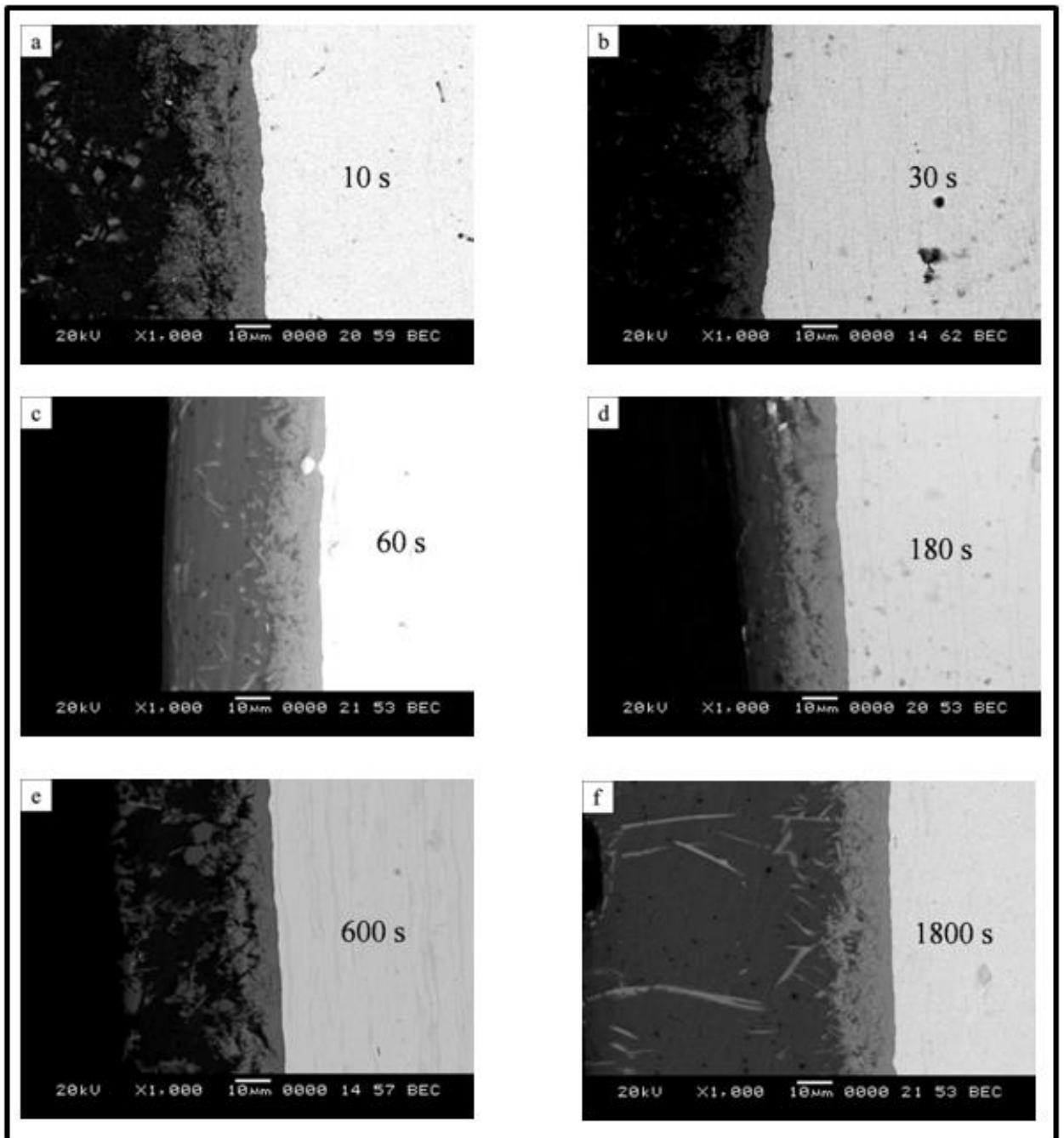
Fig. 4.20 SEM-BSE microstructures of aluminized 321 steel at various dipping durations (a) 10 s, (b) 30 s, (c) 60 s, (d) 180 s, (e) 600 s, and (f) 1800 s. The average intermetallic layer thickness is in the range of 10-15 μm.
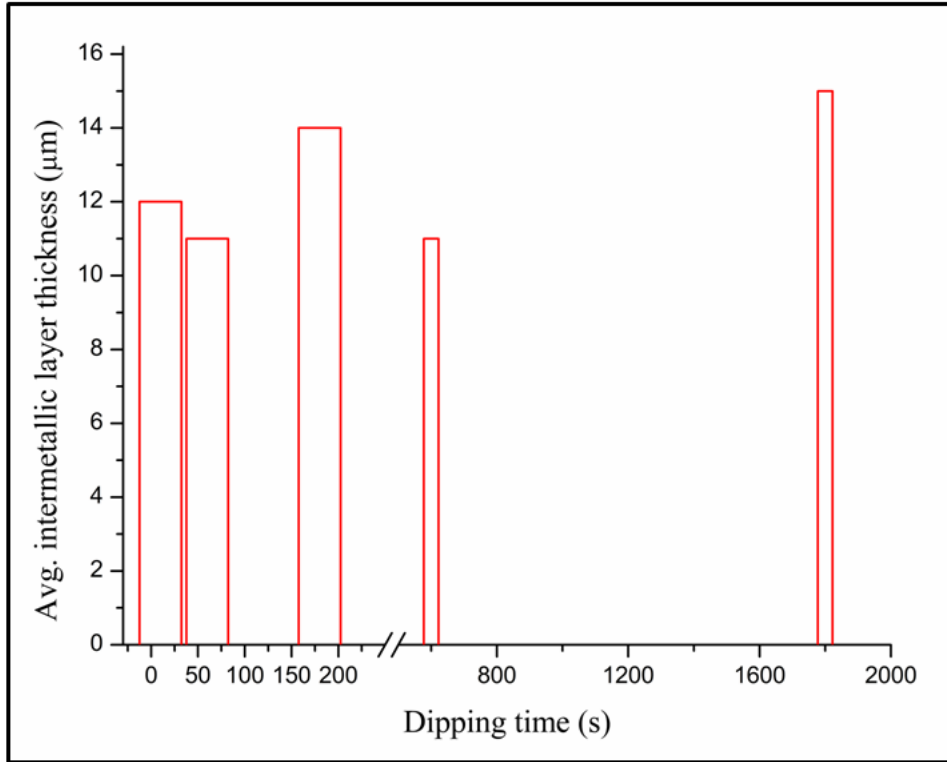
Fig. 4.21 Plot of average intermetallic layer thickness with dipping durations.

4.4 Discussion

4.4.1 Fe/Al system

The interaction between the solid Fe and molten Al proceeds by formation of the intermetallic layer at the interface (Kobayashi and Yakou 2002; Springer et al. 2011; Chen et al. 2016). The intermetallic layer is comprised of two phases: $Al_{13}Fe_4$ and Fe_2Al_5 phases. The mechanism of intermetallic layer formation and the phase formation sequence has been proposed by several authors. According to Liberski et al. (2008) at the moment when the cold iron substrate comes in contact with the molten aluminum, heat transfer takes place from liquid aluminum to solid iron and bath temperature drops locally. This takes place until the substrate attains the temperature to initiate a reaction between solid iron and liquid aluminum to form Fe-Al intermediate phases. In the next step, two directional diffusion of atoms takes place and in a relatively short span of time, the phases anticipated by the binary Fe –Al system are formed. Further growth of

54

the layer takes place by interdiffusion of species through an already formed layer. Several models were put forth to predict first phase formation and sequence of subsequent phase formation (d'Heurle 1994; Walser and Bené 1976; Philibert 1993; Dybkov 2013; Pretorius et al. 1991). By assuming local equilibrium at the solid steel-liquid Al interface, thermodynamic data can be applied to predict the phase nucleation and growth. Aluminum-rich phases are favoured to form at the interface compared to Fe rich phases because of thermodynamics considerations (Shahverdi et al. 2002; Kobayashi and Yakou 2002). Accordingly, $Al_{13}Fe_4$ and Fe_2Al_5 phases should form at the interface. According to the EHF (effective heat of formation) model proposed by Pretorius et al. (1991) the phase with the most negative heat of formation at the lowest melting eutectic forms first. As per binary Al-Fe equilibrium diagram (Kattner and Burton 1992), eutectic point at 0.02 wt.% Fe, $Al_{13}Fe_4$ phase forms first and later followed by Fe_2Al_5 phase formation with subsequent interdiffusion of atoms.

Considering the interplay between the process of growth and dissolution, the mechanism of formation of the intermetallic layer could be explained as follows.

i. Iron dissolves into molten aluminum at the instance when the solid iron comes in contact with the molten Al. The Fe atoms dissolving into molten Al spread into the molten bath by a diffusion process.

Figure 4.22 shows an enlarged portion of the binary Al-Fe equilibrium phase diagram in the aluminum rich side. The solubility of iron in molten Al at 700 °C is close to 2.43 wt.%. When the concentration of Fe increases to more than 2.43 wt.%, the liquid aluminum is supersaturated with Fe atoms at the interface. Consequently, nucleation of $Al_{13}Fe_4$ phase takes place in the liquid Al. The $Al_{13}Fe_4$ phase then grows by reaction-diffusion of Al and Fe atoms and coalesces to form a layer at the interface.

ii. Once the $Al_{13}Fe_4$ layer is formed, further diffusion of atoms (Al towards Fe side and Fe towards liquid Al side) takes place through the solid $Al_{13}Fe_4$ layer. It is be noted that the difference between the composition of $Al_{13}Fe_4$ (θ) phase and Fe_2Al_5 (η) is only about 2.4 at. % Al. The $Al_{13}Fe_4$ phase could be transformed to Fe_2Al_5 phase by the diffusion of Fe atoms from the steel side or diffusion of Al atoms to the steel side.

Nucleation of the Fe_2Al_5 phase is expected when the composition reaches to that corresponding to Fe_2Al_5 phase. Further growth takes place by interdiffusion of atoms.
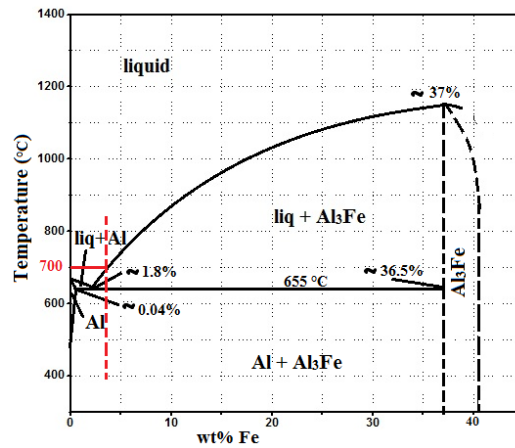
Fig. 4.22 Al-Fe binary phase diagram in the aluminium rich region (redrawn from Allen et al. (1998))

The Fe_2Al_5 phase grows towards the steel side. The fact that this phase forms the major fraction of the intermetallic layer is due to its favourable growth kinetics. For the opposite reason, the $Al_{13}Fe_4$ phase is thin and does not grow with the dipping time. Bouché et al. (1998) reported that the growth kinetics of $Al_{13}Fe_4$ phase obeys a parabolic law, while Bouayad et al. (2003) observed a linear growth relationship. Rezaei et al. (2015) reported that the $Al_{13}Fe_4$ forms by dissolution and precipitation of intermetallic compounds. In the present investigation, the thickness of $Al_{13}Fe_4$ does not vary visibly with the dipping time. According to Dybkov (2013), in case of the simultaneous growth of two layers, the second layer can grow by consuming the first layer. Also, the formed $Al_{13}Fe_4$ layer can dissolve back into the molten aluminum. Therefore, from the above discussion, it could be stated that the growth behaviour of $Al_{13}Fe_4$ is not well established.

The growth behaviour of the intermetallic phase shown in Fig. 4.3 obeys a parabolic law implying that the growth is controlled by a diffusion process. The tongue like morphology observed for Fe_2Al_5 phase is due to the rapid diffusion of the atoms along c-axis of the orthorhombic structure. This fact is also confirmed by EBSD studies carried out by Springer et al. (2011) and Cheng and Wang (2009). The orthorhombic

crystal structure consists of 30 per cent vacancies along [001] c-axis (Schubert et al. 1953). Accordingly, the rapid diffusion of Al along the c-axis leads to the tongue like morphology.

The aluminum topcoat is formed by solidification of liquid aluminum during cooling to room temperature. The Fe atoms dissolved from the base metal is present in molten Al. Further, Fe atoms diffuse through intermetallic layers and get dissolved into the bulk of molten Al. The binary Al-Fe phase diagram shown in Fig. 4.22 presents an invariant reaction at 1.8 wt. % Fe, and 655 °C. The dissolved Fe atoms precipitate as $Al_{13}Fe_4$ phase by eutectic reaction during cooling.

4.4.2 SS 430/Al system

The microstructure at the interface between SS 430 and molten Al shows similar features as observed for the Fe/Al system. The solidified Al topcoat after 10 minutes of dipping time (Fig. 4.4 (a)) predominantly shows $Al_{13}Fe_4$ phase along with Al. This fact is also confirmed by TEM studies (Fig. 4.7). The $Al_{13}Fe_4$ phase present in the intermetallic layer shows fine domains of a few nanometer size showing microtwins or faults. The electron diffraction pattern shown in Fig. 4.12 (a) confirms the presence of twins. The twinning is observed around (100) plane. A detailed study on the structure of $Al_{13}Fe_4$ phase is reported by (Skjerpe 1987). The structure of $Al_{13}Fe_4$ is monoclinic, corresponding to space group C2/m, with lattice parameters a=1.549 nm, b=0.808 nm, c=1.248 nm and β=107.8 °. The twinning is around (100) plane and could be observed when viewed along [010] orientation, while, faults are formed on (001) plane. It was also observed that the arrangement of stacking faults at z=0.5 and displacement of ½[100] which shows the same atomic arrangements as of two successive twin operations making it difficult to distinguish between stacking faults and multiple twinning.

The intermetallic layer comprised of Fe based intermetallic phases while Cr based phases were not observed. Chromium is found to be dissolved in both $Al_{13}Fe_4$ and Fe_2Al_5 phases. Fig. 4.23 shows a ternary Al-Fe-Cr isothermal section at 700 °C. At the Al-rich corner, a three-phase equilibrium of $Al_7Cr + Al_3Fe + liquid\ Al$ is stable. The

intermetallic compound Al$_7$Cr is formed by the invariant reaction $liquid + Al_{11}Cr_2 \rightleftharpoons Al_7Cr$, whereas Al$_{13}Fe_4$ is formed by the eutectic reaction at 655 °C.
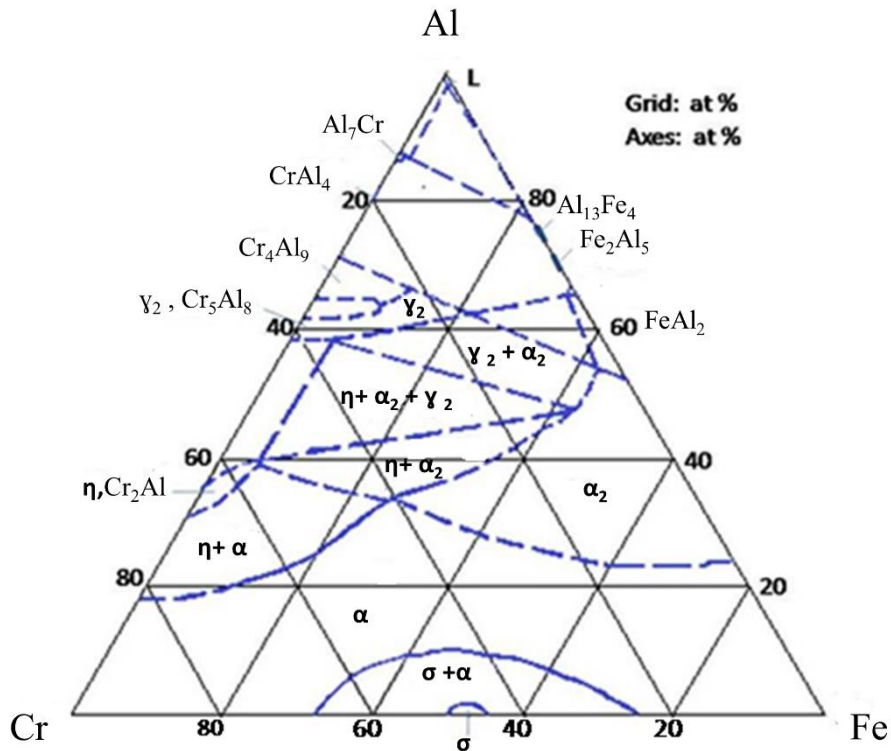
Fig. 4.23 Al–Cr–Fe isothermal section at 700 °C (redrawn from Effenberg and Ilyenko (2006))

In order to establish this equilibrium, Fe and Cr should dissolve from the base metal and nucleate in the liquid aluminum to form Fe and Cr based compounds. At the instant when the base-metal contacts the molten Al, several events take place

i. heat transfer from the molten Al to base metal

ii. solidification of the molten Al on the surface of base metal

iii. dissolution of the elements from the base metal in order to establish equilibrium.

The solidified Al layer might be short-lived as the volume of molten aluminum is very large compared to the base metal. Further, with the continuation of the transfer of heat, partial or full re-melting of the solidified Al takes place. Since a nonequilibrium condition exists at the interface, metastable solubility of the elements can be expected

as the equilibrium solubility takes place at an infinitesimally slow rate. Therefore, a concentration greater than that of saturation concentration exists due to metastable dissolution. Hence, a driving force exists for the nucleation of intermetallic phases. Based on the binary phase diagram, the solubility of Fe is 2.5 wt.% and that of Cr is 0.7 wt.% (ASM Handbook 1992). Five intermetallic phases are present in Fe-Al system of which $Al_{13}Fe_4$ phase is thermodynamically more favourable. From the supersaturated liquid Al, $Al_{13}Fe_4$ phase nucleates first and grows. As the diffusion of elements continues, nuclei coalesce and form the intermetallic layer. A schematic of the process is shown in Fig. 4.24
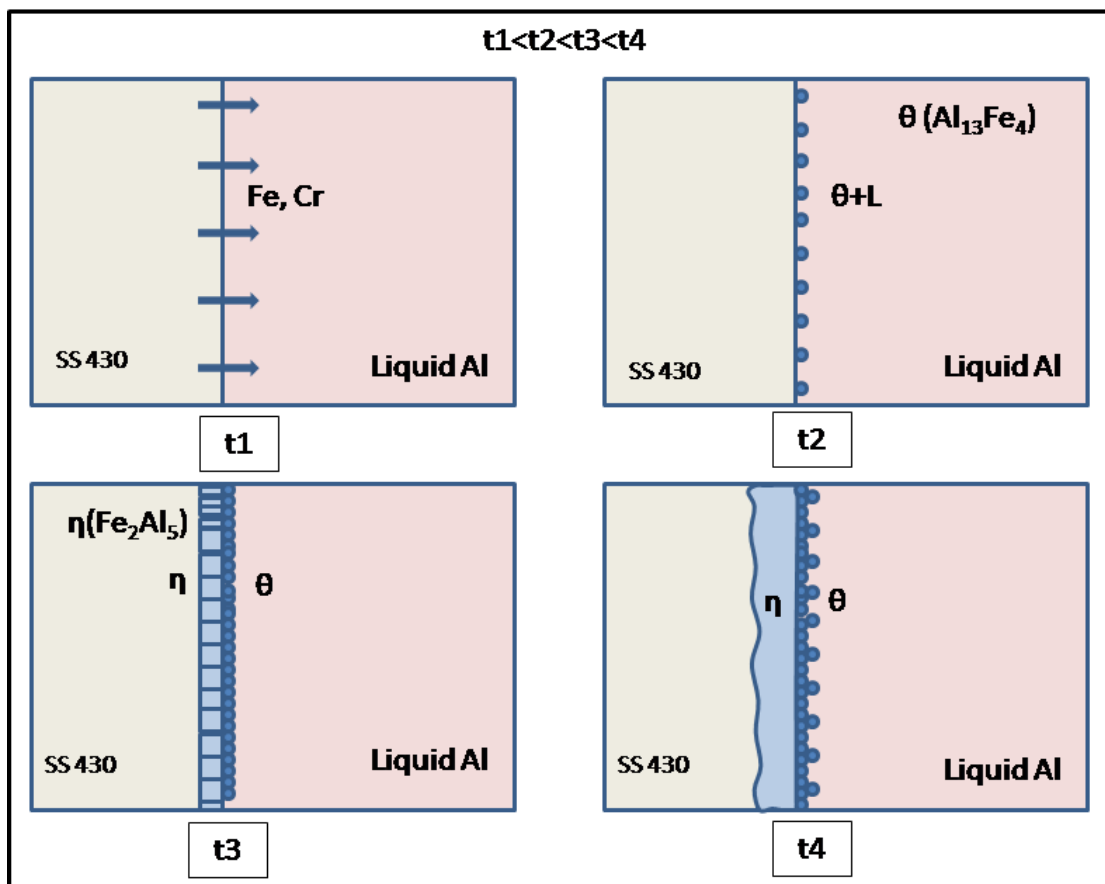
Fig. 4.24 Schematic representation of the formation of the intermetallic layer during aluminizing

The process starts with the dissolution of elements from the base metal followed by nucleation of $Al_{13}Fe_4$ phase at the interface. These nuclei coalesce and grow by the reaction-diffusion mechanism. Further diffusion of Fe from base metal and Al from

molten Al takes place through the $Al_{13}Fe_4$ phase. Nucleation of the Fe_2Al_5 phase occurs when the favourable composition is attained. Further, the growth of these phases takes place by reaction-diffusion. The Fe_2Al_5 phase is kinetically favoured and rapid growth of the phase is observed. Whereas, the $Al_{13}Fe_4$ phase is observed in the intermetallic layer as well as in the solidified aluminum topcoat. From the TEM-EDS analysis presented in Fig. 4.8 and 4.13, the chromium dissolved in $Al_{13}Fe_4$ phase formed in the topcoat is close to 1.7 at. %, while it is close to 4.5 at. % for the $Al_{13}Fe_4$ phase present in the intermetallic layer. The maximum solubility of Cr in $Al_{13}Fe_4$ phase at 1000 °C is 6.4 at.% Cr (Palm 1997). Therefore, the mechanism of formation of the $Al_{13}Fe_4$ phase found in the aluminum topcoat is different to that of the $Al_{13}Fe_4$ phase formed in the intermetallic layer. The $Al_{13}Fe_4$ phase in the reaction layer is formed by a reaction-diffusion mechanism, while that in the topcoat is formed during cooling through the eutectic point.

The thickness, as well as growth kinetics of the intermetallic layer in the case of SS 430/Al system, is reduced compared to the Fe/Al system. Although the interface formation mechanism is similar in both the system (i.e. by reaction-diffusion type), the change in the thickness and growth kinetics is the effect of the presence of the alloying element.

According to the literature reports, the addition of the alloying element to the molten Al bath has a significant influence on the microstructure. The element silicon added to molten Al has been a "star" element in reducing intermetallic layer thickness (Cheng and Wang 2011; Springer et al. 2011; Yin et al. 2013; Han et al. 2018; Shin et al. 2018). Silicon present in the melt helps in reduction of intermetallic layer thickness. It is reported that the silicon occupies structural vacancies in the Fe_2Al_5 layer thereby reducing the diffusivities of Fe and Al (Cheng and Wang 2009).

On the contrary, chromium addition to molten Al bath had no effect on the morphology and growth kinetics of the intermetallic layer. Figure 4.25 shows the typical cross-sectional microstructure of Fe-Al intermetallic layer with Cr addition to molten Al. With the addition of chromium, Al_7Cr intermetallic phase formation was observed close to the Fe-Al intermetallic layer. However, the effect Cr on the intermetallic layer

thickness and morphology was not observed. SEM-EDS on the intermetallic layer showed no chromium content suggesting that chromium does not play any role in the growth of the intermetallic layer.
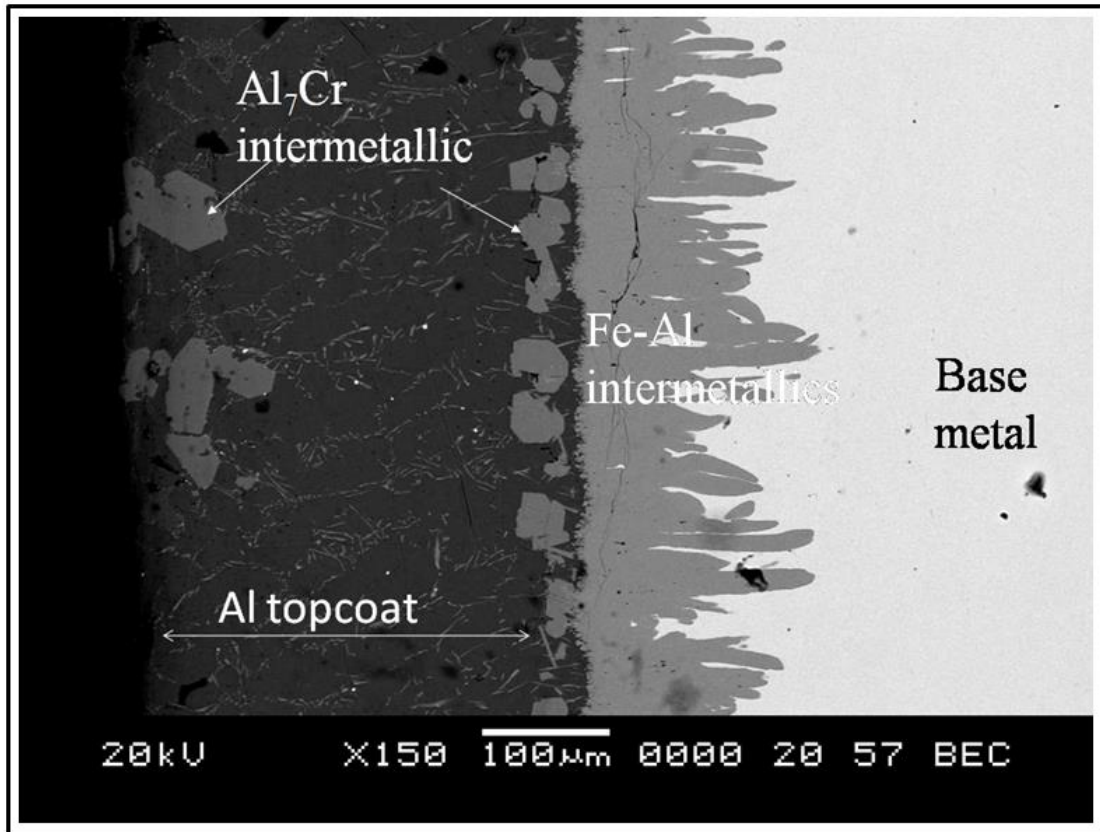
Fig. 4.25 Typical cross-sectional SEM-BSE micrograph of the Fe-Al intermetallic layer with the chromium addition.

Dangi et al. (2018) reported that the addition of alloying elements into the base metal reduces the intermetallic layer thickness. Silicon had the maximum effect compared with Mn and Ni in the base metal. The presence of chromium in the base metal of ferritic grade SS 430 steel plays a similar role by occupying structural vacancies in the Fe_2Al_5 phase, which reduces the vacancy concentration. Thus, by occupying excess vacancy chromium may reduce the interdiffusion coefficients of Fe and Al through the Fe_2Al_5 layer.
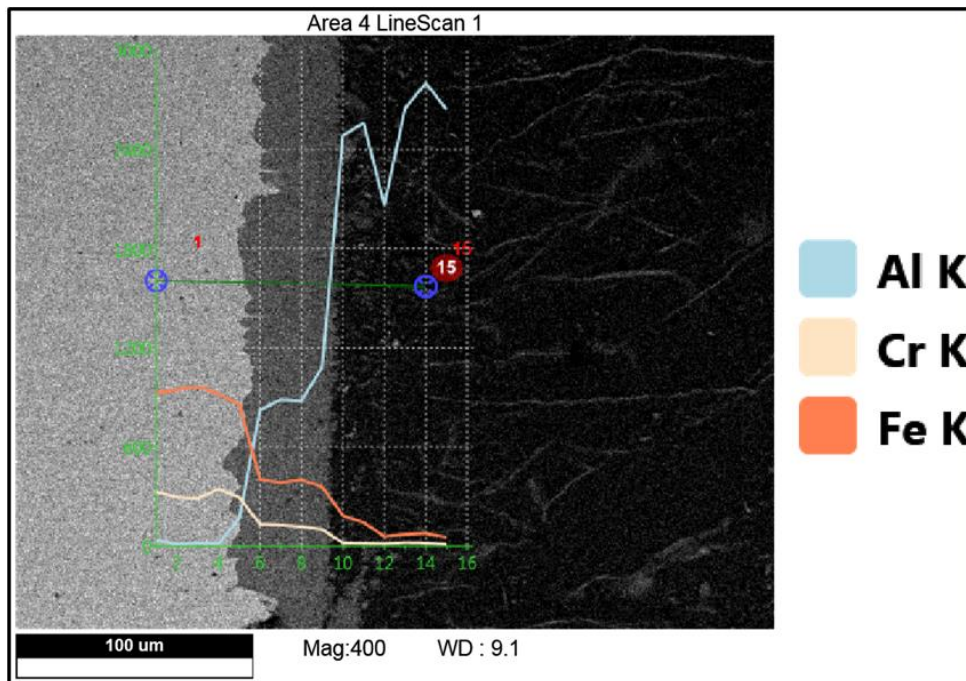
Fig. 4.26 SEM-EDS line profile analysis

The SEM-EDS line analysis is presented in Fig.4.26 shows 6 at. % Cr dissolved in the Fe_2Al_5 layer. The chromium dissolved is uniformly distributed in the Fe_2Al_5 layer without any gradient within the layer as observed in the EDS line profile analysis. It also suggests the absence of any second phase. Hence, the presence of chromium has reduced the growth rate of the intermetallic layer when compared to pure Fe/Al system. Therefore, we conclude that the presence of chromium in the base metal makes Fe_2Al_5/SS 430 interface smoother and reduces Fe_2Al_5 layer growth kinetics as compared to Fe/Al system. On the contrary, chromium in the bath had no effect on the morphology and growth of the intermetallic layer.

4.4. SS 321/Al system

The morphology of the intermetallic layer, as well as that of the Al-topcoat, is different in this system as compared to Fe/Al and 430/Al system. The growth kinetics of the intermetallic layer does not follow any trend and thickness seems to remain constant with dipping time. Detailed transmission electron microscopic investigations are carried out and the mechanism of microstructural evolution is discussed in the next chapter.

Page intentionally left blank

Page intentionally left blank

CHAPTER 5

TEM INVESTIGATION ON THE EVOLUTION OF MICROSTRUCTURE AT THE INTERFACE BETWEEN AISI 321 STAINLESS STEEL AND MOLTEN ALUMINUM

This chapter deals with understanding the microstructural evolution at the interface between SS 321 and molten aluminum. Detailed TEM investigations are carried out, results are presented, and the mechanism of microstructural formation is derived.

5.1 Interaction Between Solid AISI 321 Steel-Liquid Aluminum: Evolution of the Microstructures with Different Dipping Durations

It is observed from the previous discussion that the growth behaviour of the intermetallic layer formed at the interface between the Fe/Al and SS 430/Al system followed a parabolic one. On the contrary, for the case of SS 321/Al system, the growth behaviour of the intermetallic layer is independent of the dipping time. Careful observation on the cross-sectional SEM micrographs, presented in Fig. 4. 20 shows a small difference in the microstructure of the aluminum-topcoat with different dipping durations, while the exact microstructural features of the aluminide layer could not be ascertained with only SEM investigations. Therefore, detailed TEM investigations were carried out on both the aluminide layer and the topcoat formed with different dipping durations to understand the mechanism of microstructural formation.

5.1.1 Dipping time: 10 seconds

The steel sample was dipped in the molten Al bath for 10 seconds and air cooled. The analysis was carried out to study the formation of microstructural features at the initial stages of interaction. Figure 5.1 shows the typical cross-sectional SEM-BSE micrograph of the hot-dip aluminized sample dipped for 10 seconds. It exhibits two distinct regions which are classified as (i) an intermetallic layer at the interface between

base metal and aluminum and (ii) an outer aluminum topcoat. The average thickness of the former is about 15 ± 2 µm. while that of latter is in the range of 50-60 µm.
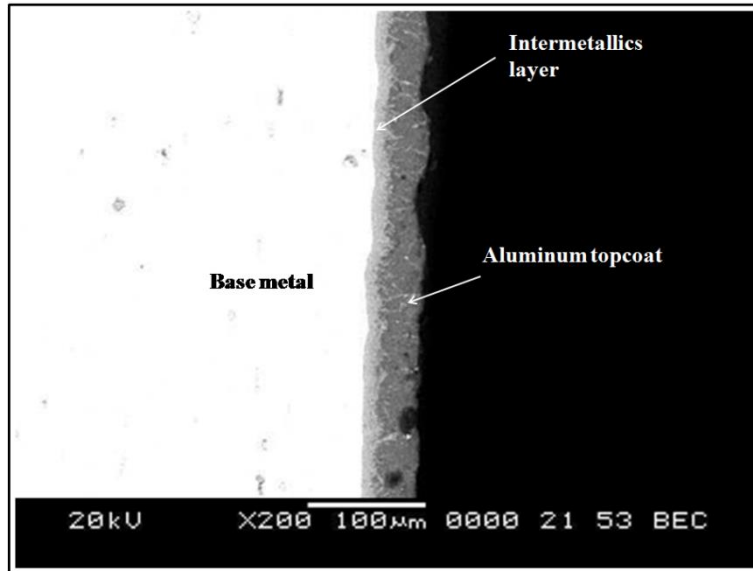
Fig. 5.1 Typical SEM-BSE micrograph of the aluminized sample. Two regions are identified in the coating: the intermetallic layer at the interface and solidified aluminum topcoat.

5.1.1.1 Intermetallic layer

Figure 5. 2 shows the SEM-BSE micrograph of the intermetallic layer having been formed at the interface. The layer comprises of blocky intermetallic phases with size less than a micrometre. Fragments of the base metal being embedded in the coating are also observed (marked by black arrow). SEM-EDS presented in Fig. 5.3 also confirm this fact.
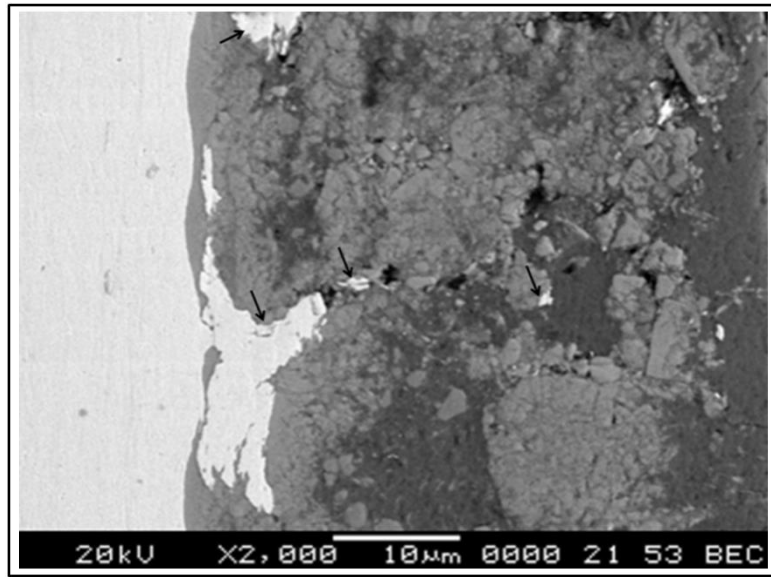
Fig. 5.2 High magnification SEM-BSE micrograph at the interface. Fragments of base metal being embedded into Al (marked by black arrow) are seen.
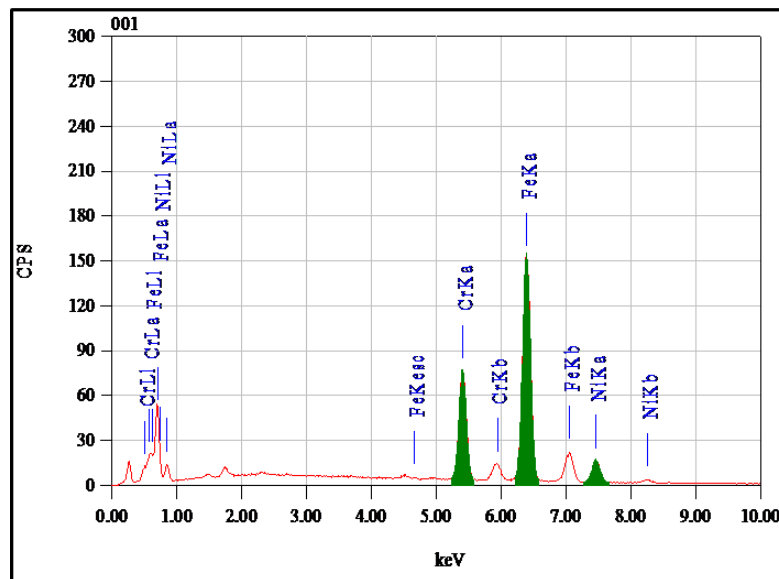
Fig. 5.3 SEM-EDS point analysis corresponding to the embedded base metal in the Al.

The investigations carried out by Transmission electron microscopy (TEM) at the interface also reveals these blocky phases as shown in Fig. 5.4 (a) and (b). The size of these phases ranges from sub-micrometer level to 1 micrometer. The analysis of electron diffraction patterns presented in Fig. 5.4 (c) and (d) confirms the tetragonal lattice of FeAl$_m$ phase. The diffraction patterns are recorded along [010] and [111] major zone axis of the FeAl$_m$ phase. The lattice parameters measured are a=b=8.84 Å

and c=21.6 Å. The FeAl$_m$ is an Al-rich metastable phase and the value of m ranges from 4 to 4.4 as per the literature data (Celil et al. 1998; Dunlap et al. 1998). Further, the elemental analysis by TEM-EDS depicts the composition to be Al: 80.4 at. %, Fe: 17 at. %, Ni: 2.6 at. % which is close to the chemical composition of FeAl$_m$ phase.
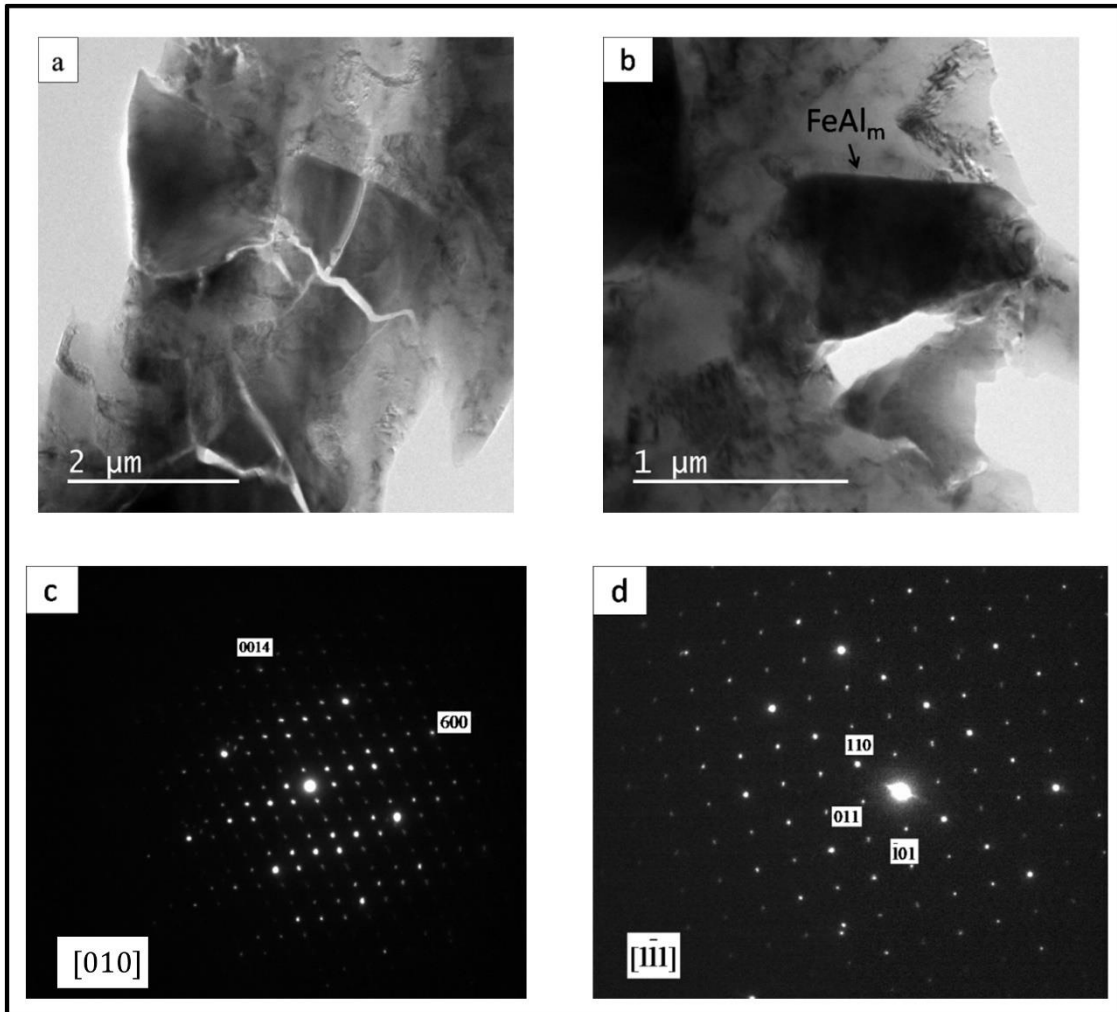
Fig. 5.4 (a) and (b) Bright field TEM micrographs of metastable phase FeAl$_m$, (c) SAED pattern along [010] zone axis, and (d) along [111] zone axis of the body-centred tetragonal lattice.

Figure. 5.5 (a) reveals that some of these blocky phases displays peculiar rosette type morphology. The bright field TEM image presented in Fig. 5.5 (a) reveals the characteristic ten-armed branching. The size of this phase is close to 1 μm and the electron diffraction pattern presented in Fig. 5.5 (b) shows a pseudo tenfold diffraction pattern of arguably the quasicrystalline phase. Figure 5.5 (c) portrays threefold

diffraction pattern and the high magnification micrograph shown in Fig. 5.5 (d) reveals contrast due to twinning.
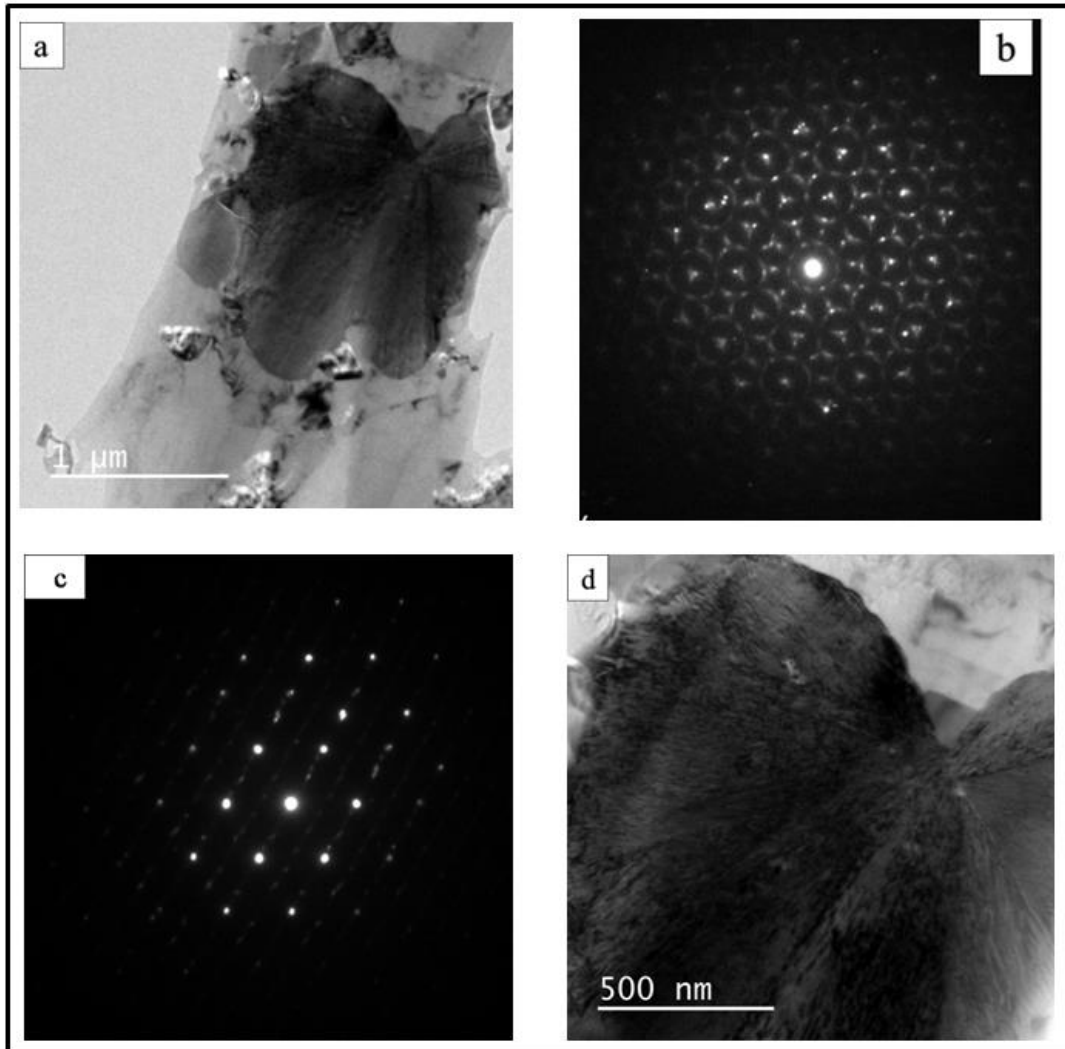
Fig. 5.5 (a) Bright field TEM micrograph of the intermetallic phase showing rosette type morphology, (b) pseudo tenfold diffraction pattern due to multiple twinning, (c) Pseudo threefold diffraction pattern, and (d) high magnification micrograph showing contrast due to twinning.

Within the intermetallic layer close to the base metal side, few entities with fine grain microstructure are observed, as shown in Fig. 5.6. Bright field TEM micrographs of such a phase are shown in Fig. 5.6 (a) and (c). The grain size measured is in the range of 20-30 nm. Selected area electron diffraction presented in Fig. 5.6 (b) confirms the phase to be a ferritic (body-centered cubic). The TEM-EDS analysis shows composition

to be (in at. %) Fe: 62, Cr: 24, Ni: 6 and Al: 8. An increase in chromium content and a decrease in nickel content are observed along with a small percentage of aluminum.
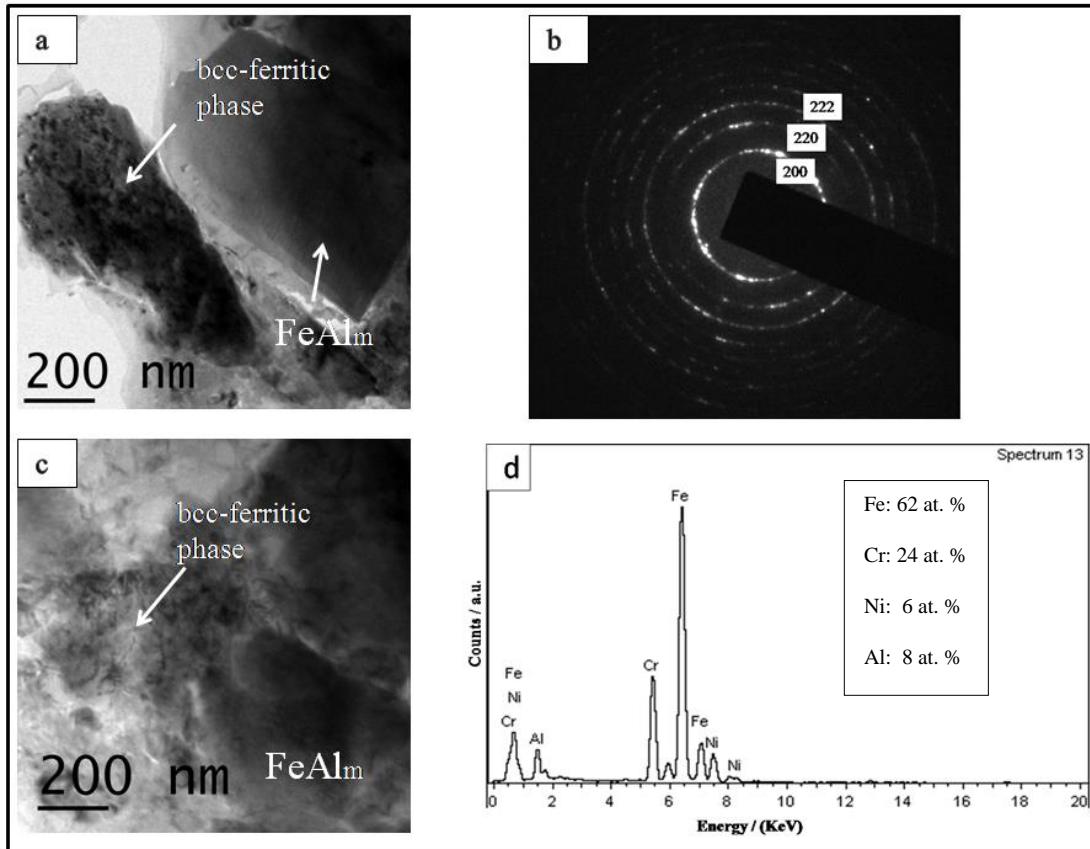
Fig. 5.6 (a) and (c) Bright field TEM micrographs of a fine-grained ferritic (body-centred cubic) phase, (b) selected area electron diffraction pattern confirming the ferritic phase, and (d) corresponding TEM-EDS spectrum showing an increase in Cr content.

5.1.1.2 Aluminum topcoat

Figure 5.7 shows SEM-BSE image of the region of aluminum topcoat. It forms during solidification when the base metal is removed from the melt. During the cooling stage, the adhering Al solidifies incorporating intermetallic phases dispersed in the Al matrix. Some of the dispersed intermetallic phases are observed to be formed as one of the eutectic phases. The microstructure is further analyzed in detail by TEM.
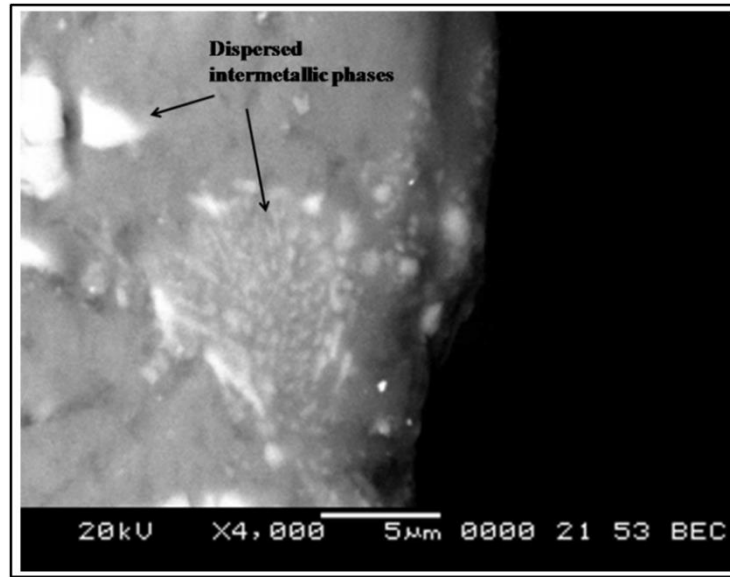
Fig. 5.7 SEM-BSE micrograph of the aluminum topcoat. Presence of dispersed intermetallic phases is seen.

Figure 5.8 (a) and (b) shows bright field TEM micrographs of the intermetallic phase showing rod-like eutectic morphology. The inset in Fig. 5.8 (a) shows corresponding electron diffraction patterns of the two phases. Fig. 5.8 (c) shows rod-like eutectic morphology observed parallel to the electron beam. The rod has a maximum length is 2 μm and the diameter ranges from 100-300 nm. Figure 5.8 (d) presents the TEM-EDS elemental analysis of the rod-like intermetallic phase which reveals the composition as Ni: 12, Fe: 9, and Al: 79 (all in at. %).

Figure 5.9 shows the electron diffraction patterns taken along the three major zone axis of the intermetallic phase. Further, the analysis of these diffraction patterns reveals the orthorhombic structure. The lattice parameters measured are a= 5.3 Å, b= 10.2 Å, c= 17.3 Å and consistent with the angles between the zone axis. The angles are measured using the goniometer tilt recording system attached to the instrument.
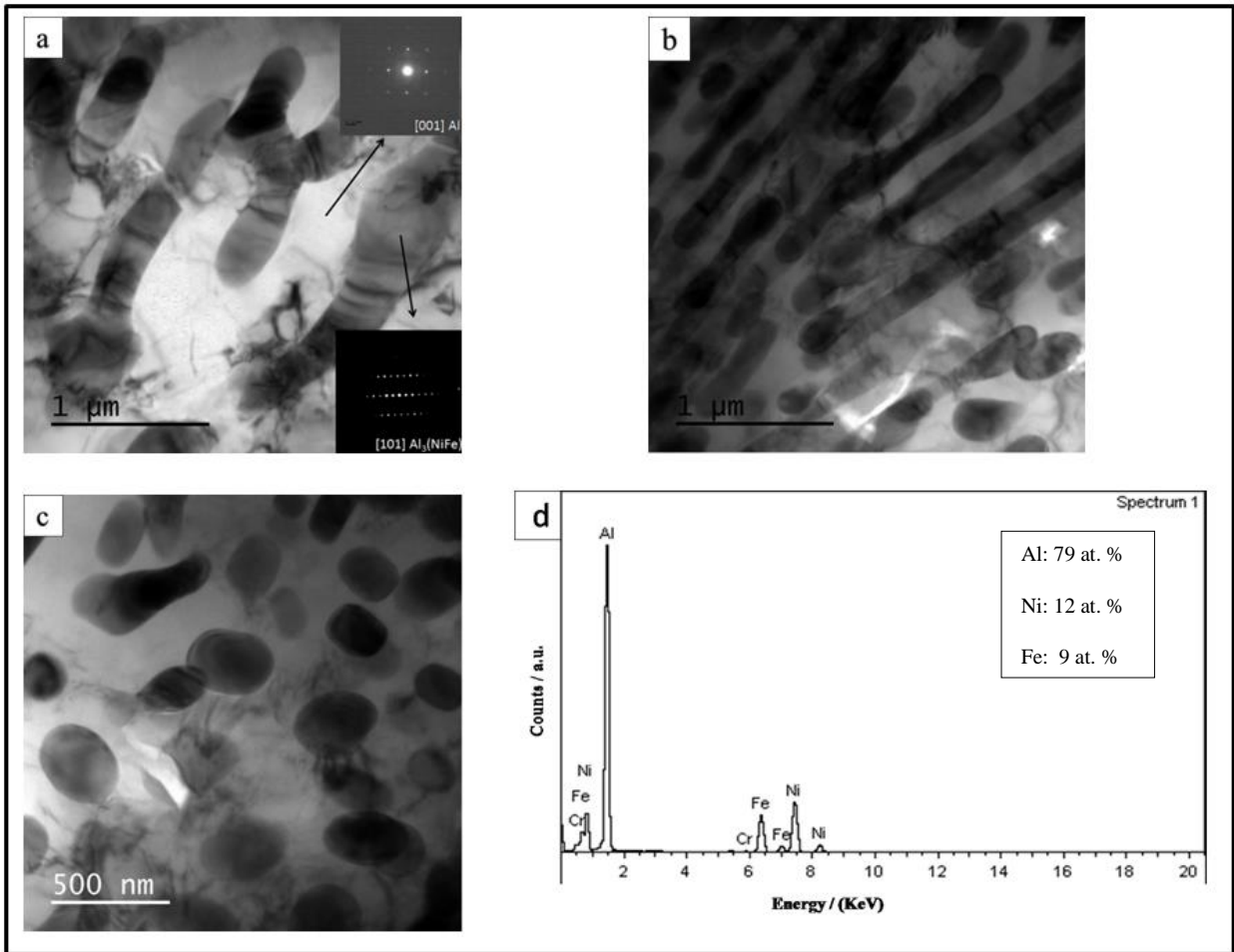
Fig. 5.8 (a) and (b) Bright field TEM micrograph showing the eutectic morphology of the intermetallic phase near the top surface. Inset in Fig. (a) shows corresponding diffraction patterns of α-Al and $Al_3(NiFe)$ phases, (c) rod-like eutectic morphology seen parallel to the electron beam, and (d) TEM-EDS spectrum of $Al_3(NiFe)$ phase.
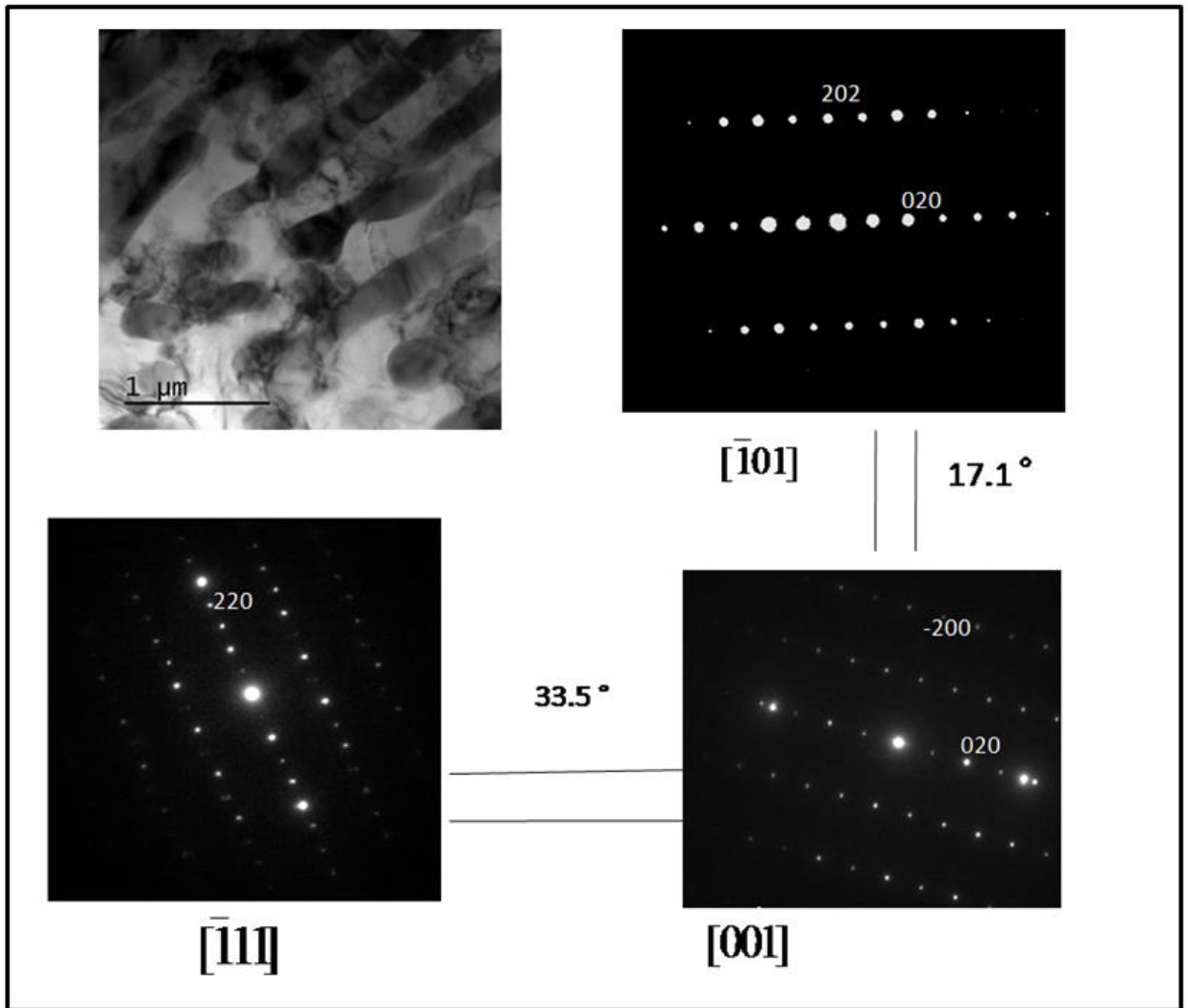
Fig. 5.9 Electron diffraction patterns along three major zone axis of metastable Al$_3$(NiFe) orthorhombic phase.

Figure 5.10 shows the diffraction patterns which establish the orientation relationship between the aluminum matrix and the phase dispersed in it. Accordingly following orientation relationships are found to be existing:

(220) Al3(NiFe) ‖ (200) matrix

(020) Al3(NiFe) ‖ (111) matrix.
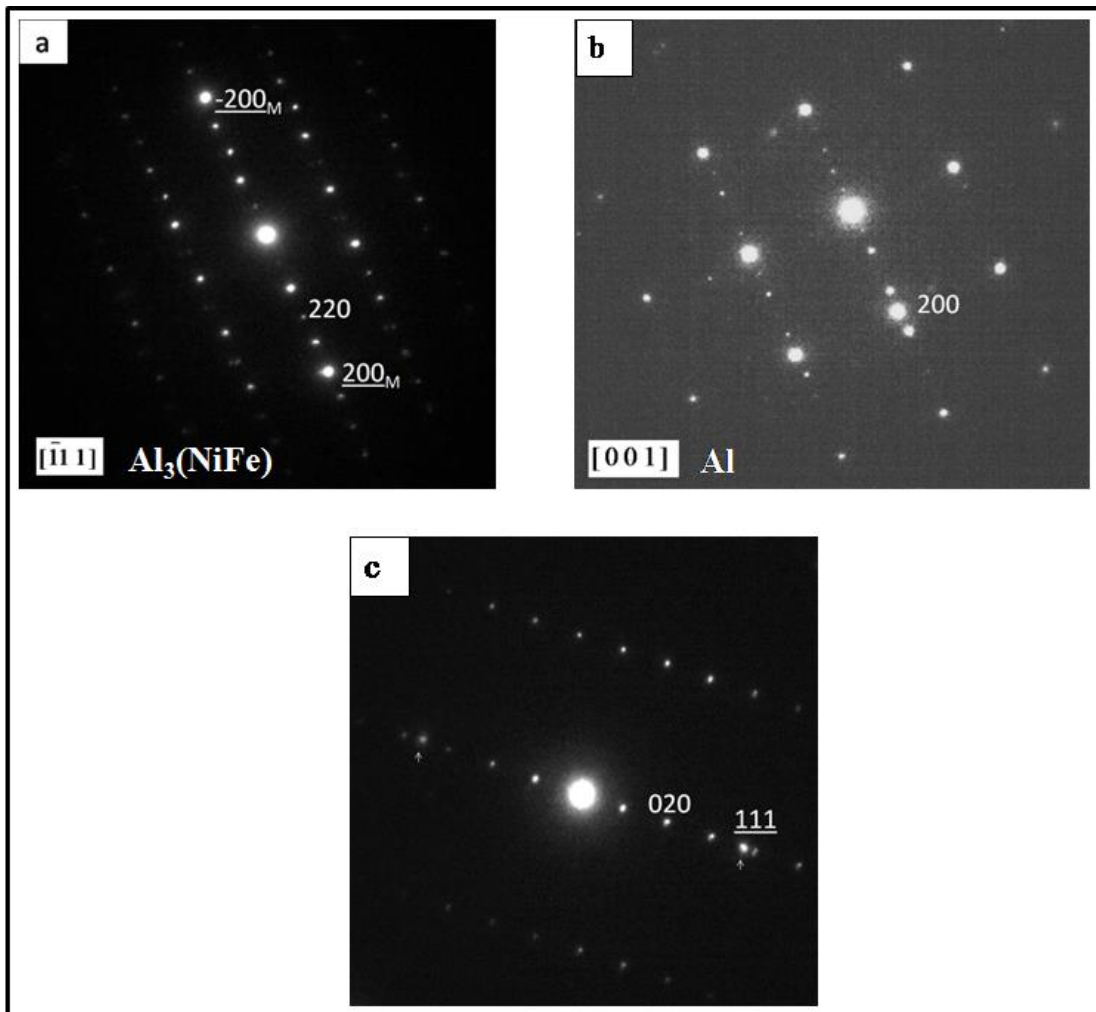
Fig. 5.10 Electron diffraction patterns showing orientation relationship between $Al_3(NiFe)$ phase and aluminum matrix (a) along [-111] zone axis of $Al_3(NiFe)$), (b) along [001] zone axis of Al matrix, and (c) another orientation variant (020) $Al_3(NiFe)$ || (111) matrix.

Figure 5.11 shows the X-ray diffraction patterns of the coating . Figure 5.11 (a) shows the pattern of the aluminum topcoat. All the Bragg reflections correspond to Al phase. The $Al_3(NiFe)$ phase present in the aluminum topcoat could not detected due to its small volume fraction. Figure 5.11 (b) shows the X-ray diffraction pattern of the intermetallic layer. The observed Bragg reflections are in close agreement with $FeAl_m$ and Al phases. The Bragg reflections are indexed according Skjerpe (1988) and the major reflections for the $FeAl_m$ phase correspond to (413) and (330) planes.
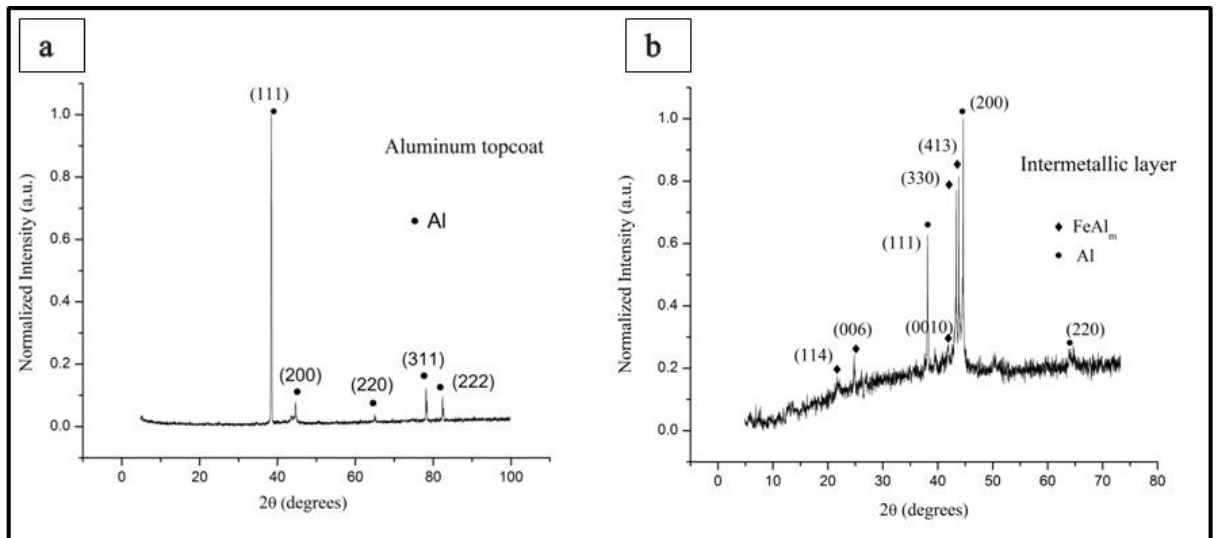
Fig. 5.11 XRD patterns of (a) aluminium topcoat and (b) intermetallic layer

5.1.2 Dipping time: 60 seconds

The growth kinetics of the intermetallic layer is studied by holding the base metal in molten aluminum for various time durations. The typical microstructure as shown previously (Fig. 5.1) consists of the two regions, (i) the intermetallic layer and (ii) the solidified aluminum topcoat. The microstructural details are further revealed through TEM studies.

5.1.2.1 Intermetallic layer.

TEM investigations on this layer reveal that the microstructure is similar to that seen for 10 seconds of interaction time. Figure 5.12 shows TEM micrographs obtained on the intermetallic layer. The layer consists of several phases. Figure 5.12 (a) shows a metastable $FeAl_m$ phase with a size close to one micrometre. Figure 5.12 (b) shows the associated electron diffraction pattern for the $FeAl_m$ phase. Further, the layer also consists of fine-grained ferritic phase, which is expected to form during the dissolution process. It is shown in Fig. 5.12 (c). The rod-shaped phase shown in Fig. 5.12 (d) corresponds to Al_7Cr phase. The length of this phase measured is in the range of 2-3 micrometres and the width is close to 300 nanometers.
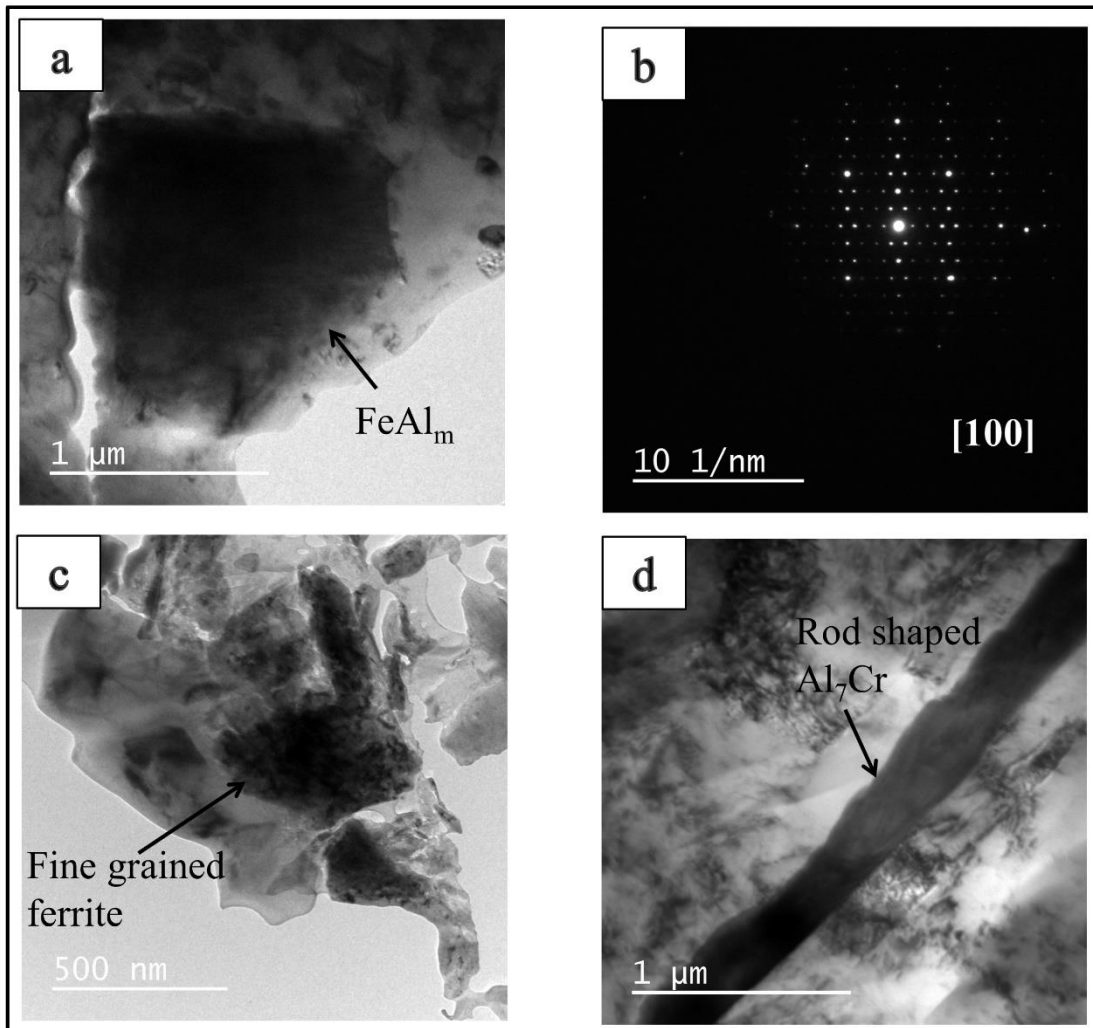
Fig. 5.12 (a) Bright field TEM micrograph of FeAlm phase, (b) corresponding SAED pattern of the $FeAl_m$ phase along [100] zone axis, (c) fine-grained ferritic phase, and (d) rod-shaped Al_7Cr phase.

5.1.2.2 Aluminum topcoat

The microstructure in the topcoat is similar to that obtained for the sample dipped and held for 10 seconds. It is seen that the topcoat consists of dispersed intermetallic phases of orthorhombic $Al_3(NiFe)$ in the aluminum matrix. Figure 5.13 shows the metastable $Al_3(NiFe)$ phase being formed as one of the eutectic phases with Al.
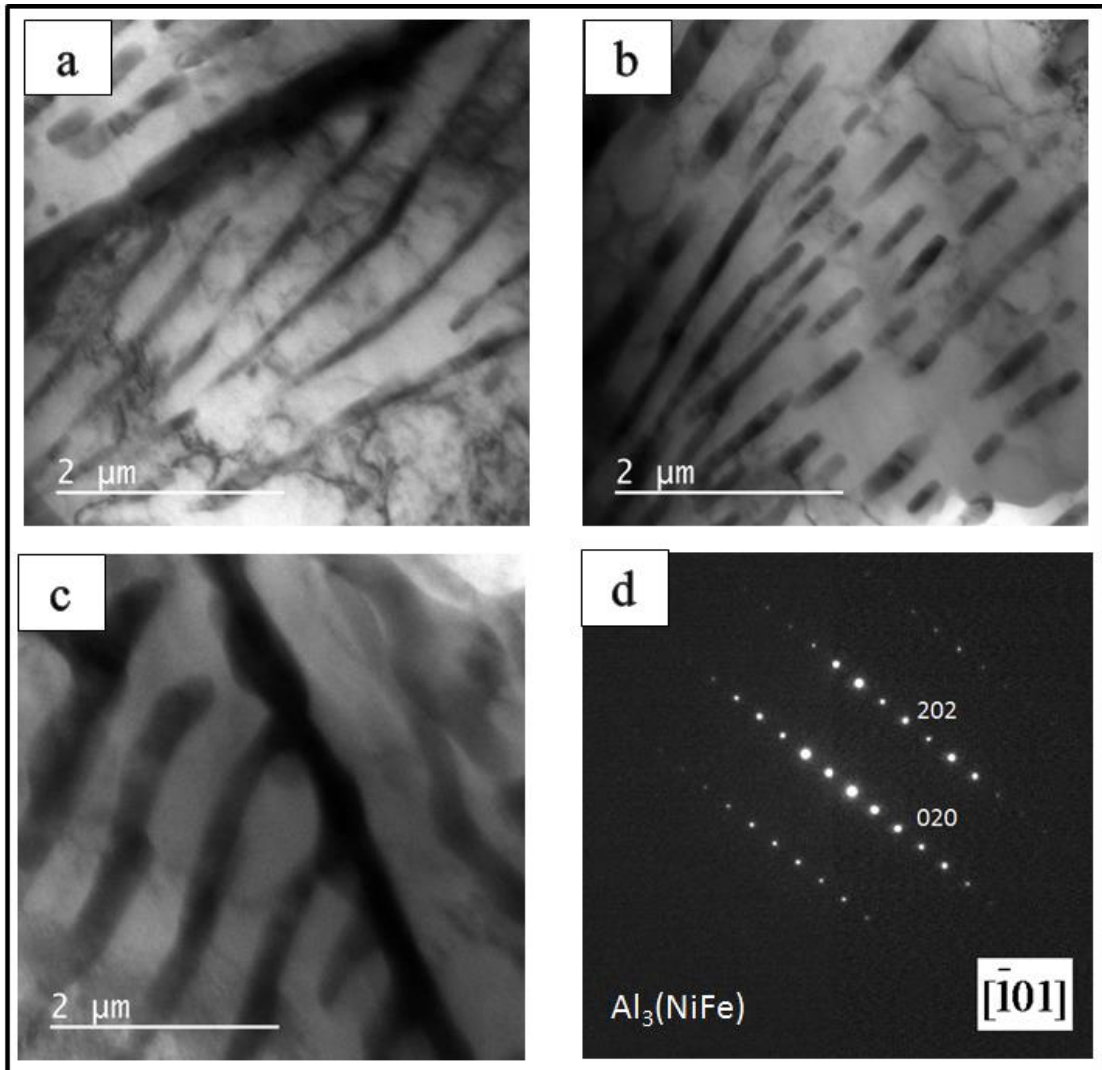
Fig. 5.13 (a-c) Bright field TEM micrograph of metastable eutectic $Al_3(NiFe)$ phase formed in the topcoat, and (d) SAED pattern of the $Al_3(NiFe)$ phase along [-101] orientation.

TEM-EDS analysis carried out on this phase shows composition as Al: 78, Fe: 13 and Ni: 9 (all in at. %). An increase in iron content is noted here compared to the samples dipped for 10 seconds. TEM-EDS spectrum of this phase is shown in Fig.5.14. It shares the same orientation relationship with the Al matrix, as mentioned previously. Figure 5.15 shows TEM micrograph of the interface between $Al_3(NiFe)$ phase and Al matrix. It reveals the presence of dislocations in the Al matrix close to the interface. This indicates that quite a large amount of mismatch strain exists over the interface.
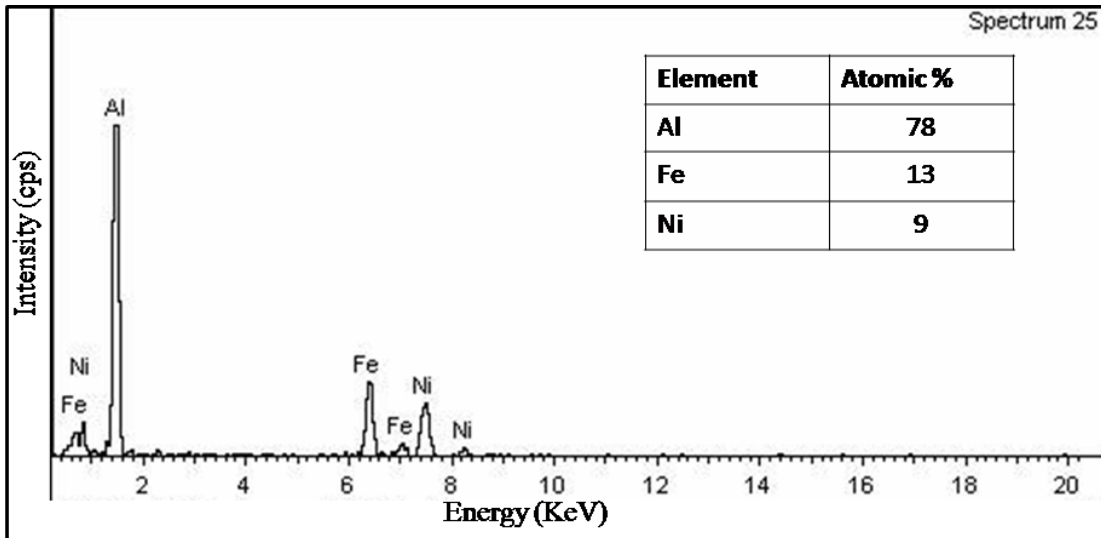
Fig. 5.14 TEM-EDS spectrum of $Al_3(NiFe)$ phase
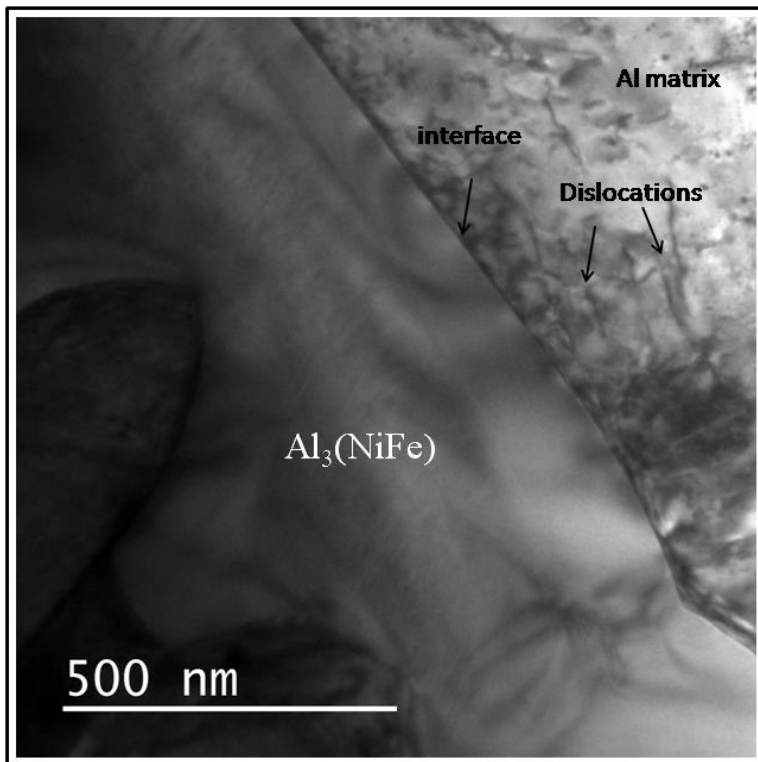
Fig. 5.15 Bright field TEM micrograph showing the interface between $Al_3(NiFe)$ and Al matrix. Dislocations are also observed

The high-resolution lattice-fringe image is shown in Fig. 5.16. The FFT image shown in Fig. 5.16 (b) shows (020) Al_3(NiFe) || (111) matrix orientation relationship.
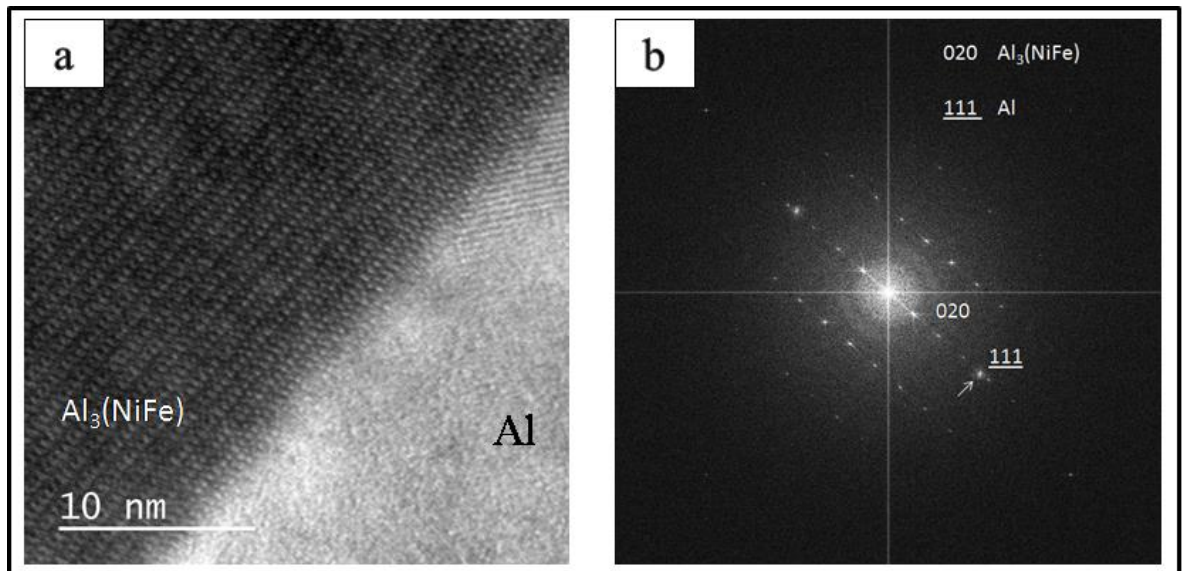
Fig. 5.16 (a) Lattice fringe image at the interface, and (b) FFT image.

5.1.3 Dipping time: 5 minutes

With the increase in dipping time to five minutes, the interface microstructure consists of chromium-based intermetallic phases along with iron-based phases. Figure 5.17 (a) shows a fine-grained Al_7Cr phase whose diffraction pattern is shown in Fig. 5.17 (b). It consists of nanosized grains with size in the range of 30 to 50 nm. The intermetallic layer also consists of equilibrium Al_7Cr and $Al_{13}Fe_4$ phases as shown in Fig. 5.17 (c) & (d). The $Al_{13}Fe_4$ phase is observed to be formed as acicular shaped with a size close to 1 micrometre. The Al_7Cr phase has a polygonal shape with a size close to 500 nm is shown in Fig. 5.17 (d). The fine-grained ferritic phase is also seen to be present as was observed in the previous cases. This is shown in Fig. 5.18 (a). This might be the indication of incomplete dissolution of the base metal. The depletion of nickel during the dissolution process stabilizes ferritic phase. A small amount of Al and Ni are also present and TEM-EDS presented in Fig. 5.18 (b) confirms the same.
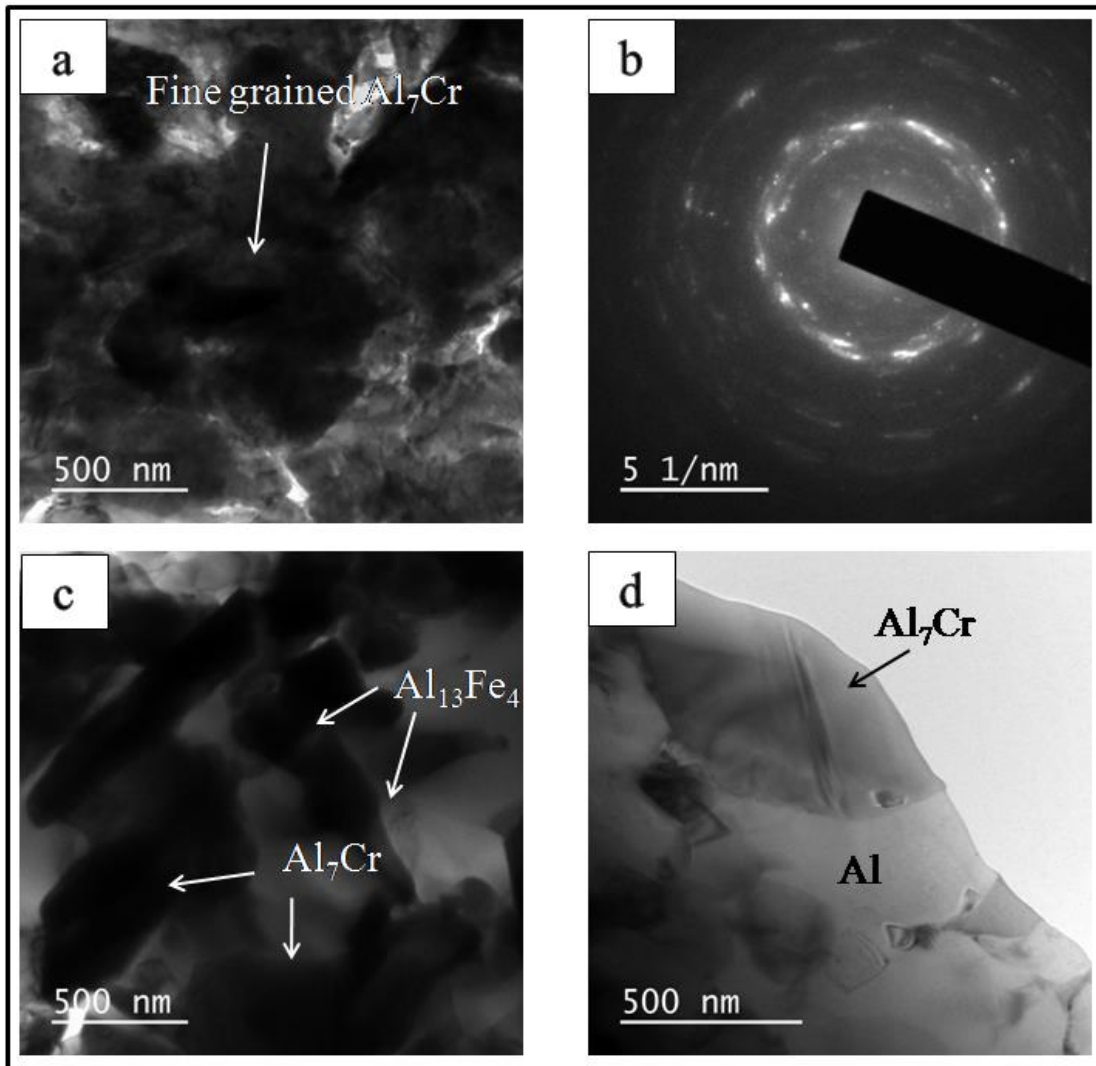
Fig. 5.17 (a) Bright field TEM micrograph showing fine grained Al_7Cr phase, (b) associated electron diffraction pattern, (c) intermetallic phases Al_7Cr and $Al_{13}Fe_4$ being formed as polygonal and acicular shape respectively, and (d) polygonal Al_7Cr phase along with Al matrix.
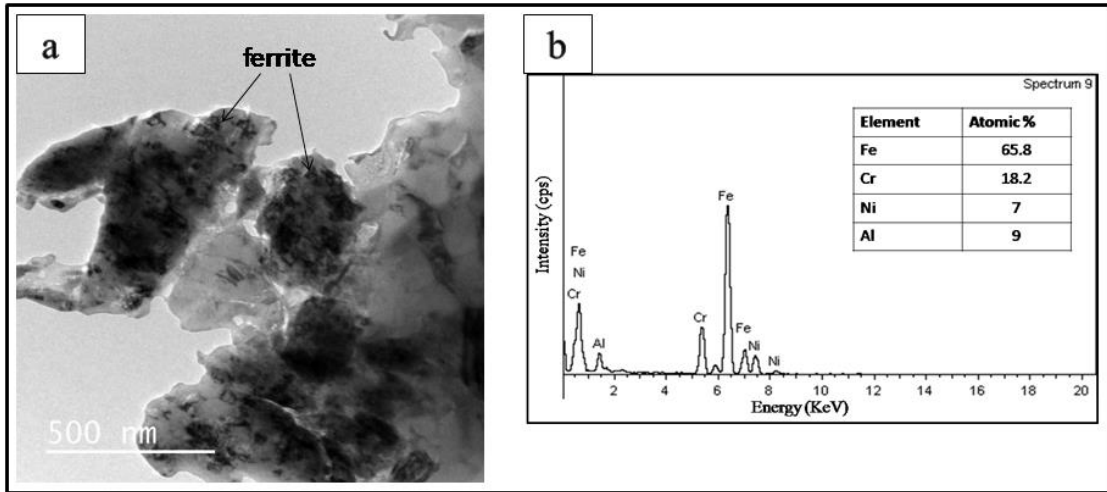
Fig. 5.18 (a) TEM micrograph showing fine-grained ferritic phase, and (b) TEM-EDS spectrum shows the presence of Al and Ni.

The topcoat predominantly consists of aluminum matrix in which acicular $Al_{13}Fe_4$ and polygonal Al_7Cr phases are embedded. Figure 5.19 shows the dispersed intermetallic phases in the topcoat.
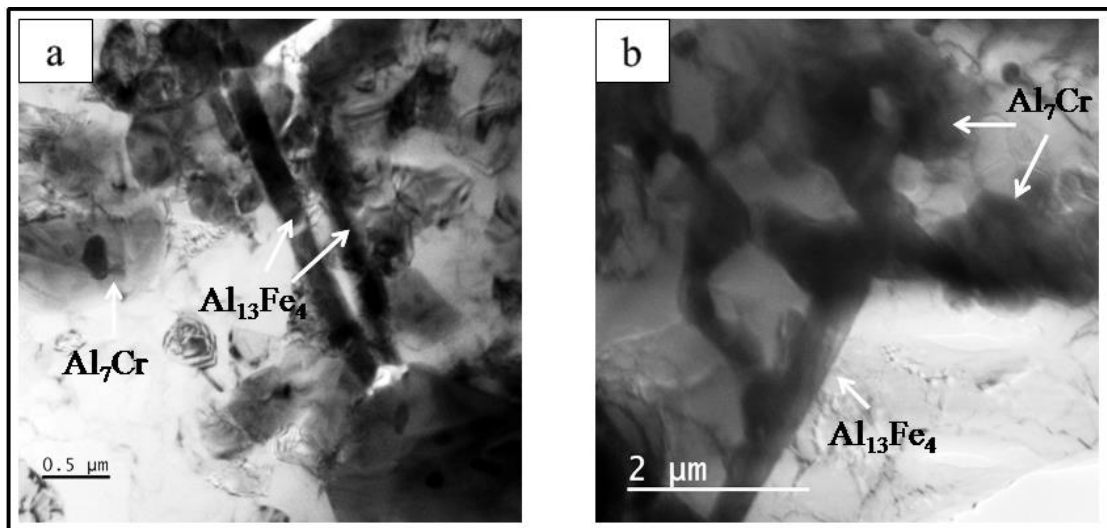
Fig. 5.19 TEM bright field micrograph showing dispersed intermetallic phases of $Al_{13}Fe_4$ and Al_7Cr in the aluminum topcoat.

5.1.4 Dipping time: 10 minutes

The prolonged increase in the dipping time between the molten Al and the base material for 10 minutes does not change the typical microstructure developed at the interface albeit qualitatively. The cross-sectional backscattered electron (BSE) SEM micrograph is presented in Fig. 5.20. The coating appears to be uniform in thickness throughout with the average thickness in the range of 43 ± 0.3 µm. Figure 5.20 (b) presents magnified micrograph of the region shown in Fig. 5.20 (a). The intermetallic layer at the interface is labelled as Region 1 and has a thickness of 12 ± 3 µm. The aluminium topcoat is labelled as Region 2 with intermetallic phases embedded in the aluminium matrix having a thickness of 32 ± 2.5 µm.
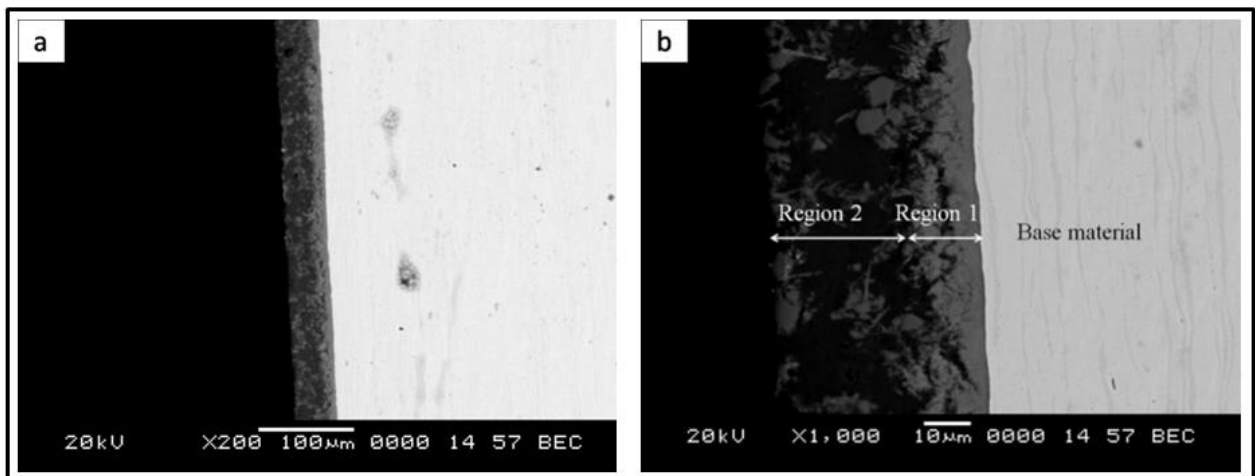
Fig. 5.20 (a) Low magnification SEM-BSE micrograph of the aluminized sample showing a coating of uniform thickness, and (b) Selected region from 'a' is magnified. It shows three distinct regions.

5.1.4.1 Intermetallic layer

The average thickness of the intermetallic layer measured is close to 12 µm. With an increase in interaction time from 10 seconds to 10 minutes the average thickness of this region remains to be of the same. The high magnification SEM backscattered micrograph is shown in Fig. 5.21. The image contrast observed within the intermetallic layer depicts that the layer consists of multiple phases.
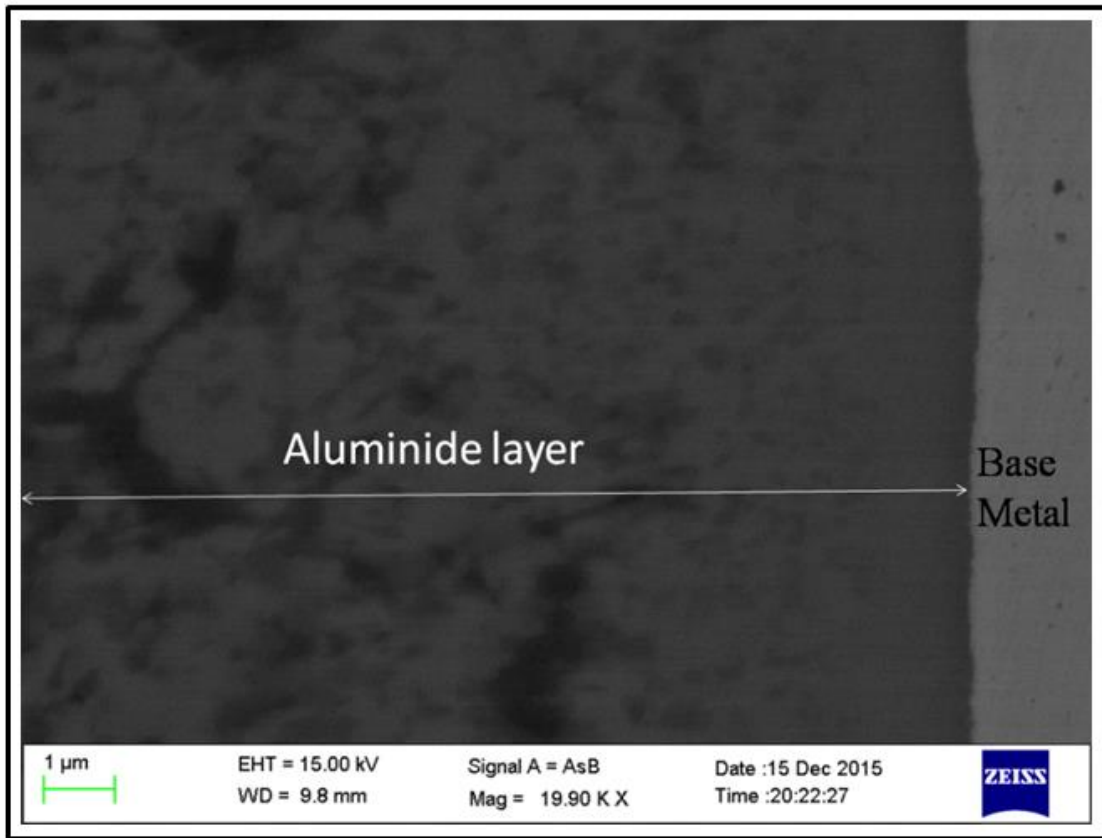
Fig. 5.21 SEM-BSE micrograph showing contrast in the micrograph due to the presence of a mixture of phases in the aluminide layer.

TEM investigations are carried out in this region of the intermetallic layer. The analysis of the same identifies fine-grained microstructure in the aluminium matrix. Figure 5.22 shows TEM micrograph of the fine-grained microstructure of the Fe_2Al_5 phase along with the Al matrix. These are formed as clusters in the aluminium matrix. Within these clusters, fine grains with an average size close to 40 nm are observed. This is shown in the higher magnification micrograph presented in Fig. 5.22 (b). The electron diffraction pattern shown in the inset is quite complex. The pattern could be indexed close to that of the Fe_2Al_5 phase. It should be noted that the structure of $Al_{13}Fe_4$ and Fe_2Al_5 phases are complex and are closely related. The structure of $Al_{13}Fe_4$ is reported to be c-centred monoclinic with 104 atoms per unit cell, while Fe_2Al_5 phase has c-centred orthorhombic phase. The composition obtained from TEM-EDS is Al: 70.4 at. %, Fe: 26.7 at. %, Cr: 1.7 at. %, Ni: 1.2 at.%. which is in close agreement to the composition of Fe_2Al_5 phase.
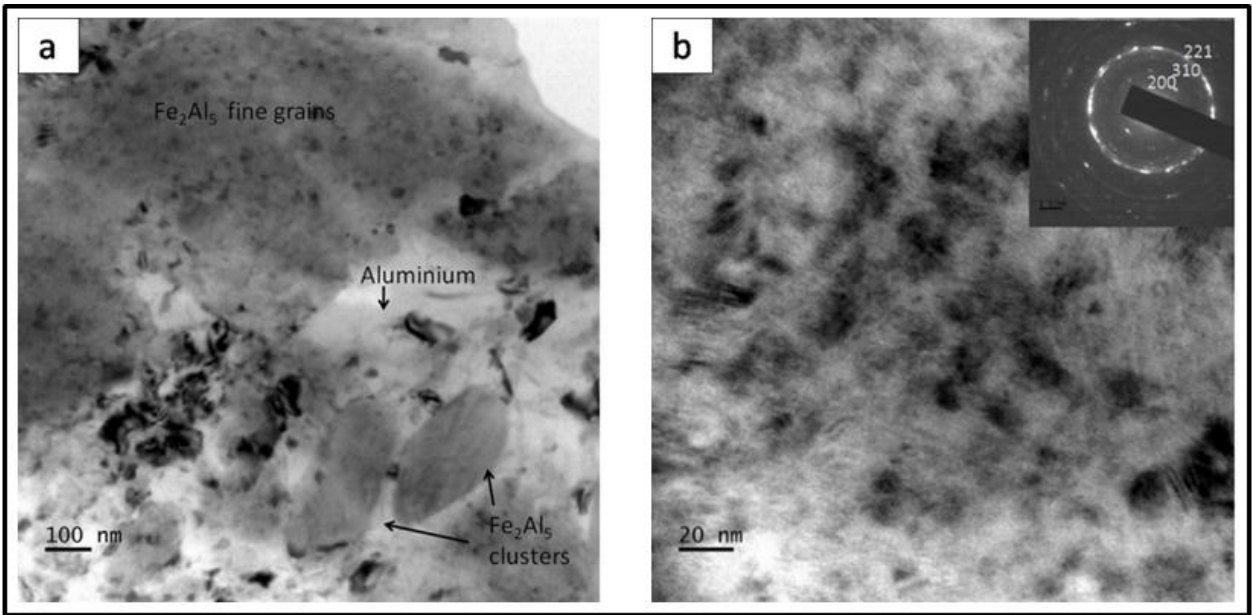
Fig. 5.22 (a) Bright field TEM micrograph showing clusters of Fe_2Al_5 phase, and (b) Fine grains of Fe_2Al_5, SAED pattern is shown as inset.
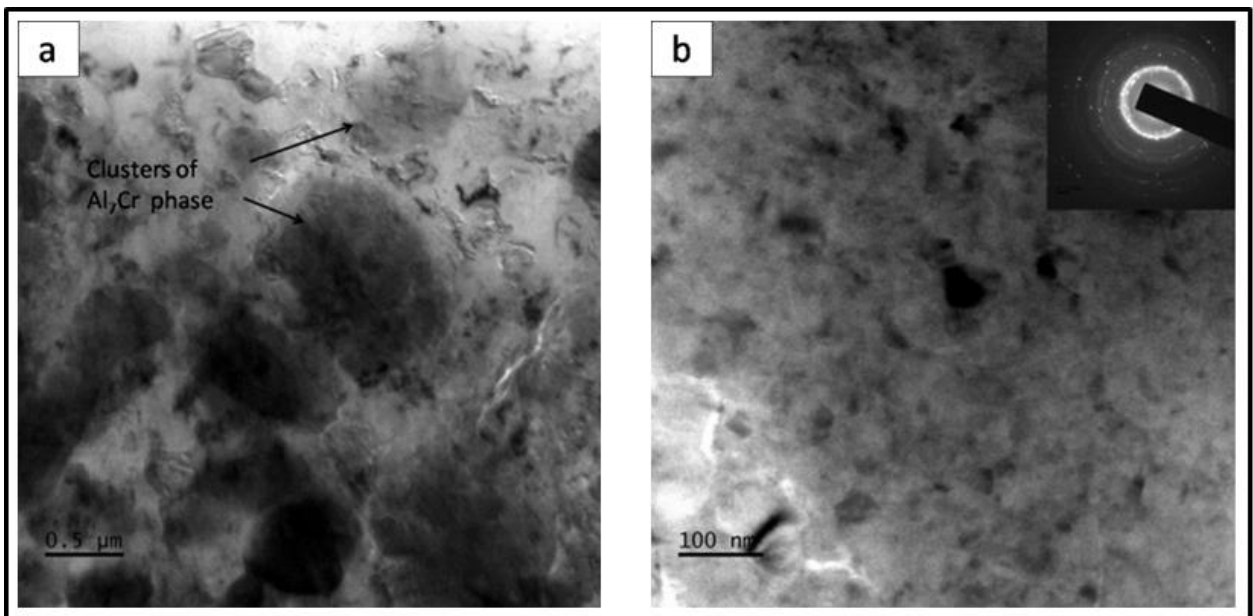
Fig. 5.23 (a) Bright field TEM micrograph showing clusters of Al_7Cr phase, and (b) high magnification micrograph showing fine grain structure of Al_7Cr observed within the cluster. Inset shows the corresponding SAED pattern.

Figure 5.23 (a) shows TEM micrograph of the clusters of Al_7Cr phase. As in the case of Fe_2Al_5 phase, the fine grain microstructure is observed. This is shown in Fig. 5.23

(b). TEM-EDS elemental analysis on this phase shows the composition to be Al: 81 Cr: 13.9 Fe: 4.1 Ni: 1 (all in at. %). The composition is in close agreement to that reported in the literature. The Al_7Cr phase shows a large amount of soluble iron to the tune of 4.1 at. % compared to the reported value of 2.2 at. % (Palm 1997). It is observed that the aluminide layer consists of Fe_2Al_5, Al_7Cr and aluminium. Fine aluminium grains are observed surrounding the clusters of the Fe_2Al_5 and Al_7Cr phases as illustratively shown in Fig. 5.24.
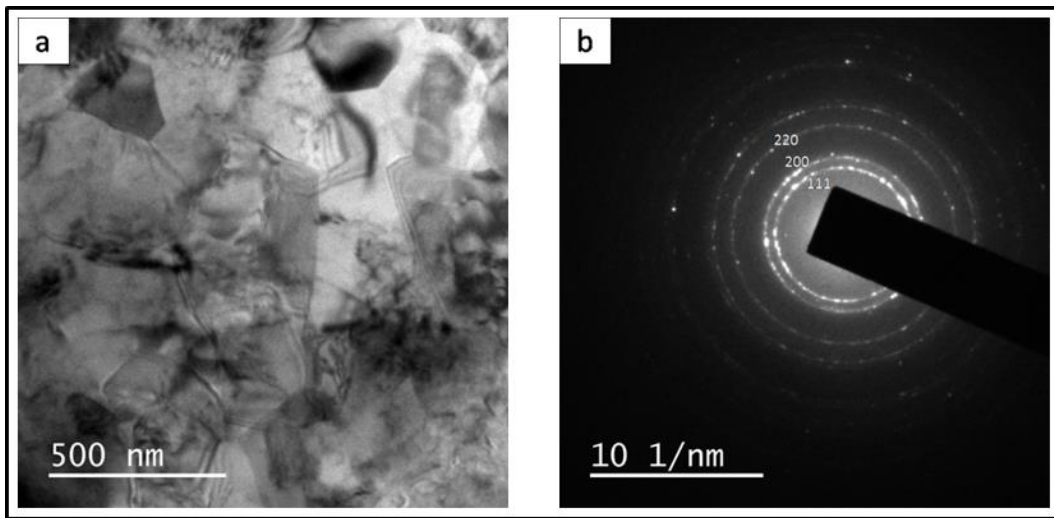
Fig. 5.24 (a) Bright field TEM micrograph showing nanocrystalline aluminium grains, and (b) associated diffraction pattern.
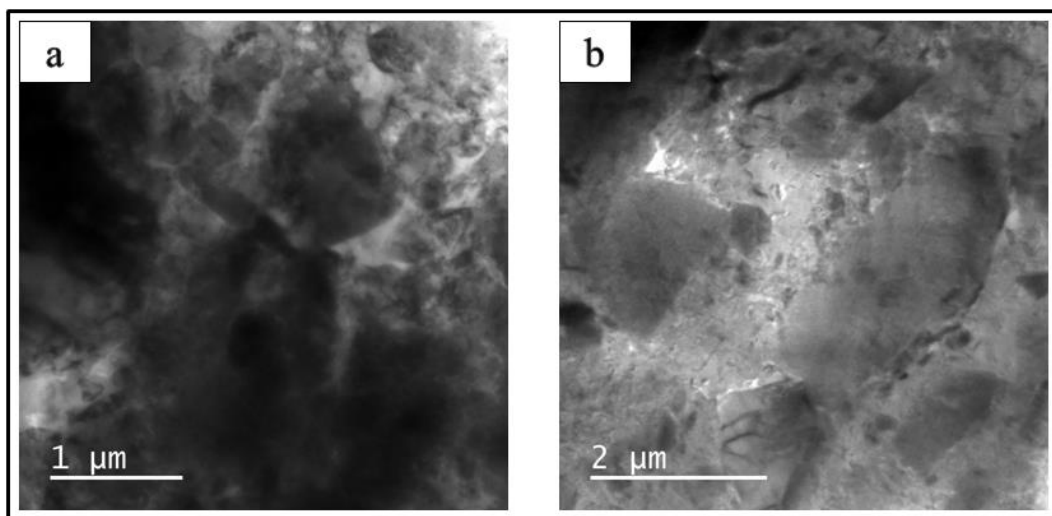
Fig. 5.25 (a & b) Bright field TEM micrographs of the intermetallic phases present in the aluminide layer

The intermetallic layer also contains other phases along with the fine-grained clusters. This is shown in Fig. 5.25. The size of these intermetallic phases ranges from submicrometer level to 2 micrometres. From TEM-EDS analysis, these are identified as chromium and iron-based aluminides. Some of these phases are complex and are closely related to quasicrystalline phases. The SAED pattern presented in Fig. 5.26 and Fig. 5.27 give a strong proof to argue so.
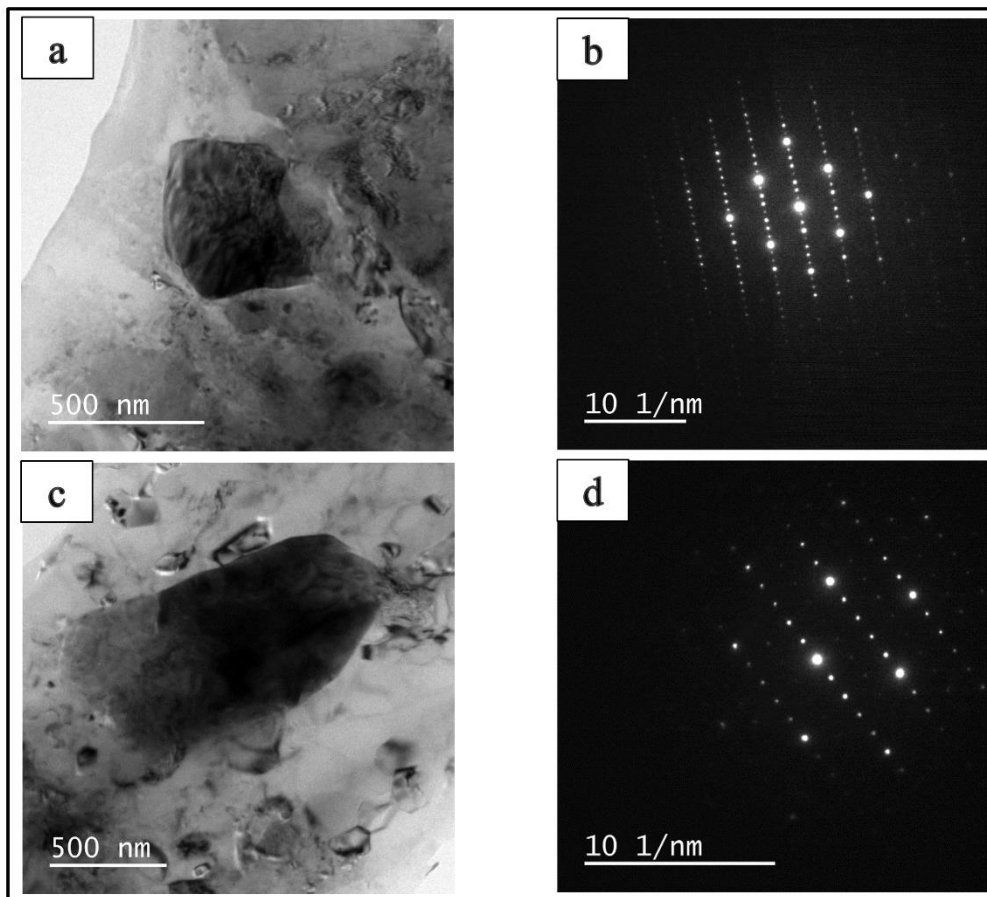
Fig. 5.26 (a) Bright field TEM micrograph of crystalline approximant, (b) associated electron diffraction pattern. The reciprocal space between transmitted beam and [200] reflection is divided into eight parts, (c) Bright field TEM micrograph of another variant, and (d) associated diffraction pattern with reciprocal space along [200] divided into five parts.

The electron diffraction patterns in Fig. 5.26 (b) and (d) is indexed to basic CsCl type cubic structure. The main reflections correspond to CsCl type cell (ordered B2 type) with lattice parameter close to 2.9 Å. Further analysis of the diffraction patterns in Fig.

5.26 (b) and (d) reveals satellite reflections along <100> direction. The reciprocal vector from transmitted beam to [200] plane is divided into eight parts and for another variant, it is divided into five parts. Fig. 5.26 (b) shows an 8 layered structure and Fig. 5.26 (d) shows a 5 layered one along [200] row of reflection.
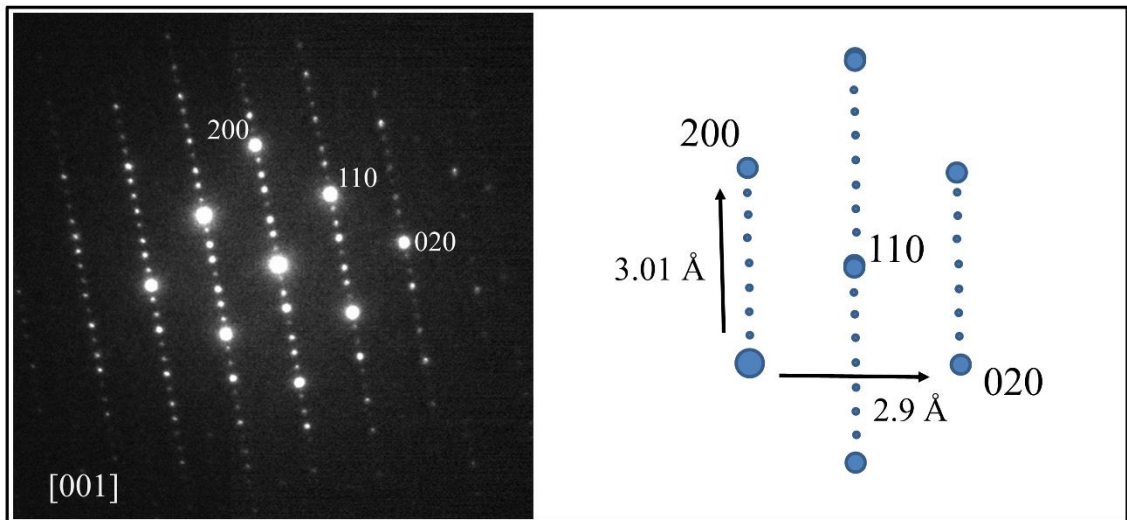
Fig. 5. 27 Commensurate ordering along <100> direction with an 8 layered structure. Symmetry breaking from cubic to tetragonal due to ordering is observed.

The lattice repetition in an 8 layered structure shows a 12 Å periodicity. The symmetry breaks down to tetragonal lattice from the cubic one due to ordering as represented schematically in Fig. 5.27. Also it should be noted that the number of ordered layers follow Fibonaci chain (1, 1, 2, 3, 5, 8, 13..) with strong spots following the Fibonacci sequence along [200] row of reflections.
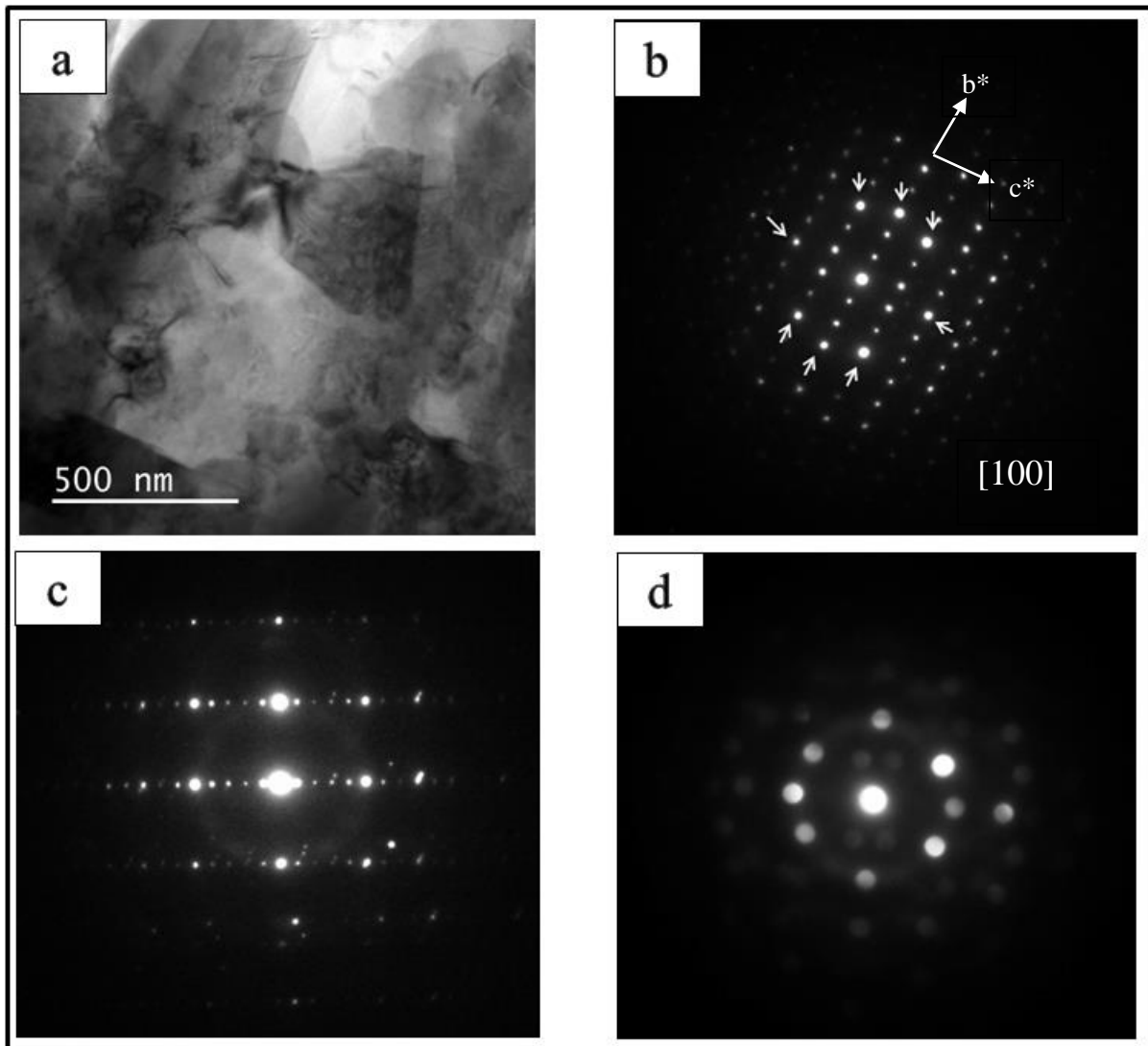
Fig. 5.28 (a) Bright field TEM micrograph of the approximant phase, (b) two-fold symmetry pattern of an orthorhombic type approximant with strong spots marked with arrows, (c) two-fold pattern with 5 number of spots to the bright spot with 12 Å periodicity, and (d) nanobeam electron diffraction showing the twofold symmetry pattern.

Figure 5.28 shows another crystalline approximant phase, which is possibly a closely related structure to the decagonal phase. Figure 5.28 (b) can be indexed to an orthorhombic lattice with one of the lattice parameter b ≈ 12.4 Å. Figure 5.28 (c) & (d) corresponds to a two-fold symmetry pattern. Another orthorhombic approximant phase with a=12.4 Å and c=14.2 Å is observed and is shown in Fig. 5.29. This is designated as O_E type orthorhombic approximant by Demange et al. (2004) and the two lattice

parameters in the present case are in close agreement with reported values. This is a ternary Al-Cr-Fe based orthorhombic approximant to the decagonal quasicrystal.
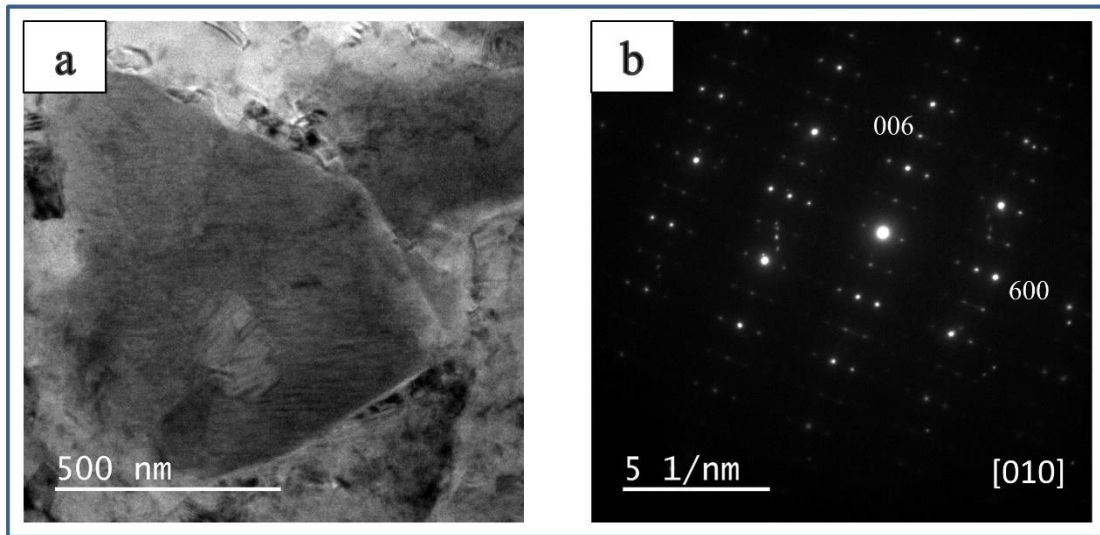
Fig. 5.29 (a) TEM micrograph of the O_E type orthorhombic approximant phase, and (b) Electron diffraction pattern along [010] zone axis.

5.1.4.1 Aluminum topcoat

The aluminum topcoat after 10 minutes of interaction time consists of equilibrium intermetallic phases dispersed in solidified aluminum. The topcoat is found to consists of Al_7Cr and $Al_{13}Fe_4$ intermetallic phases which are shown in Fig. 5.30.
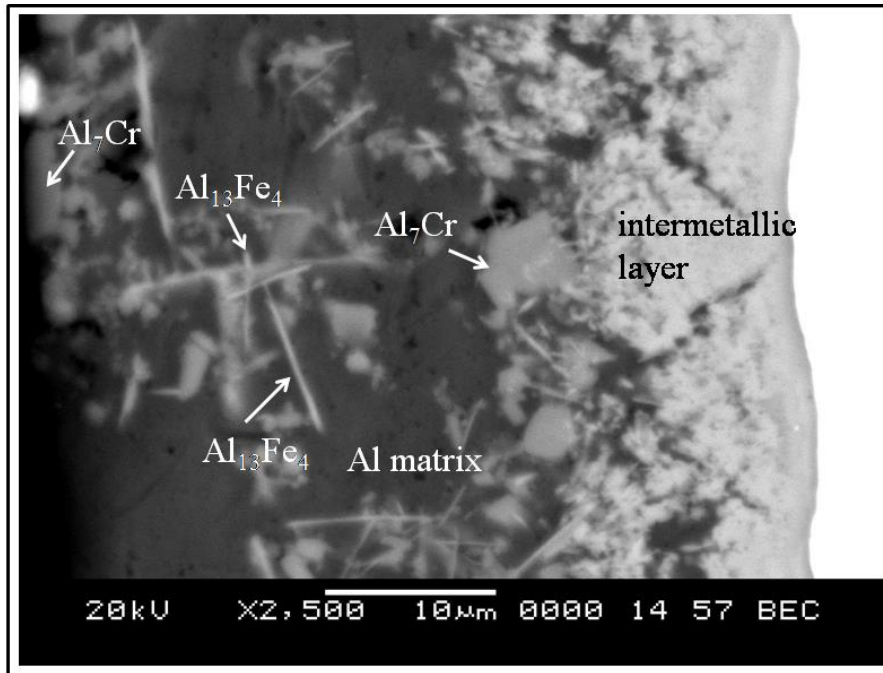
Fig. 5.30 SEM micrograph of the Al topcoat showing dispersed intermetallic phases present in the aluminum matrix.

The $Al_{13}Fe_4$ phase is observed to be formed as acicular shaped and the Al_7Cr is observed as polygonal shaped. The size of the Al_7Cr phase as observed from SEM micrographs ranges from sub-micrometer scale to 5 µm, while the acicular $Al_{13}Fe_4$ has a length in the range of 2 to 3 µm and a width less than 0.5 µm. The STEM (scanning transmission electron micrograph) of the aluminum topcoat is shown in Fig. 5.31. The polygonal Al_7Cr phases and acicular $Al_{13}Fe_4$ are observed along with aluminum. Fig. 5.31 (b) shows high magnification micrograph revealing the polygonal Al_7Cr phases with varying size. Fig. 5.32 shows STEM micrograph of the acicular $Al_{13}Fe_4$ phase.
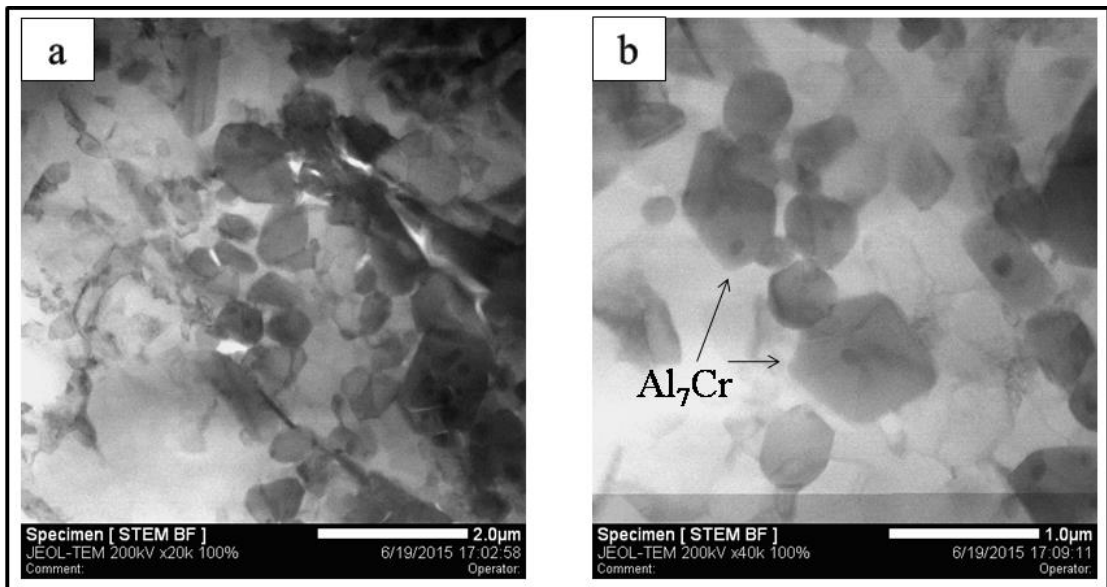
Fig. 5.31 (a) STEM bright field micrograph from the alumiunum topcoat showing dispersed intermetallic phases, and (b) higher magnification micrograph of the polygonal Al_7Cr phase.
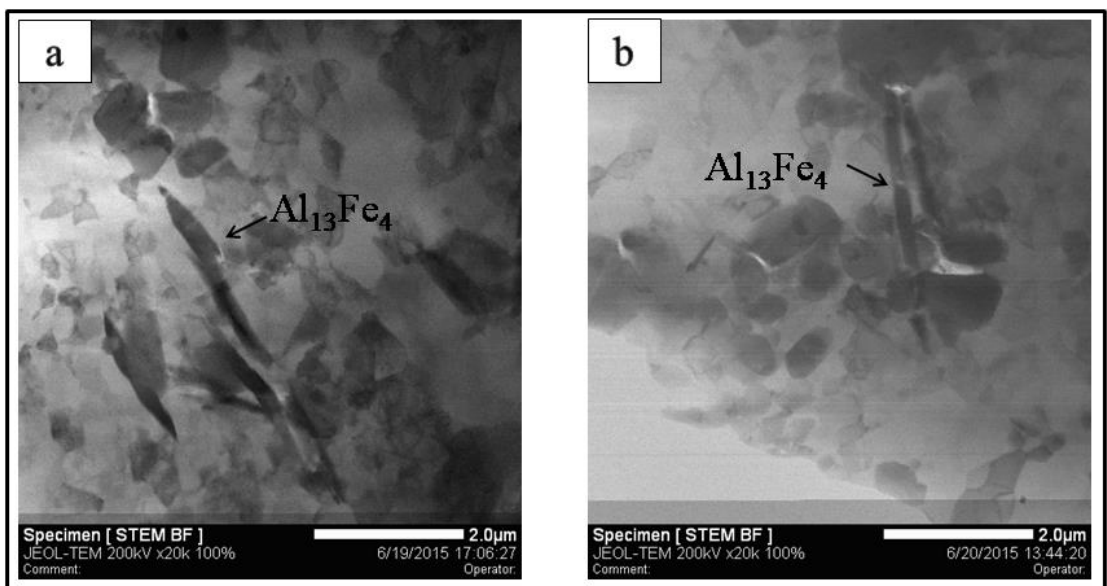
Fig. 5.32 (a) & (b) STEM bright field micrographs showing formation of the acicular $Al_{13}Fe_4$ phase along with the polygonal Al_7Cr in the Al topcoat.

The bright field TEM micrograph of the polygonal Al_7Cr phase distributed in aluminium matrix is shown in Fig. 5.33 (a) and TEM- EDS analysis as presented in Fig. 5.33 (b). The composition is observed to be Al: 84.9, Cr: 12.3, Fe: 2.8 at. % which is in

close agreement with that of Al$_7$Cr phase. Figure 5.34 (a) and (b) shows TEM micrographs of twinned Al$_7$Cr and the corresponding SAED pattern showing twinning around (001) plane.
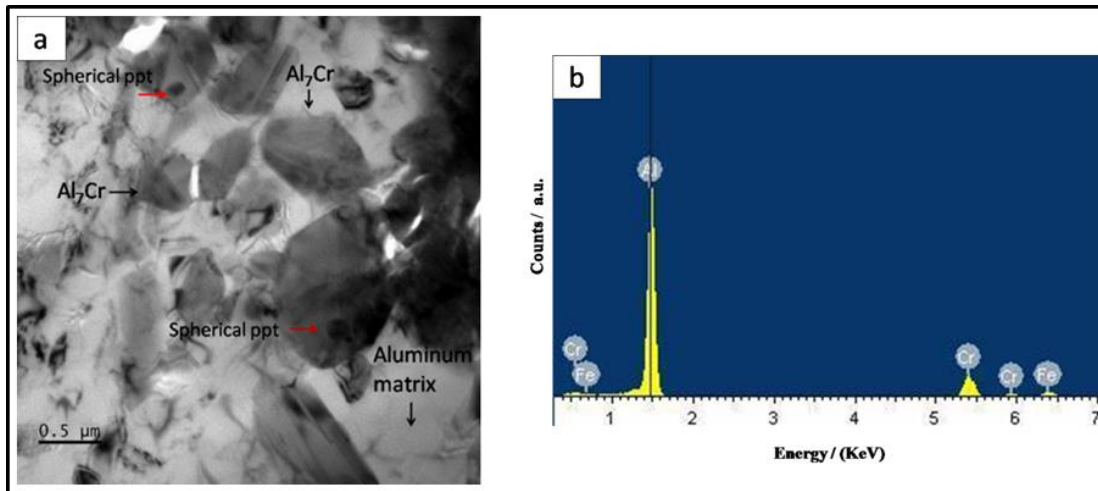
Fig. 5.33 (a) Bright field TEM micrograph of the Al$_7$Cr phase distributed in the aluminium matrix, and (b) TEM-EDS spectrum of the Al$_7$Cr phase.
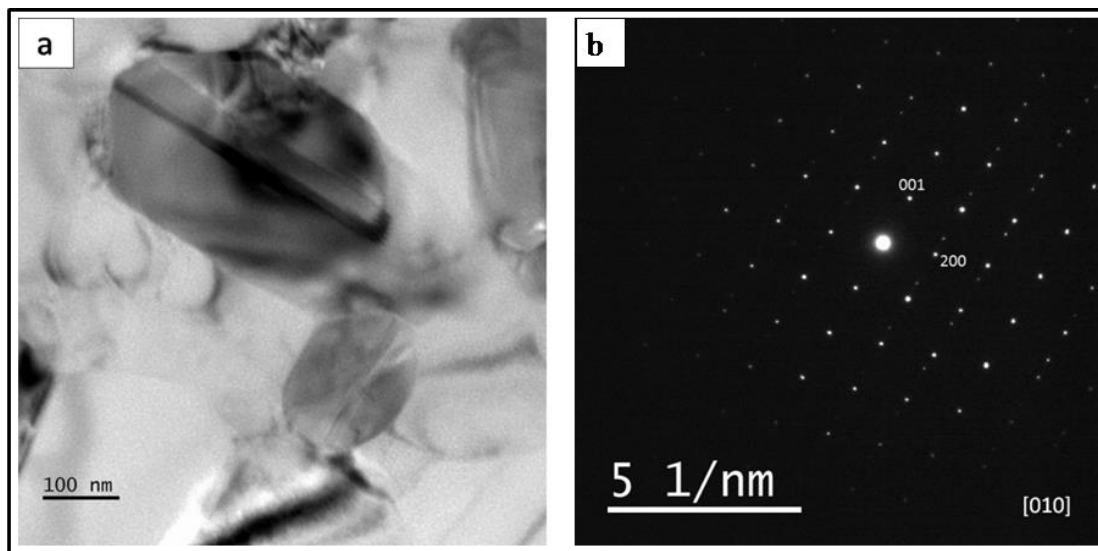
Fig. 5.34 (a) Bright field TEM micrograph showing twinned Al$_7$Cr phase, and (b) corresponding diffraction pattern showing twinning around (001) plane.

Figure 5.35 (a) shows a bright field TEM micrograph of Al$_{13}$Fe$_4$ phase present in aluminium topcoat and Fig. 5.35 (b) shows the corresponding TEM-EDS spectrum. The

TEM-EDS elemental analysis shows the composition to be Al: 75.8 at%, Fe: 20.3 at%, Cr: 1.40 at%, Ni: 2.5 at%. The size of these phases is in the range of 1 to 3 μm in length.
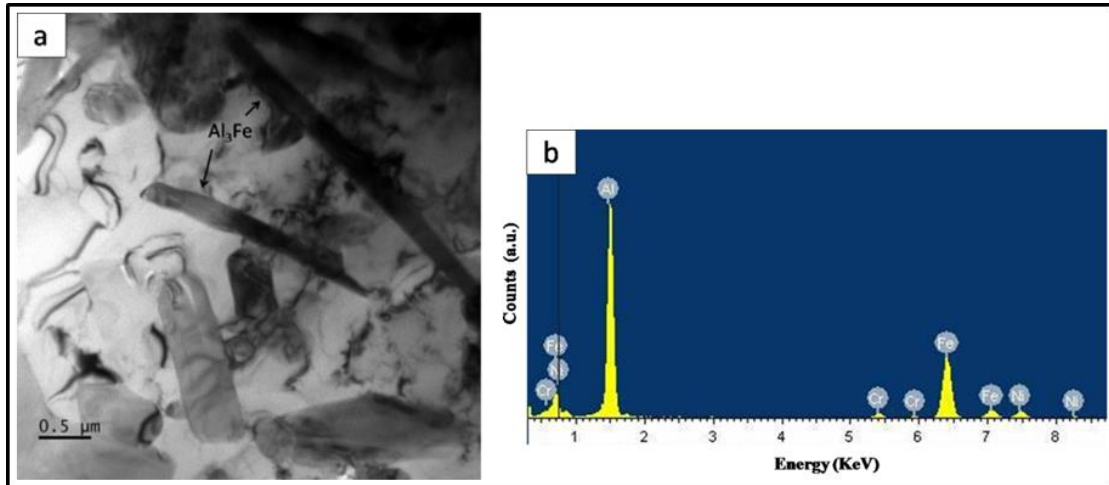
Fig. 5.35 (a) Bright field TEM micrograph of acicular $Al_{13}Fe_4$ plates formed in aluminium topcoat, and (b) TEM-EDS spectrum of $Al_{13}Fe_4$ phase.

At higher magnifications twins within these plates are also noticable. Figure 5.36 (a) shows higher magnification bright field TEM micrograph showing twinning within the $Al_{13}Fe_4$ phase. Fig. 5.36 (b) shows the diffraction pattern of the twinned $Al_{13}Fe_4$ along [010] zone axis.
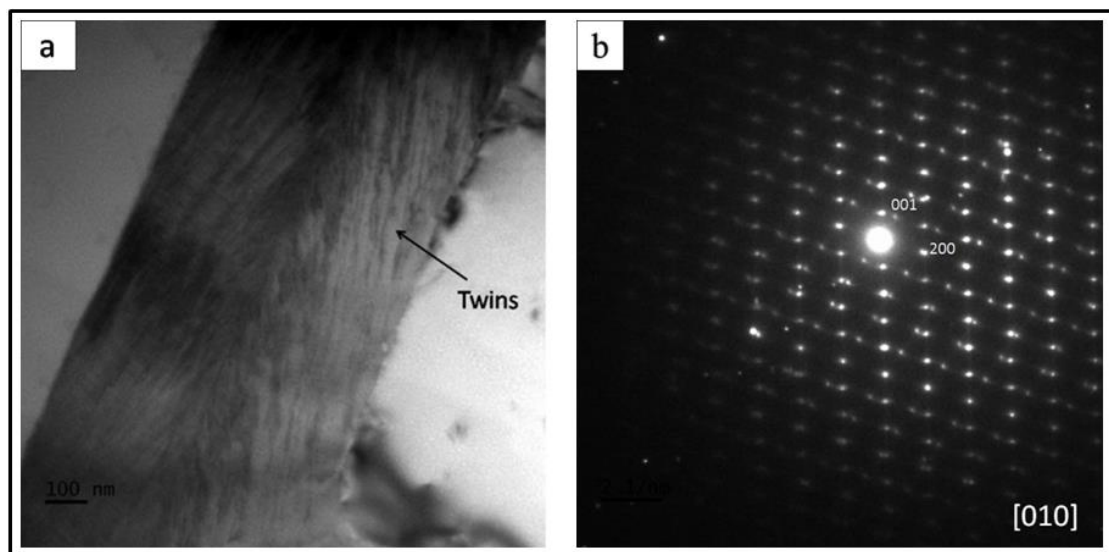
Fig. 5.36 (a) Bright field TEM micrograph showing twins in the $Al_{13}Fe_4$ phase, and (b) diffraction pattern along [010] zone axis of the twinned $Al_{13}Fe_4$.

The aluminum matrix in the topcoat shows fine grained microstructure, ans is shown in the Fig. 5.37. The average grain size of aluminium matrix measures about 1 - 2 µm. Some amount of dislocation is also seen near the grain boundaries
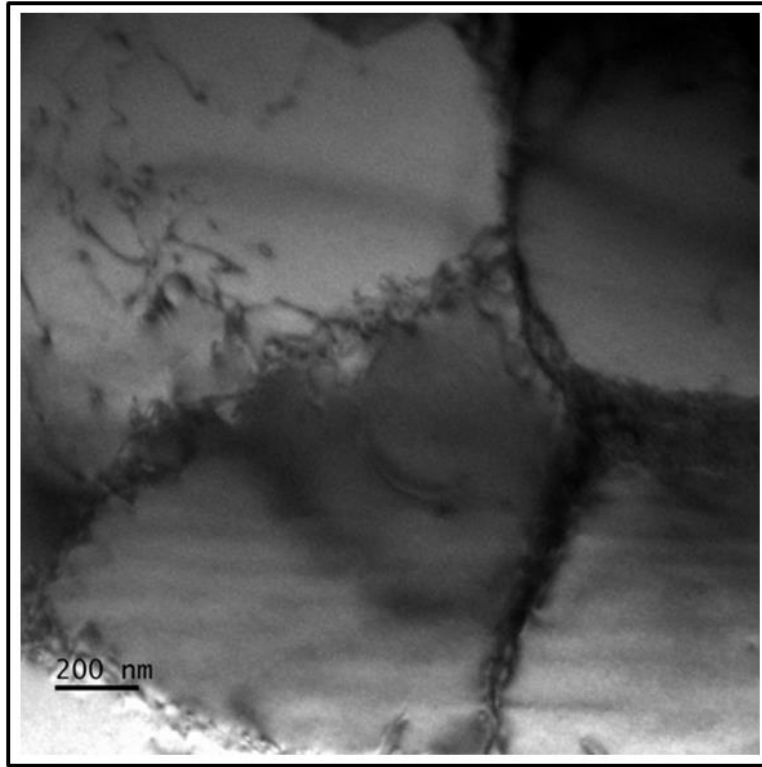
Fig. 5.37 Bright field TEM micrograph of the aluminium grains formed in the topcoat.

After 10 minutes of interaction with the molten aluminum, the base material region, very close to the interface shows fine grained microstructure. The average grain size measured is in the range of 30-40 nm as shown in Fig. 5.38. The SAED pattern shown in the inset in Fig. 5.38 (a) reveals the structure as ferritic (body centered cubic) in contrast to the austenitic (face centred cubic) phase of the base metal. The chemistry in this region is richer in chromium with the composition Cr: 31 at. % Fe: 63 at. % Ni: 3.69 Si: 1.73 at.%. TEM-EDS spectrum is presented in Fig. 5.38 (b). The microstructure of the base metal, slightly away from the interface is austenitic. The microstructure is shown in Fig. 5.39 (a) and the corresponding diffraction pattern of austenite phase is presented in Fig. 5.39 (b).
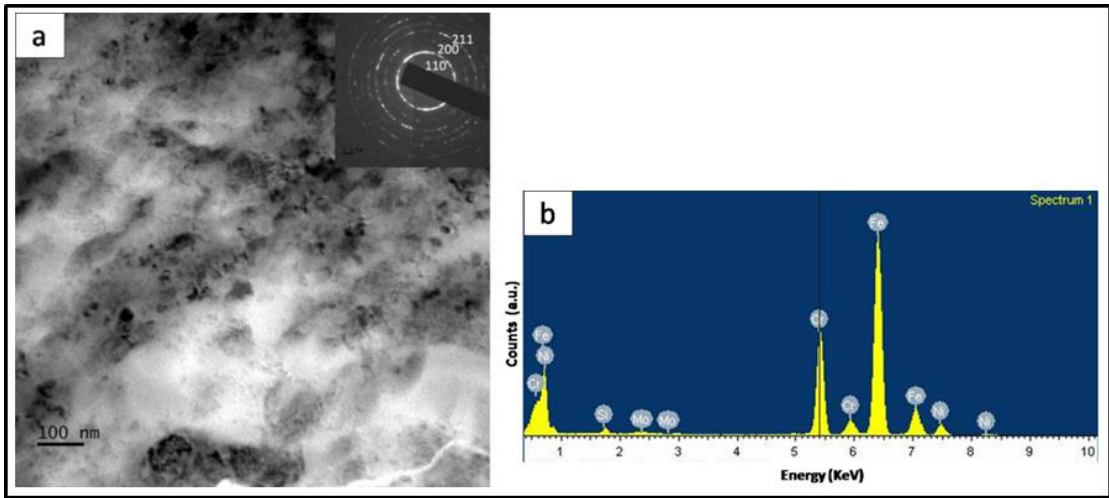
Fig. 5.38 (a) Bright field TEM micrograph of base material adjacent to interface, and (b) TEM-EDS spectrum showing higher chromium content.
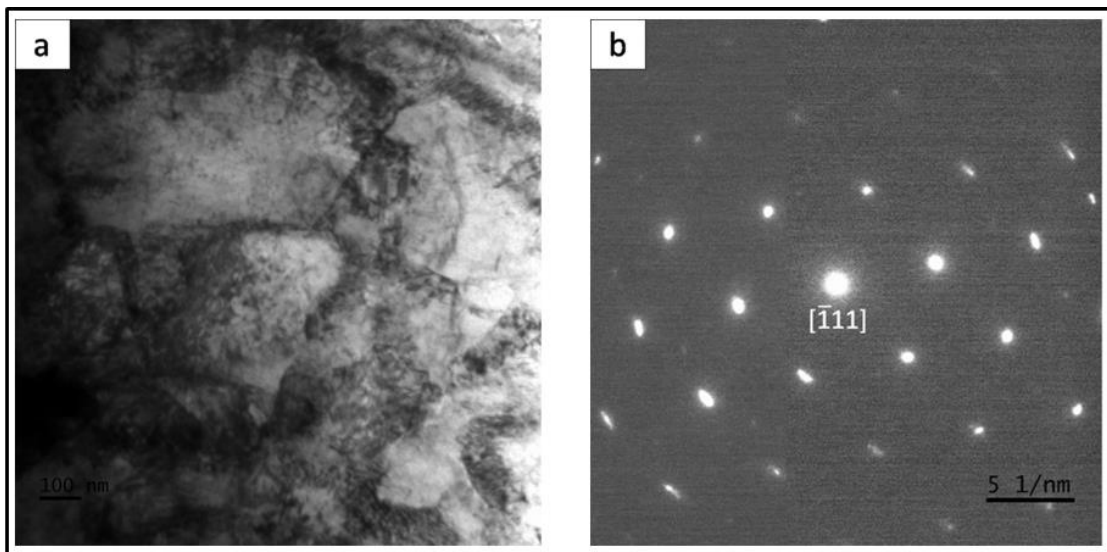
Fig. 5.39 (a) Bright field TEM micrograph of the base metal away from the interface, and (b) corresponding SAED pattern indicating face centered cubic structure.

5.2 Discussion

The general mechanism for the formation of phases between two dissimilar metals is of the reaction-diffusion type. The phases first form by nucleation and their growth takes place by reaction-diffusion between the end members as explained in chapter 4. However, the interaction between the stainless steel 321 and molten aluminum follows a different mechanism. The mechanism of microstructure formation at the interface is found out to be of dissolution-nucleation type. The base metal first dissolves into molten aluminum and intermetallic phases nucleates in the molten aluminum. The dissolution of the base metal is due to solutal melting rather than the thermal melting. Such dissolution is observed during dissimilar metal welding and during soldering of Cu-Sn (Chatterjee and Abinandanan 2008; Laurila et al. 2005).

At the instant when the base metal comes in contact with the molten aluminum several events are expected to occur:

i) Dissolution of the base metal into molten Al for attaining constitutional equilibrium at the interface.

ii) The solubility of elements higher than equilibrium solubility is expected due to metastable dissolution. Equilibrium solubility is expected to occur only at an infinitely slow rate of dissolution. However, practically, as equilibrium conditions do not prevail over the interface, metastable dissolution is possible. This causes enrichment of solute atoms ahead of the interface. The metastable concentration of individual species could be calculated based on reliable thermodynamic data (Laurila et al. 2005; Vuorinen et al. 2008).

A hypothetical concentration profile ahead of the stainless-steel substrate is shown in Fig. 5.40. Parameter C_m is the metastable concentration, C_{eq} is the equilibrium concentration, and C_∞ is the concentration far from the interface. Concentration higher than the equilibrium concentration is expected because the system is under nonequilibrium conditions.
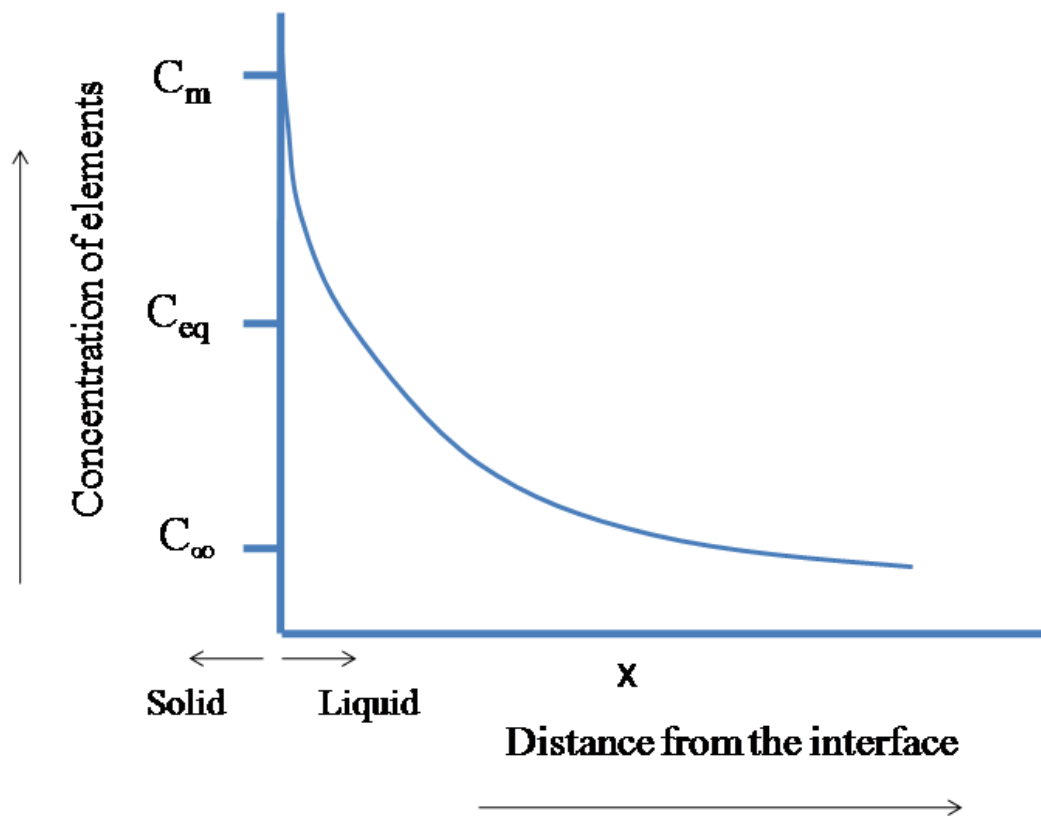
Fig. 5.40 Schematic representation of a hypothetical concentration profile during the interaction between SS 321 and molten aluminum.

iii) Diffusion of solute atoms from the interface to the bulk of the liquid sets a concentration profile.

The nature of the concentration profile depends on the dissolution rate and diffusion rate of the elements. The dissolution and diffusion rate of individual species will be different and therefore each species develop their own concentration profiles.

iv) The driving force exists up to a certain distance from the interface for nucleation of intermetallic phases due to (a) liquid supersaturated with elements (b) large undercooling and (c) heat transfer through the base metal.

The SEM micrographs in Fig. 4.20 reveal that the average thickness of the intermetallic layers is almost constant with varying dipping time. Also, the microstructure looks similar with different dipping durations. However, the detailed transmission electron

microscopy revealed that the microstructures comprise of different phases (both equilibrium and non-equilibrium phases).

At the instant when the base metal comes in contact with the molten aluminum, the former starts to dissolve in the latter. The equilibrium solubility of the individual element is predicted from the binary phase diagram at 700 °C. The equilibrium solubility of pure Fe at 700 °C in molten Al is 2.5 wt. %, that of pure Cr is 0.7 wt. %, while nickel has the highest solubility of 10 wt. % (Dybkov 2013).

In the initial stage, rapid dissolution of Ni is expected since nickel has the highest solubility in molten Al. The dissolved Ni atoms further diffuse away into liquid Al by the diffusion process. Thus, a Ni concentration profile is built up ahead of the solid/liquid interface. A hypothetical diagram of events taking place is shown in Fig. 5.41.
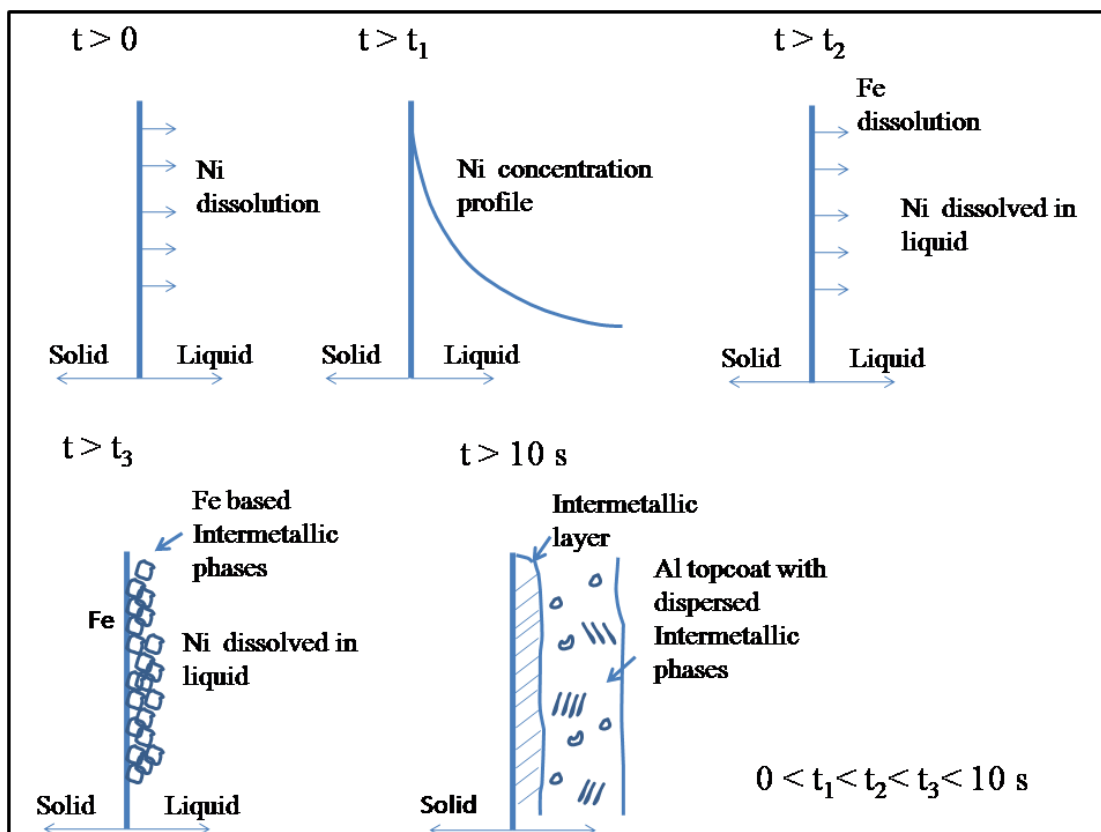
Fig. 5.41 Schematic representation of the events taking place during the interaction of the base metal with the molten Al.

The elements Fe and Cr are expected to dissolve and develop concentration profiles by a similar process. The driving force for nucleation of Fe based and Cr based intermetallic phases exist due to their limited solubility in liquid Al as seen by the phase diagram. Further, the solid/liquid interface also assist in heterogeneous nucleation. The base metal plate acts as a source of heat sink and extracts heat. Simultaneous process of dissolution and heat transfer gives rise to rapid nucleation and growth of intermetallic phases. Also, due to the high solidification rate, both nucleation and growth of the existing nuclei will be severely stunted and fail to reach equilibrium composition. Thereby, the formation of equilibrium $Al_{13}Fe_4$ phase would be suppressed and that of metastable $FeAl_m$ will be supported. The equilibrium $Al_{13}Fe_4$ could be replaced by metastable $FeAl_m$ at higher cooling rates (>10 K/s) (Liu et al. 1986; Young and Clyne 1981). Alloying additions such as Si, V, Cu, Cr, TiB_2 promotes the formation of $FeAl_m$ phase instead of $FeAl_6$ or $Al_{13}Fe_4$ phases (Li and Arnberg 2004; Allen et al. 1998). From the TEM-EDS elemental analysis, close to 2.7 at. % of Ni is dissolved in $FeAl_m$ and it is logical to say that Ni could have stabilized $FeAl_m$ phase.

The parent austenite phase near the interface gets destabilized due to depletion of Ni content by dissolution process. This Ni depleted region transforms to the ferrite (body-centred cubic) phase (observed in Fig. 5.6) due to compositional adjustment, where chromium acts as a ferritic phase stabilizer. The small amount of Al that has diffused into the base material during the process also helps in the transformation from FCC to BCC phase. The interaction time of 10 seconds is observed to be short for dissolution of chromium and to form intermetallic phases with Al. Therefore, chromium based intermetallic phase are not observed.

The peculiar rosette type morphology shown in Fig. 5.5 (a) is reported to form under rapid solidification conditions (Zhang et al. 1989; Fung et al. 1987). The observed Pseudo tenfold diffraction pattern shown in Fig. 5.5 (b) is proved to be due to multiple twinning. The tenfold growth morphology of $Al_{13}Fe_4$ phase takes place by alternate twinning mechanism around the (100)-$(20\bar{1})$ planes (Louis et al. 1980). The β angle of the monoclinic $Al_{13}Fe_4$ phase is close to 108° which forms the basis for pseudo tenfold electron diffraction pattern. Based on the glide-reflection mechanism Ma et al. (1996) proposed a structural model for (100)- $(20\bar{1})$ five-fold twins. Alternatively, ten-fold

$Al_{13}Fe_4$ twins could be formed by the decomposition of decagonal Al-Fe phase (Kim and Cantor 1994). Fung et al. (1987) confirmed the coexistence of decagonal Al-Fe phase and twinned $Al_{13}Fe_4$ phase based on high-resolution electron microscopic investigations. Multiple twinned $Al_{13}Fe_4$ phase is found to coexist with decagonal Al-Fe phase. Decagonal quasicrystal shares close orientation relationship with twinned $Al_{13}Fe_4$ phase such that the [010] zone axis of $Al_{13}Fe_4$ is parallel to the decagonal axis (Zou et al. 1987).

The nickel is present in the dissolved state in the molten aluminum. As the topcoat solidifies during cooling, the nickel precipitates out in the form of intermetallic phases in the aluminum topcoat. According to the Al-Fe binary equilibrium phase diagram, $Al_{13}Fe_4$ (Al_3Fe) compound forms by the eutectic reaction at 660 °C, while, Ni-based intermetallic phase $NiAl_3$ forms by eutectic reaction at 640 °C. In the present investigation, the intermetallic phase forms due to the eutectic reaction. The intermetallic phase has an orthorhombic crystal structure. The $NiAl_3$ phase also possesses an orthorhombic structure having the space group Pnma with lattice parameters: a=6.59 Å, b= 7.35 Å, and c=4.80 Å. The maximum solubility of Fe in the $NiAl_3$ phase is up to 2.5 at. % (Grushko and Velikanova 2007). The TEM-EDS analysis shown in Fig. 5.8 (d) presents higher nickel content than the iron. Therefore, the phase observed in the present investigation is arguably the metastable extension of $NiAl_3$ phase with increased iron solubility. The metastable $Al_3(NiFe)$ phase shares crystallographic orientation relationship with the aluminum matrix. This implies that one phase acts as a heterogeneous nucleating site for the other to minimise the interfacial energy during their growth. However, the crystallographic relationship observed for the metastable Al-$Al_3(NiFe)$ eutectic in the present investigation is different from the one reported for Al-Al_3Ni eutectic in directionally solidified eutectic (Cantor and Chadwick 1974; Garmong et al. 1973).

With the increase in dipping time to 60 seconds, the intermetallic layer consisted of the metastable Al_mFe, fine-grained ferritic phase and few acicular Al_7Cr phases. The aluminum topcoat consisted of metastable Al-$Al_3(NiFe)$ eutectic. The TEM-EDS analysis shows the metastable $Al_3(NiFe)$ contains higher Fe content than Ni. With an increase in interaction time, more of Fe and Cr dissolves into molten Al bath. Further,

Ni can only come out when the base metal layer enriched with Fe and Cr dissolves completely. For that reason, more Fe is found to be present in the metastable Al-Al_3(NiFe) eutectic. At the dipping duration of 5 minutes, the topcoat consisted of equilibrium intermetallic phases of Al_7Cr and $Al_{13}Fe_4$. At the interface, fine grains of Al_7Cr and ferritic phase were present. The chromium present in the base metal after the dissolution of Ni and Fe dissolves with prolonged dipping duration. Therefore, at 5 minutes of dipping time, more of chromium-based intermetallic phase is observed along with $Al_{13}Fe_4$ phase. The nickel that was dissolved initially is further taken away into the molten melt by a diffusion process. This causes the topcoat depleted with the nickel. Thereby, the topcoat is formed by Fe and Cr aluminides. A similar observation is made when the sample is dipped for 10 minutes duration. The aluminides in the topcoat are equilibrium $Al_{13}Fe_4$ and Al_7Cr phases as predicted by the phase diagram. A fine-grained Fe and Cr aluminides are found in the intermetallic layer. It also consisted of approximant phases which are closely related to quasicrystalline phases.

The crystalline approximants are periodic crystals which exhibits close similarity with the quasicrystals. The ordered structures observed in the present investigation (Fig. 5.26) is closely related to the vacancy ordered phases (VOPs) reported to be present in binary and ternary Al-transition metal (TM) systems (VanSande et al. 1978; Chattopadhyay et al. 1987; Sastry et al. 1982). These phases are popularly known as τ phases. In these phases, ordering of the layers takes place along the three-fold (triad) axis of the basic CsCl type of unit cell. The sequence of ordering of Al-TM-vacancy is along [111] direction. A different sequence of ordering leads to different varients of these ordered phases and are designated as τ_3, τ_5, τ_8... following the Fibonacci sequence based on the number of divisions made by Bragg peaks along [111] direction. A τ_3 phase will have Bragg peaks divided into 3 parts and a τ_5 will have Bragg peak divided into 5 parts along [111] direction and so on. Also, vacancy ordered phases showing non-Fibonacci type sequence have been reported (Van Tendeloo et al. 1989). A schematic of the Al-TM ordering based on CsCl type unit cell is shown in Fig. 5.42 and the sequence of the ordering of Al-TM-vacancy proposed by Van Tendeloo et al. (1989), Chattopadhyay et al. (1987) is shown in Table 5.1
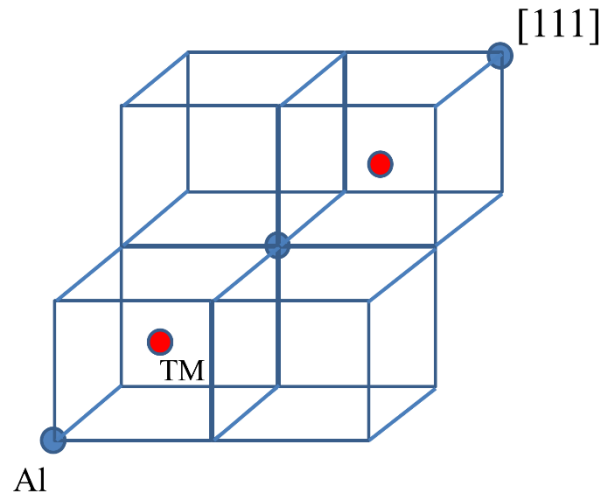
Fig. 5.42 Schematic representation of ordering in Al-TM alloy along [111] direction in a CsCl type unit cell

Table 5.1 Stacking sequence of vacancy ordered phases (Chattopadhyay et al. 1987; Van Sande et al. 1978), M represents transition metal and V is vacancy.

	chain	composition	Al %	V%
τ_1	AlM	$Al_1M_1V_0$	50	0
τ_2	AlMAlV	$Al_2M_1V_1$	66.6	16.6
τ_3	AlMAlMAlV	$Al_3M_2V_1$	60	16
τ_5	AlMAlVAlMAlMAlV	$Al_5M_3V_2$	62.5	20
τ_8	AlMAlMAlVAlMAlVAlMAlMAlV	$Al_8M_5V_3$	61.5	18
τ_{13}	AlMAlVAlMAlMAlVAlMAlMAlVAlMAlVAlMAlMAlV	$Al_{13}M_8V_5$	61.8	19.2

In the present investigation, the ordering of layers is along the [200] direction which is different from the ordering in τ phases. The possible ordering of the layers is represented schematically in Fig. 5.43. The ordering is along the twofold axis. This type of phases with ordering along one of the twofold axis are designated as diagonal phases by Ranganathan and Chattopadhyay (1991). A diagonal phase in Ti-Fe-Si alloys has been reported by Mandal et.al (1992). It is possible that the sequence of ordering is similar to that in the VOPs with vacancy ordering. Another possibility would be that this phase could be transition metal ordered, i.e. $Al-M_1-M_2$ type of sequence. Where M_2 is ordered in the Fibonacci series. However, due to the non-availability of reliable compositional data, this statement cannot be ascertained at this moment and the matter will be subjected to further investigations.
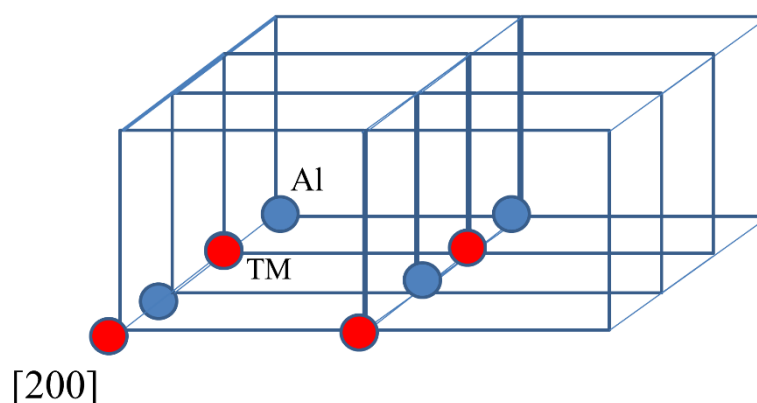
Fig. 5.43 Schematic representation of the possible ordering of layers along [200] directions.

Noting the proposal of Chattopadhyay et al. (1987) that the vacancy ordered phases are approximants to 1-D quasicrystals, this relationship has been proved by He et al. (1988) in Al-Ni-Si, Al-Cu-Mn and Al-Cu-Co alloys. It is also to be noted that the 8 layered variant in the present case show periodicity of 12 Å. Lately, Demange et al. (2004) discovered ternary Al-Cr-Fe decagonal quasicrystal with 12 Å periodicity along the decagonal axis. Ranganathan and Chattopadhyay (1991) reported that such an ordered phase inherits the periodicity of the decagonal phase. Thus, there exists a strong relationship between an 8 layered variant and the decagonal quasicrystal with a 12 Å

periodicity. Alternatively, this phase could be a transformational product of the decagonal quasicrystal.

The overall interaction process and phase evolution is explained by the schematic diagram shown in Fig. 5.44 and Fig. 5.45
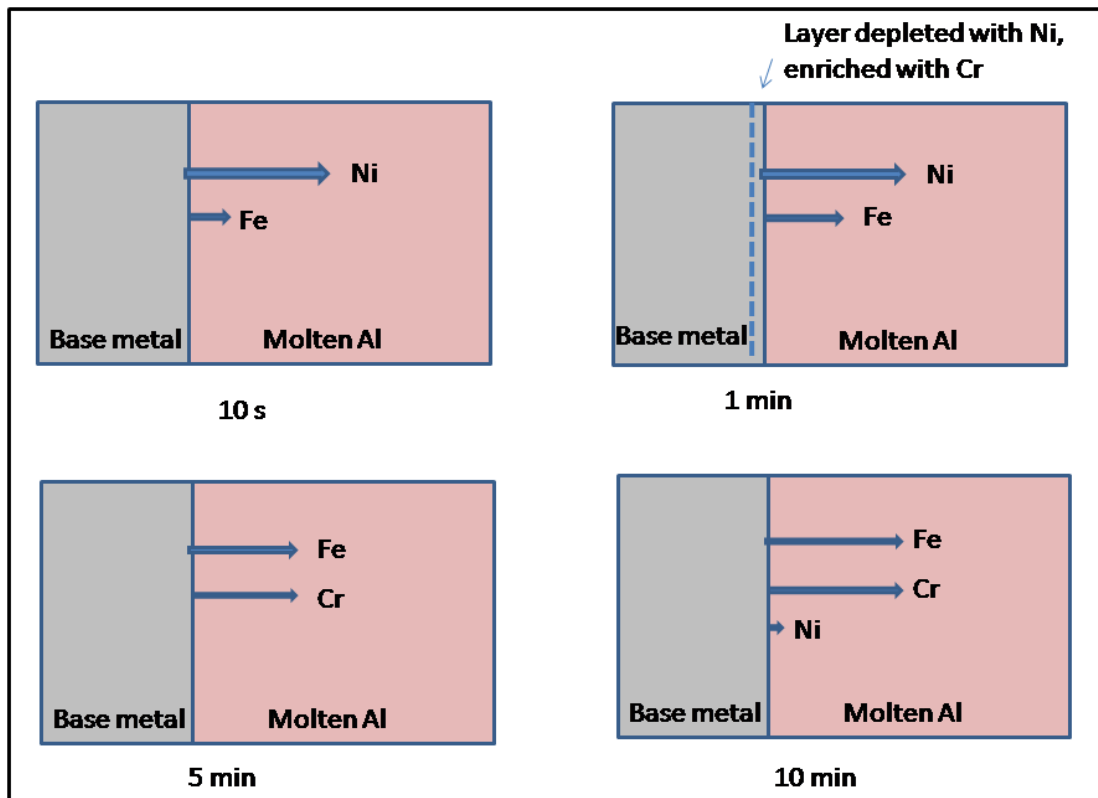
Fig. 5.44 Schematic representation of the dissolution process during the interaction between SS 321 and molten Al.

Figure 5.44 shows the hypothetical representation of the nature of the dissolution process taking place during the interaction between SS 321 and molten Al at 700 °C. At the initial stage, nickel dissolves preferentially because it has the highest solubility in molten Al. This is followed by Fe dissolution, while chromium has the least solubility. It is reported by Dybkov (2013) that the rate of dissolution of these elements follows parabolic law. During the initial stages, the rate of dissolution is high and reduces with interaction time. After 1 min of interaction time, at the base metal side region, a layer with depleted nickel and enriched Cr is formed. With further increase in

the interaction time, this layer dissolves into molten Al thereby forming majorly chromium and iron aluminides.
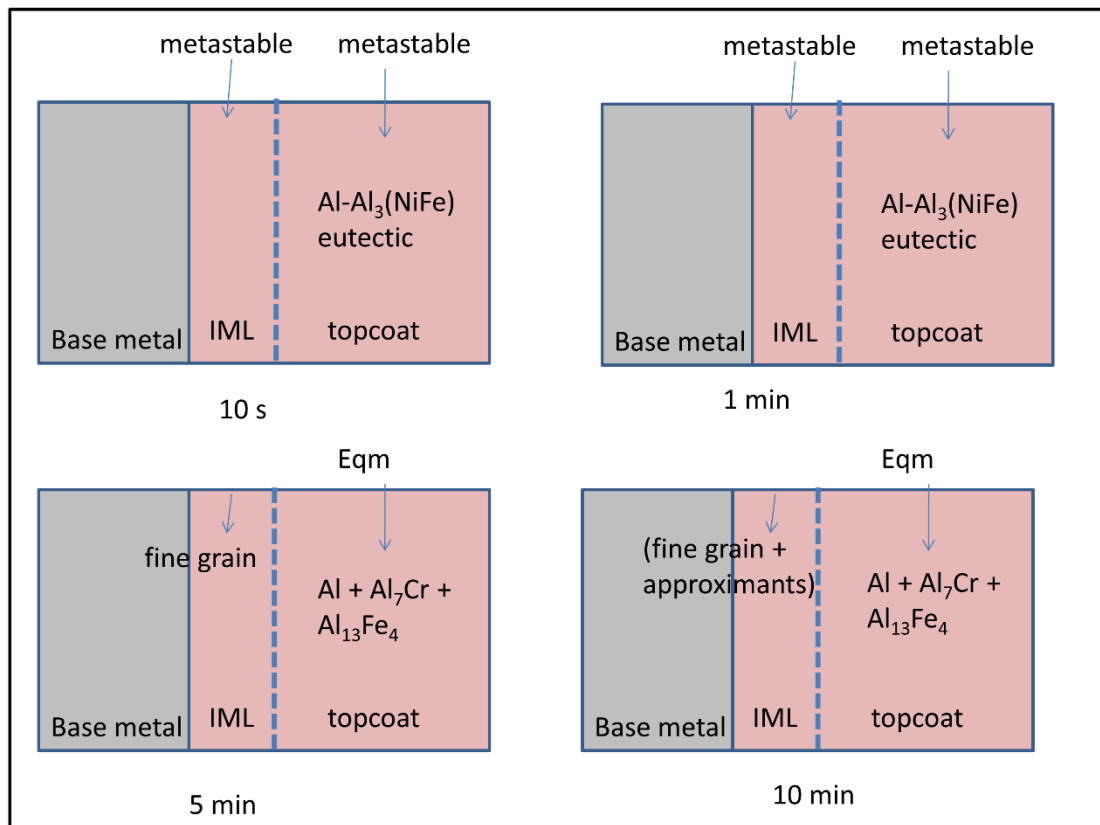
Fig. 5.45 Schematic representation of the evolution of the microstructural features during the interaction between SS 321 and molten Al at 700 °C

Figure 5.45 shows the schematic representation of the evolution of microstructural features. At short interaction times, metastable phases are formed in both the intermetallic layer as well as in the topcoat. Long interaction time equilibrium phases in the topcoat are formed, while, fine-grained microstructures and some quasicrystalline approximants are observed within the intermetallic layer. The occurrence of non-equilibrium or metastable phases could be conceived by considering a control volume where nucleation events take place. A schematic representation is shown in Fig. 5.46. The control volume acts like an open system where the atom fluxes enter from base metal by dissolution process and leave by diffusion process into the bulk of the molten metal.
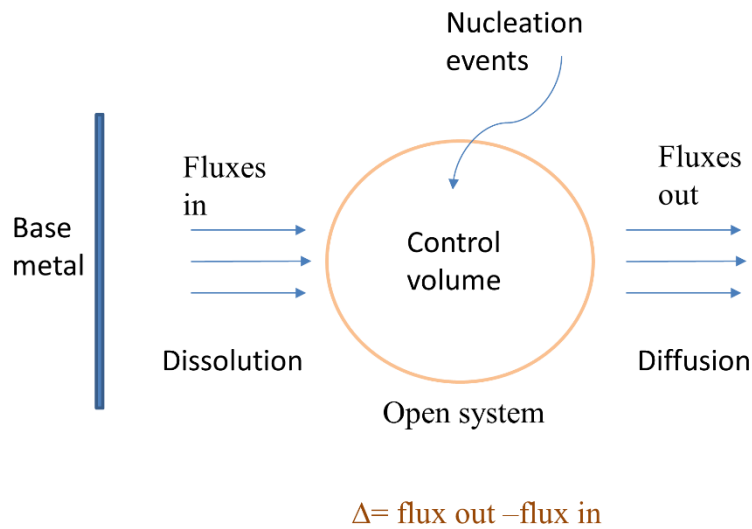
Fig. 5.46 Schematic representation of the factors controlling nucleation events within a control volume.

The nucleation and growth of thermodynamically stable nuclei become a function of Δ. Where delta (Δ) is the difference in the outgoing and incoming fluxes. The negative value of delta assists nucleation, while, a positive one suppresses nucleation. Further, a positive value of delta provides the condition for the nucleation of metastable phases. Also, the growth of the nuclei is stunted by the nucleation of multiple phases and the mutual growth competition between the neighbouring phases. Overall, the formation of the microstructure at the interface can be controlled by controlling the diffusion fluxes.

In summary, the evolution of the microstructure at the interface follows a dissolution-nucleation mechanism. The elements from the base metal first dissolve into the molten bath followed by nucleation of intermetallic phases. Various types of intermetallic phases are formed with different dipping durations. The intermetallic phases are dispersed in Al matrix and do not form a continuous layer. Both equilibrium and metastable phases including quasicrystalline approximants are formed. On the contrary, the formation of the microstructure in case of Fe/Al and SS 430/Al system follows a reaction-diffusion mechanism. The intermetallic phases form a continuous layer.

Page intentionally left blank

Page intentionally left blank

CHAPTER 6

MICROSTRUCTURAL TRANSFORMATIONS DURING DIFFUSION TREATMENT OF ALUMINIZED AISI 321 STAINLESS STEEL

This chapter deals with the phase transformations of the hot-dip aluminized stainless steel 321. Such aluminized samples are intended to be used at high temperature. During the service, phase transformation takes place in the coating due to the interdiffusion of elements. In the present work, diffusion treatment is carried out at temperatures 700 °C and 900 °C. The microstructural transformation is studied in detail by transmission electron microscopy and the results are presented below.

6.1 Microstructural Development During Diffusion Treatment at 700 °C

The coating, when exposed to high temperature, undergoes phase transformation due to interdiffusion of species. The sample before the diffusion treatment was hot-dip aluminized for 10 minutes and it is shown in Fig. 6.1 (a). Figure 6.1(b) shows the SEM-BSE cross-sectional micrograph after diffusion treatment for 1 hour. The aluminide layer at the interface transformed into a layered structure with multiple phases. Total thickness increased to about 100 μm from the initial 40 μm. The dispersed intermetallic phases in the aluminum topcoat are also observed to grow as shown in Fig. 6.2.
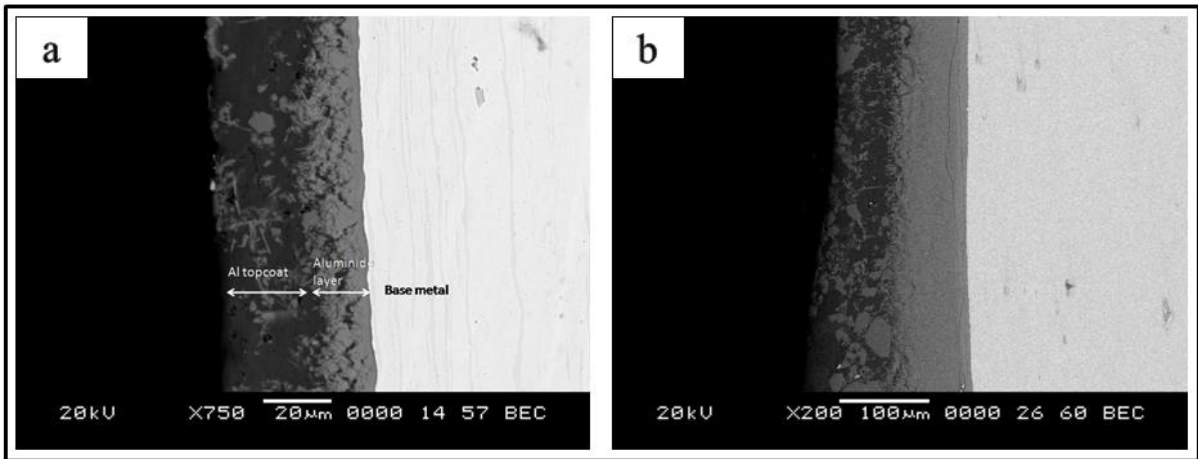
Fig. 6.1 (a) SEM-BSE micrograph of hot-dip aluminized sample dipped for 10 min, and (b) after diffusion treatment for 1 hr at 700 °C.
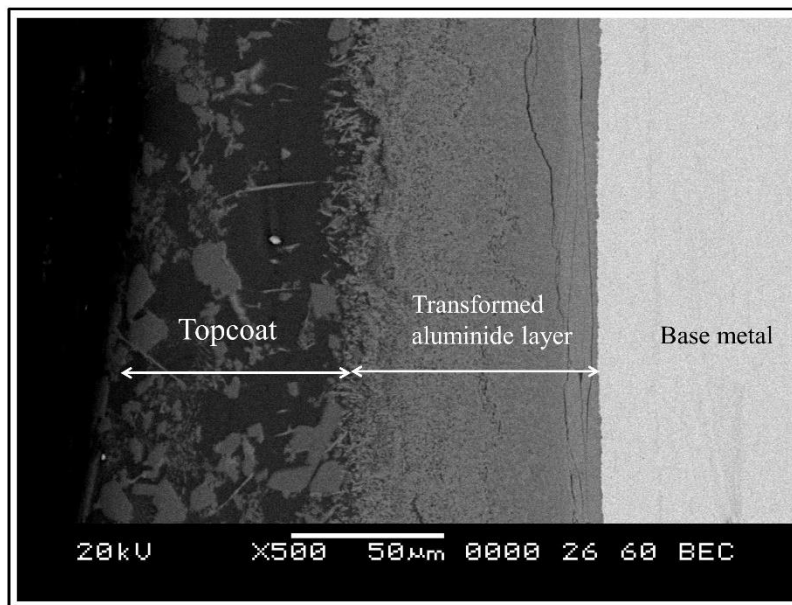
Fig. 6.2 Cross-sectional SEM-BSE micrograph of the coating after diffusion treatment for 1 hour at 700 °C.

The aluminide layer further consisted of multiple phases. Figure 6.3 shows a collage image of SEM micrographs on the aluminide layer. It shows the formation of three layers marked as 1, 2 and 3. TEM study is carried out on the layer 1 and it reveals that the layer consisted of $Al_{13}Fe_4$ and Al as the two phases. This is highlighted in the magnified image in Fig.6.4. The average size of $Al_{13}Fe_4$ phase is close to 1 μm. Figure

6.5 presents a bright field TEM micrograph showing $Al_{13}Fe_4$ and Al phases formed in layer 1. The Layers 2 and 3 show complex microstructures which are further analyzed by TEM. The layer presents microstructures with a slight difference in contrast as observed under backscatter electron imaging, shown in Fig. 6.6. SEM-EDS analysis is carried out and is presented in Table 6.1.
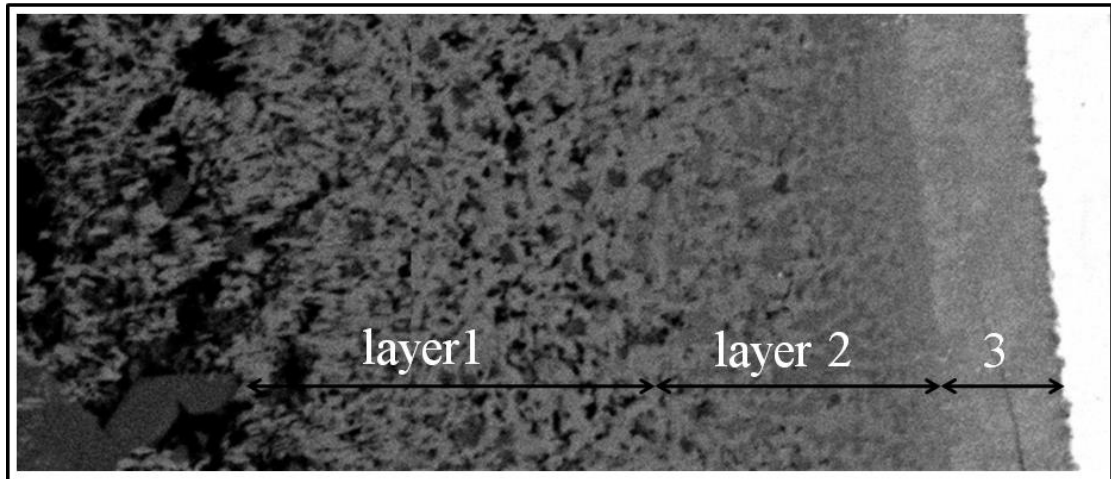
Fig. 6.3 Collage of SEM micrographs in the aluminide layer showing three layers.
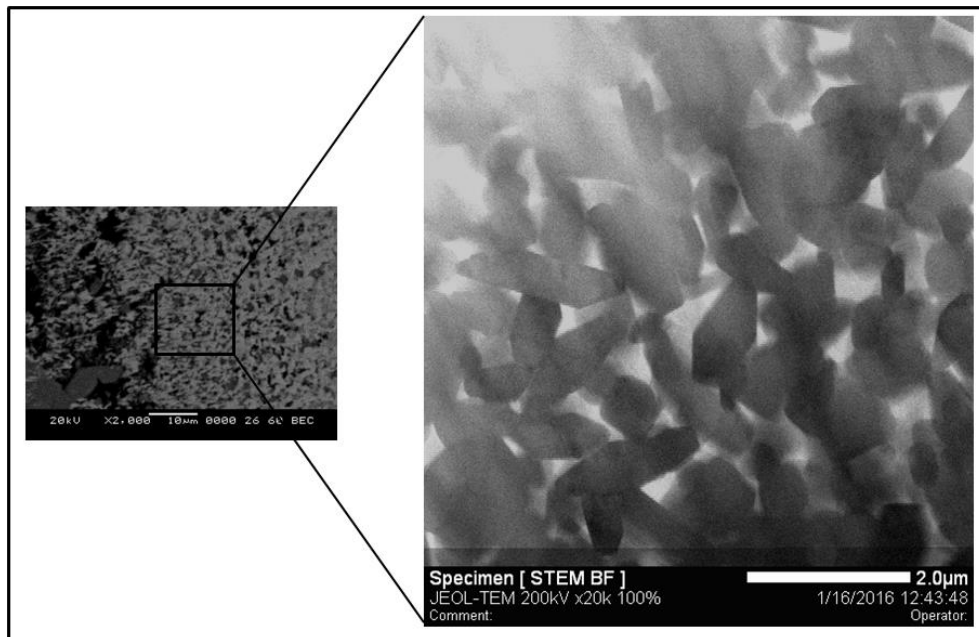
Fig. 6.4 Bright field STEM micrograph showing two phases with dark contrast as $Al_{13}Fe_4$ and light contrast as Al.
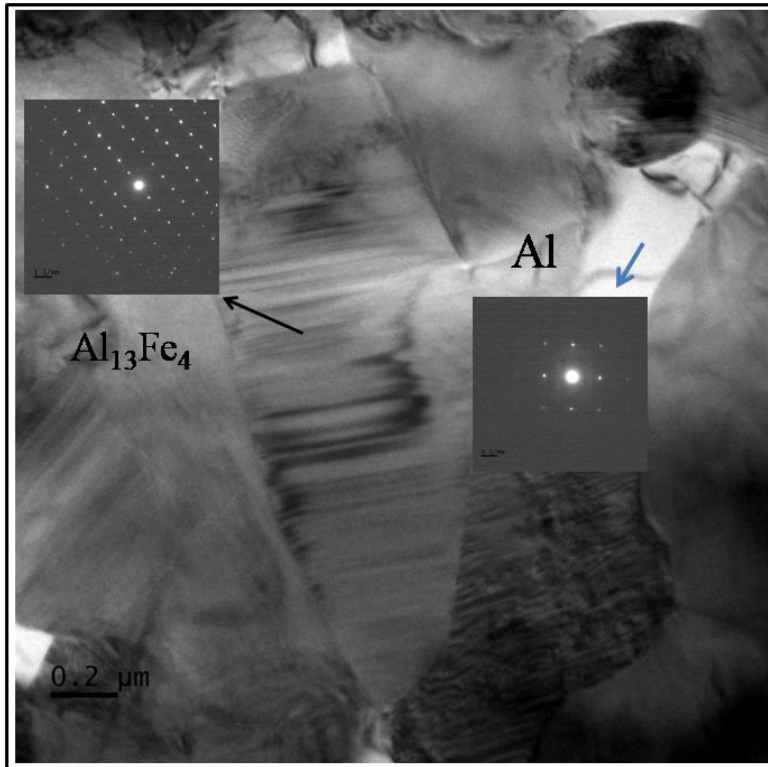
Fig. 6.5 Bright field TEM micrograph showing $Al_{13}Fe_4$ and Al phases formed in layer 1. The inset shows the corresponding SAED pattern.
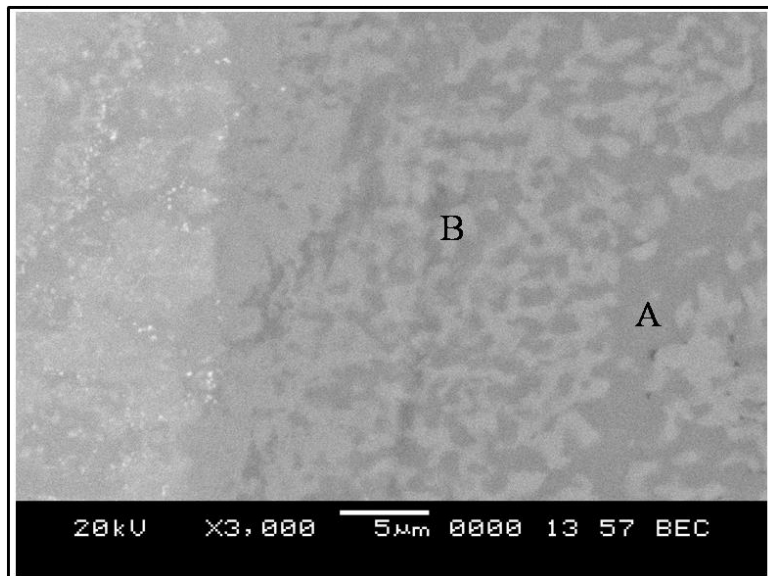
Fig. 6.6 SEM-BSE micrograph showing two phases with varying contrast marked as A and B.

Table 6.1 SEM-EDS analysis on phase A and B (composition mentioned in at. %)

Elements	Phase A	Phase B
Al	82.3	80.4
Fe	11.1	15.7
Cr	5.1	2.4
Ni	1.6	1.5

SEM-EDS mapping is carried out and the elemental distribution in the two phases are presented in Fig. 6.7.
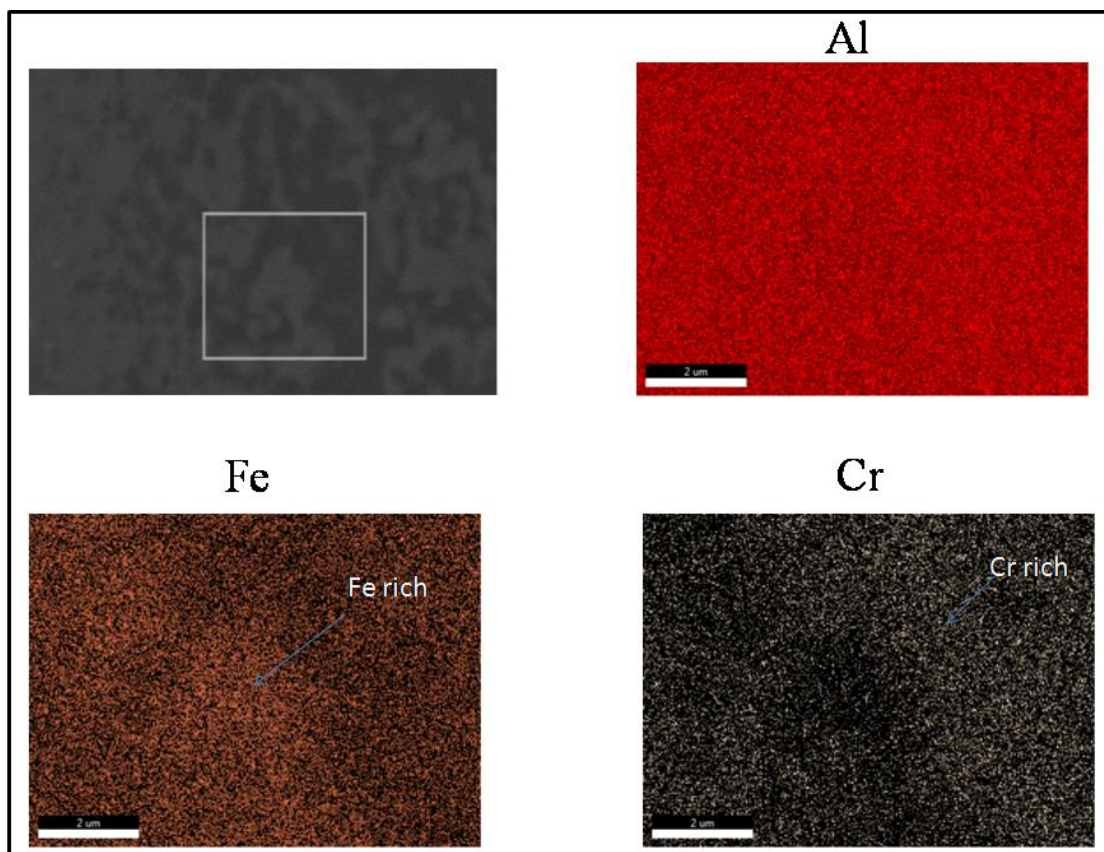
Fig. 6.7 SEM-EDS mapping showing elemental distribution among the two phases

The TEM analysis shown in Fig. 6.8 depicts a complex electron diffraction pattern. The third and the fifth spot are bright and the pattern could be closely related to cubic

superstructure (Demange et al. 2004) or an orthorhombic approximant closely related to T phase as reported by Singh and Ranganathan (1994). The exact nature of this phase is unidentified and the matter will be subjected to further investigations.
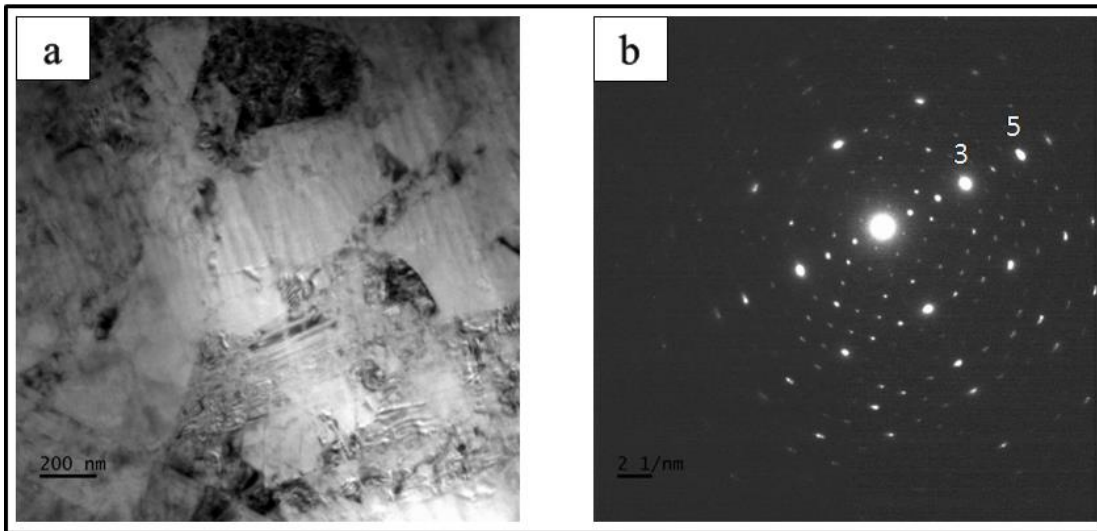
Fig. 6.8 (a) BF TEM micrograph and (b) corresponding electron diffraction pattern.

The aluminide layer grows with increasing diffusion time. Figure 6.9 shows the SEM micrographs of samples heat treated for 1 hour, 3 hours, 5 hours and 7 hours, at 700 °C respectively. Cracks within the aluminide layer are observed for all these conditions which are shown by the arrow mark on the micrographs in Fig. 6.9. Cracks are observed predominantly in layer 2 of the aluminide layer. Therefore, TEM investigations on these layers could not be carried out. Such degradation is detrimental from the mechanical integrity point of view. Diffusion treatment at a relatively higher temperature is carried out, i.e. at 900 °C and results are discussed in the next section.
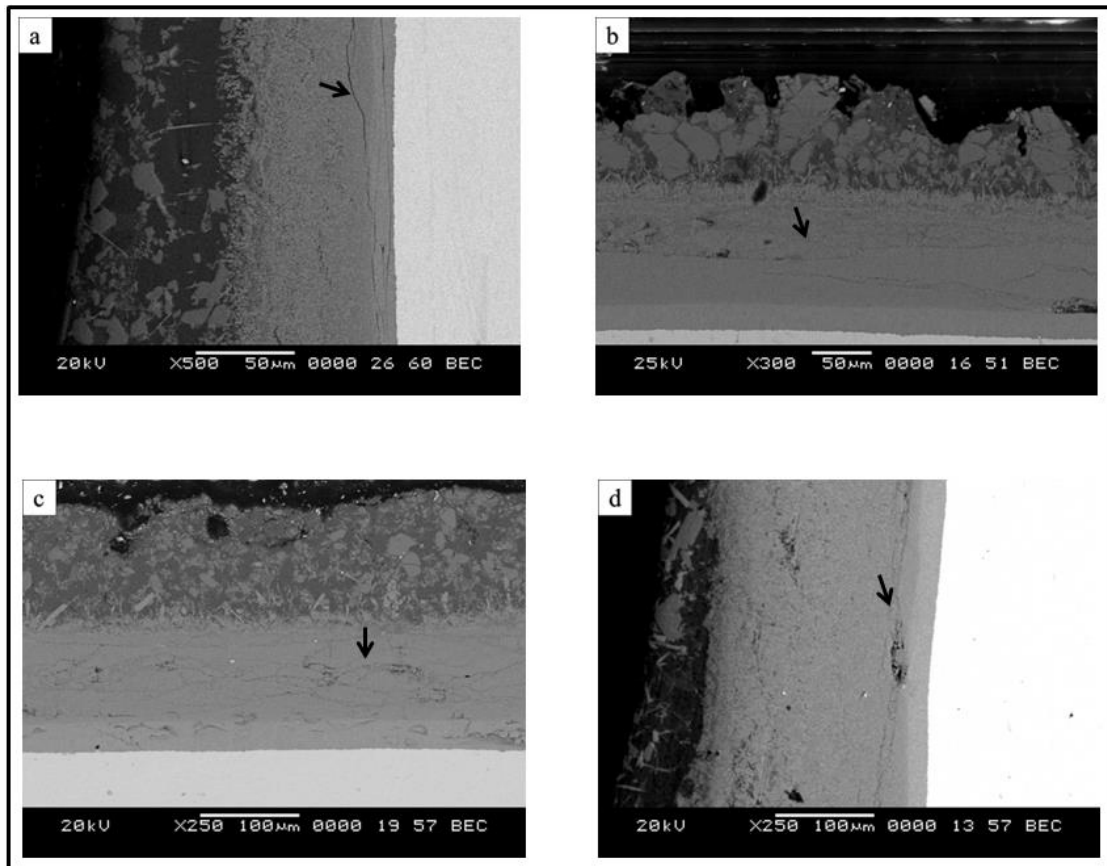
Fig. 6.9 SEM micrograph of heat-treated samples at 700 °C for (a) 1 hour, (b) 3 hour, (c) 5 hour, and (d) 7 hour.

6.2 Microstructure Development During Diffusion Treatment at 900 °C.

The diffusion treatment at a higher temperature of 900 °C is carried out and the microstructural transformation in the coating is investigated. Figure 6.10 shows SEM micrographs of diffusion treated aluminized samples for 3 hours, 5 hours and 24 hours, respectively. The coating has transformed into a layered structure. The average coating thickness measured is 196 μm for 3 hours, 292 μm for 5 hours and for 24 hours the thickness is 358 μm.
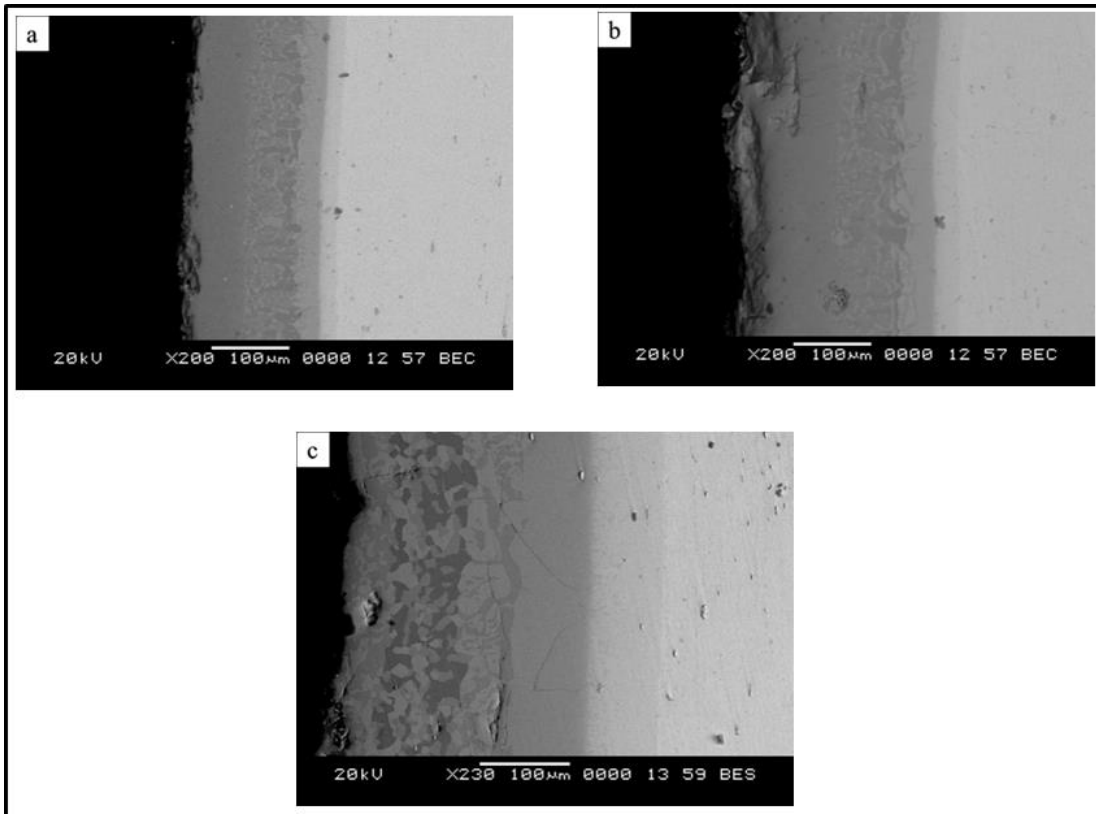
Fig. 6.10 SEM micrograph of samples diffusion treated at 900 °C for (a) 3 hours, (b) 5 hours, and (c) 24 hours.

The higher magnification micrograph shown in Fig. 6.11 presents the layered structure in detail after the diffusion treatment for three hours. Four layers are observed in the coating. The outermost layer (marked as layer I in Fig. 6.11) measures about 70 μm. The thickness of the Layer II measured is also close to 70 μm and consists of a mixture of phases. Towards the base metal side, two layers are present. Layer III measures about 30 μm and Layer IV is found to measure around 25 μm.
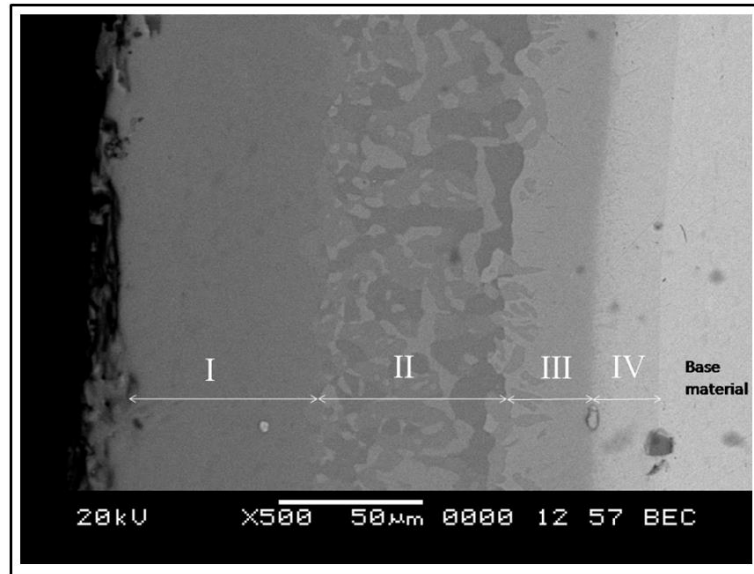
Fig. 6.11 Cross-sectional SEM-BSE micrograph of the coating after diffusion treatment showing layered structure. Four layers are marked I to IV.

6.2.1 Layer I

The elemental composition obtained from SEM-EDS analysis on this layer indicates to be Al: 71.5 %, Fe: 26.5 % and Cr: 2% (all in at. %). The composition values are in close agreement to that of Fe_2Al_5 phase. Figure. 6.12 (a) and (b) shows the TEM micrographs corresponding to Fe_2Al_5 phase observed in layer I. Twins are seen as evident from the micrograph presented in Fig. 6.12 (b) and the corresponding diffraction pattern is shown in Fig. 6.12 (d). The width of the twin measured is in the range of 20 to 30 nm. The TEM-EDS elemental analysis is found to be Al: 69, Fe: 26, Cr: 4.2, Ni: 0.8 (all in at. %) which is also in close agreement with the Fe_2Al_5 stoichiometry. Presence of $Al_{13}Fe_4$ phase with the size is close to 500 nm is also observed as seen in Fig. 6.13. Figure 6.13 (b) shows the electron diffraction pattern showing ten strong spots (shown by marked arrow). It reveals that the phase has a relationship with the quasicrystalline phase and could be a crystalline approximant phase.

117
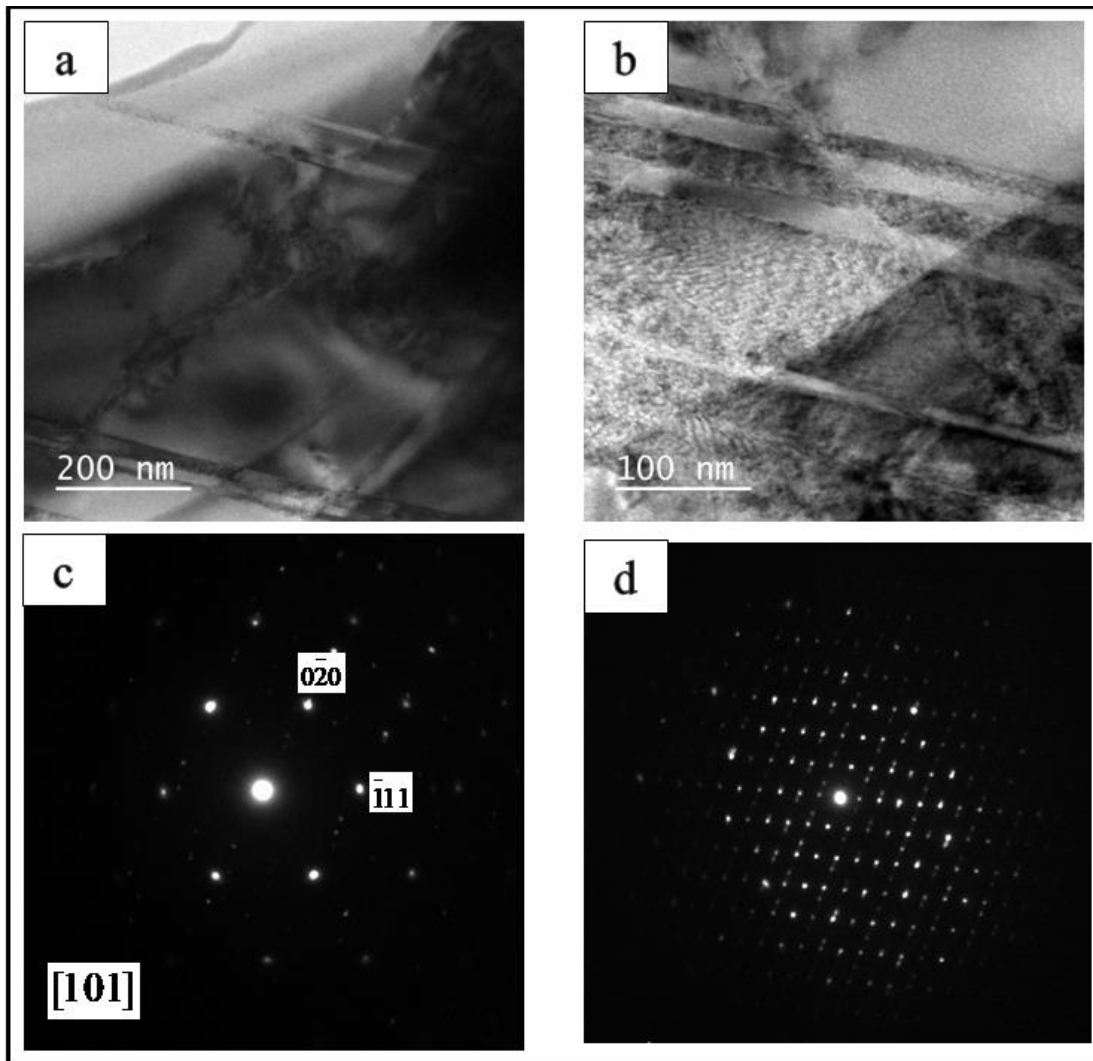
Fig. 6.12 (a) Bright field TEM micrograph of the Fe_2Al_5 phase, (b) high magnification micrograph showing the presence of twins, (c) electron diffraction pattern along [101] zone axis of the Fe_2Al_5 phase, and (d) electron diffraction pattern showing twinning.
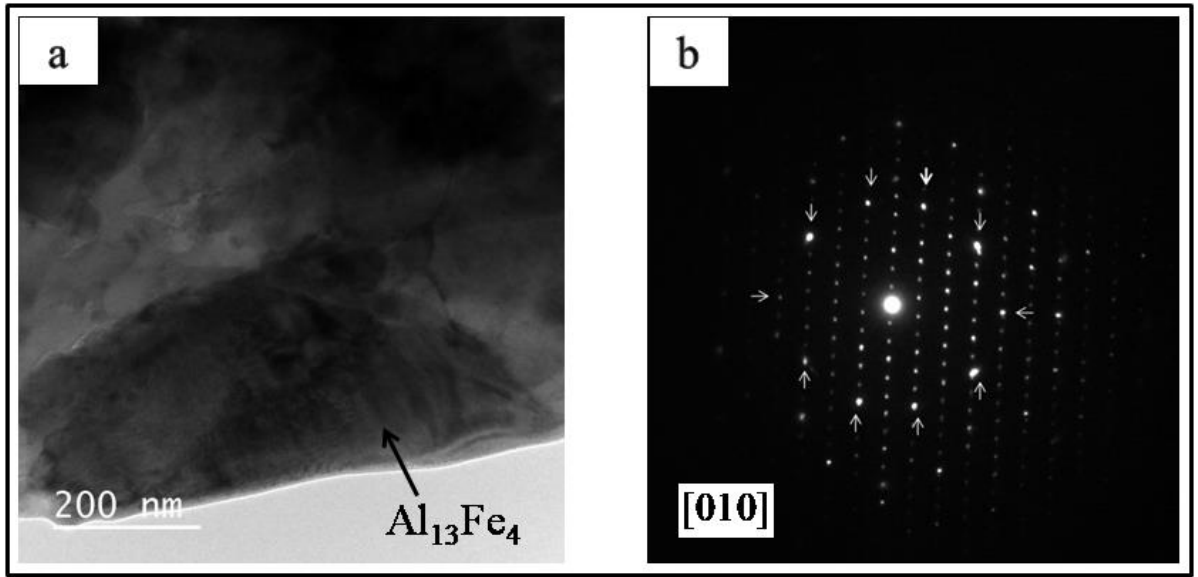
Fig. 6.13 (a) Bright field TEM micrograph showing $Al_{13}Fe_4$ phase, and (b) associated electron diffraction pattern along [010] zone axis showing 10 strong spots revealing a close relationship with the quasicrystalline phase.

6.2.2 Layer II

Figure 6.14 shows a high magnification SEM-BSE micrograph of the details present in layer II. The contrast observed from the backscatter image reveals that the layer comprises of a mixture of phases. These phases are labelled as 1, 2 and 3. SEM-EDS elemental analysis is carried out on these phases and the compositional values are tabulated in Table 6.2. Phase 3 is found to be an Al-rich layer and the composition obtained is in close agreement to that of Fe_2Al_5 phase. Phases 1 and 2 shows Al content close to 50 at. % which falls in the homogeneity range of FeAl phase in the binary Fe-Al system. SEM-EDS mapping is shown in Fig. 6.15.
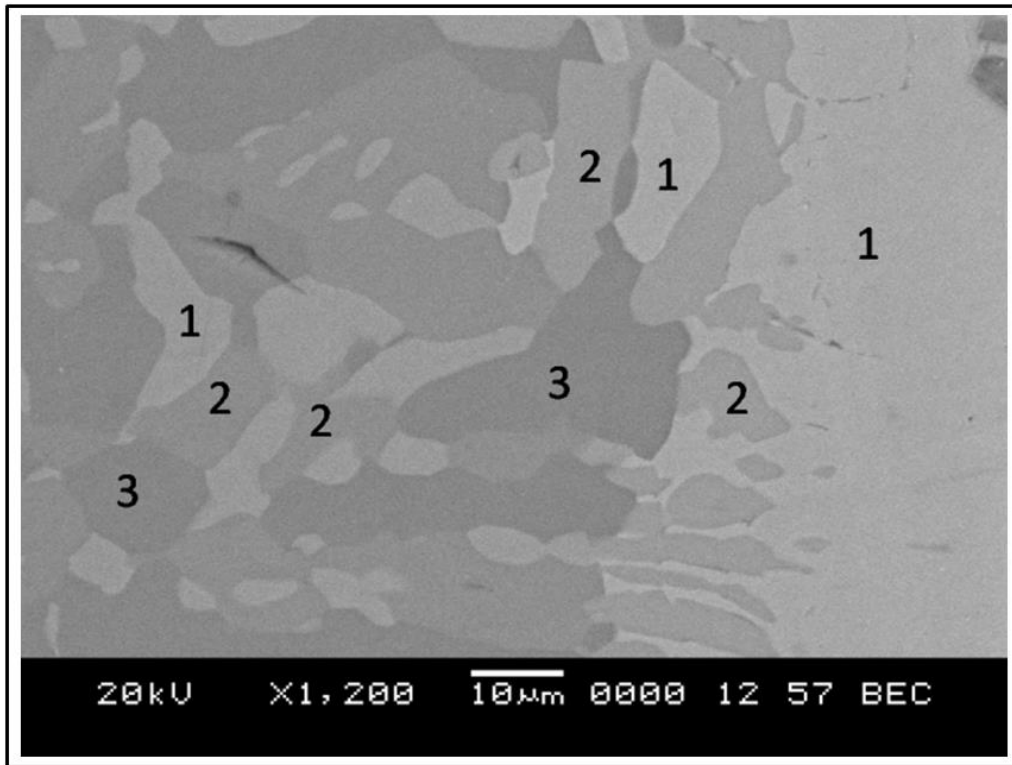
Fig. 6.14. SEM-BSE micrograph showing various phases which are labelled as 1, 2 and 3.

Table 6.2 SEM-EDS compositional analysis on the locations marked in Fig. 6.14

Element	Location		
	1	2	3
Al (at %)	50.43	57	68.42
Fe	34.37	26.07	29.11
Cr	7.73	16.44	2.04
Ni	6.84	-	0.43
Phase	FeAl	?	Fe_2Al_5
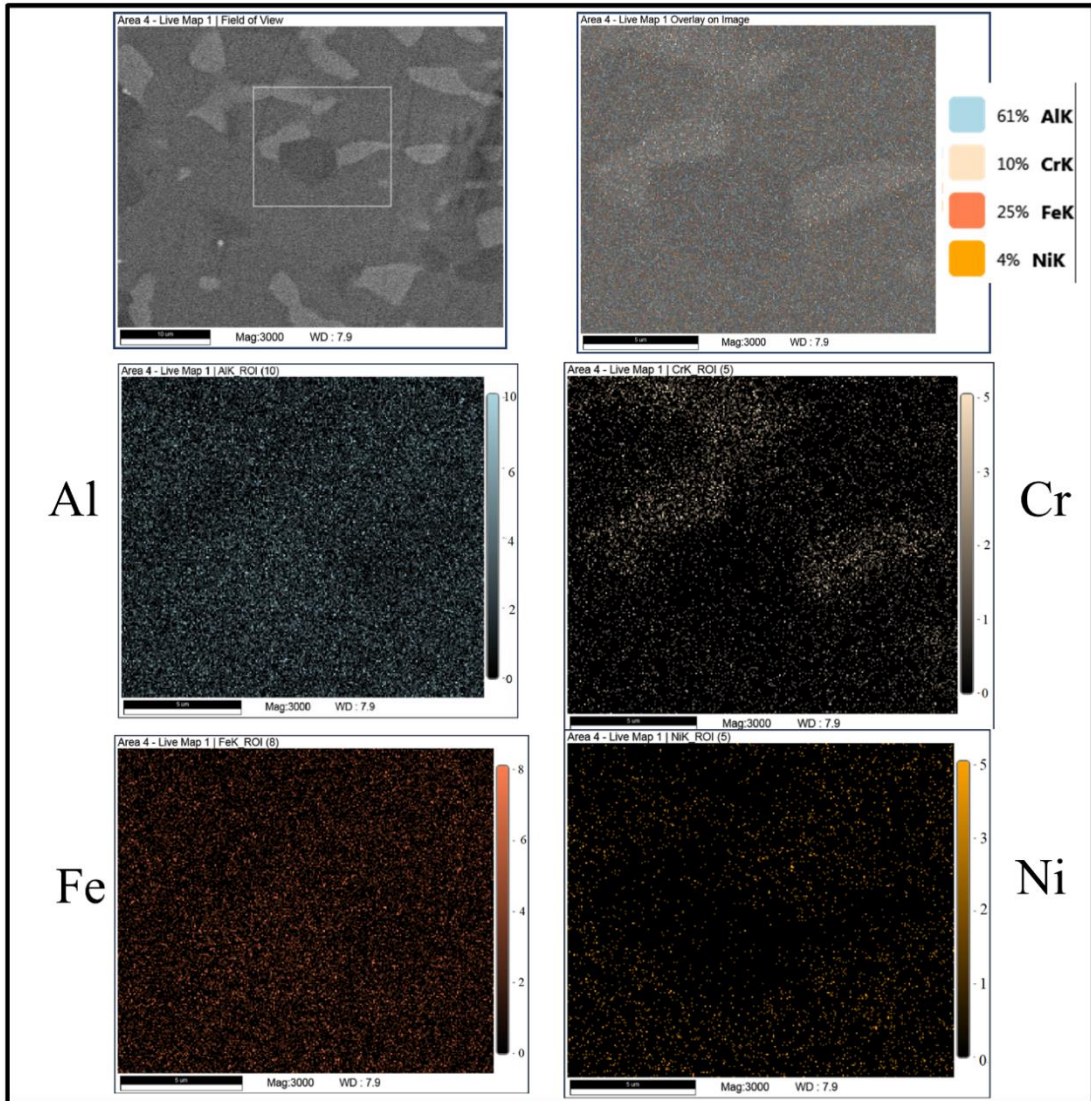
Fig. 6.15 SEM-EDS elemental mapping showing the distribution of the elements among the three phases.

From the SEM-EDS point and mapping analysis, it is noted that the nickel is partitioned between phases 1 and 2. Close to 7 at. % Ni is present in phase 1, while it is negligible in phase 2. Phase 1 was subjected to TEM studies, and electron diffraction patterns taken along three major zone axis is presented in Fig. 6.16. The analysis of SAED pattern indicates that the phase has a body-centred cubic structure. Superlattice reflections were not observed in the electron diffraction patterns and it indicates the absence of order. The elemental composition by TEM-EDS also found to be in the

homogeneity range of FeAl phase. The FeAl phase is known to possess an ordered B2 structure (CsCl type superlattice) at low temperature with a lattice parameter, a=2.9 Å. The lattice parameter of the disordered FeAl phase measured in the present investigation is, a=4.8 Å.
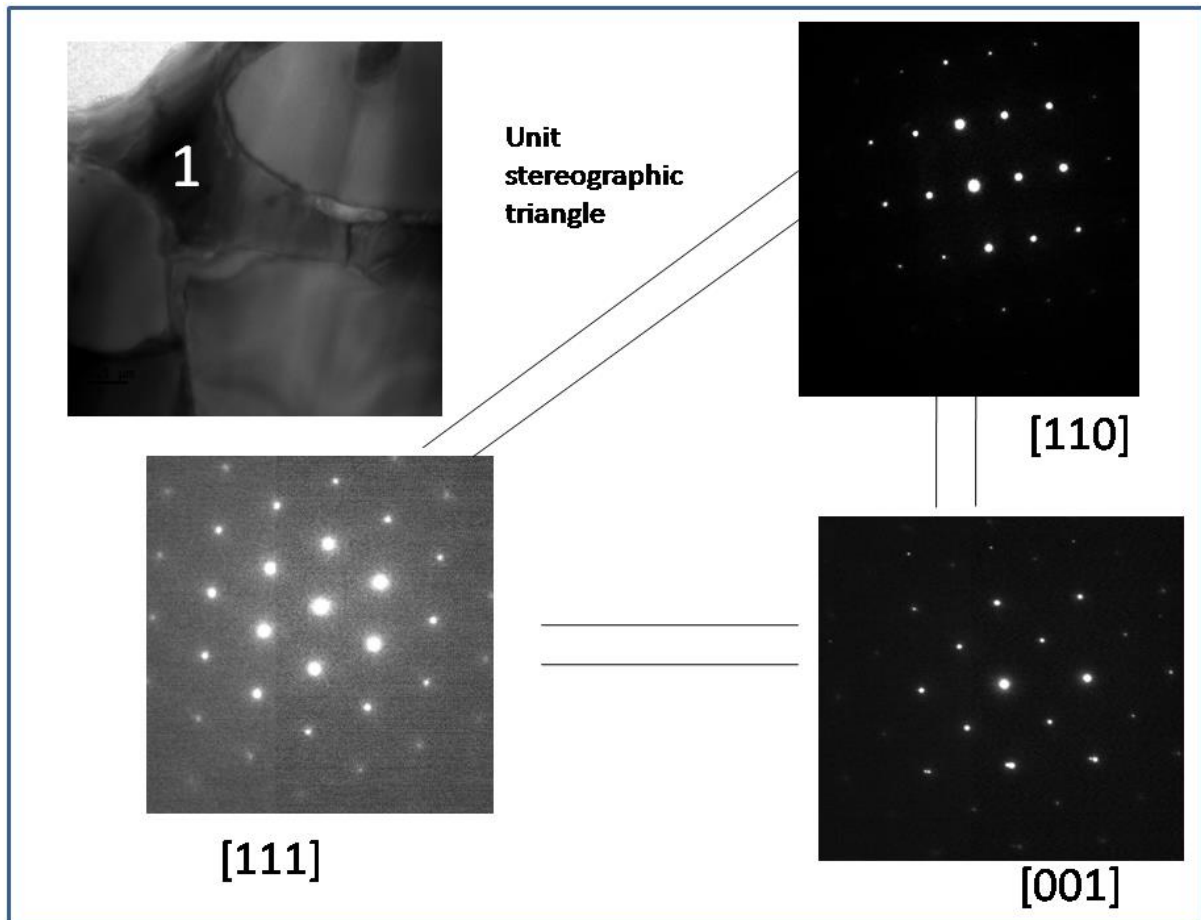
Fig. 6.16 Electron diffraction patterns of phase 1 (marked in Fig. 6.14) along three major zone axis within unit stereographic triangle. The structure is determined as cubic I, i.e., bcc structure.

Fig. 6.17 shows electron diffraction patterns along three major zone axis for the phase 2. The analysis indicates that this phase has a primitive cubic (simple cubic structure). Composition using TEM-EDS analysis is obtained to be Al: 53 at.%, Fe: 29 at%, Cr: 18 at.%. This composition corresponds to B2 FeAl phase region according to equilibrium ternary phase diagram (Effenberg and Ilyenko 2006). However, no such primitive cubic phase is to be present in that particular region of equilibrium phase

diagram. This is a new phase being reported in the present investigation. The lattice parameter of this phase measured is, a=7.2 Å. It may be a complex cubic phase and might be related to the phase shown in Fig. 6.8. Crystallographic orientation relationship between the simple cubic phase and the disordered FeAl phase is observed. It has exactly the cube on cube crystallographic orientation relationship. Fig. 6.18 shows composite electron diffraction pattern of the two phases showing orientation relationship.
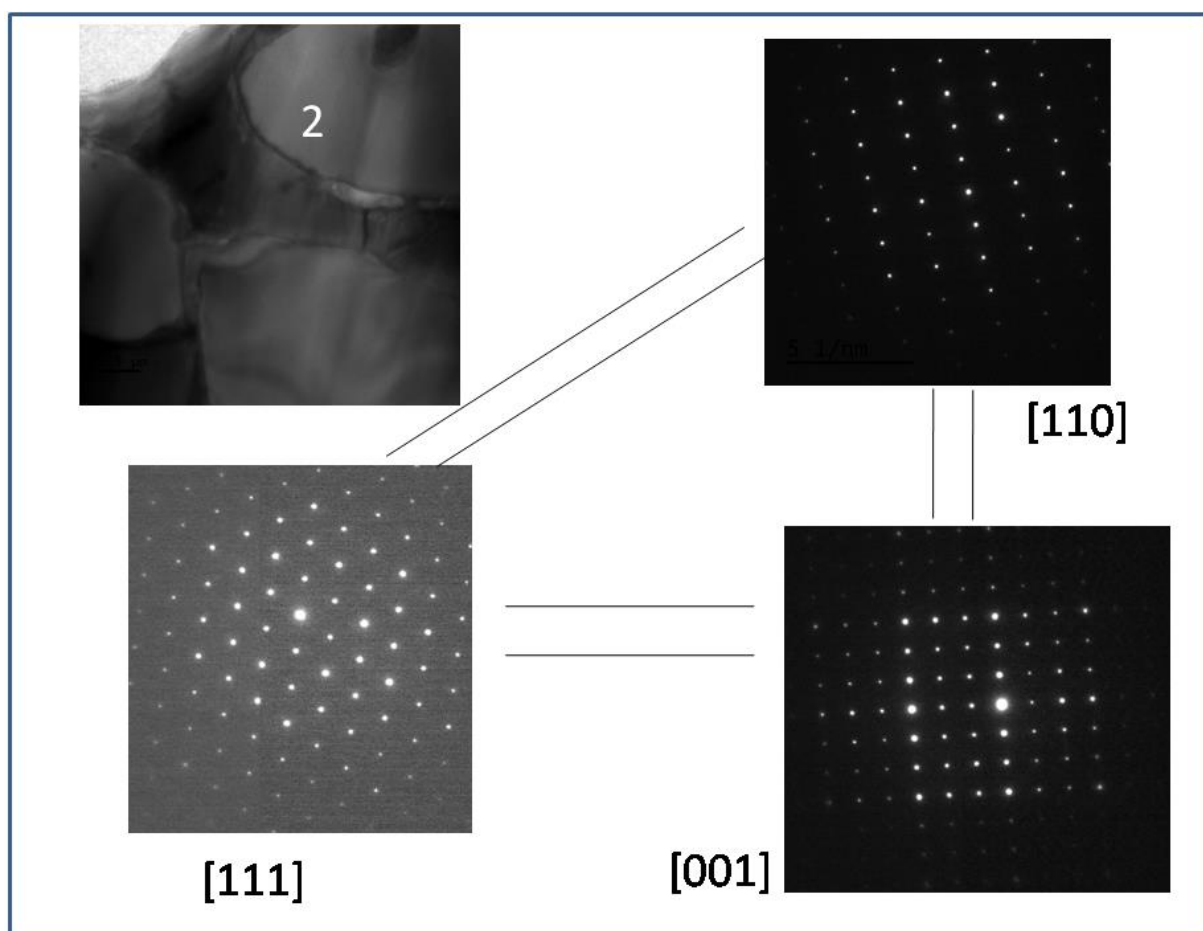
Fig. 6.17 Electron diffraction pattern of phase 2 (marked in Fig. 6.14) along three major zone axis within the unit stereographic triangle. The structure is determined as cubic P, i.e., simple cubic structure.
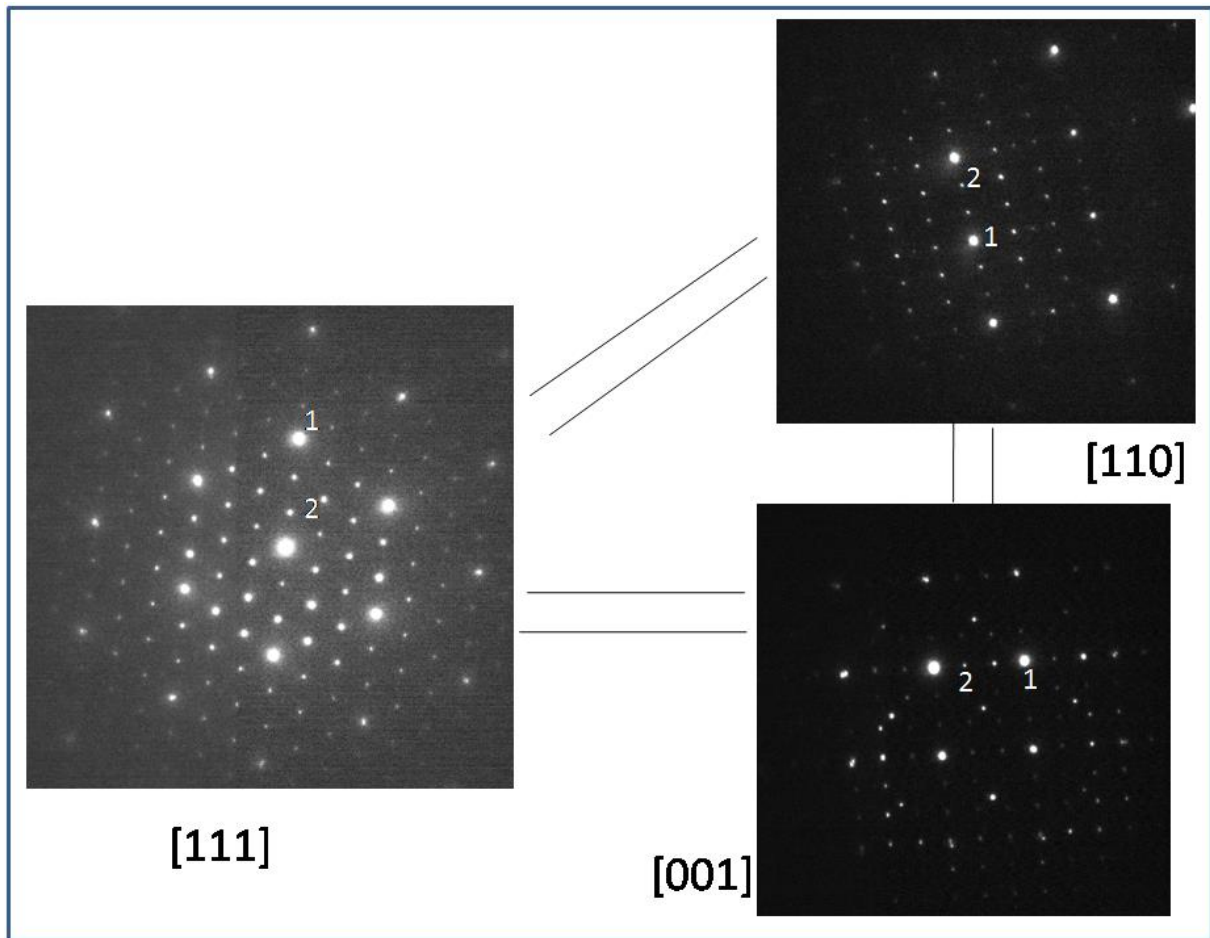
Fig. 6.18 Composite electron diffraction patterns along three major zone axis showing cube on cube crystallographic orientation relationship between phase 1 and 2.

6.2.3 Layer III

The layer III comprises of the disordered FeAl phase. The presence of defect structure is evident as shown in Fig. 6.19. Dislocations and misfitting plate precipitates are observed in it. Misfit precipitates are discernible by lobes of black/black contrast with the line of no contrast in-between. This is observable under the method of two beam conditions technique. The spherical strain field arises due to the small lattice mismatch between the matrix and the precipitate. A similar contrast is exhibited even by the dislocation loop, as well as vacancy and interstitial. In order to differentiate between dislocation loop and misfit precipitate, two beam technique with different g vectors are chosen and the images of which are shown in Fig. 6.20.
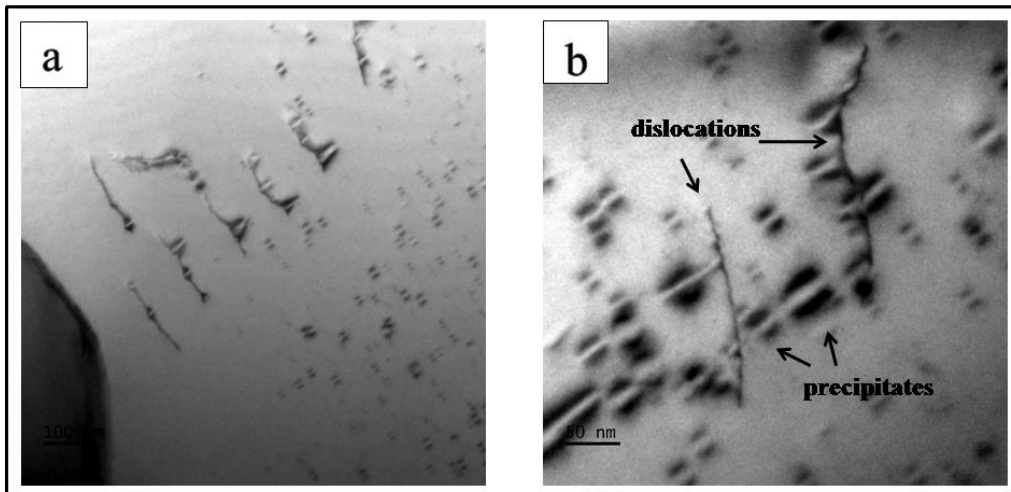
Fig. 6.19 (a) Bright field TEM micrograph showing misfit plate precipitates and dislocations, and (b) high magnification TEM micrograph showing misfit precipitates consisting of lobes of contrast. Dislocations cutting through these precipitates are also seen.
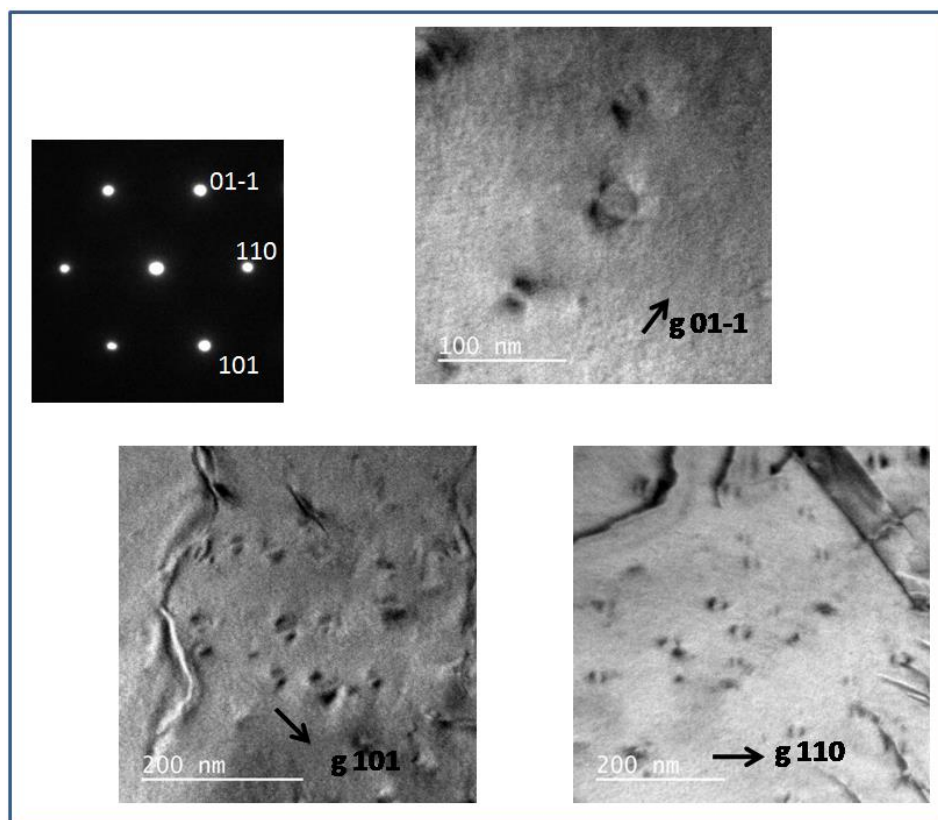
Fig. 6.20 Bright field TEM micrographs under two beam conditions. The line of no contrast is perpendicular to g vector for misfit precipitates.

6.2.4 Layer IV

The SEM-BSE micrograph in the region of Layer IV is shown in Fig. 6.21. The SEM-EDS investigations on this layer indicate the composition as Fe: 60.6; Cr: 22; Al: 9.8; Ni: 6.6 (all in at. %). Fine precipitates are present in this layer evident from the contrast observed in the back-scattered SEM micrograph. Further, the TEM analysis shows that this layer is α-Fe, ferrite phase along with the precipitates, which are nickel-rich NiAl phase precipitated in the ferrite matrix.
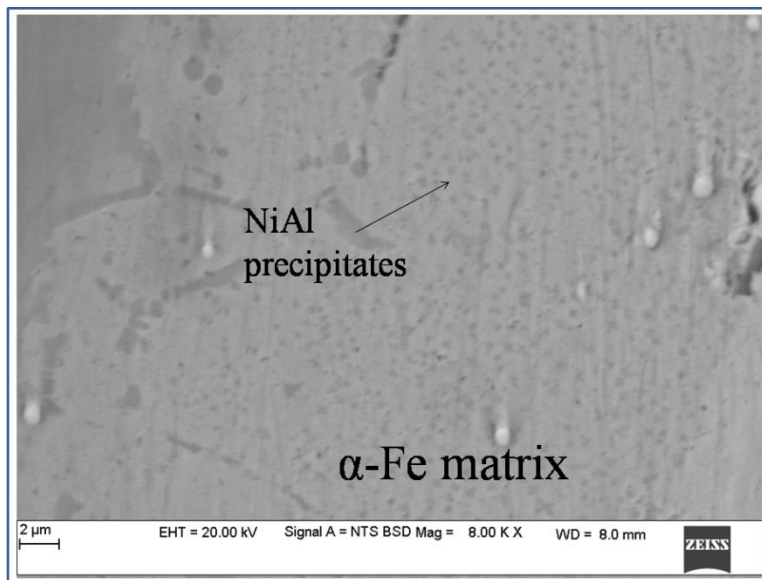
Fig. 6.21 SEM micrograph in layer IV showing fine NiAl precipitates in ferrite matrix

Table 6.3 TEM-EDS elemental composition in the α-Fe layer.

Element	Ferritic matrix	NiAl
Al (at %)	7.17	28.04
Fe	62.94	19.69
Cr	25.43	2.93
Ni	4.09	48.31
Ti	0.38	1.03

Figure 6.22 (a) shows TEM micrograph of the ferrite matrix. Surrounding the precipitates and in the matrix, dense dislocation networks are seen. TEM-EDS analysis (Table 6.3 & Fig.6.22 (d)) on this phase shows that the region is richer in nickel content compared to the matrix. Fig. 6.22 (b) shows SAED pattern of precipitates. The analysis of the SAED pattern indicates that the precipitates to be NiAl phase. Fig. 6.22 (c) shows g [101] dark-field micrograph of the precipitates. The size of these precipitates is measured to be in the range of 100-150 nm.
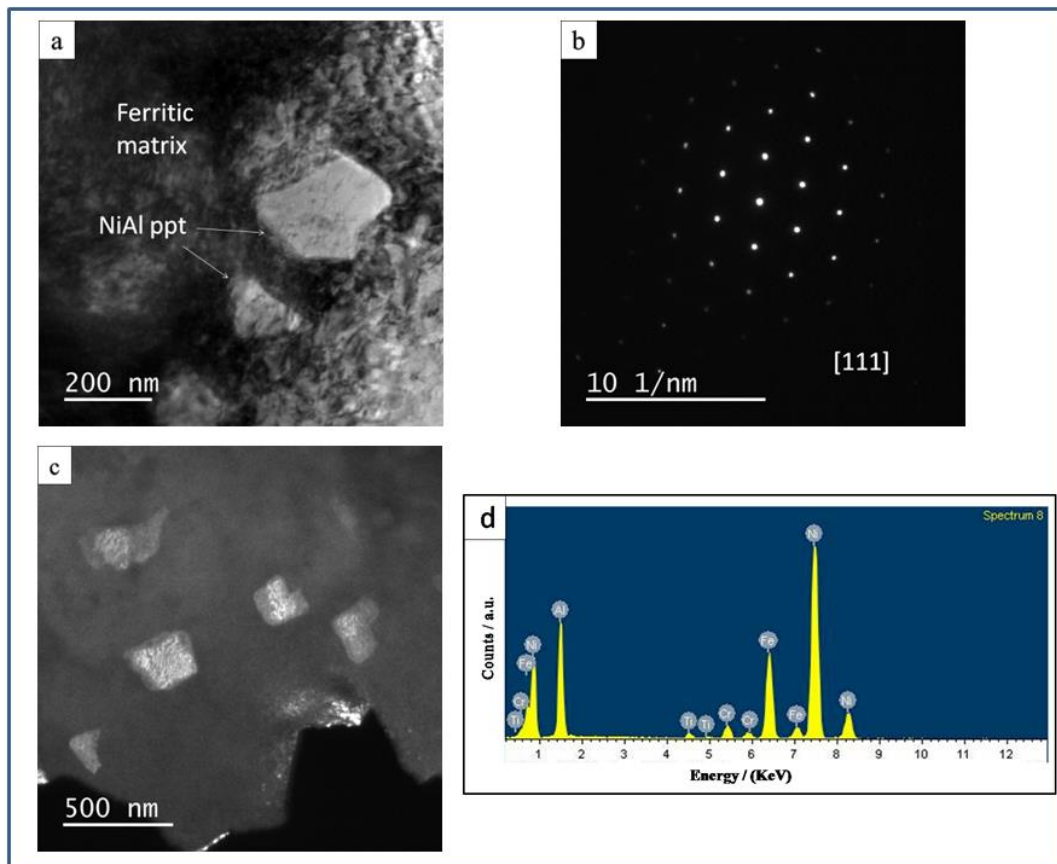
Fig. 6.22 (a) Bright field micrograph showing ferritic matrix with NiAl precipitates, (b) [111] zone axis pattern of B2 NiAl phase in the ferritic matrix, (c) TEM dark field micrograph of the NiAl precipitates with g= [101] reflection, and (d) TEM-EDS spectrum of the NiAl phase.

6.3 Microstructural Changes During Initial Stages of Diffusion Treatment at 900 °C

Figure 6.23 shows the SEM micrograph of the diffusion treated samples at 900 °C for 5 min to 20 min. Intermetallic phases in the aluminum topcoat grow during the interdiffusion process as seen in Fig. 6.23 (a). Coarsening of polygonal Al_7Cr and growth of acicular $Al_{13}Fe_4$ phase could be observed in the topcoat. Towards the base metal side α-Fe and FeAl phases form. With an increase in the duration of heating, these phases tend to grow on the base metal side.
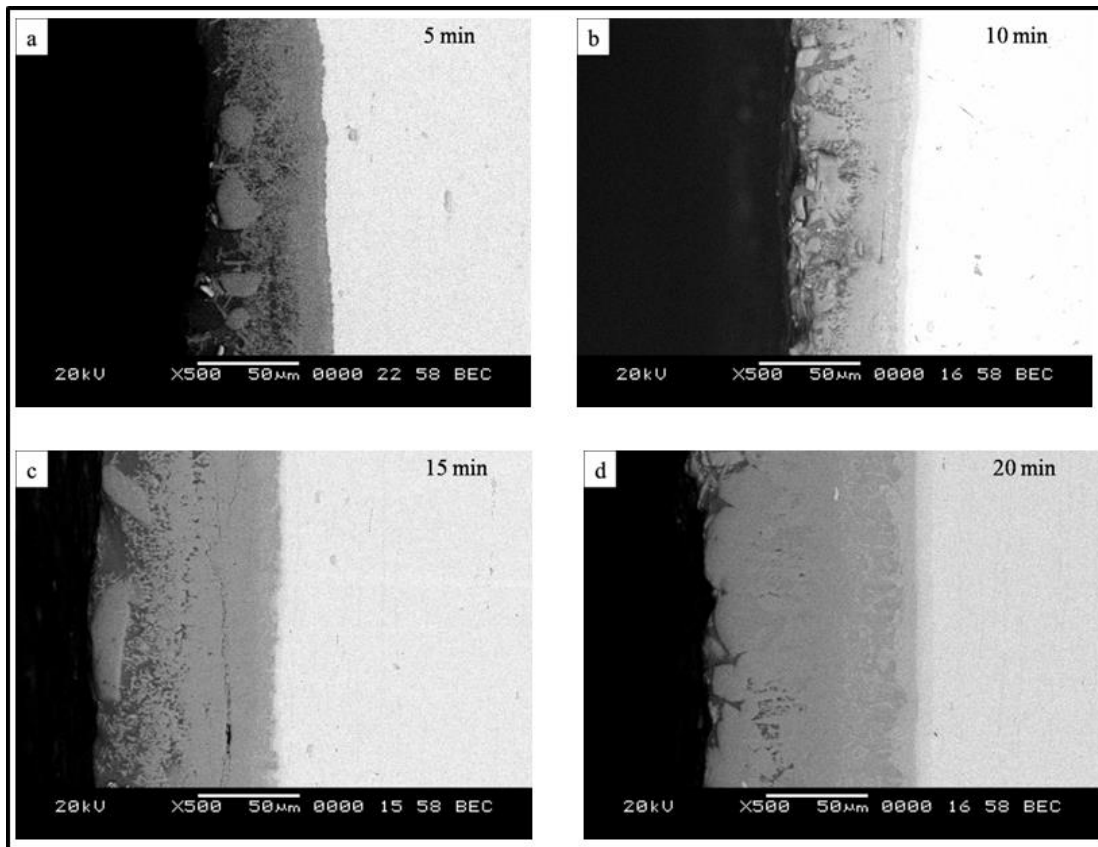
Fig. 6.23 SEM micrograph of diffusion treated samples at 900 °C for (a) 5 min, (b) 10 min, (c) 15 min, and (d) 20 min.

A layer with three phase mixture is observed at the interface for the duration of 5 minutes of diffusion. Adjacent to this layer the Fe_2Al_5 layer is seen growing towards Al side. Further, with an increase in diffusion time, growth of Fe_2Al_5 phase is observed. The growth of this phase is predominantly towards the topcoat side. The average

coating thickness increases from 70 μm for 5 min diffusion time to 110 μm for 20 minutes diffusion time. For 1-hour diffusion time, the Al topcoat is completely converted to Fe_2Al_5 phase. However, Kirkendall porosity is not observed during this transformation. It could be inferred that the growth of these intermetallic phases takes place predominantly by diffusion of the elements from the base metal side towards the Al side. After 1-hour diffusion time, coating consisted of 4 layers. The outermost layer is Fe_2Al_5 phase followed by a layer of mixed phases. Towards the base metal side, α-Fe layer followed by the disordered FeAl layer is observed.

6.4 Discussion

The microstructure before the diffusion treatment initially consisted of an aluminum topcoat and the aluminide layer at the interface. During the diffusion treatment, at 700 and 900 °C interdiffusion of elements are expected to occur, with increased diffusion kinetics at higher temperature. Aluminum from the topcoat diffuse towards the steel side and the elements Fe, Cr and Ni diffuse from the base metal side towards Al topcoat. Above 700 °C, the aluminum in the topcoat is expected to melt as the temperature is above the melting point of Al. The SEM microstructure shown in Fig. 6.3 and the TEM investigation shown in Fig. 6.4 reveals that the topcoat comprised of $Al_{13}Fe_4$ phase and Al. This is formed by diffusion of Fe from the base metal side into molten Al and precipitation of $Al_{13}Fe_4$ phase in molten Al due to supersaturation. It is known from the previous discussion (section 4.4, Chapter 4) that the elements Fe and Cr have limited solubility in molten Al. Diffusion of elements towards the Al side leads to supersaturation and nucleation of these intermetallic phases. The presence of $Al_{13}Fe_4$ phase predominantly in the topcoat depicts that Fe diffuses much faster compared to Cr and Ni. With an increase in diffusion time more of $Al_{13}Fe_4$ phase forms in the Al topcoat. With further diffusion of Fe atoms, a favorable condition for the transformation of $Al_{13}Fe_4$ phase to Fe_2Al_5 phase exists due to increase in Fe concentration as observed at 900 °C. A schematic representation of the sequence of phase transformation during the diffusion treatment at 900 °C is presented in Fig. 6.24. During this treatment, the growth of Fe_2Al_5 phase occurs by interdiffusion of atoms; mainly due to the outward diffusion of Fe atoms from the base metal side. The $Al_{13}Fe_4$ and the Al_7Cr phase initially present will tend to grow and also new phases nucleate with the diffusion of Fe and Cr

from base metal.
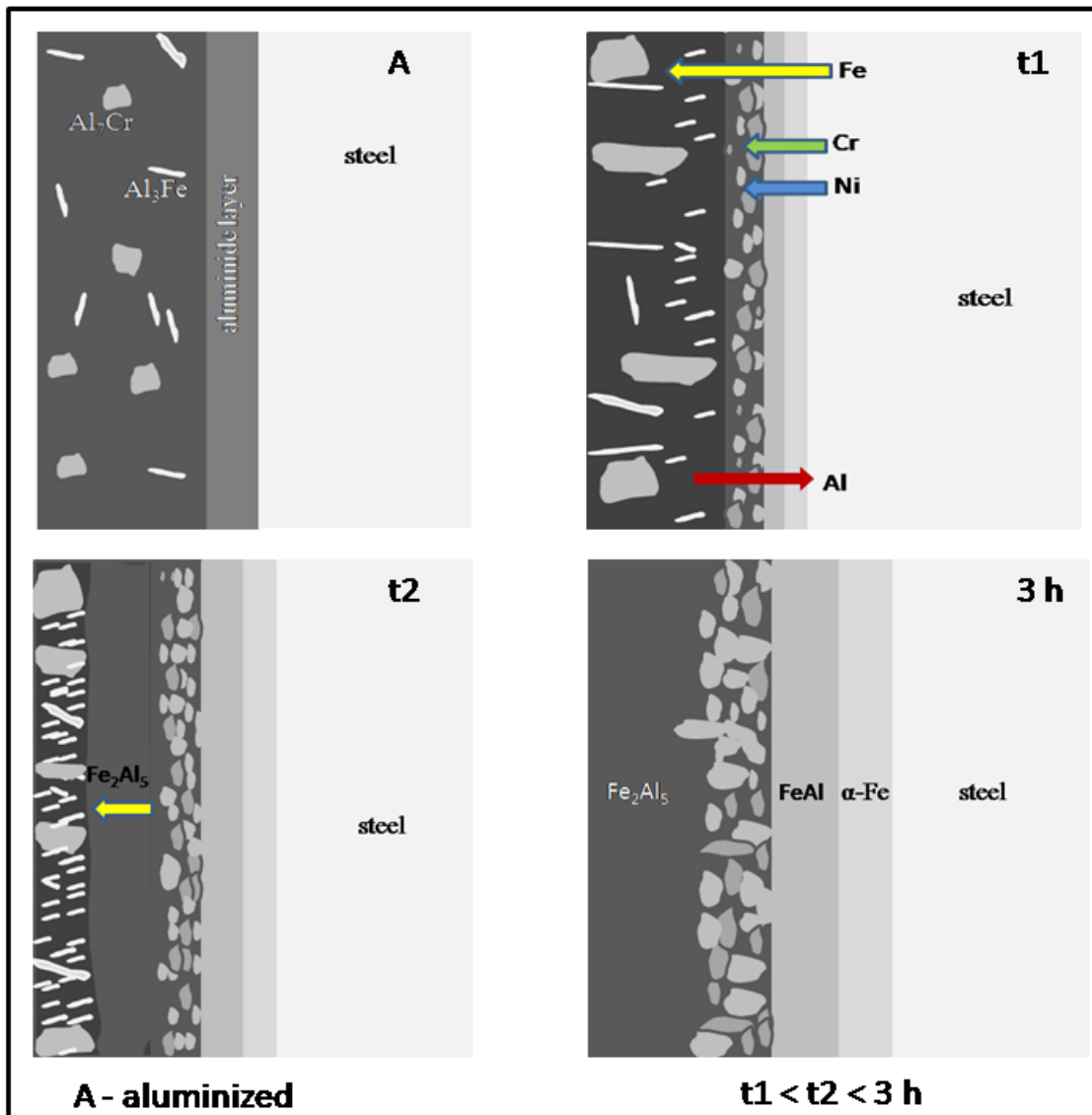
Fig. 6.24 Suggested schematic interpretation of the growth of various phases during interdiffusion treatment.

The austenite phase of the stainless steel transforms to ferrite (α-Fe) by the diffusion of Al atoms from the topcoat side to base metal side. It is known that Al in steel is a strong ferrite stabilizer, even when it has limited solubility in austenite as evidenced by equilibrium Al-Fe phase diagram (ASM Handbook 1992). Also, this transformation is assisted by the precipitation of NiAl phase. This leads to a reduction in the nickel content of austenite phase leading to more favourable condition for stabilization of the

ferrite phase. The solubility of nickel in α-Fe is also limited as revealed by equilibrium Fe-Ni phase diagram (ASM Handbook 1992). In addition, further inward diffusion of Al atoms along with the reduction in nickel content due to precipitation promotes the growth of α-Fe layer. The TEM-EDS elemental analysis carried out on these precipitates (Table 6.2) shows that close to 3 at. % Cr is dissolved, while the reported value of Cr solubility in the NiAl phase is up to 10 at. % at high temperatures (Tian et al. 1999). Further, More of chromium is observed to be present in the α-Fe layer, rather than to be dissolved in NiAl precipitates. The high density of dislocation which is discernible in the TEM micrograph shown in Fig. 6.22 (a) could be attributed to local strained region due to volume changes by interdiffusion of elements.
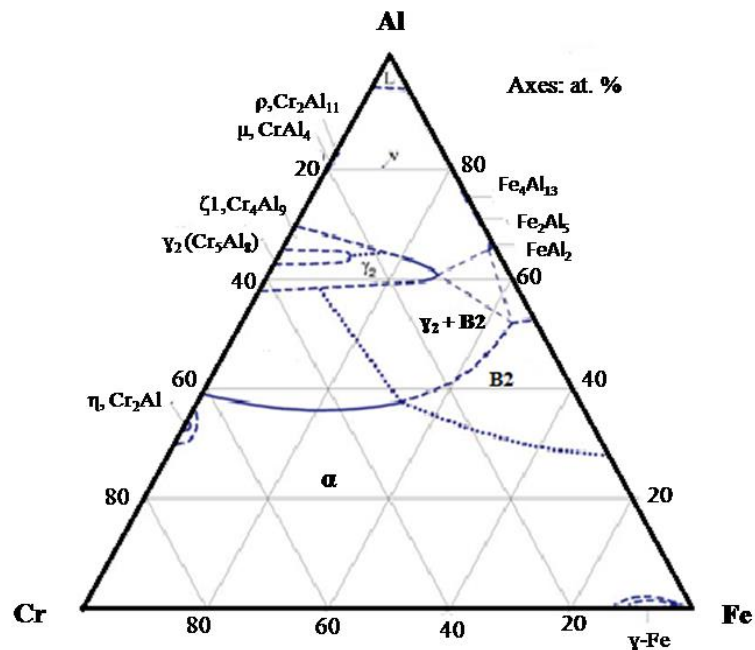
Fig. 6.25 Al-Cr-Fe isothermal section at 900 °C (redrawn from Effenberg and Ilyenko (2006))

The layer which is formed adjacent to the α-Fe layer is that of the disordered FeAl phase. The growth of this phase takes place by inward diffusion of Al atoms from the topcoat and outward diffusion of Fe atoms from the base metal through the α-Fe layer. On reading the equilibrium ternary phase diagram at 900 °C, as presented in Fig. 6.25, it could be expected that ordered B2 FeAl should co-exist with γ_2 (Cr_5Al_8) phase. However, the present TEM study could not specifically observe Cr_5Al_8 but could

observe a FeAl phase. The TEM-EDS analysis carried out on the disordered FeAl phase detects 10 at. % Cr and is 9 at.% Ni, while, the Ordered FeAl is reported to dissolve a large amount of chromium up to 30 at. %, and offers complete solubility for nickel (Effenberg and Ilyenko 2006; Budberg et al. 1991).

The phenomenon of disordering and associated lattice expansion of FeAl phase are reported to be happening during mechanical milling of ordered FeAl powders (Gialanella 1995; Peng and Collins 1997). In such cases, the order in the crystal is destroyed due to the high concentration of defects formed during mechanical milling. Defects such as V_{Fe} (vacancy on Fe sublattice), V_{Al} (vacancy on Al sublattice) Fe_{Al} (Fe atoms on Al site) and Al_{Fe} (Al atoms on Fe site) are reported to be responsible for disordering. Unlike the diffusion mechanisms in the metallic phases, the diffusion in ordered phases is rather more complex. The order is said to be retained by the special diffusion mechanism (Mehrer 1996). A random jump type of diffusion mechanism in FeAl would lead to the formation of vacancies and antisite defects causing disorder in the structure.

The phases present in the aluminide layer initially (before diffusion treatment) are Fe_2Al_5, Al_7Cr and Al. After diffusion treatment, the phases observed are Fe_2Al_5, simple cubic phase (Al57Fe27Cr16) and FeAl phase. The nanocrystalline Fe_2Al_5 phase present initially is expected to grow and form the Fe_2Al_5 grains in layer II. The formation of the intermetallic phase during the interdiffusion takes place in three steps; i) supersaturation of the parent phase ii) nucleation of the intermetallic phase in the parent phase and iii) subsequent growth of the nuclei by diffusion of atoms. The diffusion of elements like Fe, Cr, Ni from the base metal into the aluminum matrix causes supersaturation. The solubility of these elements in aluminum is low (ASM Handbook 1992). Further, the nucleation and growth of stable phase or a metastable phase take place based on the local diffusion fluxes. The formation of non-equilibrium or metastable phases during interdiffusion is due to kinetic constraints rather than thermodynamic reasons. The nucleation and growth of a phase is controlled by the flux of atoms in the interdiffusion zone. According to the theory of flux driven nucleation proposed by Paul and Divinski (2017), the probability for the growth of thermodynamically critical nuclei depends on the atom fluxes passing through the

nuclei and the neighbouring phases. The subcritical embryo starts to grow and the growth of thermodynamically stable nuclei may be arrested based on diffusion fluxes. The disordered FeAl phase observed in this investigation might be kinetically more favoured than B2 ordered FeAl.

The new phase (Al57Fe27Cr16) with a primitive cubic crystal structure is reported in the present investigation. This phase possesses higher chromium concentration compared to that of disordered FeAl phase. The Fe and Al concentrations are similar to that of disordered FeAl phase. The nickel content observed is almost nil in this phase. However, the equilibrium phase diagrams do not present any such phase with a simple cubic structure. During the studies on aperiodic crystals, cubic phases with large lattice parameters are formed as approximant phase to icosahedral quasicrystals (Quivy et al. 1996; Sugiyama et al. 2000; Taylor et al. 2006). Also, The arrangement of atoms in the crystal structure of $Al_{13}Fe_4$ and Al_7Cr exhibit quasicrystalline symmetry (Barbier and Tamura 1993; He et al. 2006; Kriener 1995). It is possible that during interdiffusion, Al_7Cr phase could transform to a simple cubic approximant. Also, this phase shares a cube on cube crystallographic orientation relationship with disordered FeAl phase. The metastable approximant phases reported in the previous chapters are also closely related structures to quasicrystalline phase. These phases may have a role to play in the formation of the simple cubic structure during interdiffusion.

Page intentionally left blank

CHAPTER 7

HOT-CORROSION AND CYCLIC OXIDATION STUDIES OF ALUMINIZED AISI 321 STAINLESS STEEL

This chapter deals with details of cyclic hot corrosion test and cyclic oxidation test of aluminized 321 steel and the results are compared with the uncoated one. Hot-corrosion and cyclic oxidation tests were carried out by thermogravimetric analysis. The results are presented and discussed below.

7.1 Cyclic Hot-corrosion

Cyclic hot-corrosion studies were carried out using a salt mixture of 60% V_2O_5 + 40% Na_2SO_4 at 700 °C. The cycle parameters are heating for 1 hour at 700 °C and cooling for 20 minutes. The details regarding the experimental procedure are mentioned in chapter 3. Fig. 7.1 shows the results of hot corrosion behaviour of base metal (uncoated) and aluminized sample (coated) in the molten salt mixture at 700 °C. It shows a profile of cumulative weight gain vs the number of cycles. The cumulative weight gain for the uncoated sample was highest as compared to the coated sample. The weight gain measured for the uncoated sample at the end of 50 cycles is 5.87 mg/cm^2, and that of the aluminized sample is 2.3 mg/cm^2. By plotting square of specific weight gain with time, the hot corrosion rate constant was evaluated (Sidhu et al. 2006) and that plot is shown in Fig.7.2. The parabolic rate constant K_p (in 10^{-10} g^2 cm^{-4} s^{-1}) evaluated for the uncoated sample is 2.02 while, that for the coated sample is 0.14 respectively. The oxide growth rate observed in the case of the uncoated sample is significantly higher than that of aluminized one. Surface characterization on the uncoated samples by X-ray diffraction shows the formation of chromia scales, and it is shown in Fig. 7.3. Figure 7.4 presents SEM micrographs of the oxide scales formed after hot corrosion for 50 cycles on the uncoated sample. Spallation of the oxide scales in such samples is also observed as seen in Fig.7.4 (c) and also evident from the change in the slope observed in Fig. 7.1
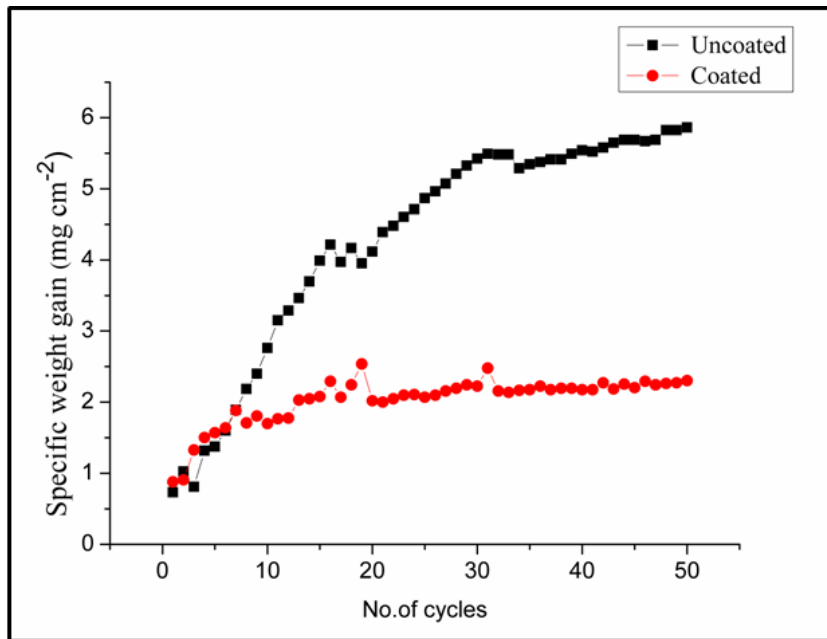
Fig. 7.1 Plot of specific weight gain vs. number of cycles for the coated and uncoated samples subjected to hot corrosion.
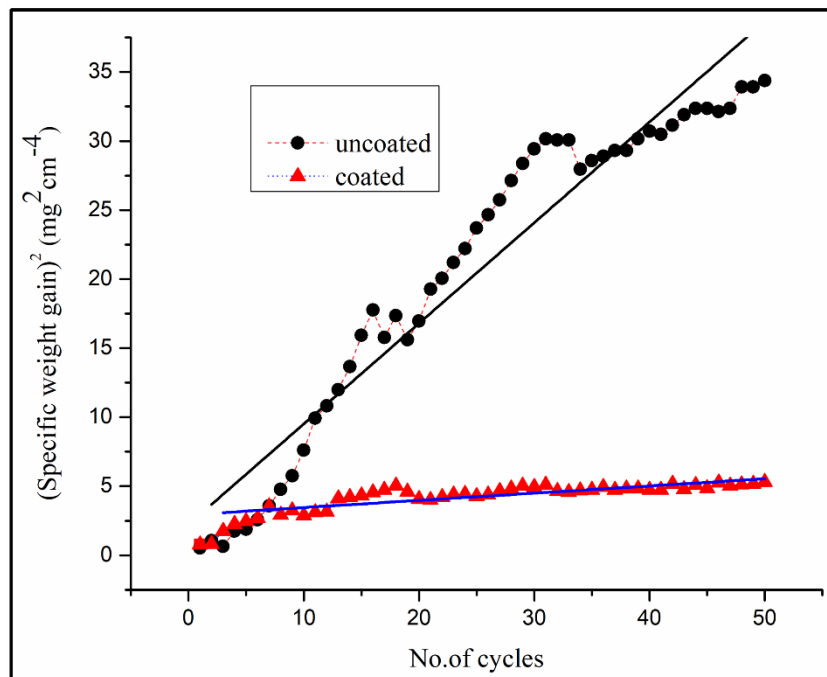
Fig. 7.2 Plot of square of specific weight gain vs. number of cycles.
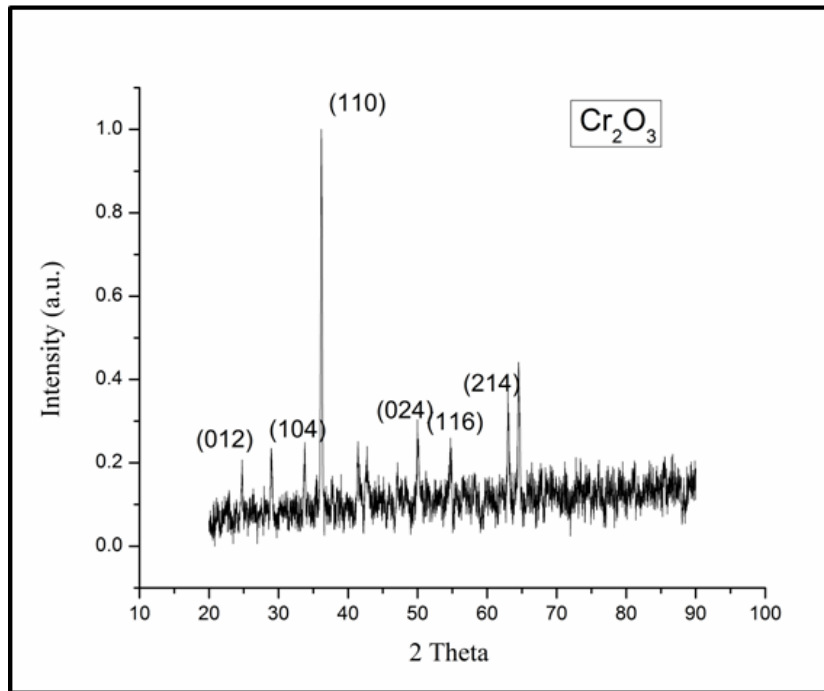
Fig. 7.3 XRD pattern of the uncoated sample subjected to hot corrosion.
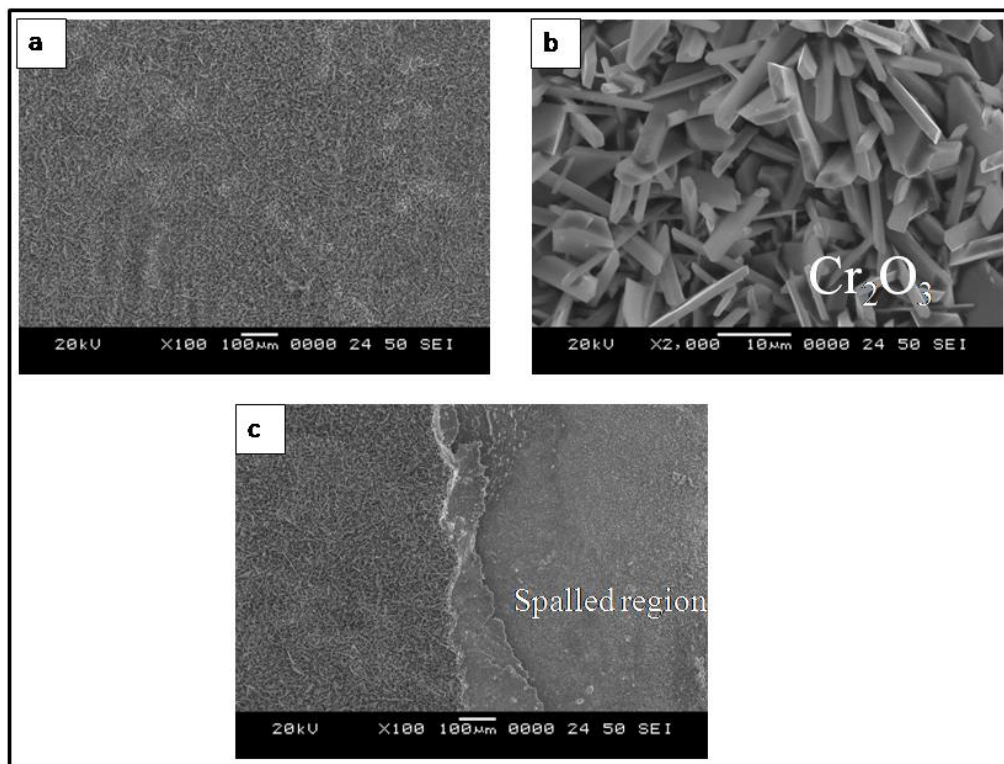
Fig. 7.4 (a) SEM micrograph of the uncoated sample after hot corrosion, (b) high magnification micrograph showing Cr_2O_3 scales, and (c) oxide scale spallation

The growth of the chromium oxide scales is also observed under cross-section SEM micrograph shown in Fig. 7.5
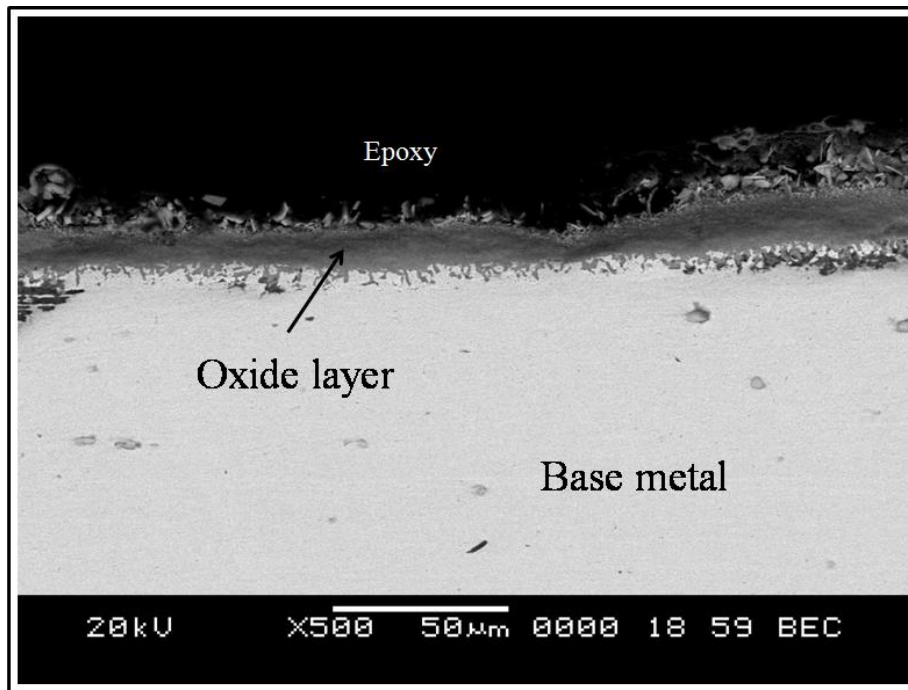
Fig. 7.5 Cross-sectional SEM-BSE micrograph of the uncoated sample showing the formation of the oxide scales after subjecting to hot corrosion test.

Figure 7.6 shows the top surface of the aluminized sample after hot corrosion test. The surface is covered with oxide scale and molten salt deposits. The oxide scales showed two different morphologies and could be theta and alpha-type oxides (Prasanna et al. 1996). Figure 7.7 shows the XRD pattern of the aluminized sample after hot corrosion test. The presence of salt deposit such as V_2O_5, Na_2O, and Na_2S along with Al_2O_3 is observed. Figure 7.8 shows cross-sectional SEM micrograph of the aluminized sample after hot corrosion test. The aluminide coating is uniform with thickness is close to 280 μm. Cracking and spalling of the aluminide coating is not specifically observed. Figure 7.9 shows high magnification micrograph of that presented in Fig.7.8. The formation of an oxide layer on top of the aluminide layer is seen. Figure 7.10 shows point EDS spectrum on the oxide scale, which shows the presence of the molten salt deposit.
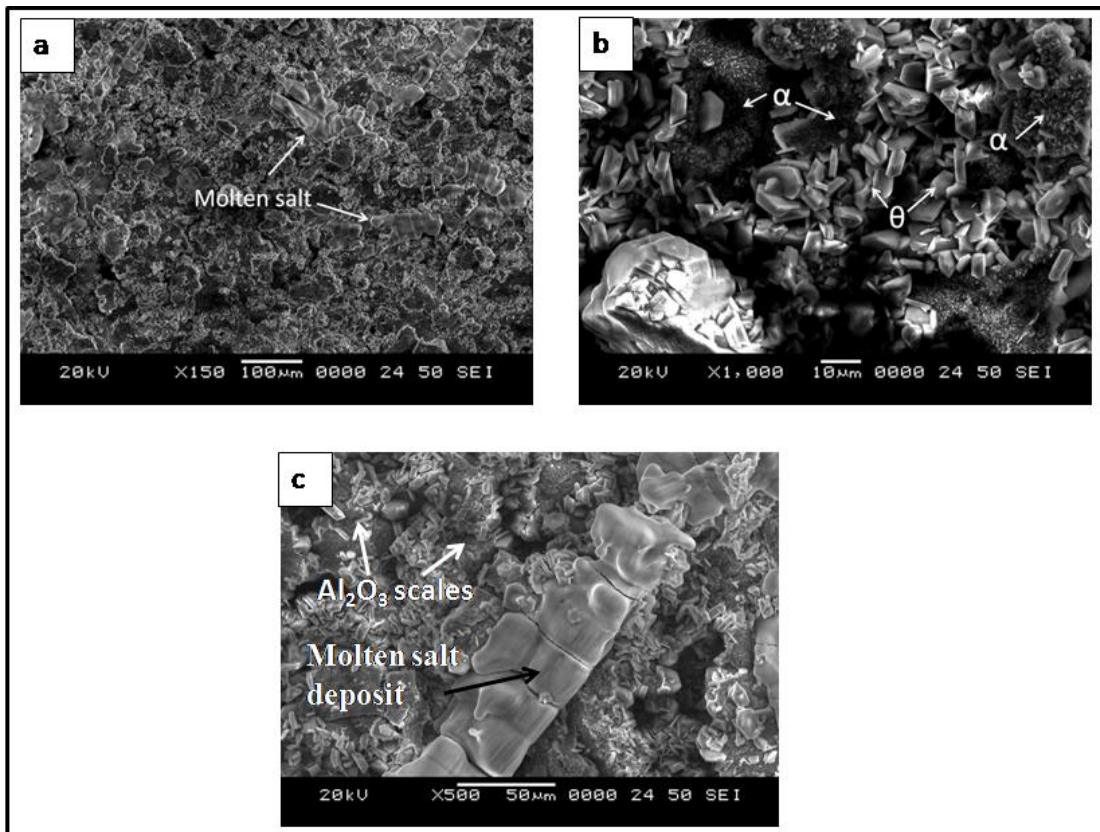
Fig. 7.6 (a) low magnification SEM micrograph of the top surface of the aluminized sample subjected to hot corrosion (b) high magnification micrograph showing mixed θ + α alumina scales (c) presence of the molten salt deposits along with Al_2O_3 scales.
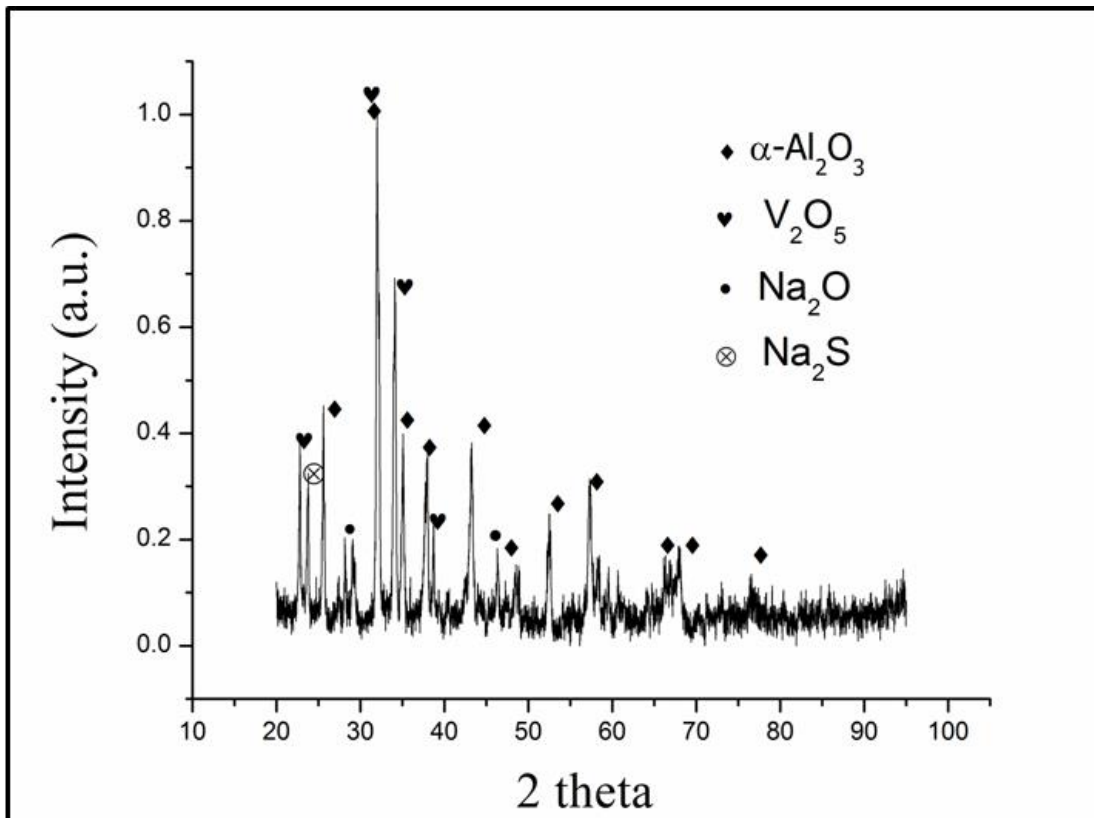
Fig. 7.7 XRD pattern of the coated sample subjected to hot corrosion.
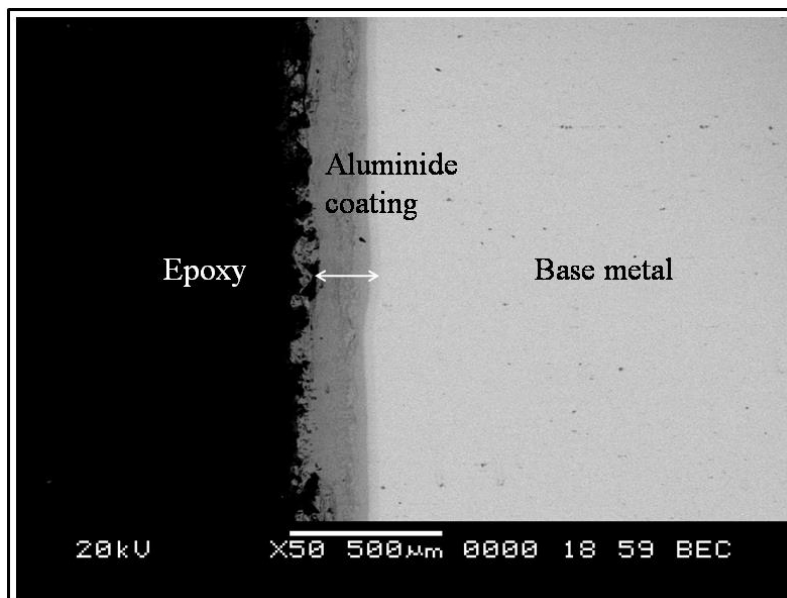
Fig. 7.8 Cross-sectional SEM-BSE micrograph of the coated sample showing uniform aluminide layer.
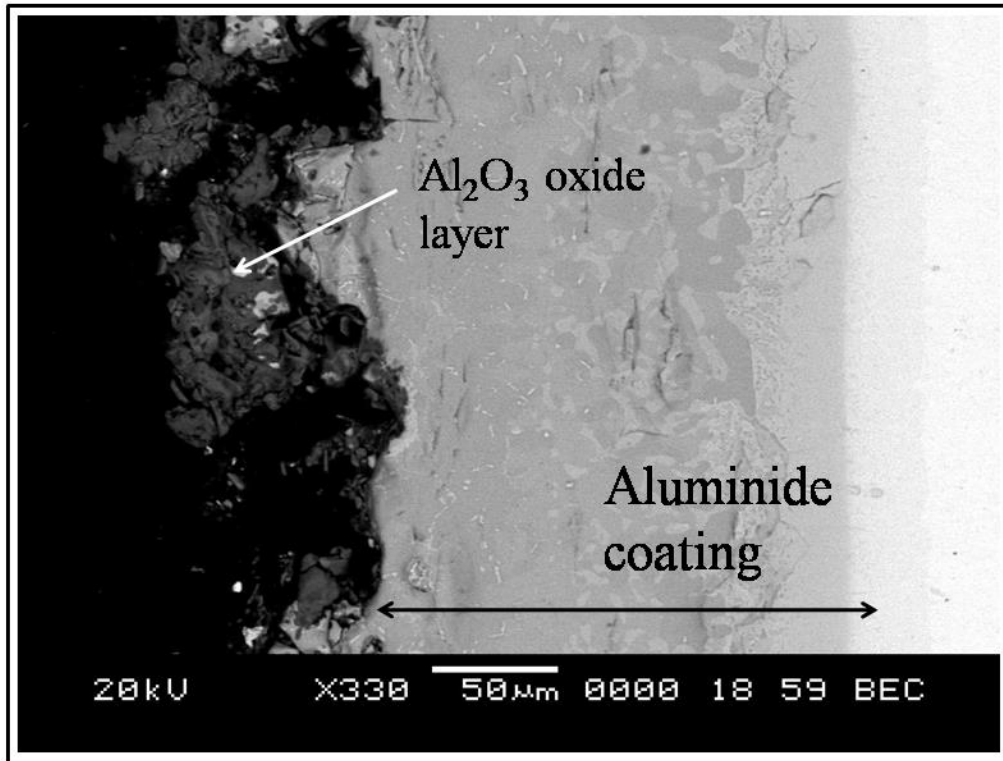
Fig. 7.9 Higher magnification SEM-BSE micrograph showing grown alumina scale grown on the aluminide layer.
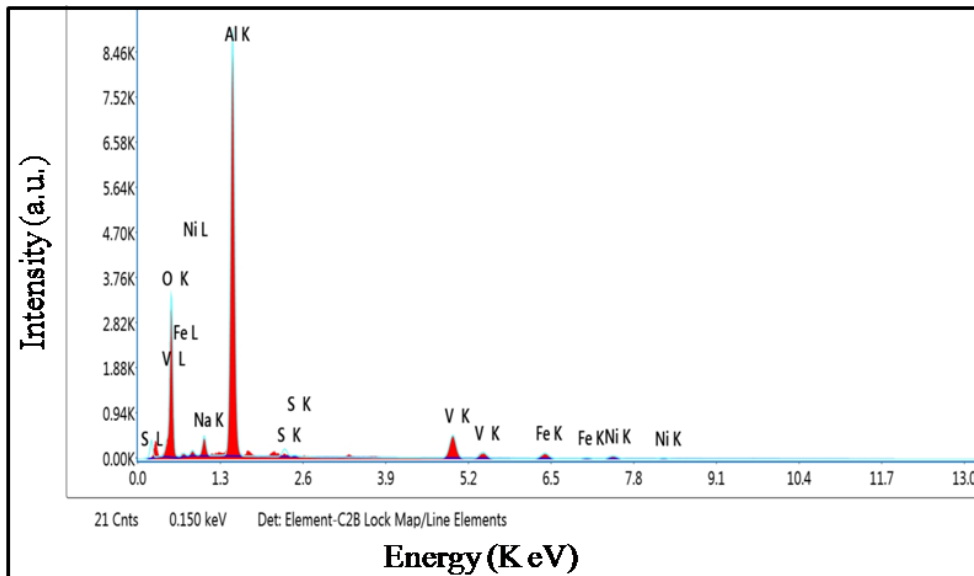
Fig. 7.10 Point EDS spectrum corresponding the outer oxide layer taken using SEM. Small amount of vanadium and sulphur corresponding to molten salt deposit are present.

7.2 Cyclic Oxidation

The cyclic oxidation test was carried out on aluminized and uncoated (base metal) samples at 900 °C in an open atmosphere for 50 number of cycles. The samples were heated for 1 hour at 900 °C and then cooled to room temperature for 20 minutes. Figure 7.11 shows a plot of specific weight gain vs the number of cycles for the aluminized and uncoated sample.
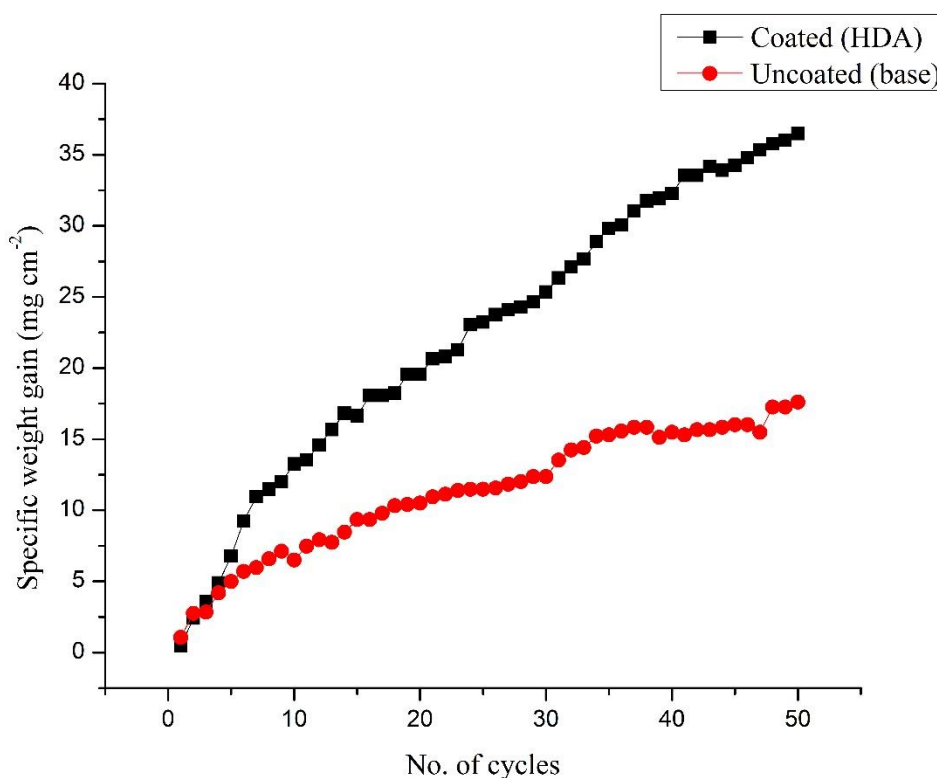
Fig. 7.11 Plot of specific weight gain vs the number of cycles

The aluminized sample showed the highest weight gain compared to the uncoated sample. Fig. 7.12 shows the surface oxide scales formed on the uncoated sample. The oxide scale formed is uniform and compact. Fig.7.13 shows higher magnification micrograph showing two types of oxide morphology; one with the pyramid type morphology and the other with plate type morphology.
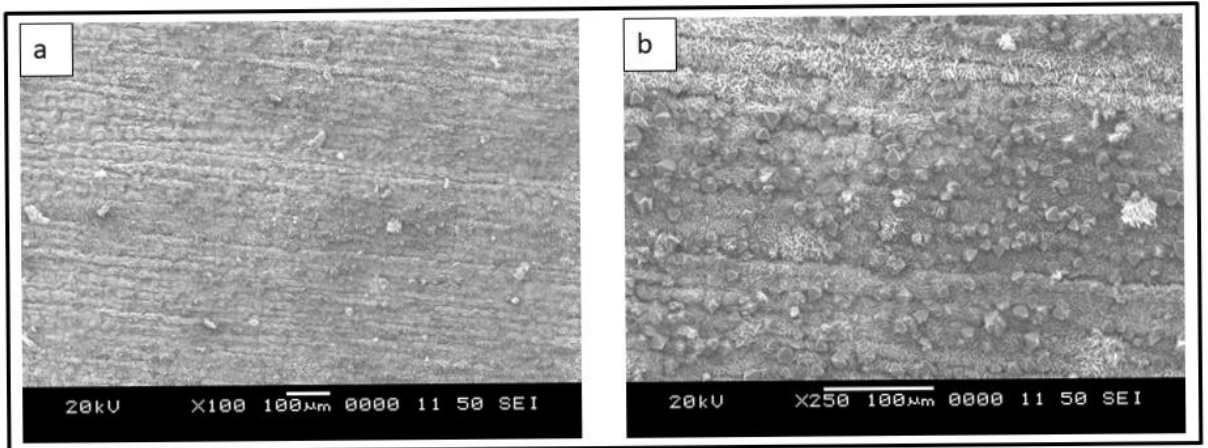
Fig. 7.12 (a) and (b) SEM micrograph of the oxide scales formed on the surface of the uncoated sample after cyclic oxidation tests at 900 °C for 50 cycles
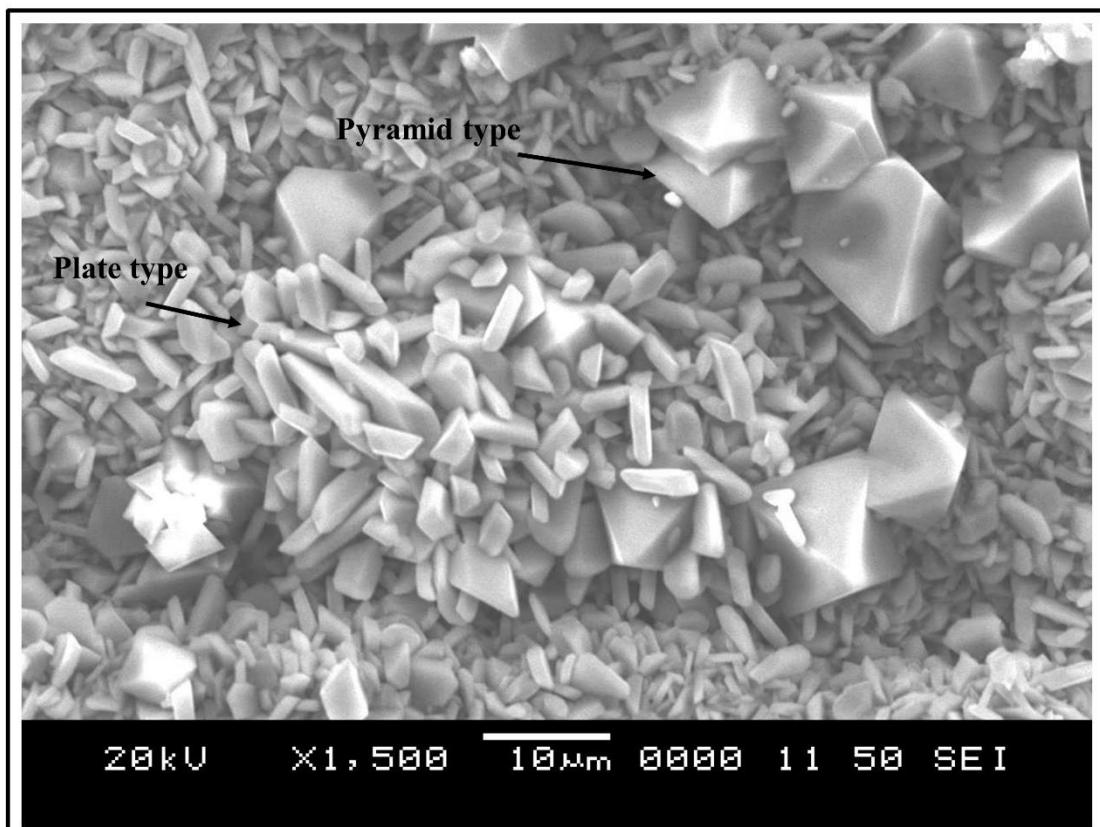
Fig. 7.13 High magnification SEM micrograph showing two types of oxide morphology; pyramid type and plate type morphology.
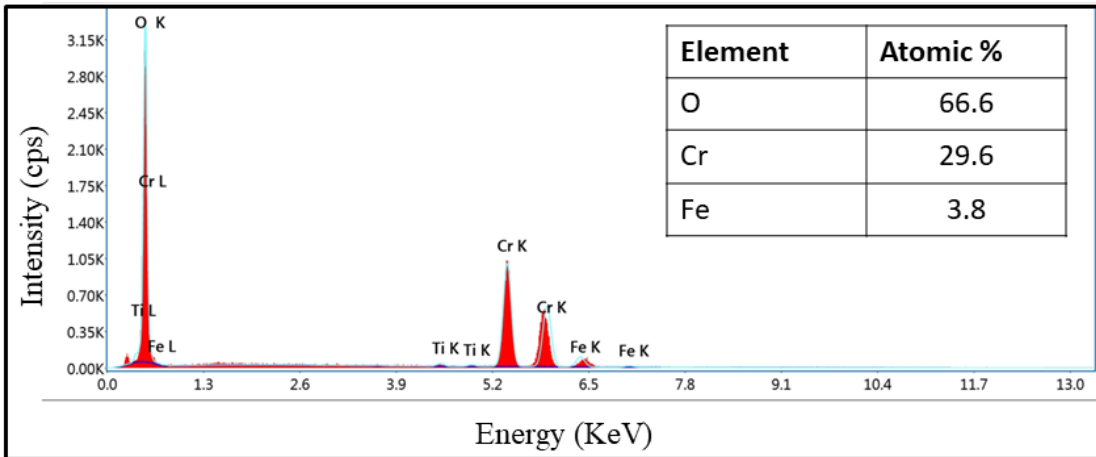
Fig. 7.14 SEM-EDS spectrum corresponding to the oxide scale with pyramid morphology.

The SEM-EDS analysis on the pyramid type of oxide scale is presented in Fig. 7.14. The composition comes close to that of the Cr_2O_3 type oxide phase. The SEM-EDS analysis on the plate type of the oxide is presented in Fig. 7.15. The composition observed is in close agreement to the CrO type of the oxide phase.
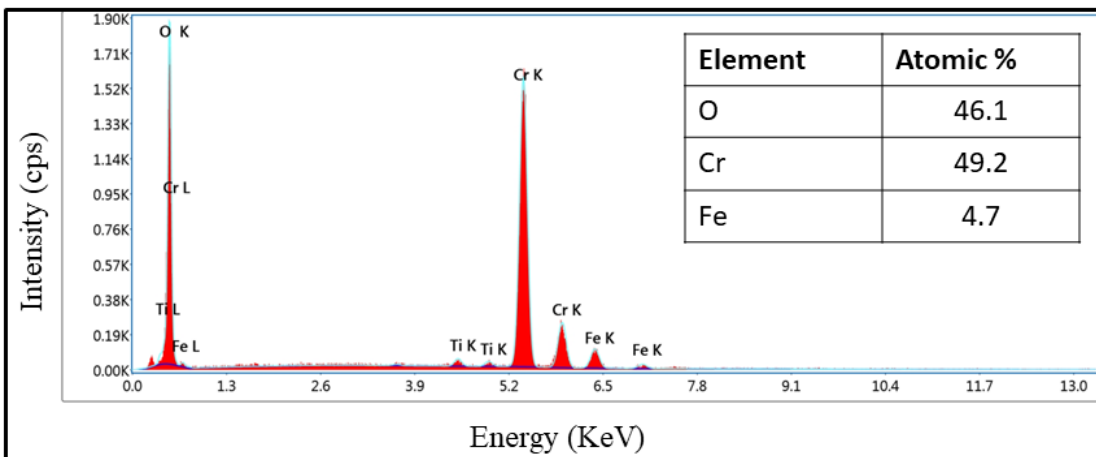
Fig. 7.15 SEM-EDS spectrum corresponding to the oxide scale with plate morphology.

The oxide scales observed on the aluminized sample is shown in Fig. 7.16. The scales observed are discontinues with spallation, cracks, and large quantity of pores.
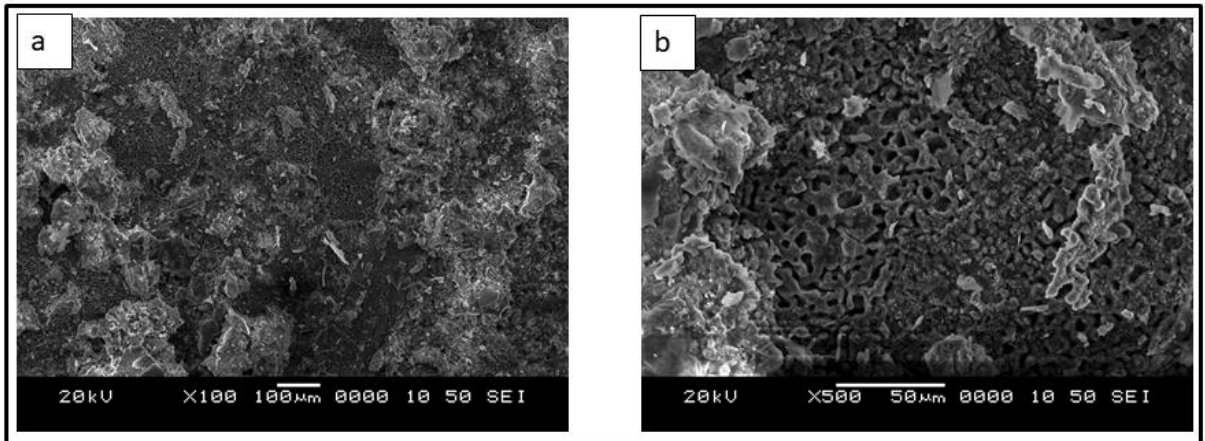
Fig. 7.16 SEM micrographs of the oxide scales formed on the aluminized sample subjected to cyclic oxidation test at 900 ℃.
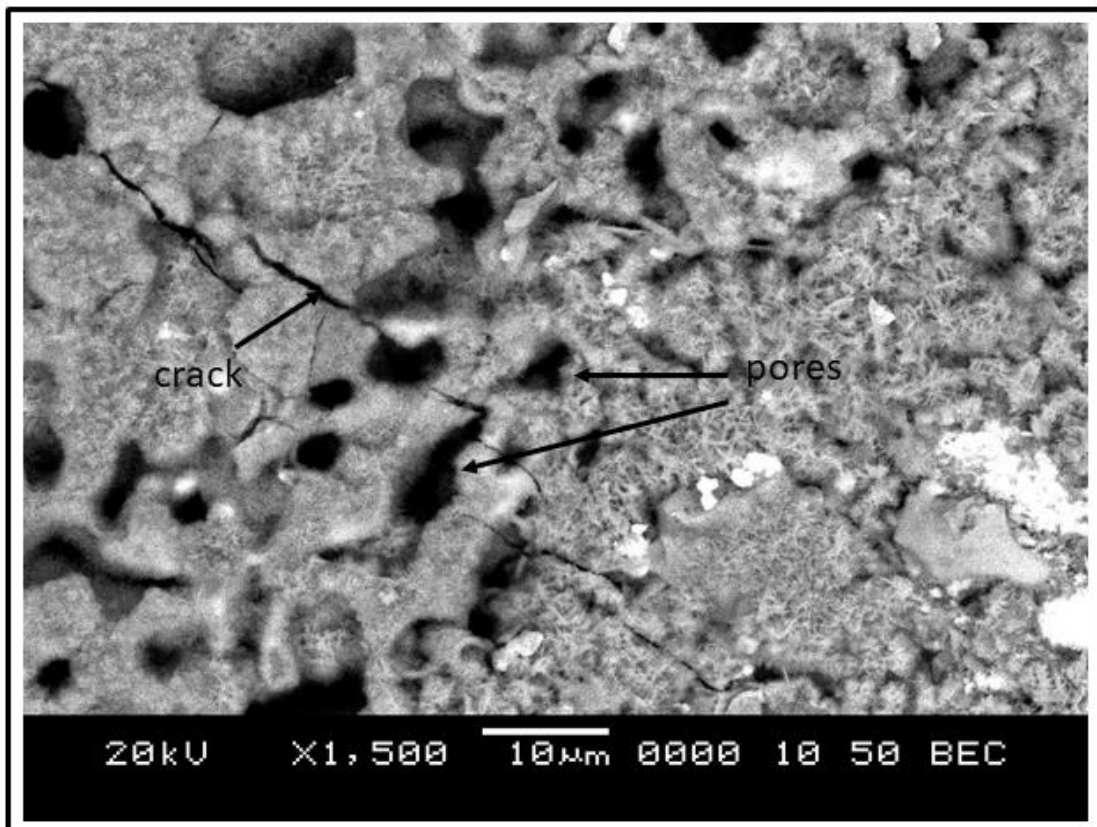
Fig. 7.17 SEM micrograph of the oxide scale formed on the aluminized sample. Pores and cracks are observed on the oxide scale.

7.3 Discussion

Hot corrosion is defined as the accelerated oxidation of materials induced by thin film of fused salt at elevated temperatures (Rapp and Zhang 1994). Low-grade petroleum fuels used for power generation generally contain impurities like vanadium, sulphur and sodium. During combustion, they form molten sulphates, vanadates, chlorides, carbonates causing severe material degradation. The mixture of V_2O_5 and Na_2SO_4 in the ratio (60:40) forms a low melting eutectic at 550 °C (Yugeswaran et al. 2012) and accelerates the hot corrosion attack. The severity of the attack depends on the composition of the salt deposit, the temperature of the gas, thermal cycle, and the alloy composition and microstructure (Rapp and Zhang 1994). The mechanism of hot corrosion attack takes place in two stages: initiation stage and the propagation stage. The initiation stage starts once the alloy surface is partially or fully wetted by the salt. In the present test condition, the salt applied is in the molten state and expected to wet the surface completely at the test temperature. During the initiation stage, the composition of the base metal and the salt deposit gets altered (to make the alloy susceptible for rapid attack). This takes place by the movement of species from the base metal to the salt deposit and vice a versa. This includes diffusion of the elements like Al and Cr (which forms protective oxides) towards the salt deposit, incorporation of the elements from the salt deposit (like sulphur) into the base metal, dissolution of oxide into molten salt deposit and development of defects such as cracks and pores in the oxide scale. Finally, this leads to penetration of the liquid salt to penetrate through the oxide scale and spread along the base metal-oxide interface leading to degradation process to the next stage of rapid corrosion attack (Birks et al. 2006).

The reactions taking place during the hot-corrosion are written as follows (Birks et al. 2006)

$$Na_2SO_4 + V_2O_5 = 2NaVO_3 + SO_3 \tag{1}$$

$$Al_2O_3 + 2NaVO_3 = 2Al(VO_4) + Na_2O \tag{2}$$

$$Al_2O_3 + V_2O_5 = 2Al(VO_4) \qquad\qquad (3)$$

Further, Al_2O_3 oxide scale could be dissolved by the reaction with vanadate ions

$$Al_2O_3 + VO_3^- = 2Al^{3+} + 3VO_4^{3-} \qquad\qquad (4)$$

The coated sample shows the presence of the salt deposits such as V_2O_5, Na_2O, Na_2S along with with Al_2O_3 the result of which is based on the X-ray diffraction analysis as shown in Fig. 7.7. The alumina scales possess low oxygen diffusion rate (Ma et al. 2012) and the Al_2O_3 is deposited on YSZ (yittria stabilized Zirconia) showed improved resistance to hot-corrosion (Wang et al. 2016). The formation of spinel oxides also reduces the oxygen diffusion rate (Zhu et al. 2013) but no such spinel oxide is observed in the present study.

Acidic dissolution of chromium oxide takes place by the reaction (Sidhu et al. 2006; Hwang and Rapp 1989)

$$\tfrac{1}{2}\,Cr_2O_3 + 3/2\,Na_2SO_4 = Cr_2(SO_4)_3 + 3/2\,Na_2O \qquad\qquad (5)$$
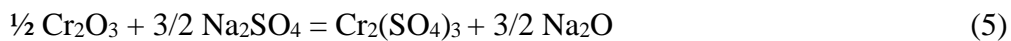
The disruption of Cr_2O_3 scales by reaction with the salt and formation of corrosion products further induces stress in the oxide film causing defects and cracks. This further leads to infiltration of the molten salts causing further damage which is also assisted by thermal stress. The dissolution of Cr_2O_3 scales into salt and subsequent spallation of deposit leads to the rapid oxidation of the base metal. After initial exposure, the increased spallation of oxide scales leads to propagation stage. On the other hand oxide scales formed on the aluminized sample were not dissolved in the molten salt. Presence of salt deposit was also seen. The alumina scales formed on the coated samples were adherent with minimum spallation. Therefore, aluminized steel showed improved resistance to hot-corrosion compared to the base steel.

The cyclic oxidation studies showed that the base steel formed dense compact oxide scales with two types of morphology. The oxide scales were adherent with minimum spallation. The oxide scales formed on the aluminized steel showed spallation with cracks and pores shown in Fig. 7.17. These defects act as an easy diffusion path for oxygen, thereby, increasing the kinetics of oxidation. These defects could be formed due to the difference in the coefficient of thermal expansion between the coating and

the substrate. A dense and complete oxide could not be formed after the test for 50 cycles. It is reported that chromium present in the bulk of Fe-Al alloys helps in the formation of α-Al_2O_3 (Tortorelli and DeVan 1992). Addition of 2-5% wt.% Cr to Fe_3Al alloys showed improved long term oxidation performance (Pint et al. 1999). Also, The the presence of chromium in the alloy reduces this critical aluminum concentration required to form continuous alumina scale (Tomaszevicz and Wallwork 1984; Tortorelli and DeVan 1992). With an increase in diffusion time (increase in the number of test cycles) it could be expected that more chromium diffuses towards the surface and provide assistance for the formation of compact alumina scales. The response of the aluminized samples after longer durations will be studied in the future investigations.

CHAPTER 8

CONCLUSIONS

In the present work, solid-liquid interaction of AISI 321 steel with molten aluminum was carried out by hot-dip aluminizing. The microstructure at the interface was investigated by scanning and transmission electron microscopy. The mechanism of the formation of microstructural features was compared with Fe/Al and SS 430/Al systems. Based on the experimental results and discussion presented, the following conclusions are drawn

- Two phases $Al_{13}Fe_4$ and Fe_2Al_5 are identified in the aluminide layer of Fe/Al system and AISI 430 SS/Al system. The $Al_{13}Fe_4$ phase in the AISI 430 SS/Al system possesses a twinned morphology with twinning around (100) plane.

- The growth kinetics of the intermetallic layer was parabolic one for Fe/Al and AISI 430 SS/Al system. AISI 430 SS/Al showed a lower growth rate compared to Fe/Al system.

- Chromium present in the AISI 430 stainless steel influenced the thickness and growth kinetics of the intermetallic layer, while, Cr in the Al bath had no influence on morphology and growth kinetics of the intermetallic layer.

- The mechanism of the formation of microstructure at the interface for Fe/Al system and AISI 430 SS/Al system is the reaction-diffusion, while, for the case of AISI 321 SS/Al it is dissolution-nucleation; a new mechanism proposed in the present study.

- In the AISI 321/Al system, metastable microstructures formed during short interaction time are identified as $FeAl_m$, multiple twinned $Al_{13}Fe_4$ and $Al_3(NiFe)$. The $Al_3(NiFe)$ shows a crystallographic orientation relationship with the Al.

- Nanostructured intermetallic phases of Al_7Cr and Fe_2Al_5 are formed in the aluminide layer during long interaction time of 10 minutes.

- Crystalline approximants closely related to decagonal quasicrystals are observed. O_E type ternary Al-Fe-Cr orthorhombic approximant is identified. Commensurate ordered phases with ordering along [100] directions are formed. Two variants, a five layered and eight layered ordered phases are approximants to a 1-D quasicrystal.

- After the diffusion treatment, the microstructure of the hot-dip aluminized steel transforms into a layered structure. Four layers are formed in which Fe_2Al_5 phase forms as the outermost layer. The other layers are; the layer of mixed phases, disordered FeAl and α-Fe.

- A new phase (Al57Fe27Cr16) possessing a simple cubic structure with a lattice parameter of 7.2 Å is observed in the layer of mixed phases. This phase shares a cube on cube crystallographic orientation relationship with the disordered FeAl phase.

- The aluminized steel showed improved hot-corrosion resistance under the salt mixture of 60% V_2O_5 + 40% Na_2SO_4 at 700 °C. The formation of adherent Al_2O_3 scales on the coated sample provided increased resistance to hot corrosion.

- Cyclic oxidation resistance in atmospheric air at 900 °C of the aluminized sample was poor compared to the uncoated sample. It is because, the oxide scales in case of the uncoated sample was continuous and adherent, while, the oxide scales on the aluminized samples were discontinuous and showed cracking and spalling.

Scope for further studies

In the present study, hot-dip aluminizing of AISI 321 stainless steel is carried out and the formation of microstructural features was studied by transmission electron microscopy. The study revealed dissolution-nucleation as the dominant mechanism in case of AISI 321 SS/Al system while reaction-diffusion was the dominant mechanism in case of the other two systems. The study also identified a few metastable and quasicrystalline approximant phases. Based on these findings, further studies can be focused on

o To explore the possibility of other metastable or approximant phases by varying processing conditions like the temperature of molten Al bath.

o To study the cyclic oxidation behaviour of the aluminized sample subjected to longer durations i.e. for more than 100 cycles

o The intermetallic phases formed generally possess high hardness. Therefore, wear behaviour of the coated sample could be studied.

o The issue in fusion welding of steel to aluminum is the thickness of the intermetallic layer formed at the interface. A layer thickness, greater than critical thickness is detrimental to mechanical integrity. It is observed from the present investigation that the thickness of the intermetallic layer in case of AISI 321 SS/Al system is in the range of 10-15 µm and does not seem to vary with dipping duration. In this regard, the fusion welding of AISI 321stainless steel to Al can be explored and the concept of dissolution-nucleation mechanism could be utilized to minimize the intermetallic layer thickness.

REFERENCES

Abdolahi, B., Shahverdi, H. R., Torkamany, M. J., and Emami, M. (2011). "Improvement of the corrosion behavior of low carbon steel by laser surface alloying." *Appl. Surf. Sci.*, 257(23), 9921–9924.

Akdeniz,V., Mekhrabov, A. O. and Turgay, Y. (1994). "The role of silicon addition on the interfacial interaction in Fe-Al diffusion layer." *Scr. Metall. Mater.*, 31(12), 1723-1728.

Allen, C. M., O'Reilly, K. A. Q., Cantor, B., and Evans, P. V. (1998). "Intermetallic phase selection in 1XXX Al alloys." *Prog. Mater. Sci.*, 43(2), 89–170.

Ashby, M. F. (2005). Materials Selection in Mechanical Design., Burlington: Butterworth-Heinemann.

ASM Handbook, (1992). "Alloy Phase Diagrams", 3, *ASM International.*

ASM Handbook, (1994). "Surface Engineering", 5, *ASM International*.

Awan, G. H. and Hasan, Ul. F. (2008). "The morphology of coating/substrate interface in hot-dip-aluminized steels." *Mater. Sci. Eng.*, A 472(1–2), 157–165.

Barbier, J.-N., Tamura, N., Verger-Gaugry, J.-L. (1993). "Monoclinic Al13Fe 4 approximant phase : a link between icosahedral and decagonal phases." *J. Non. Cryst. Solids*, 154, 126–131.

Barnes, T., and Pashby, I. (2000). "Joining techniques for aluminium spaceframes used in automobiles: Part I — solid and liquid phase welding." *J. Mater. Process. Technol.*, 99(1–3), 62–71.

Bhat, K.U. (2015). "Mild Steel Plates : Aluminizing." *Encycl. Iron, Steel, Their Alloy.*, 2274–2283.

Bhat, K.U., Huilgol, P. and Jithin, J. (2013). "Aluminising of Mild steel plates." *ISRN Metallurgy*, 2013, 6.

Bindumadhavan, P.N., Makesh, S., Gowrishankar, N., Heng Keng Wah, and Prabhaker, O. (2000). "Aluminising and subsequent nitriding of plain carbon steels for piston ring applications." *Surf. Coat. Technol.*, 127, 252-259.

Birks, N., Meier, G. H., and Petit, F. S. (2006). Introduction to the high temperature oxidation of metals. *Cambridge Univ. Press*, United Kingdom.

Bouayad, A., Gerometta, C., Belkebir, A. and Ambari, A. (2003). "Kinetic interactions between solid iron and molten aluminium." *Mater. Sci. Eng.*, *A* 363(1–2), 53–61.

Bouché, K., Barbier, F., and Coulet, A. (1998). "Intermetallic compound layer growth between solid iron and molten aluminium." *Mater. Sci. Eng. A*, 249(1–2), 167–175.

Budberg, P., Prince, A., Cacciamani, G., Ferro, R., Grushko, B., Perrot, P., and Schmid-fetzer, R. (1991). "Aluminium–iron–nickel. Ternary Alloys." *VCH, Weinheim,* 1, 309–323.

Cantor, B., and Chadwick, G. A. (1974). "Growth Crystallography of Unidirectionally Solidified Al-Al3Ni Eutectic." *J. Cryst. Growth*, 23, 12–20.

Cao, W., Ge, S., Song, J., and Luo, D. (2016). "deuterium permeation barrier by hot-dipping aluminizing on AISI321 steel." *Int. J. Hydrogen Energy*, 41(48), 23125–23131.

Celil, A., Ahravci and Pekguleryuz, M. O. (1998). "Calculation of phase diagrams for the metastable Al-Fe phases forming in direct-chill (DC) – cast aluminium alloy ingots." *Calphad*, 22(2), 147-155.

Chatterjee, S., and Abinandanan, T. A. (2008). "Phase-Field Simulation of Fusion Interface Events during Solidification of Dissimilar Welds : Effect of Composition Inhomogeneity." *Metall. Mater. Trans. A*, 39 A, 1638.

Chattopadhyay, K., Lele, S., Thangaraj, N., and Ranganathan, S. (1987). "Vacancy Ordered Phases and One-Dimensiqnal Quasiperiodicity." *Acta Metall.*, 35(3), 727–733.

Chen, S., Yang, D., Yang, J., Huang, J., and Zhao, X. (2018). "Nanoscale structures of the interfacial reaction layers between molten aluminium and solid steel based on thermophysical simulations." *J. Alloys Compd.*, 739, 184–189.

Chen, S., Yang, D., Zhang, M., Huang, J., and Zhao, X. (2016). "Interaction Between the Growth and Dissolution of Intermetallic Compounds in the Interfacial Reaction Between Solid Iron and Liquid Aluminum." *Metall. Mater. Trans. A*, 47(10), 5088–5100.

Cheng, W. J., and Wang, C. J. (2009). "Growth of intermetallic layer in the aluminide mild steel during hot-dipping." *Surf. Coatings Technol.*, 204(6–7), 824–828.

Cheng, W. J., and Wang, C. J. (2011). "Effect of silicon on the formation of intermetallic phases in aluminide coating on mild steel." *Intermetallics*, 19(10), 1455–1460.

Cheng, W. J. and Wang, C. J. (2011). "Study of microstructure and phase evolution of hot-dipped aluminide mild steel during high-temperature diffusion using electron backscatter diffraction." *Appl. Surf. Sci.*, 257(10), 4663–4668.

Cheng, W.J. and Wang, C.J. (2013). "High-temperature oxidation behavior of hot-dipped aluminide mild steel with various silicon contents." *Appl. Surf. Sci.*, 274, 258–265

Cho, W.D. and Kim, I. (1999). "High-temperature corrosion of FeAl$_3$ in chlorine-containing environments." *Mater. Sci. Eng., A* 264, 269-278.

d'Heurle, F. M. (1994). "Interface Reactions with Formation of a Solid Phase on a Solid Substrate: A Short Overview." *Mater. Sci. Forum*, 156–156, 1–14.

Dangi, B., Brown, T. W., and Kulkarni, K. N. (2018). "Effect of silicon, manganese and nickel present in iron on the intermetallic growth at iron - aluminum alloy interface." *J. Alloys Compd.*, 769, 777–787.

Demange, V., Ghanbaja, J., Beeli, C., Machizaud, F., and Dubois, J. M. (2004). "Study of decagonal approximant and γ-brass-type compounds in Al-Cr-Fe thin films." *J. Mater. Res.*, 19(8), 2285–2297.

Deqing, W. (2008). "Phase evolution of an aluminized steel by oxidation treatment." *Appl. Surf. Sci.*, 254(10), 3026–3032.

Dorcheh, A. S., and Galetz, M. C. (2016). "Slurry aluminizing: A solution for molten nitrate salt corrosion in concentrated solar power plants." *Sol. Energy Mater. Sol. Cells*, 146, 8–15.

Dunlap, R.A., Lloyd, D. J., Christie, I. A., Stroink, G. and Stadnik, Z. M, (1988). "Physical properties of a rapidly quenched Al-Fe alloys." *J. Phys. F: Met. Phys.*,18 (7), 1329.

Dunlap, R.A., Dini, K., Stronik, G., Collins, G. S. and Jha, S. (1986). "An Fe Mössbauer effect study of metastable $Al_{86}Fe_{14}$ prepared by rapid solidification." *Hyperfine Interactions,* 28(1-4), 963-966.

Dybkov, V. I. (1994). "Phase stability during growth of compound layers." *Mater. Sci. Forum*, 155-156, 31-38.

Dybkov, V. I. (2013). "Solid State Reaction Kinetics", *IPMS Publications*, kyiv, Ukraine.

Effenberg, G., and Ilyenko, S. (2006). "Ternary Alloy Systems Phase Diagrams, Crystallographic and Thermodynamic Data."

Eggeler, G., Auer, W. and Kaesche, H. (1986). "On the influence of silicon on the growth of the alloy layer during hot dip aluminizing." *Mater. Sci.*, 21, 3348-3350.

Forcey, K. S., and Ross, D. K. (1991). "The formation of hydrogen permeation barriers on steels by aluminising." *J. Nucl. Mater.*, 182, 36–51.

Forcey, K. S., Ross, D. K., and Earwaker, L. G. (1985). "Investigation of the Effectiveness of Oxidised Fecralloy as a Containment for Tritium in Fusion Reactors*." *Zeitschrift für Phys. Chemie*, 143, 213–228.

Fukumoto, S., Inuki, T., Tsubakino, H., Okita, K., Aritoshi, M., and Tomita, T. (1997). "Evaluation of friction weld interface of aluminium to austenitic stainless steel joint." *Mater. Sci. Technol.*, 13(8), 679–686.

Fung, K. K., Zou, X. D., and Yang, C. Y. (1987). "Transmission electron microscopy study of Al 13 Fe 4 tenfold twins in rapidly cooled Al – Fe alloys." *Pholosophical Mag. Lett.*, 55(1), 27–32.

Garmong, G., Rhodes, C. G., and Spurlemg, R. A. (1973). "Crystallography and morphology of as-grown and coarsened Al-Al3Ni directionally solidified eutectic." *Metall. Trans.*, 4(3), 707–714.

Gebhardt, E. and Obrowski, W. (1954)."On the Constitution of the Copper-Lead-Oxygen System". *Z. Metallkde.*, *45*, 332-338.

Gialanella, S. (1995). "FeAl alloy disordered by ball-milling." *Intermetallics*, 3(1), 73–76.

Giggins, C. S. and Petit, F. S. (1971). "Oxidation of Ni-Cr-Al alloys between 1000°C and 1200°C." *J. Electrochem. Soc.*, 118, 1782-1789

Glasbrenner, H., Nold, E. and Boss, Z. (1997). "The influence of alloying elements on the hot-dip aluminizing process and on the subsequent high-temperature oxidation." *J. Nucl. Mater.*, 249, 39-45.

Grushko, B., and Velikanova, T. (2007). "Formation of quasiperiodic and related periodic intermetallics in alloy systems of aluminum with transition metals." *Calphad Comput. Coupling Phase Diagrams Thermochem.*, 31(2), 217–232.

Han, Y., Chen, X., Li, L., Zhang, X., and Zhou, D. (2018). "Effect of Si on the Formation and Growth of Intermetallic Compounds at Roll-Bonded Aluminum–Steel (Al-St) Interface." *J. Mater. Eng. Perform.*, 27(2), 333–343.

Hansen, M., Anderko, K. and Salzberg, H. W. (1958). "Constitution of binary alloys." *J. Electrochem. Soc.*, 105(12), 260-261.

He, L. X., Li, X. Z., Zhang, Z., and Kuo, K. H. (1988). "One-Dimensional Quasicrystal in Rapidly Solidified Alloys." 61(August), 1–6.

He, Z. B., Zou, B. S., and Kuo, K. H. (2006). "The monoclinic Al 45 Cr 7 revisited." *J. Alloys Compd.*, 417(1–2), 9–13.

Heumann, T. and Dittrich, S. (1959). "Structure character of the Fe_2Al_5 intermetallics compound in hot dip aluminizing process." *Z. Metallkde*, *50*, 617-625.

Huilgol, P. and Bhat, K. U. (2013). "Hot-Dip aluminizing of low carbon steel using Al-7Si-2Cu alloy Baths." *Journal of Coatings*, 2013, 6

Hwang, Y.-S., and Rapp, R. A. (1989). "Thermochemistry and Solubilities of Oxides in Sodium Sulfate-Vanadate Solutions." *Corrosion*, 45(11), 933–937.

Jones, R. D. and Dennier, S. D. (1980), "Proceedings of the 10th World congress in Metal Finishing." *Metal finishing society of Japan*, Kyoto.

Jones, R. H., Thomas, G. J. (2008). *Materials for the Hydrogen Economy*. Boca Raton: *CRC Press*.

Kattner, U. R. and Burton, B. P. (1992). "Al-Fe (Aluminum-Iron) Phase Diagrams of Binary Iron Alloys.*" ASM International, Materials Park, OH*, 12-28.

Kaufman, L., Bernstein, H. (1970). "Computer calculation of phase diagrams. With special reference to refractory metals." *Acad. Press*, 4, 344.

Kim, D. H., and Cantor, B. (1994). "Structure and decomposition behaviour of rapidly solidified Al-Fe alloys." *J. Mater. Sci.*, 29(11), 2884–2892.

Kim, S. H., Obulan Subramanian, G., Kim, C., Jang, C., and Park, K. M. (2018). "Surface modification of austenitic stainless steel for corrosion resistance in high temperature supercritical-carbon dioxide environment." *Surf. Coatings Technol.*, 349, 415–425.

Kobayashi, S., and Yakou, T. (2002). "Control of intermetallic compound layers at interface between steel and aluminum by diffusion-treatment." *Mater. Sci. Eng. A*, 338(1–2), 44–53.

Komatsu, N., Nakamura, M. and Fujita, H. (1981). "Reactions of iron with liquid aluminum." *J. Jpn. Inst. Met.*, 45, 416

Kriener, G., and Franzen, H. F. (1995). "A new cluster concept and its application to quasi-crystals of the i-A1MnSi family and closely related crystalline structures." *J. Alloys Compd.*, 221, 15–36.

Kwok, C. T., Cheng, F. T., and Man, H. C. (2006). "Cavitation erosion and corrosion behaviors of laser-aluminized mild steel." *Surf. Coatings Technol.*, 200(11), 3544–3552.

Laurila, T, Vuorinen V, Mattilla, T.T., Turunen, M., Paulasto-Krockel, M, Kivilahti, J. K. (2012). *Interfacial Compatibility in Microelectronics*. London: Springer.

Laurila, T., Vuorinen, V., and Kivilahti, J. K. (2005). "Interfacial reactions between lead-free solders and common base materials." 49, 1–60.

Lee, J.-Y., Heo, H., Kang, N., and Kang, C.-Y. (2018). "Microstructural Evolution of Reaction Layer of 1.5 GPa Boron Steel Hot-Dipped in Al-7wt%Ni-6wt%Si Alloy." *Metals.*, 8(12), 1069.

Lee, K., and Kumai, S. (2006). "Characterization of Intermetallic Compound Layer Formed at the Weld Interface of the Defocused Laser Welded Low Carbon Steel/6111 Aluminum Alloy Lap Joint." *Mater. Trans.*, 47(4), 1178–1185.

Lemmens, B., Springer, H., Duarte, M. J., Graeve, I. De, Strycker, J. De, Raabe, D., and Verbeken, K. (2016). "Atom probe tomography of intermetallic phases and interfaces formed in dissimilar joining between Al alloys and steel." *Mater. Charact.*, 120, 268–272.

Lemmens, B., Springer, H., Duarte, M. J., Graeve, I. De, Strycker, J. De, Raabe, D., and Verbeken, K. (2016). "Atom probe tomography of intermetallic phases and interfaces formed in dissimilar joining between Al alloys and steel." *Mater. Charact.*, 120, 268–272.

Levchuk, D., Koch, F., Maier, H., and Bolt, H. (2004). "Deuterium permeation through Eurofer and α-alumina coated Eurofer." *J. Nucl. Mater.*, 328(2–3), 103–106.

Li, Y. J., and Arnberg, L. (2004). "Solidification structures and phase selection of iron-bearing eutectic particles in a DC-cast AA5182 alloy." *Acta Mater.*, 52(9), 2673–2681.

Liberski, P., Gierek A., Kania, H., Podolski, P. and Tatarek, A. (2008). "Formation of coatings from liquid phase on the surface of iron-base alloys." *Arch. Foundry Eng.*, 8(4), 93-98.

Liu, B., Yang, Q., and Wang, Y. (2019). "Intereaction and intermetallic phase formation between aluminum and stainless steel." *Results Phys.*, 12, 514–524.

Liu, P., Thorvaldsson, T., and Dunlop, G. L. (1986). "Formation of intermetallic compounds during solidification of dilute Al–Fe–Si alloys." *Mater. Sci. Technol.*, 2(10), 1009–1018.

Louis, E., Mora, R., and Pastor, J. (1980). "Nature of star-shaped clusters of FeAl3 in aluminium-iron alloys." *Met. Sci.*, 14(12), 591–594.

Ma, X. L., Liebertz, H., Koster, U. (1996). "Multiple Twins of Monoclinic A113Fe4 Showing Pseudo-Orthorhombic and Fivefold Symmetries." *Phys. Status Solidi*, 158, 359–367.

Ma, X., He, Y., Wang, D., and Zhang, J. (2012). "Enhanced high-temperature corrosion resistance of (Al2O3-Y2O3)/Pt micro-laminated coatings on 316L stainless steel alloy." *Corros. Sci.*, 54(1), 183–192.

Mandal, P, Mandal, R K, Tiwari, R S, Srivastava, O. N. (1992). "Commensurate ordering in rapidly solidified Ti-Fe-Si alloys." *Phys. Rev. B*, 45(13), 7521–7524.

Mehrer, H. (1996). "Diffusion in Intermetallics." *Mater. Trans.*, 37(6), 1259–1280.

Morris, D. G., Munoz-Morris, M.A. and Chao, J. (2004). "Development of High Strength, High ductility and high creep resistant iron aluminide." *Intermetallics,* 12, 821-826.

Murakami, T., Nakata, K., Tong, H., and Ushio, M. (2003). "Dissimilar Metal Joining of Aluminum to Steel by MIG Arc Brazing Using Flux Cored Wire." *ISIJ Int.*, 43(10), 1596–1602.

Naoi, D. and Kajihara, M. (2007). "Growth behavior of Fe_2Al_5 during reactive diffusion between Fe and Al at solid-state temperatures." *Mater. Sci. Eng.*, A 459 (1-2), 375–382.

Nernst, W. (1904). "Theorie der Reaktiongeschwindigkeit in heterogenen Systemen." *Z. Physik. Chemie.*, 47(1), 52-55.

Palm, M. (1997). "The Al–Cr–Fe system–Phases and phase equilibria in the Al-rich corner." *J. Alloys Compd.*, 252(1–2), 192–200.

Paul, A., and Divinski, S. (2017). *Handbook of Solid State Diffusion*. Amsterdam, Netherlands: Elsevier Inc.

Peng, L. S. J., and Collins, G. S. (1997). "Disordering of FeAl by Mechanical Milling." *Mater. Sci. Forum*, 235–238, 535–540.

Pérez, F. J., Hierro, M. P., Pedraza, F., Carpintero, M. C., Gómez, C., and Tarín, R. (2001). "Effect of fluidized bed CVD aluminide coatings on the cyclic oxidation of austenitic AISI 304 stainless steel." *Surf. Coatings Technol.*, 145(1–3), 1–7.

Philibert, J. (1993). "Interplay of Diffusion and Interface Processes in Multiphase Diffusion." *Defect Diffus. Forum*, 95–98, 493–506.

Pint, B.A., Tortorelli, P.F. and Wright, I.G. (1999). "Long-term oxidation performance of ingot-produced Fe$_3$Al alloys." *Mater. High Temp.*, 16(1), 1–13.

Prasanna, K. M. N., Khanna, A. S., Chandra, R., and Quadakkers, W. J. (1996). "Effect of θ-alumina formation on the growth kinetics of alumina-forming superalloys." *Oxid. Met.*, 46(5–6), 465–480.

Pretorius, R., Marais, T.K. and Theron, C.C. (1993). "Thin film compound phase formation sequence: An effective heat of formation model." *Mater. Sci. Eng.*, 10, 1-83.

Pretorius, R., Vredenberg, A. M., Saris, F. W., and Reus, R. De. (1991). "Prediction of phase formation sequence and phase stability in binary metal aluminum thinfilm systems using the effective heat of formation rule." *J. Appl. Phys.*, 70, 3636.

Qiu, R., Satonaka, S., and Iwamoto, C. (2009). "Effect of interfacial reaction layer continuity on the tensile strength of resistance spot welded joints between aluminum alloy and steels." *Mater. Des.*, 30(9), 3686–3689.

Quivy, A., Quiquandon, M., Calvayrac, Y., Faudot, F., and Gratias, D. (1996). "A cubic approximant of the icosahedral phase in the (Al – Si)– Cu – Fe system." *J. Phys. Condens. Matter*, 8, 4223–4234.

Raghavan, V. (1987). Solid state phase transformations. *PHI Learning Pvt. Ltd.*, New Delhi.

Ranganathan, S. and Chattopadhyay, K. (1991). "Quasicrystals." *Annu. Rev. Mater. Sci.*, 21, 437–462.

Rapp, R. A., and Zhang, Y. S. (1994). "Hot corrosion of materials: Fundamental studies." *J. Miner. Met. Mater. Soc.*, 46(12), 47–55.

Rezaei, H., Akbarpour, M. R., and Shahverdi, H. R. (2015). "Effects of Interfacial Layers Fracture on the Dissolution Mechanism of Solid Fe in Liquid Al." 67(7), 1443–1450.

Richardson, O. W. (1904). "The Solubility and Diffusion in Solution of Dissociated Gases." *Philos. Mag.*, 7, 266–274.

Ryabov, V.R. (1985) "Aluminizing of Steel". *Oxonian Press*, New Delhi.

Sah, S. P., Tada, E., and Nishikata, A. (2018). "Enhancing Corrosion Resistance of Type 310S Stainless Steel in Carbonate Melt by Hot-Dip Aluminizing." *J. Electrochem. Soc.*, 165(7), C403–C411.

Sastry, G. V. S., Suryanarayana, C., VanTandaloo. G. (1982). "A Structural Study of Vapour-Deposited Al-Pd Alloys." *Phys. Status Solidi*, 73, 267–278.

Schubert, K., Rosler, U., Kluge, M., Anderko, K., and Harle, L. (1953). "Kristallographische Ergebnisse an Phasen mit Durchdringungsbindung." *Naturwissenschaften*, 40(16), 437–437.

Shahverdi, H. R., Ghomashchi, M. R., Shabestari, S., and Hejazi, J. (2002). "Microstructural analysis of interfacial reaction between molten aluminium and solid iron." *J. Mater. Process. Technol.*, 124, 345–352.

Sharafi, S., and Farhang, M. R. (2006). "Effect of aluminizing on surface microstructure of an HH309 stainless steel." *Surf. Coatings Technol.*, 200(16–17), 5048–5051.

Shin, D., Lee, J.-Y., Heo, H., and Kang, C.-Y. (2018). "TEM Microstructural Evolution and Formation Mechanism of Reaction Layer for 22MnB5 Steel Hot-Dipped in Al–10% Si." *Coatings*, 8(12), 467.

Sidhu, H. S., Singh Sidhu, B., and Prakash, S. (2006). "The role of HVOF coatings in improving hot corrosion resistance of ASTM-SA210 GrA1 steel in the presence of Na2SO4–V2O5 salt deposits." *Surf. Coatings Technol.*, 200(18–19), 5386–5394.

Singh, A., and Ranganathan, S. (1994). "Rational approximants to the decagonal phase in A1-Mn-M (M = Ni , Cu , Zn) systems." *Mater. Sci. Eng. A*, 182, 754–757.

Skjerpe, P. (1987). "An electron microscopy study of the phase Al3Fe." *J. Microsc.*, 148(1), 33–50.

Skjerpe, P. (1988). "Structure of AlmFe." *Acta Crystallogr. Sect. B*, 44(5), 480–486.

Springer, H., Kostka, A., Payton, E. J., Raabe, D., Kaysser-Pyzalla, A., and Eggeler, G. (2011). "On the formation and growth of intermetallic phases during interdiffusion between low-carbon steel and aluminum alloys." *Acta Mater.*, 59(4), 1586–1600.

Stein, F., Vogel, S.C., Eumann, M. and Palm, M. (2010)."Determination of the crystal structure of the ε phase in the Fe-Al system by high temperature neutron diffraction." *Intermetallics*, 18, 150-156.

Stroosnijder, M. F., Mevrel, R. and Bennett, M. J. (1994). "The interaction of surface engineering and high temperature corrosion protection." *Mater. High Temp.*, 12(1), 53-66

Suehiro, M., Kusumi, K., Miyokashi, T., Maki, J., Ohgami, M. (2003). "Properties of aluminum coated steels for hot-forming." *Nippon steel technical report*., (88), 16-21

Sugiyama, K., Hiraga, K., and Saito, K. (2000). "Cubic approximants in the Al – Pd – Fe and Al – Pd – Ru systems." *Mater. Sci. Eng. A*, 296, 345–347.

Sun, X., Stephens, E. V, Khaleel, M. A., Shao, H., and Kimchi, M. (2004). "Resistance Spot Welding of Aluminum Alloy to Steel with Transition Material

From Process to Performance Part I: Experimental Study." *Weld. Journal- New york*, 83, 188–195.

Sundman, B.O, Ikuo,O., Dupin, N., Kattner, U.R. and Fries, S.G. (2009)."An assessment of the entire Al–Fe system including D0$_3$ ordering." *Acta Mater.*, 57, 2896–2908.

Li, H. L., and Kuo, K. H. (1994). "Some new crystalline approximants of Al-Pd-Mn quasicrystals.", *Philos. Mag. Lett.*, 70(1), 55-62.

Tazhibaeva, I. L., Klepikov, A. K., Romanenko, O. G., Shestakov, V. P. (2000). "Hydrogen permeation through steels and alloys with different protective coatings", *Fusion Engineering and Design*, 51, 199-205.

Tian, W. H., Han, C. S., and Nemoto, M. (1999). "Precipitation of α-Cr in B2-ordered NiAl." *Intermetallics*, 7(1), 59–67.

Tomaszewicz, P. and Wallwork, G. R. (1984). "The oxidation of Fe-Al alloys containing chromium, nickel or manganese." *J. Corros. Sci. Eng.*, 40(4), 152-157

Tortorelli, P. F. and DeVan, J. H. (1992). "Behaviour of iron aluminides in oxidizing and oxidizing/sulphidizing environments." *Mater. Sci. Eng., A* 153(1-2), 573-577.

Van Sande M., De Rider R., Van Landuyt J., and Amelinckx S. (1978). "A Study by Means of Electron Microscopy and Electron Diffraction of Vacancy Ordering in Ternary Alloys of the System AlCuNi." *Physica Status Solidi (a)* 50(2), 587–599.

Van Tendeloo, G., Van Heurck, C., and Amelinkx, S. (1989). "One-Dimensional Quasi-Crystals In The Ternary System Al-Cu-Ni ?" *Solid State Commun.*, 71(9), 705–710.

Vogel, S. C., Stein, F. and Palm, M. (2010). "Investigation of the ε phase in the Fe-Al system by high temperature neutron diffraction", *Appl. Phys. A*, 99(3), 607-611.

Vuorinen, V., Yu, H., Laurila, T., and Kivilahti, J. K. (2008). "Formation of

Intermetallic Compounds Between Liquid Sn and Various CuNi x Metallizations." *J. Electron. Mater.*, 37(6), 792–805.

Walser, R. M., and Bené, R. W. (1976). "First phase nucleation in silicon – transitionmetal planar interfaces." *Appl. Phys. Lett.*, 624.

Wang, P., Deng, S., He, Y., Liu, C., and Zhang, J. (2016). "Oxidation and hot corrosion behavior of Al 2 O 3 /YSZ coatings prepared by cathode plasma electrolytic deposition." *Corros. Sci.*, 109, 13–21.

Wang, C. J., Badruddin, M. (2010). "The dependence of high-temperature resistance of aluminized steel exposed to water-vapour oxidation." *Surf. Coatings Technol.*,205, 1200-1205.

Yang, F., Xiang, X., Lu, G., Zhang, G., Tang, T., Shi, Y., and Wang, X. (2016). "Tritium permeation characterization of Al2O3/FeAl coatings as tritium permeation barriers on 321 type stainless steel containers." *J. Nucl. Mater.*, 478, 144–148.

Yang, H.G., Zhan, Q., Zhao, W.W., Yuan, X.M., Hu, Y., Han, Z.B. (2011). "Study of an iron aluminide and alumina tritium barrier coating", *J. Nuclear Materials*, 1-6.

Yang, J., Li, Y. L., Zhang, H., Guo, W., and Zhou, Y. (2015). "Control of interfacial intermetallic compounds in Fe-Al joining by Zn addition." *Mater. Sci. Eng. A*, 645, 323-327

Yin, F. C., Zhao, M. X., Liu, Y. X., Han, W., and Li, Z. (2013). "Effect of Si on growth kinetics of intermetallic compounds during reaction between solid iron and molten aluminum." *Trans. Nonferrous Met. Soc. China*, 23(2), 556–561.

Young, R. M. K., and Clyne, T. W. (1981). "An Al Fe intermetallic phase formed during controlled solidification." *Scr. Metall.*, 15(11), 1211–1216.

Yousaf, M., Iqbal, J. and Ajmal, M. (2011). "Variables affecting growth and morphology of intermetallic layer (Fe_2Al_5)." *Mater. Charact.*, 62, 517-525.

Yugeswaran, S., Kobayashi, A., and Ananthapadmanabhan, P. V. (2012). "Hot corrosion behaviors of gas tunnel type plasma sprayed La 2Zr 2O 7 thermal barrier coatings." *J. Eur. Ceram. Soc.*, 32(4), 823–834.

Zhang, H., Wang, D. H., and Kuo, K. H. (1989). "Icosahedral and decagonal quasicrystals, crystalline phases, and multiple twins in rapidly solidified Al13Cr4Si4." *J. Mater. Sci.*, 24(8), 2981–2986.

Zhu, L., Zhu, S., and Wang, F. (2013). "Hot corrosion behaviour of a Ni + CrAlYSiN composite coating in Na 2 SO 4 -25 wt.% NaCl melt." *Appl. Surf. Sci.*, 268, 103–110.

Zou, X. D., Fung, K. K., and Kuo, K. H. (1987). "Orientation relationship of decagonal quasicrystal and tenfold twins in rapidly cooled Al-Fe alloy." *Phys. Rev. B*, 35(9), 4526–4528.

Page intentionally left blank

List of Publications based on PhD Research Work

Sl. No	Title of the paper	Authors (in the same order as in the paper. Underline the Research Scholar's name)	Name of the Journal/ Conference/ Symposium, Vol., No., Pages	Month and Year of Publication	Category *
1	Formation of microstructural features in hot-dip aluminized AISI 321 stainless steel	Prashant Huilgol, K. Rajendra Udupa and K. Udaya Bhat	International Journal of Minerals, Materials & Metallurgy Vol:25, Page:190–198.	February 2018	1
2	Metastable microstructures at the interface between AISI 321 steel and molten Aluminum during Hot-dip Aluminizing	Prashant Huilgol, K. Rajendra Udupa and K. Udaya Bhat	Surface and Coatings Technology, Elsevier, Vol:348, Page:22-30	May 2018	1
3	Hot-dip Aluminizing of Low Carbon Steel in Al & Al-5wt % Cr Baths	Prashant Huilgol, K. Rajendra Udupa and K. Udaya Bhat	Materials Today: Proceedings, Elsevier, Vol: 5 (11-3), Page: 24702 to 24709	December 2018	3
4	Hot Corrosion Resistance of Hot-Dip-Aluminized AISI 321 Stainless Steel in a Salt Mixture of $60\%V_2O_5 + 40\% Na_2SO_4$ at 700 °C	Prashant Huilgol, K. Rajendra Udupa and K. Udaya Bhat	Transactions of Indian Institute of Metals, 2019	March 2019	1
5	Microstructural Investigations on the Hot-dip Aluminized AISI 321 Stainless Steel after Diffusion Treatment	Prashant Huilgol, K. Rajendra Udupa and K. Udaya Bhat	Surface and Coatings Technology, Elsevier, Vol:375, Page:544-553	October 2019	1

* Category: 1 : Journal paper, full paper reviewed
                   2 : Journal paper, Abstract reviewed
                   3 : Conference/Symposium paper, full paper reviewed
                   4 : Conference/Symposium paper, abstract reviewed
                   5 : others (including papers in Workshops, NITK Research Bulletins, Short notes etc.)
(If the paper has been accepted for publication but yet to be published, the supporting documents must be attached.)

Research Scholar

(Prashant Huilgol)
Date: 19/06/2020

Research Guides

(Prof. Udaya Bhat K.)   (Prof. K. Rajendra Udupa)
Date: Date:

Page intentionally left blank

BIO DATA

Name	: Prashant K. Huilgol
Father's name	: Krishna S. Huilgol
Date of birth	: 17-09-1987
Permanent address	: C/o K.S. Huilgol,
	"Narahari Krupa",
	Bhirdikar Compound,
	Malmaddi, Dharwad-580007
	Karnataka
Mobile	: +91-9019407581
E-mail ID	: prashanthuilgol@gmail.com

Academic qualification:

Bachelor of Engineering (B.E.) in Mechanical Engineering, from Gogte Institute of Technology, Belgaum (2009).

Master of Technology (M.Tech) in Materials Engineering, from National Institute of Technology, Karnataka (NITK), Surathkal (2012).

Google Scholar Citations

No. of publications : 16

Total citations : 116

h-index: 6

i10-index: 3

List of Publications

1. **P Huilgol**, KR Udupa, KU Bhat, (2019) "Microstructural Investigations on the Hot-dip Aluminized AISI 321 Stainless Steel after Diffusion Treatment", *Surface and Coatings Technology*, 375, 544-553

2. **P Huilgol**, KR Udupa, KU Bhat, (2019) "Hot Corrosion Resistance of Hot-Dip-Aluminized AISI 321 Stainless Steel in a Salt Mixture of 60% V_2O_5 + 40% Na_2SO_4 at 700 °C", *Transactions of the Indian Institute of Metals*, 1-4

3. **P Huilgol**, KR Udupa, KU Bhat, (2018) "Metastable microstructures at the interface between AISI 321 steel and molten aluminum during hot-dip aluminizing", *Surface and Coatings Technology 348, 22-30.*

4. **P Huilgol**, KR Udupa, KU Bhat,(2018) "Formation of microstructural features in hot-dip aluminized AISI 321 stainless steel", *International Journal of Minerals, Metallurgy, and Materials* 25 (2), 190-198.

5. GK Manjunath, **P Huilgol**, GVP Kumar, KU Bhat, (2018) "Precipitate evolution during severe plastic deformation of cast Al-Zn-Mg alloys and their thermal stability", *Materials Research Express* 6 (1), 016511.

6. M Jayalakshmi, **P Huilgol**, BR Bhat, KU Bhat, (2018) Insights into formation of gradient nanostructured (GNS) layer and deformation induced martensite in AISI 316 stainless steel subjected to severe shot peening, *Surface and Coatings Technology* 344, 295-302.

7. **P Huilgol**, KU Bhat, KR Udupa, (2018) "Hot-dip Aluminizing of Low Carbon Steel in Al & Al-5wt % Cr Baths, *Materials Today : Proceedings* 5 (11(3)), 24702-24709.

8. JR Mohan Raj, R Vittal, **P Huilgol**, U Bhat, I Karunasagar (2018), "T4-like *Escherichia coli* phages from the environment carry bla_{CTX-M}, *Letters in applied microbiology* 67 (1), 9-14

9. GK Manjunath, GVP Kumar, KU Bhat, **P Huilgol** (2018), "Microstructure and Mechanical Properties of Cast Al-5Zn-2Mg Alloy Subjected to Equal-Channel Angular Pressing, *Journal of Materials Engineering and Performance* 27 (11), 5644-5655.

10. M Jayalakshmi, **P Huilgol**, BR Bhat, KU Bhat,(2016), "Microstructural characterization of low temperature plasma-nitrided 316L stainless steel surface with prior severe shot peening, *Materials & Design* 108, 448-454.

11. A Augustin, **P Huilgol**, KR Udupa, U Bhat, (2016), Effect of current density during electrodeposition on microstructure and hardness of textured Cu coating in the application of antimicrobial Al touch surface, *Journal of the mechanical behavior of biomedical materials* 63, 352-360.

12. SM Vidya, S Mutalik, KU Bhat, **P Huilgol**, K Avadhani, (2016), "Preparation of gold nanoparticles by novel bacterial exopolysaccharide for antibiotic delivery" *Life sciences* 153, 171-179.

13. UK Bhat, RK Udupa, S Prakrathi, **P Huilgol** (2016), "Microstructure and impression creep behavior of Al based surface composite produced by friction stir processing", *Transactions of the Indian Institute of Metals* 69 (2), 623-627.

14. J Patel, **P Huilgol**, N Jamnapura, K Udaya Bhat (2015), "Hot dip Aluminizing of 9Cr-1Mo Steels and their Heat Treatment, *Materials Science Forum* 830, 143-146.

15. **P Huilgol**, S Bhat, KU Bhat (2013), "Hot-Dip Aluminizing of Low Carbon Steel Using Al-7Si-2Cu Alloy Baths", *Journal of Coatings* 2013.

16. UB Kuruveri, **P Huilgol**, J Joseph (2013), "Aluminising of mild steel plates ",*ISRN Metallurgy* 2013.